ABSTRACT

Title of thesis: OUTFLOW BOUNDARY CONDITIONS FOR LOW-MACH BUOYANT COMPUTATIONAL FLUID DYNAMICS

Ben Trettel, Master of Science, 2013

Thesis directed by: Professor Arnaud Trouvé
Department of Fire Protection Engineering

General issues with outflow boundary conditions are discussed, as are the issues specific to flow with buoyancy such as unphysical build-up of fluid at the outflow boundary. Different solutions to these problems are detailed. The sponge-layer approach is used to model the outflow boundary in buoyant jets. The successes and shortcomings of the sponge-layer approach are made clear through comparisons with long domain simulations.

OUTFLOW BOUNDARY CONDITIONS FOR LOW-MACH BUOYANT COMPUTATIONAL FLUID DYNAMICS

by

Ben Trettel

Thesis submitted to the Faculty of the Graduate School of the
University of Maryland, College Park in partial fulfillment
of the requirements for the degree of
Master of Science
2013

Advisory Committee:
Prof. Arnaud Trouvé, Chair and Advisor
Prof. André Marshall
Dr. Randall McDermott

Acknowledgements

I'd like to thank my thesis advisor, Arnaud Trouvé, for his guidance and the suggestion of a research topic as challenging and fascinating as open boundary conditions.

I'd like to thank Luis Bravo and Andrew Voegele for helping me set up LES-BLAC and for the technical advice they provided.

I'd like to thank Randy McDermott for our discussions in the spring and summer of 2013 which improved this work.

I'd like to thank Kevin McGrattan for explaining precisely which boundary conditions FDS uses to me and clarifying which boundary conditions were used in the FDS guides.

I'd like to thank my office-mates at UMD and NIST, Sebastien Vilfayeau, Zohreh Ghorbani, Vivien Lecoustre, Morgan Bruns, and Topi Sikanen, for helpful comments.

I'd like to thank Craig Weinschenk of NIST for helpful suggestions regarding the organization of this thesis.

Finally, I'd like to thank my brother, Andrew Trettel, for carefully reading my thesis.

Contents

1 Open boundary conditions background **1**

1.1 Introduction . . . 1

1.2 Continuous boundary conditions . . . 3

1.2.1 Velocity and scalar boundary conditions . . . 3

1.2.2 Pressure boundary conditions . . . 5

1.3 Boundary conditions for pressure projection methods . . . 7

1.3.1 Velocity boundary conditions . . . 7

1.3.2 Pressure boundary conditions . . . 8

1.4 Difficulties with artificial outflow boundary conditions . . . 10

1.4.1 Numerical stability . . . 10

1.4.2 Order of accuracy . . . 10

1.4.3 Reflections . . . 11

1.4.4 Semi-permeable outflows and unphysical backflow . . . 11

1.4.5 Generalization . . . 12

1.5 Solutions to difficulties . . . 12

1.5.1 Better outflow boundary conditions . . . 12

1.5.2 Sponge (or absorbing) layers . . . 13

1.5.3 Stretched grids . . . 14

1.5.4 Other ideas . . . 15

2 LES-BLAC **17**

2.1 Partial differential equations . . . 17

2.1.1 Governing equations . . . 17

2.1.2 Non-dimensionalization . . . 23

2.2 Numerics . . . 24

2.2.1 Spatial-temporal grid . . . 24

2.2.2 Time advancement scheme . . . 25

2.2.3 Discretizing the fluid equations . . . 26

2.2.4 Implementation . . . 28

2.3 Boundary conditions . . . 29

2.3.1 Pressure BCs . . . 30

2.3.2 Far-field BC . . . 30

2.3.3 Prescribed inflow BC . . . 30

2.3.4 Outflow BC . . . 30

3 Buoyant jet flow tests **31**
3.1 Physical stability criteria . . . 31
3.2 Numerical configuration . . . 34
3.2.1 Reference scales for non-dimensionalization . . . 34
3.2.2 Gravity and specified dimensionless parameters . . . 34
3.2.3 Inlet boundary condition . . . 35
3.2.4 Outlet boundary condition . . . 35
3.2.5 Far-field boundary condition . . . 35
3.2.6 Numerical grid . . . 36
3.2.7 Probes . . . 37
3.3 Simulation of jets with and without sponge-layers . . . 41
3.3.1 Comparison with experiments . . . 42
3.3.2 Comparisons between different runs . . . 42
3.4 Conclusion . . . 49

Appendix: $T/T_{\mathbf{atm}} = 1.5$ plots **50**
4.5 Instantaneous fields . . . 50
4.6 Time-averaged fields . . . 62
4.7 Instantaneous centerlines . . . 74
4.8 Time-averaged centerlines . . . 79
4.9 Instantaneous outflow profiles . . . 84
4.10 Time-averaged outflow profiles . . . 89
4.11 Probes . . . 94

Appendix: $T/T_{\mathbf{atm}} = 2$ plots **98**
5.12 Instantaneous fields . . . 98
5.13 Time-averaged fields . . . 110
5.14 Instantaneous centerlines . . . 122
5.15 Time-averaged centerlines . . . 127
5.16 Instantaneous outflow profiles . . . 132
5.17 Time-averaged outflow profiles . . . 137
5.18 Probes . . . 142

Appendix: $T/T_{\mathbf{atm}} = 4$ plots **146**
6.19 Instantaneous fields . . . 146
6.20 Time-averaged fields . . . 154
6.21 Instantaneous centerlines . . . 162
6.22 Time-averaged centerlines . . . 165
6.23 Instantaneous outflow profiles . . . 168
6.24 Time-averaged outflow profiles . . . 171
6.25 Probes . . . 174

References **177**

List of Figures

1.1 Comparison of a truncated computational domain and the full physical domain of a fire plume. 2
1.2 Unphysical reflection of vorticity off of an open boundary on the right side as seen in FDS [Tre13]. The left figure is the initial condition, which was initialized traveling to the right. The vorticity should be zero everywhere in the right figure. 11
1.3 Semi-permeable outflow plane as seen in vorticity contours in FDS [Tre13]. Each frame is separated by 0.2 s. The blue vortex on the left is shed from a plume and rises under the influence of buoyancy, and it then moves along the outflow boundary as it slowly leaves the domain. . . 12

2.1 Location of the variables in the spatial-temporal cell. 25

3.1 A buoyant helium-air jet from the experiments of Cetegen, Dong, and Soteriou [CDS98, fig. 5, p. 1662]. 32
3.2 An experimental stability diagram for buoyant jets from Cetegen, Dong, and Soteriou [CDS98, fig. 6, p. 1663]. 32
3.3 Stability diagram for heated jets based on a simple theory compared against experimental data. 33
3.4 Schematic of the jet simulations including boundary conditions and the location of the sponge-layer, when it exists. 34
3.5 Inlet profiles for the jet cases in this work. The temperature plot is an example — the maximum temperature is a parameter that was varied in the simulations. Points correspond to actual grid points. 38
3.6 Temperature contours for cases with different domain widths. Black is $T = 1.5$. White is $T = 1.0$. The black line is where $\mathrm{Ra}_x = 0.5 \times 10^7$, which corresponds approximately to where the turbulent transition occurs. 39
3.7 Temperature as a function of time in a jet for different domain widths. The 60 wide case did not run very far in time and it did not yet go unstable. 40
3.8 Temperature contours for long domain, no sponge-layer case. 43
3.9 Temperature contours for long domain, no sponge-layer case. 43
3.10 Temperature contours for short domain, no sponge-layer case. 44
3.11 Temperature contours for short domain, no sponge-layer case. 44

3.12 Time-averaged u-velocity at the outlet for short domain, no sponge-layer case. 45
3.13 u-velocity contours for short domain, no sponge-layer case. 45
3.14 Centerline temperature probe one jet width from the inlet for short domain, no sponge-layer case. 45
3.15 Temperature contours for short domain, 10 unit sponge-layer with 10-times viscosity increase case. 46
3.16 Time-averaged u-velocity at the outlet for short domain, 10 unit sponge-layer with 10-times viscosity increase case. 46
3.17 u-velocity contours for short domain, 10 unit sponge-layer with 10-times viscosity increase case. 47
3.18 Centerline temperature probe one jet width from the inlet for short domain, 10 unit sponge-layer with 10-times viscosity increase case. . . 47
3.19 Temperature contours for the short domain, 10 unit sponge-layer with 10-times viscosity increase case. 48
3.20 Temperature contours for long domain, no sponge-layer case. 48

1

Open boundary conditions background

[Open boundary conditions present] an open and substantial modeling problem that is no less challenging, and arguably no less important, than subgrid modeling for turbulence.

– Tim Colonius, Caltech [Col04]

1.1 Introduction

Often in computational fluid dynamics a user truncates the simulated domain to reduce computational cost, as shown in figure 1.1. Truncation is possible if everything outside of the truncated region has limited influence on the inside of the computational domain (e.g., everything is flowing out, especially for supersonic flows), or if the plane where the truncation occurs can be reasonably modeled (e.g., at prescribed inflows). The boundary conditions at these truncated planes are called artificial boundary conditions. Artificial boundary conditions model the effect of the domain outside of the computed domain.

Artificial boundary conditions are imperfect. Common shortcomings include reflections of outgoing waves and unphysical build-up of fluid near the boundary. The artificial boundary's location is arbitrary and not part of the physical problem, so these effects are completely unphysical. These shortcomings suggest that outflow

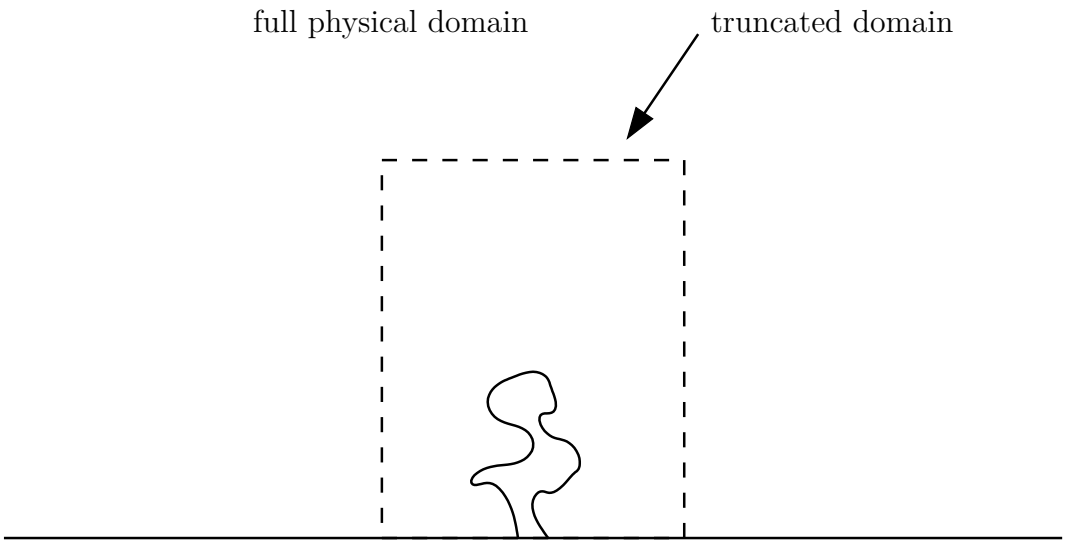

Figure 1.1: Comparison of a truncated computational domain and the full physical domain of a fire plume.

planes with artificial boundary conditions are only semi-permeable. There are two main approaches to solving these problems: increasing the convective outflow velocity and damping out gradients near the boundary. Both are used in this work.

For buoyancy-driven flows, outflow conditions often are particularly difficult. Walchshofer, Steiner, and Brenn [WSB10, p. 715] note that in buoyancy-driven nozzle flows "[as] the distance from the nozzle increases, statistically steady-state variable density jets typically feature expanded regions with reversed flow and large buoyancy-driven vortical structures, which may lead to numerical instabilities at the outflow boundary." The popular fire CFD code FDS has difficulties convecting out vorticity at the boundary in some contrived cases [Tre13]. The code used for this work, LES-BLAC, has difficulties convecting hot gases at the boundary in some cases, as shown in ch. 3. Resolving these issues allows us to use smaller, less computationally expensive domains while maintaining accuracy.

LES-BLAC is a low-Mach CFD code that uses zero-gradient boundary conditions for the pressure and Orlanski boundary conditions for the velocity. This work maintains those boundary conditions. However, a survey of the different available

boundary conditions for CFD of low-Mach flows using projection methods has not yet been done and will help in understanding the successes and failures of different approaches.

1.2 Continuous boundary conditions

1.2.1 Velocity and scalar boundary conditions

The velocity field (u_j) and scalar quantities (ϕ_k, which could be a mass fraction or temperature, for example) are transported from the computational domain at outflow boundaries. There are several ways to accomplish this.

Navier-Stokes Characteristic Boundary Conditions

Poinsot and Veynante [PV05, §9.3.5, p. 444] develop accurate boundary conditions for compressible viscous flows using characteristic analysis. Unfortunately, these boundary conditions can not be used for low-Mach flows (like in this work) because such flows neglect acoustic waves [WSB10, pp. 715-716].

Zero-gradient boundary condition

A zero-gradient — also called the Neumann boundary condition[1] or continuative [Hir13] — boundary condition is commonly used. This boundary condition is

$$\frac{\partial \phi}{\partial n} = 0 \ , \tag{1.2.1}$$

where ϕ is any scalar or velocity component and n is a direction normal to the boundary. For example, the Fire Dynamics Simulator (FDS) uses this boundary condition for the tangential velocity (u_t), divergence of the velocity field ($\partial u_l / \partial x_l$), temperatures ($T$), and mass fractions ($Y_k$) [McG+13, §4.6.1, §3.2.3].

This boundary condition makes physical sense if the boundaries are far away

1 Though Neumann boundary conditions apply in more general — the value of the gradient is not necessarily zero.

from high gradients. In physical simulations we often expect low gradients away from sources (e.g., heat sources or inflow boundaries), and enforcing the condition that quantities do not change through the boundary is one way to achieve this. Unfortunately, on occasion "far away" means too far away, leading to computationally expensive results even with stretched grids.

Zero-gradient boundary conditions cause numerical instabilities for strongly buoyant jets in at least some conditions [WSB10, p. 715].

Orlanski boundary conditions

Orlanski [Orl76] describes a simple convective boundary condition for any variable:

$$\frac{\partial \phi}{\partial t} + C\frac{\partial \phi}{\partial n} = 0 \ . \tag{1.2.2}$$

Orlanski calls this boundary condition the Sommerfield radiation condition, though any condition of this form can be called an Orlanski boundary condition, regardless of whether the phase (or convective) velocity C Orlanski defined is used.

This boundary condition makes sense because its hyperbolic nature will convect out any quantity ϕ. The boundary condition resembles the Navier-Stokes equations for this reason as well. However, its purely hyperbolic form lacks terms associated with buoyancy and viscosity which may be important in some cases where those physics are important. Fournier, Golanski, and Pollard [FGP08] modified this boundary condition to include a viscous term and demonstrate improved accuracy at the outflow.

The choice of the convective velocity. For this work, we take $C = \max u_{\mathrm{n}}$ where u_{n} is the velocity in the direction normal to the outflow boundary as suggested by Pierce [Pie01, p. 75]. Alternatives include the mean outflow velocity and a prescribed velocity following, for example, a known velocity profile to which you want the solution to relax to. The mean outflow velocity is often too low, and it leads to build-up of material near the outflow.

The Neumann boundary condition can be seen as a special class of Orlanski boundary conditions as $C \to \infty$.

1.2.2 Pressure boundary conditions

Mathematically, pressure requires no boundary condition because the pressure field is uniquely determined (up to a constant for incompressible and low-Mach flows) from the velocity, density, scalar, etc. fields via the momentum equations. However, in computational fluid dynamics, boundary conditions almost always must be applied because the solvers used expect boundary conditions.

Zero-gradient boundary condition

As in the velocity and scalar cases, a zero-gradient boundary condition can be used for the pressure. How far away the boundary must be from large gradients is unclear here, however. For incompressible wall flows at high Reynolds numbers, this boundary condition can be derived from the momentum equation.

Incompressible (divergence-free velocity field) Navier-Stokes equations

Gresho and Sani [GS87, p. 1117] use the incompressible momentum equation (with constant viscosity) to determine which pressure boundary condition the Navier-Stokes equations implies. In the direction normal to the boundary, the pressure gradient is

$$\frac{\partial p}{\partial n} = \rho \left[\nu \frac{\partial^2 u_\mathrm{n}}{\partial x_i^2} - \left(\frac{\partial u_\mathrm{n}}{\partial t} + u_i \frac{\partial u_\mathrm{n}}{\partial x_i} \right) \right] , \tag{1.2.3}$$

where u_n is the velocity in the direction normal to the boundary.

At walls, a simple high Re approximation exists [GS87, p. 1119] because u_n equals zero and $\nu \to 0$:

$$\frac{\partial p}{\partial n} = 0 . \tag{1.2.4}$$

Thus, the zero-gradient Neumann condition is correct for high Re wall flows. However, this boundary condition is not necessarily appropriate for open flows. Despite that

limitation, this boundary condition is commonly used in general.

Low-Mach N-S equations

Similar equations can be derived from the low-Mach form of the Navier-Stokes equations, e.g., from eqn. 2.1.35 in non-dimensional form:

$$\frac{\partial p}{\partial n} = \frac{\partial}{\partial x_i}\left[\frac{1}{\mathrm{Re}}\left(\frac{\partial u_i}{\partial x_j}+\frac{\partial u_j}{\partial x_i}\right)-\frac{2}{3}\delta_{ij}\frac{1}{\mathrm{Re}}\frac{\partial u_l}{\partial x_l}\right] + \frac{1}{\mathrm{Fr}_j}(1-\rho)-\left(\frac{\partial \rho u_j}{\partial t}+\frac{\partial \rho u_i u_j}{\partial x_i}\right) \tag{1.2.5}$$

Above j is the normal direction. Given the number of terms, the zero-gradient approximation seems inappropriate as a general boundary condition unless a large distance separates the boundary from gradients in the fields.

Bernoulli's principal

If all flow is inviscid and follows streamlines normal to the boundaries, Bernoulli's principal can be used to derive boundary conditions for the pressure under inflow and outflow conditions. This boundary condition was developed in FDS [McG+13, §4.61]. If the total pressure ($H \equiv p/\rho + (u_i u_i)/2$) is constant along a streamline, Dirichlet conditions for pressure can be developed. For outgoing flows, p is an external pressure and all other quantities are interpolated to locations at the boundary if necessary. For incoming flows, the velocity in the boundary condition can be found either by using another velocity boundary condition or (as is done in FDS) treating the boundary velocity as a far-field velocity. The same decisions must be made with the mass density.

When the streamlines are not normal to the boundary, this boundary condition could work poorly. FDS has difficulty convecting out some vortices [Tre13], potentially due to this shortcoming, though this is speculation at this stage. See §1.4.3 and §1.4.4 for illustrations of this phenomena.

OpenFOAM `buoyantPressure` condition

OpenFOAM [Ope11, lines 115 to 130] has the following boundary condition (called `buoyantPressure`) for the pressure at outflows in buoyancy-driven flows:

$$\frac{\partial p}{\partial n} = \frac{\partial \rho}{\partial n} g \Delta x \ . \tag{1.2.6}$$

This represents the spatial derivative of a pressure field like $p = p_0 + \rho g \Delta x$. In a sense, Δx is used to "interpolate" in space inside this pressure field.

1.3 Boundary conditions for pressure projection methods

Certain boundary conditions are more consistent with pressure projection methods. Pressure projection methods use a fractional step approach. Boundary conditions for three quantities must be considered:

1. $\widehat{u}_j^{n+1}$ (or sometimes $u_j^{n+1/2}$) — the predicted (or intermediate) velocity field
2. p^{n+1} (or sometimes $p^{n+1/2}$) — the projection pressure
3. u_j^{n+1} — the corrected velocity field

n is the time-step index and j is the direction index.

To differentiate discrete differentiation from continuous differentiation, the partial operator (∂) is used for continuous differentiation, and the delta operator (δ) is used for discrete differentiation. The precise discrete differencing procedure is unimportant given that it is stable, convergent, and conservative.

1.3.1 Velocity boundary conditions

Kim and Moin [KM85] considered the effect of the intermediate velocity field on the computation for incompressible flows. They conclude (on p. 313) that "except when the boundary conditions for the intermediate velocity field are chosen to be consistent with the governing equations, the solution may suffer from appreciable

numerical errors." Using a Taylor series analysis they derive a boundary condition for the intermediate velocity, which is a function of the desired corrected velocity boundary condition. Unless this boundary condition is used, the computation is at best first-order accurate (unless otherwise exact boundary conditions are used, e.g., periodic boundary conditions). This boundary condition is

$$\widehat{u}_j^{n+1} = u_j^{n+1} + \Delta t \frac{\delta p^n}{\delta x_j} \ . \tag{1.3.1}$$

Armfield and Street [AS03] show that such a boundary condition is only necessary when the pressure is set to zero in the momentum equation to calculate the intermediate velocity. When the pressure is set to the previous time step's pressure in the momentum equation to get the intermediate velocity, the correct order of accuracy is obtained (provided that the projection pressure is compared against the exact solution at the correct time). The CFD code used for this thesis, LES-BLAC, takes this latter approach.

1.3.2 Pressure boundary conditions

Temam [Tem91] shows that a certain configuration of the pressure projection method for incompressible flows implies zero-gradient boundary conditions for the pressure. He starts with the incompressible N-S equations,

$$\frac{\partial u_i}{\partial x_i} = 0 \ , \tag{1.3.2}$$

$$\frac{\partial u_j}{\partial t} + u_i \frac{\partial u_j}{\partial x_i} = \frac{\partial p}{\partial x_j} + \nu \frac{\partial^2 u_j}{\partial x_i^2} + f_j \ , \tag{1.3.3}$$

with the boundary condition

$$u_i v_i = 0 \tag{1.3.4}$$

where v_i is a unit vector normal to the boundary. This boundary condition implies the boundaries are impermeable walls. He derives the following pressure projection

scheme from that:

$$\frac{\widehat{u}_j^{n+1} - u_j^n}{\Delta t} + \widehat{u}_i^{n+1}\frac{\delta}{\delta x_i}\widehat{u}_j^{n+1} = \nu\frac{\delta^2}{\delta x_i^2}\widehat{u}_j^{n+1} + f_j \ , \tag{1.3.5}$$

$$\frac{u_j^{n+1} - \widehat{u}_j^{n+1}}{\Delta t} = -\frac{\delta}{\delta x_j}p^n \ , \tag{1.3.6}$$

$$\frac{\delta}{\delta x_i}u_i^{n+1} = 0 \ , \tag{1.3.7}$$

with boundary conditions

$$\widehat{u}_j^{n+1} = 0 \ , \tag{1.3.8}$$

$$v_i u_i^{n+1} = 0 \ . \tag{1.3.9}$$

The Neumann boundary condition for p can be derived by taking the dot product of v_i and eqn. 1.3.6:

$$\frac{\cancelto{0}{v_i u_i^{n+1}}^{\text{0 by eqn. 1.3.9}} - \cancelto{0}{v_i \widehat{u}_i^{n+1}}^{\text{0 by eqn. 1.3.8}}}{\Delta t} + v_i\frac{\delta}{\delta x_i}q^n = 0 \ , \tag{1.3.10}$$

which returns

$$v_i\frac{\delta}{\delta x_i}p^n = \frac{\delta}{\delta n}p^n = 0 \ , \tag{1.3.11}$$

where the subscript n refers to the normal direction, not the time step. This result is consistent with that of Gresho and Sani [GS87] for high Re wall flows.

Similar analysis can be performed for other boundary conditions. When $u_j^{n+1} = \widehat{u}_j^{n+1}$, e.g., for the case where the more accurate boundary condition by Kim and Moin [KM85] is unnecessary, the Neumann condition also applies trivially as the right hand side of eqn. 1.3.6 is zero. Using the intermediate boundary condition of Kim and Moin [KM85] leads to the pressure gradient being maintained at the boundary.

For the case where derivatives of the velocity are specified at the boundary and the

intermediate boundary condition is set to the corrected boundary condition, differentiation of eqn. 1.3.6 leads to the boundary condition

$$\frac{\delta^2}{\delta n^2} p^n = \frac{1}{\Delta t} \left(\frac{\delta}{\delta n} \widehat{u}_n^{n+1} - \frac{\delta}{\delta n} u_n^{n+1} \right) . \tag{1.3.12}$$

An alternative is to find the the implied pressure gradient directly from eqn. 1.3.6 when the intermediate and corrected velocities at the boundary are known, e.g., when using one of the previously mentioned velocity boundary conditions.

1.4 Difficulties with artificial outflow boundary conditions

1.4.1 Numerical stability

Boundary conditions can cause numerical instabilities. Generally boundary conditions are not amenable to easy stability analysis due to non-linearities in the problem, and consequently stability analysis is limited to certain difference schemes and boundary conditions [Dut88; Pet01].

1.4.2 Order of accuracy

Exact boundary conditions exist, and they are simply extensions of the interior equations, e.g., the pressure boundary condition discussed in §1.2.2. The order of accuracy of the boundary condition influences the overall order of accuracy of the computation. Often the accuracy of the spatial derivatives used decreases due to the use of one-sided differencing. Another difficulty arises with one-sided differencing: one-sided differencing is unconditionally unstable when it is performed in the direction of traveling waves. Thus, exact boundary conditions may not necessarily be stable. Incoming waves need to be specified by the boundary conditions for stability in this case [PV05, p. 436].

When a convergent boundary condition is not used, then the boundary condition is a source of a zeroth-order error. This may be acceptable if the magnitude of the error

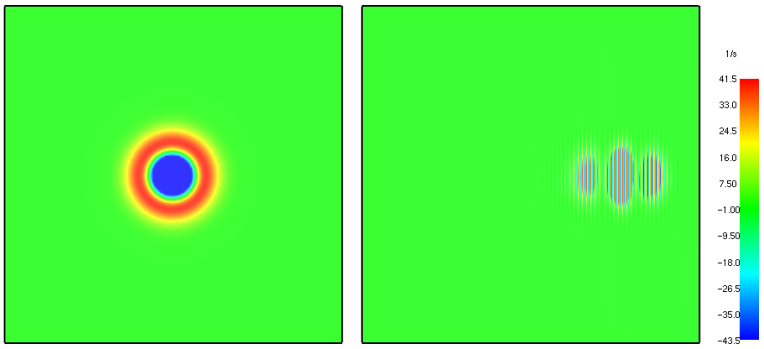

Figure 1.2: Unphysical reflection of vorticity off of an open boundary on the right side as seen in FDS [Tre13]. The left figure is the initial condition, which was initialized traveling to the right. The vorticity should be zero everywhere in the right figure.

is small, as can be determined by comparisons with experiments and long domain simulations.

1.4.3 Reflections

Another common problem with artificial outflow boundary conditions is unphysical reflections off the boundary. FDS has difficulty with this for the vorticity field, as shown in figure 1.2. A vortex traveled to the right and passed through the boundary, creating the strange reflection shown. Non-reflective boundary conditions are difficult to create, and absolute non-reflectivity of viscous boundary conditions is limited to 1d analysis even for the linearized case [Col04, p. 333].

1.4.4 Semi-permeable outflows and unphysical backflow

Often the outflow plane with an artificial boundary condition is only semi-permeable. An example of this behavior is shown in figure 1.3. A vortex is shed off a helium plume and it rises, but the artificial boundary altered its trajectory. The cause of issues like this is that the boundary is only semi-permeable, or in some cases, the flow is reversed at locations along the boundary when time-averaged. Neither behavior is physical when a time-averaged flow out of the domain is expected.

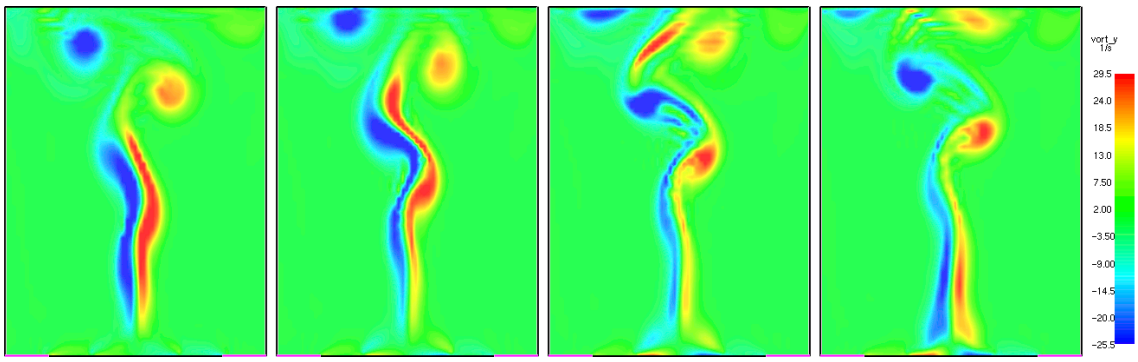

Figure 1.3: Semi-permeable outflow plane as seen in vorticity contours in FDS [Tre13]. Each frame is separated by 0.2 s. The blue vortex on the left is shed from a plume and rises under the influence of buoyancy, and it then moves along the outflow boundary as it slowly leaves the domain.

1.4.5 Generalization

Walchshofer, Steiner, and Brenn [WSB10] proposed an absorbing layer approach that biased the outflow profiles towards prescribed profiles. They found the prescribed profiles to be a source of inaccuracy. It also prevents the generalization of their method. This work relaxes this restriction by using the convective outflow condition for all outflow variables. This boundary condition is more general, though it may not work as well when the outflow profile is known.

1.5 Solutions to difficulties

Colonius [Col04] discusses a variety of approaches to construct artificial boundary conditions for inflows and outflows in compressible flows. A few of these, like the Navier-Stokes Characteristic Boundary Conditions, are applicable to only compressible flows, but many of the concepts in the paper are generally applicable.

1.5.1 Better outflow boundary conditions

One path to solve these difficulties is to use more accurate boundary conditions. Unfortunately, this is difficult. Many convergent outflow boundary conditions use one-sided differencing that is not necessarily stable. And these boundary conditions

are more complicated. Many boundary conditions were designed for essentially uniform flows, and they consequently work poorly in more complex flows that include large gradients from turbulence or other sources. Colonius [Col04] discusses these issues and suggests that in practical computations, the added computational effort may not be worth the mild improvement in accuracy.

1.5.2 Sponge (or absorbing) layers

Problems with outflow boundary conditions are often caused by large gradients near the boundary, where a zero-gradient boundary condition might be enforced. One way to damp out these gradients is to use a sponge-layer. A sponge-layer is a region of high viscosity and/or thermal conductivity before the boundary. The high viscosity will damp out significant gradients, allowing the boundary conditions to work better. The viscosity also will damp out reflections, preventing them from influencing the physical domain.

In LES-BLAC, the overall viscosity is decomposed into $\mu = \mu_{\mathrm{m}} + \mu_{\mathrm{sl}}$ where "m" refers to the (physical) molecular viscosity and "sl" refers to the sponge-layer region. The sponge-layer is implemented by adding additional viscosity (μ_{sl}) which increases quadratically from zero at the start of the sponge-layer to a terminal value at the outlet.

The main disadvantage of a sponge-layer is that you have a potentially large non-physical region of your computational domain. Likely the true non-physical region extends beyond the limits of the sponge-layer. The only way to determine what is non-physical or not is to compare against experiments or large-domain simulations where the influence of the boundaries is kept to a minimum due to the size of the domain.

One issue with sponge-layers is that the interface between the "physical" domain and the sponge layer can reflect waves [Col04, p. 334]. This issue can be resolved by using carefully designed sponge-layers. The parameters of the sponge-layer can be de-

termined via theory such that they are perfectly non-reflective for linear waves, which Colonius [Col04] notes works well, however, ad-hoc tuning also is successful. Making the viscosity increase gradually from its physical domain value to the sponge-layer value is one method that can prevent reflections.

Increasing viscosity and length of sponge-layer

The parameters to control in a sponge-layer are the shape of the viscosity profile, the maximum value of the viscosity, and the length of the sponge-layer. Increasing the viscosity and length of the sponge-layer will damp out large gradients more, allowing the outflow boundary condition to work with less difficulties. However, due to the elliptic nature of the pressure equation in LES-BLAC, the upstream flow may be influenced if the viscosity is too high. Also, longer sponge-layers can become computationally expensive; avoiding computationally expensive long domains is generally the reason better outflow treatments are desired.

Smagorinsky-type viscosity

Inspired by the Smagorinsky eddy-viscosity model, Walchshofer, Steiner, and Brenn [WSB10, pp. 721-722] develop a new type of sponge-layer where the viscosity is not increased so indiscriminately. This approach avoids the addition of unnecessary unphysical viscous dissipation, which may reduce the region of influence of the sponge-layer. They choose μ_{sl} with

$$\mu_{\text{sl}} = \rho(C\overline{\Delta})^2||\mathbf{S}|| \ , \tag{1.5.1}$$

where C is a model parameter, $\overline{\Delta}$ is the mesh size, and $||\mathbf{S}||$ is the norm of the resolved strain rate. To let the viscosity modification come into effect smoothly, C is increased from 0 at the start of the sponge-layer to 0.2 at the boundary.

1.5.3 Stretched grids

Long domains add computational cost. A stretched grid, e.g., a grid which's grid spacing increases, can reduce this expense. And like a sponge-layer, a stretched grid

could add additional viscosity (in this case artificial) that will damp out structures that the outflow boundary condition has difficulty passing.

Combining grid stretching and sponge-layers can be especially attractive. Large grid spacings in sponge layers are acceptable because accuracy is not expected where unphysically high viscosity is used. However, does the Von Neumann stability criteria restrict the time step if high viscosity is used? Not necessarily. Carefully constructed grids and sponge layers can easily maintain the same time step despite much larger grid spacings at part of the domain. The reason why is that the viscosity increases along with the grid spacing, so the time step, which is proportional to $(\Delta x)^2/\nu$ under the Von Neumann stability criteria, can stay the same or increase.

A similar idea discussed by Colonius [Col04, p. 336] is to use a coordinate transformation that maps and infinite domain to a finite one. Unfortunately, infinity is perfectly reflective, so investigators Colonius [Col04] mentions tried combining this approach with sponge-layers and found success.

1.5.4 Other ideas

The approaches listed below were not studied in detail for this work, but they are worth future research.

Forced regions. One idea is to add forcing to the momentum equation to push fluid that builds up out of the domain and (hopefully) push reflections out as well. This idea could be implemented similarly and even in combination with a sponge-layer.

Backflow control. If unphysical flows into the domain are part of the problem at outflow boundaries, why not stop all inflows by setting a minimum velocity at the outflow plane? This idea surely will prevent all backflows, physical or not. And that may be part of the problem: it does not discriminate between physical backflows and non-physical backflows. Such a harsh approach may have poor success too close to areas where transient backflows are expected. Perhaps a smarter approach which

allows for some backflows while maintaining a time-averaged outflow would be better.

2

LES-BLAC

This chapter describes the methodology and assumptions of LES-BLAC, which I used for this thesis. This code has successfully been used for many momentum-driven flows. Bravo [Bra13] discusses a variety of different verification and validation cases including turbulent non-premixed flames bounded by walls, diffusive mixing, Poiseuille flow with heat transfer, and boundary layer flow.

2.1 Partial differential equations

2.1.1 Governing equations

All general form equations and derivations follow Poinsot and Veynante [PV05, chap. 1] with some reference to Pierce [Pie01, chap. 2]. Gravity forces are included.

Conservation of momentum

$$\frac{\partial \rho u_j}{\partial t} + \frac{\partial \rho u_i u_j}{\partial x_i} = -\frac{\partial p}{\partial x_j} + \frac{\partial \boldsymbol{\tau}_{ij}}{\partial x_i} + \rho g_j \tag{2.1.1}$$

low-Mach number pressure decomposition. For low-Mach numbers the pressure can be decomposed as

$$p = \underbrace{p_0}_{\substack{\text{thermodynamic}\\ \text{component}}} + \underbrace{\rho_0 g_i x_i}_{\substack{\text{hydrostatic}\\ \text{component}}} + \underbrace{p_\text{a}}_{\substack{\text{aerodynamic}\\ \text{component}}} \tag{2.1.2}$$

where

p_0 is the thermodynamic component of the pressure that is the constant background pressure,

ρ_0 is the background density (that is a constant),

p_a is the aerodynamic component of the pressure (that is *time dependent*).

Plugging eqn. 2.1.2 into eqn. 2.1.1 returns

$$\frac{\partial \rho u_j}{\partial t} + \frac{\partial \rho u_i u_j}{\partial x_i} = -\frac{\partial p_\mathrm{a}}{\partial x_j} + \frac{\partial \boldsymbol{\tau}_{ij}}{\partial x_i} + (\rho - \rho_0) g_j \,. \tag{2.1.3}$$

Substituting in the viscous stress tensor $\boldsymbol{\tau}_{ij}$ [ATP84, p. 185] into eqn. 2.1.3 returns

$$\frac{\partial \rho u_j}{\partial t} + \frac{\partial \rho u_i u_j}{\partial x_i} = -\frac{\partial p_\mathrm{a}}{\partial x_j} + \frac{\partial}{\partial x_i}\left[\mu\left(\frac{\partial u_i}{\partial x_j} + \frac{\partial u_j}{\partial x_i}\right) - \frac{2}{3}\delta_{ij}\mu\frac{\partial u_l}{\partial x_l}\right] + (\rho - \rho_0) g_j \,. \tag{2.1.4}$$

Mass conservation

The typical compressible continuity equation is

$$\frac{\partial \rho}{\partial t} + \frac{\partial \rho u_i}{\partial x_i} = 0 \,. \tag{2.1.5}$$

The continuity equation is enforced with a pressure projection scheme.

Conservation of species k

The species conservation equation is derived by Poinsot and Veynante [PV05, p. 13]. The result is

$$\frac{\partial \rho Y_k}{\partial t} + \frac{\partial \rho u_i Y_k}{\partial x_i} = -\underbrace{\frac{\partial \rho V_{k,i} Y_k}{\partial x_i}}_{\text{diffusion correction}} + \underbrace{\dot{\omega}_k}_{\text{reaction rate of species } k} \,. \tag{2.1.6}$$

LES-BLAC has two species (i.e., $N_\mathrm{s} = 2$).

One species conservation equation is redundant—total mass conservation determines the final species' mass fraction.

Decomposition of velocity of individual species. The velocities of each species can be decomposed as

$$v_{k,i} = u_i + V_{k,i} \quad \text{for } i = 1, 2, 3 \tag{2.1.7}$$

where

$v_{k,i}$ is the macroscopic velocity of species k,

u_i is the macroscopic velocity of the mixture, and

$V_{k,i}$ is the diffusion velocity of species k.

The following identities apply by definition:

$$u_i = \sum_{k=1}^{N_s} Y_k v_{k,i} \quad , \quad \sum_{k=1}^{N_s} Y_k V_{k,i} = 0 \, . \tag{2.1.8}$$

Fick's law for the diffusion velocities. For two species systems the product of the diffusion velocity, $V_{k,i}$, and the mass fraction, Y_k is

$$Y_k V_{k,i} = -D_k \frac{\partial Y_k}{\partial x_i} \, . \tag{2.1.9}$$

Eqn. 2.1.9 does not follow the summation convention. See Poinsot and Veynante [PV05, p. 14] for more information about the derivation of eqn. 2.1.9.

Substituting in eqn. 2.1.9 into eqn. 2.1.6 leads to

$$\frac{\partial \rho Y_k}{\partial t} + \frac{\partial \rho u_i Y_k}{\partial x_i} = \frac{\partial}{\partial x_i} \left(\rho D_k \frac{\partial Y_k}{\partial x_i} \right) + \dot{\omega}_k \, . \tag{2.1.10}$$

Poinsot and Veynante [PV05, pp. 84–85] derive the equation for *mixture fraction*,

Z, from eqn. 2.1.10:

$$\frac{\partial \rho Z}{\partial t} + \frac{\partial \rho u_i Z}{\partial x_i} = \frac{\partial}{\partial x_i}\left(\rho D \frac{\partial Z}{\partial x_i}\right) . \tag{2.1.11}$$

where $Z = 1$ in the fuel and $Z = 0$ in the air.

Conservation of energy

The material derivative of f permits writing

$$\frac{\partial \rho f}{\partial t} + \frac{\partial \rho u_i f}{\partial x_i} = f\underbrace{\left[\frac{\partial \rho}{\partial t} + \frac{\partial \rho u_i}{\partial x_i}\right]}_{0} + \rho\left[\frac{\partial f}{\partial t} + u_i \frac{\partial f}{\partial x_i}\right] = \rho \frac{\mathrm{D}f}{\mathrm{D}t} . \tag{2.1.12}$$

The equation for the conservation of energy is

$$\frac{\partial \rho e_t}{\partial t} + \frac{\partial \rho u_i e_t}{\partial x_i} = \rho \frac{\mathrm{D}e_t}{\mathrm{D}t} = -\frac{\partial q_i}{\partial x_i} - \frac{\partial p u_j}{\partial x_j} + \frac{\partial \boldsymbol{\tau}_{ij} u_i}{\partial x_j} + \rho g_i u_i . \tag{2.1.13}$$

e_t is the total chemical energy,

$$e_t \equiv e + \tfrac{1}{2} u_i u_i = \int_{T_0}^{T} C_v dT + \tfrac{1}{2} u_i u_i = h + \tfrac{1}{2} u_i u_i - \frac{p}{\rho} . \tag{2.1.14}$$

A useful equation is

$$u_j \frac{\mathrm{D}u_j}{\mathrm{D}t} = \frac{\mathrm{D}\left(\frac{1}{2} u_j u_j\right)}{\mathrm{D}t} . \tag{2.1.15}$$

Another useful equation (derived from the continuity equation) is

$$\frac{\mathrm{D}\rho}{\mathrm{D}t} = -\rho \frac{\partial u_j}{\partial x_j} . \tag{2.1.16}$$

Multiply the momentum equation eqn. 2.1.1 by u_j and apply eqn. 2.1.15 to find

$$u_j \frac{\mathrm{D}u_j}{\mathrm{D}t} = \frac{1}{\rho}\left[-u_j \frac{\partial p}{\partial x_j} + u_j \frac{\partial \boldsymbol{\tau}_{ij}}{\partial x_i} + \rho g_j u_j\right] = \frac{\mathrm{D}\left(\frac{1}{2} u_j u_j\right)}{\mathrm{D}t} . \tag{2.1.17}$$

Take the material derivative of eqn. 2.1.14, multiply the result by ρ, and apply eqn. 2.1.15, eqn. 2.1.16, and eqn. 2.1.17.

$$\begin{aligned}
\rho\frac{\mathrm{D}e_t}{\mathrm{D}t} &= \rho\left[\frac{\mathrm{D}h}{\mathrm{D}t} + \frac{\mathrm{D}\left(\frac{1}{2}u_j u_j\right)}{\mathrm{D}t} - \frac{\mathrm{D}(p/\rho)}{\mathrm{D}t}\right] = \rho\left[\frac{\mathrm{D}h}{\mathrm{D}t} + u_j\frac{\mathrm{D}u_j}{\mathrm{D}t} - \frac{1}{\rho}\frac{\mathrm{D}p}{\mathrm{D}t} + \frac{p}{\rho^2}\frac{\mathrm{D}\rho}{\mathrm{D}t}\right] \\
&= \rho\left[\frac{\mathrm{D}h}{\mathrm{D}t} - \frac{1}{\rho}\frac{\mathrm{D}p}{\mathrm{D}t} - \frac{p}{\rho}\frac{\partial u_j}{\partial x_j}\right] - u_j\frac{\partial p}{\partial x_j} + u_j\frac{\partial \boldsymbol{\tau}_{ij}}{\partial x_i} + \rho g_j u_j \qquad (2.1.18) \\
&= \rho\frac{\mathrm{D}h}{\mathrm{D}t} - u_j\frac{\partial p}{\partial x_j} + u_j\frac{\partial \boldsymbol{\tau}_{ij}}{\partial x_i} + \rho g_j u_j - \frac{\mathrm{D}p}{\mathrm{D}t} - p\frac{\partial u_j}{\partial x_j} \\
&= \rho\frac{\mathrm{D}h}{\mathrm{D}t} + u_j\frac{\partial \boldsymbol{\tau}_{ij}}{\partial x_i} + \rho g_j u_j - \frac{\mathrm{D}p}{\mathrm{D}t} - \frac{\partial p u_j}{\partial x_j} \qquad (2.1.19)
\end{aligned}$$

Solving eqn. 2.1.19 for $\rho\dfrac{\mathrm{D}h}{\mathrm{D}t}$, substituting in eqn. 2.1.13 and simplifying returns

$$\begin{aligned}
\rho\frac{\mathrm{D}h}{\mathrm{D}t} &= \rho\frac{\mathrm{D}e_t}{\mathrm{D}t} - u_j\frac{\partial \boldsymbol{\tau}_{ij}}{\partial x_i} - \rho g_j u_j + \frac{\mathrm{D}p}{\mathrm{D}t} + \frac{\partial p u_j}{\partial x_j} \\
&= -\frac{\partial q_i}{\partial x_i} - \cancel{\frac{\partial p u_j}{\partial x_j}} + \frac{\partial \boldsymbol{\tau}_{ij} u_i}{\partial x_j} + \cancel{\rho g_i u_i} - u_j\frac{\partial \boldsymbol{\tau}_{ij}}{\partial x_i} - \cancel{\rho g_j u_j} + \frac{\mathrm{D}p}{\mathrm{D}t} + \cancel{\frac{\partial p u_j}{\partial x_j}} \\
&= \frac{\mathrm{D}p}{\mathrm{D}t} - \frac{\partial q_i}{\partial x_i} + \boldsymbol{\tau}_{ij}\frac{\partial u_i}{\partial x_j}\,. \qquad (2.1.20)
\end{aligned}$$

Both $\boldsymbol{\tau}_{ij}\dfrac{\partial u_i}{\partial x_j} \propto M^2 \approx 0$ (for low Mach numbers) and $\dfrac{\mathrm{D}p}{\mathrm{D}t} = \cancel{\dfrac{\partial p}{\partial t}}^{\approx 0} + u_i\dfrac{\partial p}{\partial x_i} \propto M^2 \approx 0$. Thus, the low-Mach number form of the energy equation is found,

$$\begin{aligned}
\rho\frac{\mathrm{D}h}{\mathrm{D}t} &= \cancel{\frac{\mathrm{D}p}{\mathrm{D}t}}^{0} - \frac{\partial q_i}{\partial x_i} + \cancel{\boldsymbol{\tau}_{ij}\frac{\partial u_i}{\partial x_j}}^{0} \\
&= -\frac{\partial q_i}{\partial x_i}\,. \qquad (2.1.21)
\end{aligned}$$

Poinsot and Veynante [PV05, p. 22] justify these simplifications under low-Mach numbers.

The heat flux q_i is

$$q_i = -\lambda\frac{\partial T}{\partial x_i} + \rho\sum_{k=1}^{N_\mathrm{s}} h_k Y_k V_{k,i} \qquad (2.1.22)$$

if radiation and the Dufour effect are neglected as detailed by Pierce [Pie01, p. 9–10].

The following identity helps find the temperature gradient as a function of the enthalpy gradient:

$$\begin{aligned}\frac{\partial h}{\partial x_j} &= \frac{\partial}{\partial x_j}\sum_{k=1}^{N_\mathrm{s}} h_k Y_k = \sum_{k=1}^{N_\mathrm{s}}\left(Y_k\frac{\partial h_k}{\partial x_j} + h_k\frac{\partial Y_k}{\partial x_j}\right)\\ &= \sum_{k=1}^{N_\mathrm{s}} Y_k \underbrace{\frac{\partial h_k}{\partial T}}_{c_{p,k}}\frac{\partial T}{\partial x_j} + \sum_{k=1}^{N_\mathrm{s}} h_k\frac{\partial Y_k}{\partial x_j} = c_\mathrm{p}\frac{\partial T}{\partial x_j} + \sum_{k=1}^{N_\mathrm{s}} h_k\frac{\partial Y_k}{\partial x_j}\,. \end{aligned} \tag{2.1.23}$$

Noting that the thermal conductivity (λ) and thermal diffusivity (α) are related by

$$\alpha = \frac{\lambda}{\rho c_\mathrm{p}} \tag{2.1.24}$$

then the temperature gradient multiplied by λ as in eqn. 2.1.22 is

$$\alpha\frac{\partial T}{\partial x_i} = \frac{\lambda}{c_\mathrm{p}}\left[\frac{\partial h}{\partial x_i} - \sum_{k=1}^{N_\mathrm{s}} h_k\frac{\partial Y_k}{\partial x_i}\right] = \rho\alpha\left[\frac{\partial h}{\partial x_i} - \sum_{k=1}^{N_\mathrm{s}} h_k\frac{\partial Y_k}{\partial x_i}\right]\,. \tag{2.1.25}$$

Assuming that the Lewis number is 1 ($\mathrm{Le} \equiv \alpha/D = 1$) and that the diffusion velocities are determined by Fick's law (eqn. 2.1.9) then the *final* form of the energy equation is derived:

$$\rho\frac{\mathrm{D}h}{\mathrm{D}t} = \frac{\partial}{\partial x_i}\left[\rho\alpha\frac{\partial h}{\partial x_i} + \rho\sum_{k=1}^{N_\mathrm{s}}\cancel{(D-\alpha)h_k\frac{\partial Y_k}{\partial x_i}}^{\,0}\right] = \rho\frac{\mathrm{D}h}{\mathrm{D}t} = \frac{\partial}{\partial x_i}\left(\rho\alpha\frac{\partial h}{\partial x_i}\right)\,. \tag{2.1.26}$$

Equation of state

As the thermodynamic pressure is p_0, this is the pressure that appears in the equation of state.

$$p_0 = \rho\frac{R}{M}T = \rho RT\sum_{k=1}^{N_\mathrm{s}}\frac{Y_k}{M_k} \tag{2.1.27}$$

Pressure decomposition

$$p = \underbrace{p_0} + \underbrace{\rho_0 g_i x_i} + \underbrace{p_\mathrm{a}} \tag{2.1.28}$$

Summary

$$\frac{\partial \rho}{\partial t} + \frac{\partial \rho u_i}{\partial x_i} = 0 \tag{2.1.29}$$

$$\frac{\partial \rho u_j}{\partial t} + \frac{\partial \rho u_i u_j}{\partial x_i} = -\frac{\partial p_\mathrm{a}}{\partial x_j} + \frac{\partial}{\partial x_i}\left[\mu\left(\frac{\partial u_i}{\partial x_j} + \frac{\partial u_j}{\partial x_i}\right) - \frac{2}{3}\delta_{ij}\mu\frac{\partial u_i}{\partial x_i}\right] + (\rho - \rho_0)g_j \tag{2.1.30}$$

$$\frac{\partial \rho \phi_k}{\partial t} + \frac{\partial \rho u_i \phi_k}{\partial x_i} = \frac{\partial}{\partial x_i}\left(\rho \alpha_k \frac{\partial \phi_k}{\partial x_i}\right) \tag{2.1.31}$$

$$p_0 = \rho \frac{R}{M} T \tag{2.1.32}$$

$$p = \underbrace{p_0} + \underbrace{\rho_0 g_i x_i} + \underbrace{p_\mathrm{a}} \tag{2.1.33}$$

The conserved scalars (ϕ_k) are *mixture fraction* ($\phi_1 \equiv Z$) and *enthalpy* (sensible + chemical, $\phi_2 \equiv h$).

2.1.2 Non-dimensionalization

The following non-dimensionalizations are used:

$$p^+ \equiv \frac{p}{p_0}\,, \qquad p_\mathrm{a}^+ \equiv \frac{p_\mathrm{a}}{\rho_0 U_0^2}\,, \qquad \rho^+ \equiv \frac{\rho}{\rho_0}\,, \qquad M^+ \equiv \frac{M}{M_O}\,,$$
$$T^+ \equiv \frac{T}{T_0}\,, \qquad t^+ \equiv \frac{t U_0}{L}\,, \qquad u_i^+ \equiv \frac{u_i}{U_0}\,, \qquad x_i^+ \equiv \frac{x_i}{L}\,,$$
$$\phi_k^+ \equiv \frac{\phi_k}{\phi_{k,0}}\,, \qquad \mathrm{Re} \equiv \frac{L U_0}{\nu}\,, \qquad \mathrm{Pr}_k \equiv \frac{\nu}{\alpha_k}\,, \qquad \mathrm{Fr}_j \equiv -\frac{U_0^2}{g_j L}\,.$$

The molecular mass M is used above, not the Mach number. The graviational acceleration g_j is in the direction of acceleration, so the negative sign cancels out the negative value of g_1 in LES-BLAC. g_2 and g_3 are zero.

Starting in §2.2 the + superscript will be omitted for brevity.

Mass conservation

$$\frac{\partial \rho^+}{\partial t^+} + \frac{\partial \rho^+ u_i^+}{\partial x_i^+} = 0 \tag{2.1.34}$$

Momentum conservation

$$\frac{\partial \rho^+ u_j^+}{\partial t^+} + \frac{\partial \rho^+ u_i^+ u_j^+}{\partial x_i^+} = -\frac{\partial p_{\mathrm{a}}^+}{\partial x_j^+} + \frac{\partial}{\partial x_i^+}\left[\frac{1}{\mathrm{Re}}\left(\frac{\partial u_i^+}{\partial x_j^+} + \frac{\partial u_j^+}{\partial x_i^+}\right) - \frac{2}{3}\delta_{ij}\frac{1}{\mathrm{Re}}\frac{\partial u_i^+}{\partial x_i^+}\right] + \frac{1}{\mathrm{Fr}_j}(1-\rho^+) \tag{2.1.35}$$

Scalar conservation

$$\frac{\partial \rho^+ \phi_k^+}{\partial t^+} + \frac{\partial \rho^+ u_i^+ \phi_k^+}{\partial x_i^+} = \frac{\partial}{\partial x_i^+}\left(\frac{1}{\mathrm{Re}\ \mathrm{Pr}_k}\frac{\partial \phi_k^+}{\partial x_i^+}\right) \tag{2.1.36}$$

Equation of state

$p^+ = 1$ under low-Mach number assumptions.

The equation of state implies that $p_0 = \rho_0 R T_0 / M_0$. Dividing the ideal gas law by the reference condition leads to

$$1 = \frac{\rho^+ T^+}{M^+}\,. \tag{2.1.37}$$

2.2 Numerics

This section is abbreviated such that a flavor of the algorithm used is provided to the reader; details about LES-BLAC's inner workings are available in the thesis of Bravo [Bra13].

2.2.1 Spatial-temporal grid

LES-BLAC uses a staggered spatial grid with the scalars (ρ, h, Z, p_{a}) are located at the center of the cells (i.e., $i \pm \frac{1}{2}$) and the vectors (u, ϕ) are located at the sides of the cells (i.e., i). A staggered temporal grid is also used where the scalars are located at the time steps with whole numbers and and the vectors are located at the center of

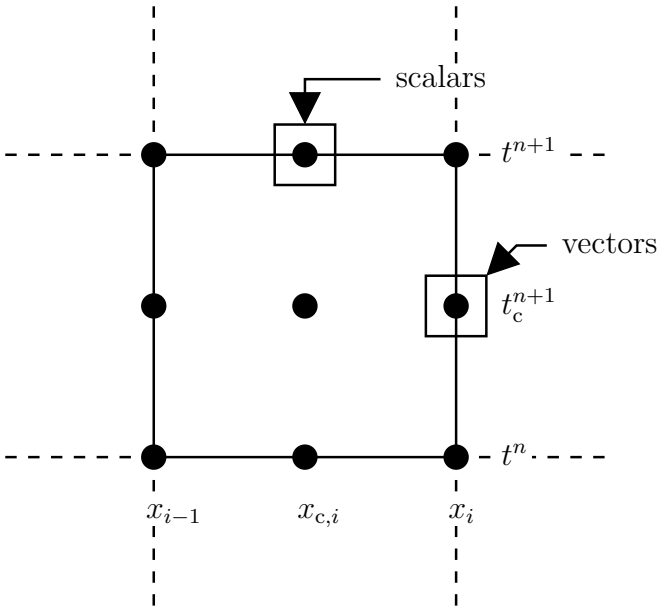

Figure 2.1: Location of the variables in the spatial-temporal cell.

the time step. Figure 2.1 shows the location of the variables in a 1d spatial-temporal cell.

The centered time and spaces are defined (in 1d) as

$$t_{\rm c}^{n+1} \equiv \frac{t^{n+1} - t^n}{2} \quad , \quad x_{{\rm c},i} \equiv \frac{x_{i-1} + x_i}{2} \,. \tag{2.2.1}$$

2.2.2 Time advancement scheme

Consider the ODE

$$\frac{{\rm d}q}{{\rm d}t} = f(q,t) \,. \tag{2.2.2}$$

The implicit scheme LES-BLAC uses to integrate differential equations in time is

$$\frac{q^{n+1} - q^n}{\Delta t} = f\left(\frac{q^{n+1} + q^n}{2}, t^{n+1/2}\right) \equiv f^{n+1/2} \,. \tag{2.2.3}$$

where $t^{n+1/2} \equiv (t^{n+1} - t^n)/2$. q could be either a vector or a scalar and thus t could either be t or $t_{\rm c}$.

LES-BLAC uses an iterative scheme to integrate eqn. 2.2.3 either explicitly or implicitly. The *explicit iterative scheme* to *implicitly integrate* eqn. 2.2.2 is

$$\frac{q^{n+1,k+1} - q^n}{\Delta t} = f\left(\frac{q^{n+1,k} + q^n}{2}, t^{n+1/2}\right) . \tag{2.2.4}$$

and the *implicit iterative scheme* to *implicitly integrate* eqn. 2.2.2 is

$$\frac{q^{n+1,k+1} - q^n}{\Delta t} = f\left(\frac{q^{n+1,k+1} + q^n}{2}, t^{n+1/2}\right) . \tag{2.2.5}$$

where k is the number of iterations

If f in eqn. 2.2.2 is decomposed as $f \equiv M + A$, where M is the component of f that is solved with an implicit iterative scheme and A is the component of f that is solved with an implicit iterative scheme then a semi-implicit scheme, to solve eqn. 2.2.2 is

$$\frac{q^{n+1,k+1} - q^n}{\Delta t} = A\left(\frac{q^{n+1,k} + q^n}{2}, t^{n+1/2}\right) + M\left(\frac{q^{n+1,k+1} + q^n}{2}, t^{n+1/2}\right) . \tag{2.2.6}$$

2.2.3 Discretizing the fluid equations

These equations are derived from the dimensionless governing equations, not the large-eddy simulation filtered equations used in LES-BLAC. This work is done in DNS mode, so the filtered terms do not appear in the final equations.

Momentum equations

Eqn. 2.2.6 is not precisely what is solved by LES-BLAC. A pressure projection scheme is used in LES-BLAC. The pressure is advanced explicitly such that

$$\begin{aligned} \frac{(\rho u_j)^{n+1,k+1} - (\rho u_j)^n}{\Delta t} &= A_j^n + M_j^n - \frac{\partial p_\mathrm{a}}{\partial x_j}^{n+1,k+1} , \\ (\rho u_j)^{n+1,k+1} &= (\rho u_j)^n + \Delta t \left(A_j + M_j - \frac{\partial p_\mathrm{a}}{\partial x_j}^{n+1,k+1}\right) , \end{aligned} \tag{2.2.7}$$

$$A_j \equiv \frac{\partial}{\partial x}\left(\frac{1}{\mathrm{Re}}\frac{\partial u_j}{\partial x}\right) + \frac{\partial}{\partial z}\left(\frac{1}{\mathrm{Re}}\frac{\partial u_j}{\partial z}\right) - \frac{\partial \rho u_i u_j}{\partial x_i} + \frac{\partial}{\partial x_i}\left[\frac{1}{\mathrm{Re}}\left(\frac{\partial u_i}{\partial x_j} + \frac{\partial u_j}{\partial x_i}\right) - \frac{2}{3}\delta_{ij}\frac{1}{\mathrm{Re}}\frac{\partial u_i}{\partial x_i}\right] + \frac{1}{\mathrm{Fr}_j}(1-\rho)\ , \tag{2.2.8}$$

$$M_j \equiv \frac{\partial}{\partial y}\left(\frac{1}{\mathrm{Re}}\frac{\partial u_j}{\partial y}\right)\ . \tag{2.2.9}$$

Defining $\delta p \equiv p_{\mathrm{a}}^{n+1,k+1} - p_{\mathrm{a}}^{n+1,k}$ leads to

$$(\rho u_j)^{n+1,k+1} = (\rho u_j)^n + \Delta t\left(A_j^n + M_j^n - \frac{\partial p_{\mathrm{a}}}{\partial x_j}^{n+1,k} - \frac{\partial \delta p}{\partial x_j}\right)\ . \tag{2.2.10}$$

For the fully-explicit approach

$$A_{j,\mathrm{explicit}} \equiv \frac{\partial}{\partial x_i}\left(\frac{1}{\mathrm{Re}}\frac{\partial u_j}{\partial x_i}\right) - \frac{\partial \rho u_i u_j}{\partial x_i} + \frac{\partial}{\partial x_i}\left[\frac{1}{\mathrm{Re}}\left(\frac{\partial u_i}{\partial x_j} + \frac{\partial u_j}{\partial x_i}\right) - \frac{2}{3}\delta_{ij}\frac{1}{\mathrm{Re}}\frac{\partial u_i}{\partial x_i}\right] + (\rho - \rho_0)g_j\ , \tag{2.2.11}$$

$$M_{j,\mathrm{explicit}} \equiv 0\,. \tag{2.2.12}$$

A prediction for $(\rho u_j)^{n+1,k+1}$ is

$$(\widehat{\rho u_j})^{n+1,k+1} = (\rho u_j)^n + \Delta t\left(A_j^n + M_j^n - \frac{\partial p_{\mathrm{a}}}{\partial x_j}^{n+1,k}\right)\ , \tag{2.2.13}$$

that implies

$$(\rho u_j)^{n+1,k+1} = (\widehat{\rho u_j})^{n+1,k+1} - \Delta t\frac{\partial(\delta p)}{\partial x_j}\,. \tag{2.2.14}$$

We can find $(\rho u_j)^{n+1,k+1}$ once δp and $(\widehat{\rho u_j})^{n+1,k+1}$ are known.

Pressure Poisson equation

Take the divergence of eqn. 2.2.14 and rearrange the result to find

$$\frac{\partial^2(\delta p)}{\partial x_i^2} = \frac{1}{\Delta t}\left(\frac{\partial \widehat{\rho u_i}}{\partial x_i}^{n+1,k+1} - \frac{\partial \rho u_i}{\partial x_i}^{n+1,k+1}\right)\ . \tag{2.2.15}$$

Rearranging the continuity equation leads to

$$\frac{\partial(\rho u_i)}{\partial x_i} = -\frac{\partial \rho}{\partial t} \,. \tag{2.2.16}$$

So the pressure Poisson equation is

$$\frac{\partial^2(\delta p)}{\partial x_i^2} = \frac{1}{\Delta t}\left(\frac{\partial \widehat{\rho u_i}}{\partial x_i}^{n+1,k+1} + \frac{\partial \rho}{\partial t}^{n+1,k+1}\right) . \tag{2.2.17}$$

In LES-BLAC, the density time derivative term is calculated by dividing the difference between the current iteration's density and the previous time step's density by the time step size. More details about this iterative procedure are in §2.2.4.

Scalar equations

The numerical scheme used for the scalar equations resembles the scheme used for the momentum equations, except that it does not have a projection step.

$$(\rho\phi_j)^{n+1,k+1} = (\rho\phi_j)^n + \Delta t\left(N_j^n + B_j^n\right) \,, \tag{2.2.18}$$

$$B_j \equiv \frac{\partial}{\partial x}\left(\frac{1}{\mathrm{Re}\ \mathrm{Pr}_j}\frac{\partial \phi_j}{\partial x}\right) + \frac{\partial}{\partial z}\left(\frac{1}{\mathrm{Re}\ \mathrm{Pr}_j}\frac{\partial \phi_j}{\partial z}\right) - \frac{\partial \rho u \phi_j}{\partial x} - \frac{\partial \rho w \phi_j}{\partial z} \,, \tag{2.2.19}$$

$$N_j \equiv \frac{\partial}{\partial y}\left(\frac{1}{\mathrm{Re}\ \mathrm{Pr}_j}\frac{\partial \phi_j}{\partial y}\right) - \frac{\partial \rho v \phi_j}{\partial y} \,. \tag{2.2.20}$$

2.2.4 Implementation

The basic algorithm used in LES-BLAC iterates and follows 7 steps.

Step 1: Initialization

Linear extrapolation estimates the density at the next time step:

$$(\rho^n)^{\mathrm{iter}=0} = 2\rho^{n-1} - \rho^{n-2} \,. \tag{2.2.21}$$

The other variables are maintained at their previous time-step's values. This step is not part of the iteration because it just finds the initial guesses for the variables.

Step 2: Scalar equations

Next, the scalar equations are advanced with eqn. 2.2.18.

Step 3: Equation of state

The mass density is computed via the equation of state, eqn. 2.1.37.

Step 4: Update scalar fields

The scalars (ϕ_k) are computed from the value of $\rho\phi_k$ found in step 2.

Step 5: Momentum equation

The momentum equations are advanced via eqn. 2.2.7.

Step 6: Pressure equation

Then, the pressure Poisson equation (eqn. 2.2.17) is solved. (This only finds the change in pressure between iterations.)

Step 7: Update velocity and pressure

Finally, the corrected velocities and the final aerodynamic pressure for the iteration are computed.

Continue iterating or move to next time step?

The iterative loop runs for each time step 11 times or until $\max\left(\rho^{\text{iter}} - \rho^{\text{iter}-1}\right) < 1 \times 10^{-6}$ and $\max\left(\text{RHS}^{\text{iter}} - \text{RHS}^{\text{iter}-1}\right) < 1 \times 10^{-3}$ where RHS is the right-hand side of the pressure Poisson equation, eqn. 2.2.17.

2.3 Boundary conditions

LES-BLAC has many different boundary conditions available The boundary conditions used in this work include far-field BCs, inflow BCs, and outflow BCs.

2.3.1 Pressure BCs

A zero-gradient BC is used for the pressure at all boundaries, as discussed in §1.2.2.

2.3.2 Far-field BC

The far-field boundary condition is used when the boundary is far away from the main flow. In two dimensions, this boundary condition is

$$\begin{aligned} u &= u_{\text{far-field}}, \\ \frac{\mathrm{d}\phi}{\mathrm{d}y} &= 0 \ , \end{aligned} \tag{2.3.1}$$

where ϕ is any scalar or the v or w velocity.

The boundary condition is only appropriate when the gradients of ϕ are zero or nearly zero at the boundary in an infinite domain solution. Even slight deviations from these boundary conditions near the boundary could cause inaccuracies and numerical instabilities.

2.3.3 Prescribed inflow BC

At an inflow, all of the incoming flow variables are specified.

2.3.4 Outflow BC

As discussed in ch. 1, an Orlanski boundary condition (eqn. 1.2.2) with the convective velocity set to the maximum outflow plane velocity is used.

3

Buoyant jet flow tests

The time evolution of planar buoyant jets was computed to test the effects of the sponge-layer on the flow. The experimental setup of Cetegen, Dong, and Soteriou [CDS98] is similar to the jets I modeled, except that buoyancy was generated via He-air mixtures in their experiment. An example of a He-air jet is shown in figure 3.1. In my numerical experiments, buoyancy is generated with a temperature difference.

3.1 Physical stability criteria

The experiments of Cetegen, Dong, and Soteriou [CDS98] found the stability diagram for planar buoyant jets. Their stability diagram is written in terms of Re and a density ratio. This transition diagram is misleading for buoyant flows as it neglects any terms related to gravity. One way to interpret this plot is in terms of a critical Rayleigh (Ra_x) number. For a jet with initial width w the Ra_x number can be decomposed into [Tro12]

$$\mathrm{Ra}_x = \left(\frac{\Delta T}{T_\infty}\right) \mathrm{Pr}\,\mathrm{Fr}\,\mathrm{Re}^3 (x^+)^3 \ , \tag{3.1.1}$$

where $\mathrm{Fr} \equiv gw/U_\mathrm{p}^2$, $\mathrm{Re} \equiv U_\mathrm{p} w/\nu$, $x^+ \equiv x/w$, and U_p is the jet inlet velocity.

In this simple argument, when the critical Ra_x is exceeded, the jet starts to become unstable and turbulent. Eqn. 3.1.1 can be solved for Re and written in terms of the

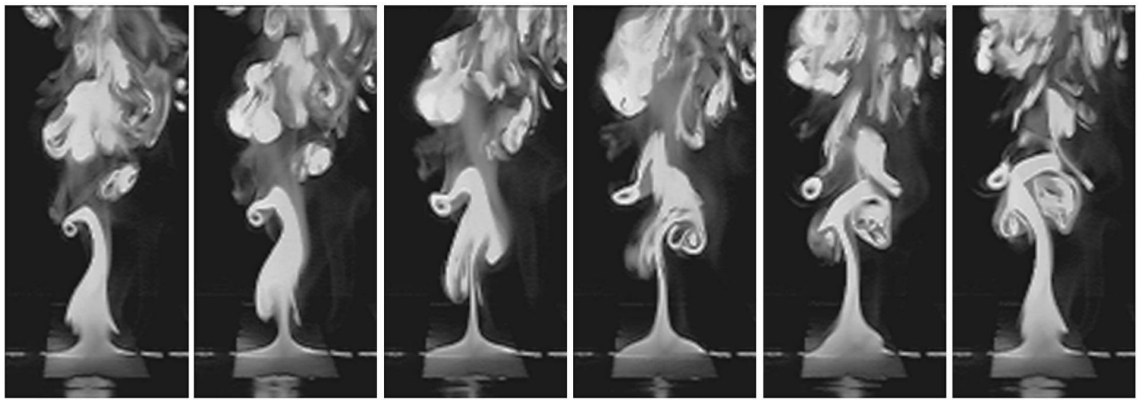

Figure 3.1: A buoyant helium-air jet from the experiments of Cetegen, Dong, and Soteriou [CDS98, fig. 5, p. 1662].

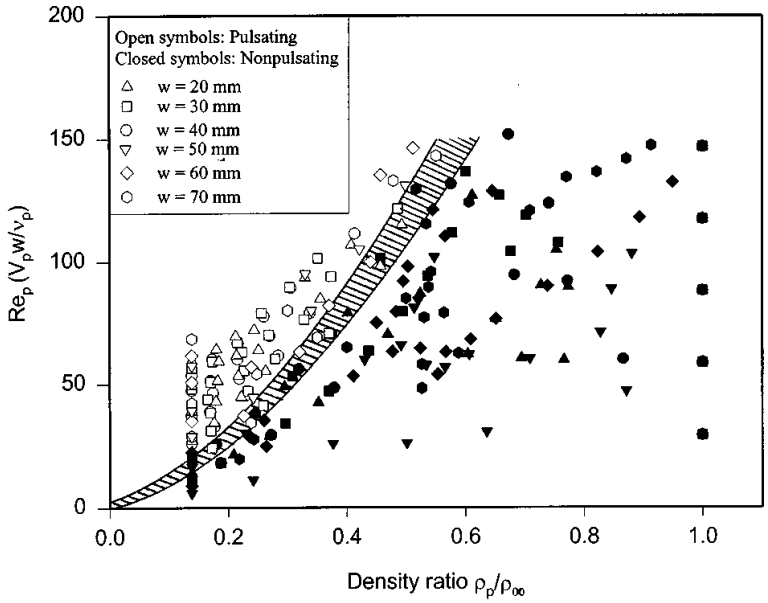

Figure 3.2: An experimental stability diagram for buoyant jets from Cetegen, Dong, and Soteriou [CDS98, fig. 6, p. 1663].

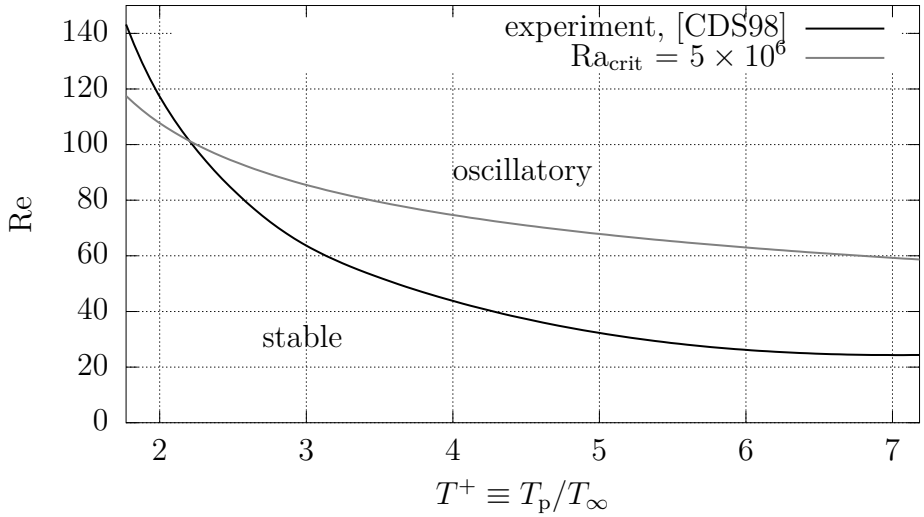

Figure 3.3: Stability diagram for heated jets based on a simple theory compared against experimental data.

temperature ratio ($T^+ \equiv T_\mathrm{p}/T_\infty$) where T_p is the jet temperature:

$$\mathrm{Re} = \left(\frac{1}{T^+ - 1}\right)^{1/3} \left(\frac{\mathrm{Ra}_{\mathrm{crit}}}{(x^+)^3 \,\mathrm{Pr}^2 \,\mathrm{Fr}}\right)^{1/3} \tag{3.1.2}$$

Cetegen, Dong, and Soteriou [CDS98] defined a pulsating jet to be one that had measurable oscillations in pressure at a distance of two initial jet widths from the nozzle at the centerline. Thus, for their plot, $x^+ = 2$. Then for $\mathrm{Pr} = 1$, $\mathrm{Fr} = 0.5$, and $\mathrm{Ra}_{\mathrm{crit}} = 0.5 \times 10^7$ (a rough guess based on experience with transition in heat transfer over hot plates), the stability diagram can be found. This stability diagram is shown in figure 3.3.

The simple transition criteria is qualitatively correct when compared against the experiment of Cetegen, Dong, and Soteriou [CDS98]. This criteria was used in this work to estimate approximately where jets should become hydrodynamically unstable. Jets that became unstable before this point appear to do so because of numerical instabilities.

3.2 Numerical configuration

3.2.1 Reference scales for non-dimensionalization

The reference velocity scale (U_0) was chosen to be the inlet velocity for the jet. This prescription sets the non-dimensional inlet velocity to be 1.

The reference length scale was chosen as the initial jet width ($L = w$). Thus, all lengths in this study can easily be compared against the initial jet width.

The reference time scale is w/U_0 as discussed in §2.1.2, and all times are normalized by this time scale. The jet fluid travels approximately 1 dimensionless distance in a unit of non-dimensional time. Thus, the length of the domain is approximately the flow-through time of the domain.

3.2.2 Gravity and specified dimensionless parameters

Gravity was set to act in the negative x direction. Thus, in plots in this work, gravity acts to the left, not down as the reader may expect.

For these cases $\mathrm{Re} = 50$ and $\mathrm{Fr} = 2$ (as they are defined in §2.1.2).

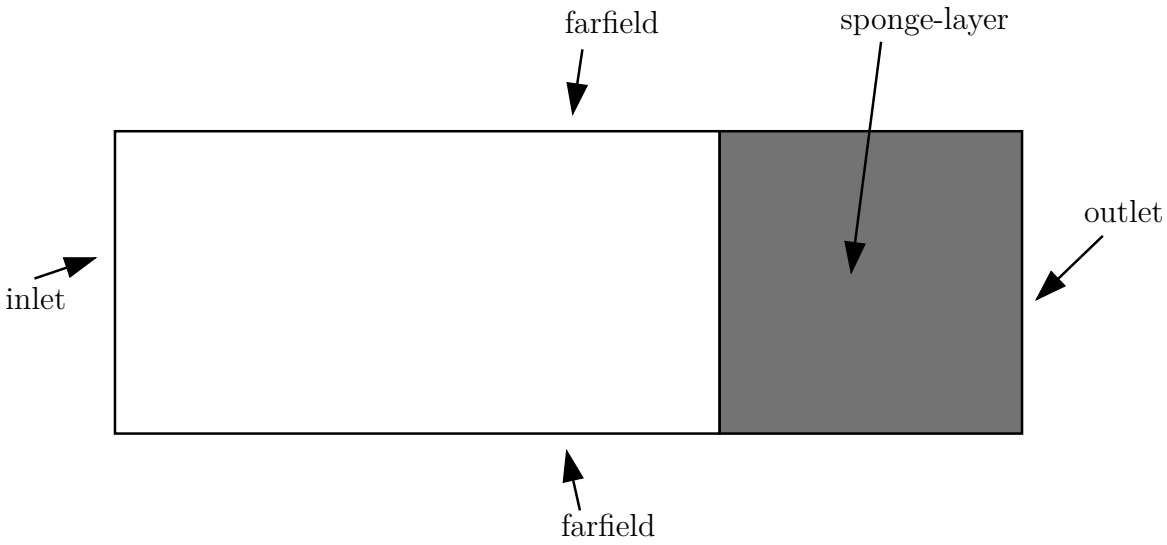

Figure 3.4: Schematic of the jet simulations including boundary conditions and the location of the sponge-layer, when it exists.

3.2.3 Inlet boundary condition

The inlet profiles are specified. The v velocity is set to zero, and the u and T profiles are set to "top-hat"-like profiles created with hyperbolic tangent functions. The peak value of u (which again, is dimensionless) is set to 1 (as discussed earlier such that the jet reference velocity is the inlet velocity). The peak value of temperature is set to whatever temperature ratio (i.e., T/T_{atm}) is being modeled. The far-field u velocity is set to a small fraction of the center velocity (here 2%) for numerical stability reasons. The far-field temperature is set to atmospheric, i.e., 1. Plots of the steady-state inlet profiles appear in figure 3.5.

White noise (0.5% of the local temperature) is added to the temperature to promote the growth of a hydrodynamic instability. No noise is added to any other variable. The white noise starts at a set value and eventually decreases in magnitude to zero following a hyperbolic tangent function with a transition time of 50 time units. If the desired jet temperature is above 2, the inlet temperature is linearly ramped up from 2 to its final value over a period of 25. This was necessary to prevent the development of numerical instabilities for high temperature jets.

3.2.4 Outlet boundary condition

The Orlanski boundary condition (eqn. 1.2.2) is used at the outlet. A sponge-layer (a region of elevated viscosity used to smooth the flow to make the outflow boundary condition work better) is used near the outlet in some cases; see §1.5.2 and §3.3 for details of the sponge-layer's configuration.

3.2.5 Far-field boundary condition

The far-field boundary condition (eqn. 2.3.1) is used at the top and bottom of the domain.

3.2.6 Numerical grid

Evenly spaced grid cells are used in the x direction with a grid spacing of 0.1 units. This spacing was found to be slightly inadequate to resolve the initial jet inlet (see figure 3.5), however, it is more than adequate to resolve the large vortices shed off the jet. Practically, this resolution is at essentially the limit of what could be afforded for this work.

A stretched grid in the sponge-layer was attempted as suggested in §1.5.3, however, stretched grids in x were found to cause numerical instabilities with buoyancy enabled. Attempts to remedy this problem by using less severe stretching and extremely high viscosities (increasing to 20 times the initial value) in the sponge-layer were unsuccessful. Further, the high viscosity cases were slower than the long domain cases due to the von Neumann stability criteria. Thus, the sponge layer cases may not be computationally cheaper than the long domain cases in this work, but they act as a proof-of-concept pending further research into this stability issue.

A stretched grid was used in the y direction in both the positive and negative directions. 300 grid points were used with a stretching ratio of 1.02 and a overall width in the y direction of 150 units.

A domain this wide was found to be essential in delaying numerical instabilities from the far-field boundary conditions. See figure 3.6 for an example of these instabilities. The top two cases are unstable at the time shown. The v velocity field is slowly growing unboundedly, leading to wild flapping of the jet. The second case is not obviously unstable at this instant, but the jet flaps too widely.

This flapping is delayed as the domain becomes wider as shown in figure 3.7. The instability causes the temperature to go near ambient because the wide flapping makes the plume miss the probe most of the the time as shown in figure 3.6. The time required for this problem to develop is seen to increase as the width of the domain (listed in the legend) increases. Note that while this test was done without

a sponge-layer, the sponge-layer was not shown to stop this flapping instability in subsequent tests as will be shown in §3.3; in fact in some cases it appears to help cause this instability.

3.2.7 Probes

"Probes" which recorded temperature, velocity components, density, viscosity, and pressure were placed in the domain. A 3-by-3 array of probes was placed near the inlet. The first row of probes was one jet width from the inlet, the second row was two jet widths from the inlet, and the third was three jet widths from the inlet. One column of probes was placed at the centerline and two other columns were placed one jet width above and below the centerline.

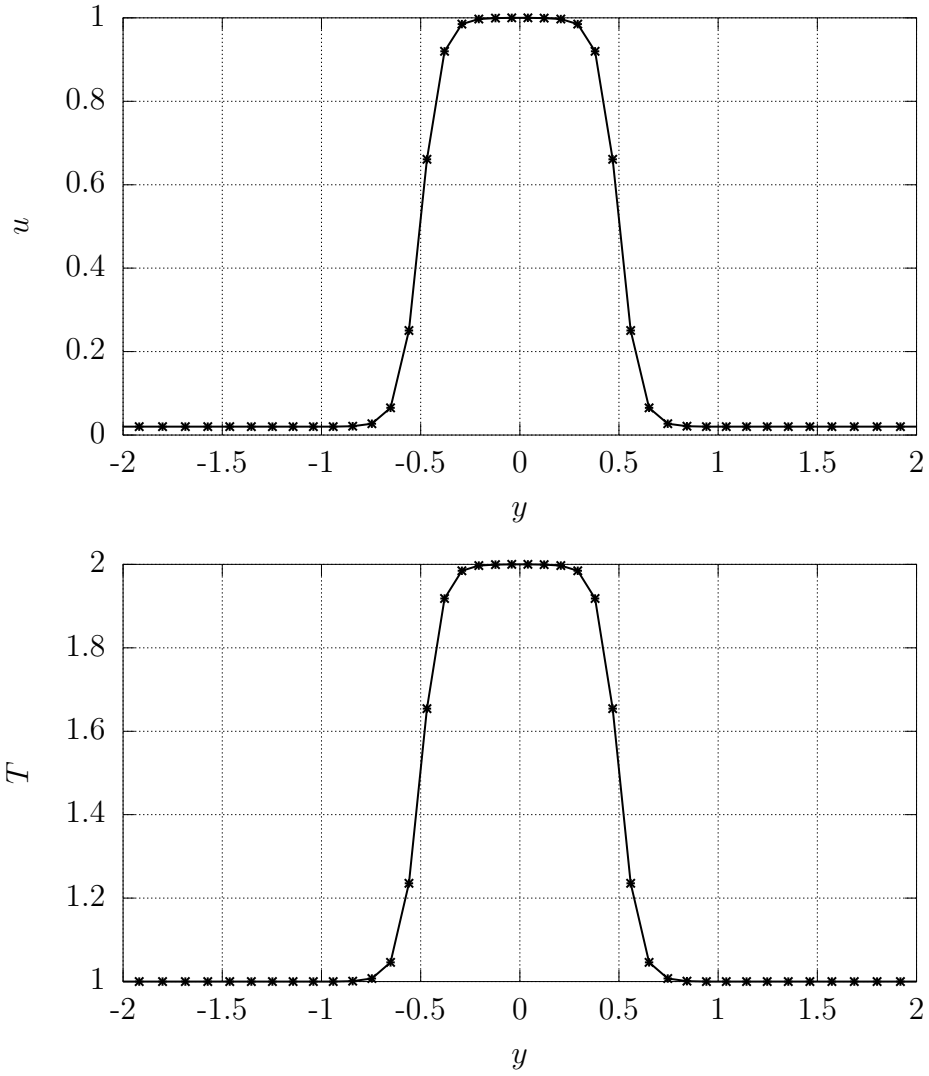

Figure 3.5: Inlet profiles for the jet cases in this work. The temperature plot is an example — the maximum temperature is a parameter that was varied in the simulations. Points correspond to actual grid points.

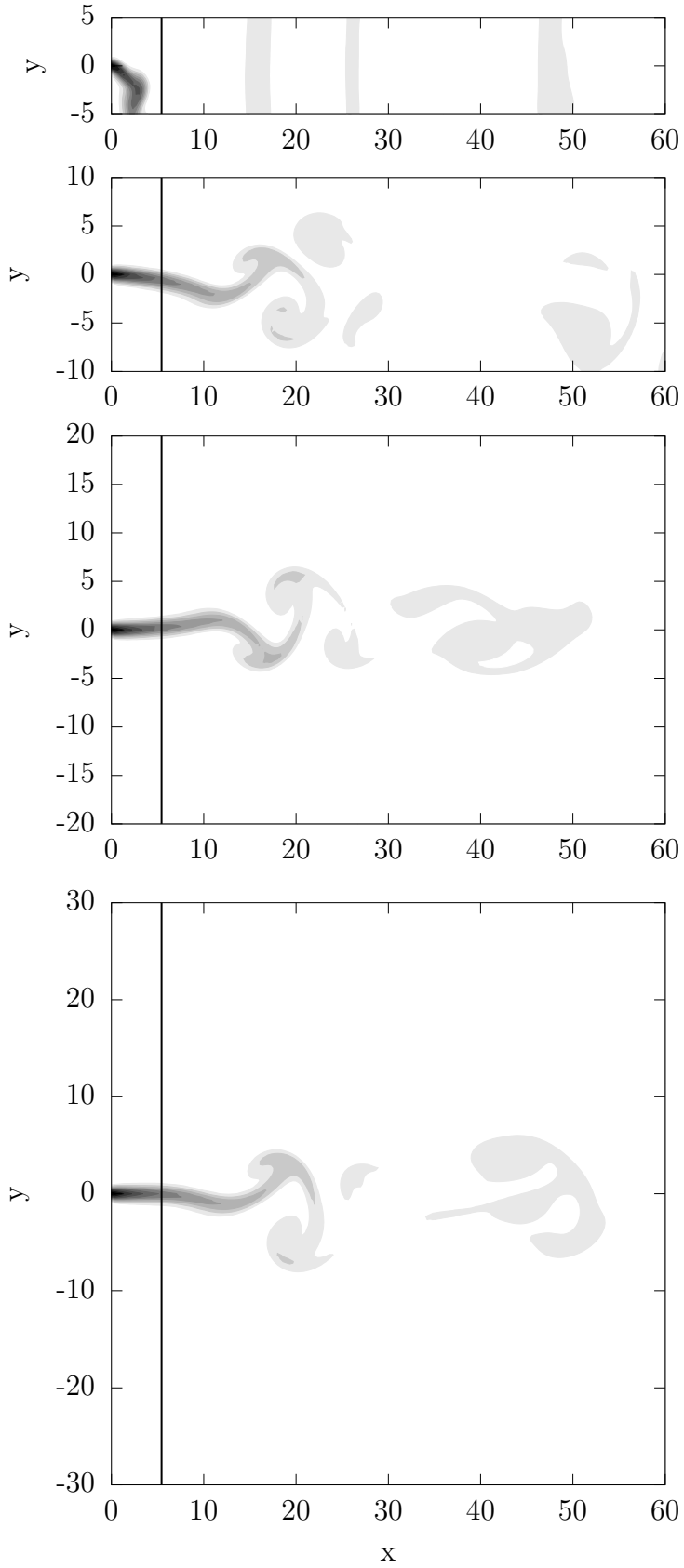

Figure 3.6: Temperature contours for cases with different domain widths. Black is $T = 1.5$. White is $T = 1.0$. The black line is where $\mathrm{Ra}_x = 0.5 \times 10^7$, which corresponds approximately to where the turbulent transition occurs.

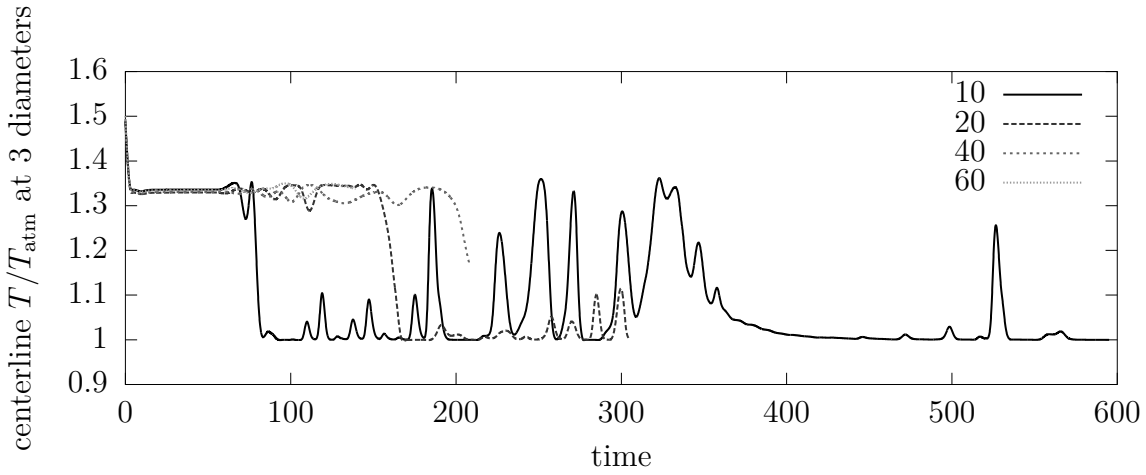

Figure 3.7: Temperature as a function of time in a jet for different domain widths. The 60 wide case did not run very far in time and it did not yet go unstable.

x-length	SL length	T/T_{atm}	$\nu_{\max}/\nu$	end time	notes
40	0	1.5	—	270.90	
40	0	2.0	—	195.09	
40	0	4.0	—	82.71	
20	0	1.5	—	605.53	
20	0	2.0	—	398.96	
20	0	4.0	—	147.40	
20	10	1.5	5	477.77	
20	20	1.5	5	254.50	
20	10	2.0	5	249.80	
20	20	2.0	5	258.14	
20	10	4.0	5	174.71	
20	20	4.0	5	101.52	
20	10	1.5	10	359.92	
20	20	1.5	10	358.27	
20	10	2.0	10	437.90	
20	20	2.0	10	210.28	
20	10	4.0	10	—	unstable
20	20	4.0	10	—	unstable

Table 3.1: Details of each simulation run in this work.

3.3 Simulation of jets with and without sponge-layers

A wide variety of different sponge-layer configurations and temperatures were tested in this work as detailed in table 3.1.[1] Ultimately, all temperatures were found to perform similarly with respect to accuracy near the outflow. Thus, comparisons with only one temperature is adequate in summary. For the full details of each simulation, see the appendices. Short-hand notation is used in the legends; e.g., "short, 20 SL, 5" means "short domain (length of 20)" with a 20 unit long sponge layer that increased viscosity 5 times."

In these plots, "outlet" refers to the plane 20 units from the inlet. This plane is at the center of the long-domain, actual outflow plane for the short-domain case without sponge-layers, and the start of the sponge-layer for the sponge-layer cases.

1 The highest temperature cases were found to be unstable if too much viscosity was added to the sponge-layer.

3.3.1 Comparison with experiments

The jet simulations in this work do not look entirely like the experimental results shown in figure 3.1. Compare figure 3.1 and figure 4.21. The location of the onset of the instability appears to be similar. But, the simulated vortex structures appear to be much larger than those seen in the experiment. There are several potential explanations for this discrepancy. The influence of the artificial boundary conditions may force the flow, creating larger structures. The photo from the experiment also shows colored dye, which may not be perfectly analogous with the temperature in the simulations. One last potential explanation is that these simulations are purely 2d. Cetegen, Dong, and Soteriou [CDS98, p. 1660] note that "two-dimensionality is preserved for heights up to three to four nozzle widths", so it is possible that the simulations can not be compared against the experiments beyond that distance, which is where the large (turbulent) vortex structures are seen. However, that explanation is put into doubt given that Soteriou, Dong, and Cetegen [SDC02] successfully modeled their previous experiment with 2d direct numerical simulation via a vortex method.

3.3.2 Comparisons between different runs

The long-domain case is compared against the shorter domain cases with and without sponge-layers. These comparisons are neither verification or validation, rather, they are an internal consistency check. As the size of the truncated domain approaches the size of the real physical domain, the error between the two cases is assumed to decrease. Thus, the long domain cases are the basis for comparison in this work.

Time-averaged temperature fields were computed. These fields are not perfectly statistically converged due to difficulties in running cases with buoyancy very far in time. The flapping numerical instability mentioned earlier in this chapter appears to develop in all cases eventually. The present data, however, does indicate that the sponge-layer approach improves accuracy near the outflow plane.

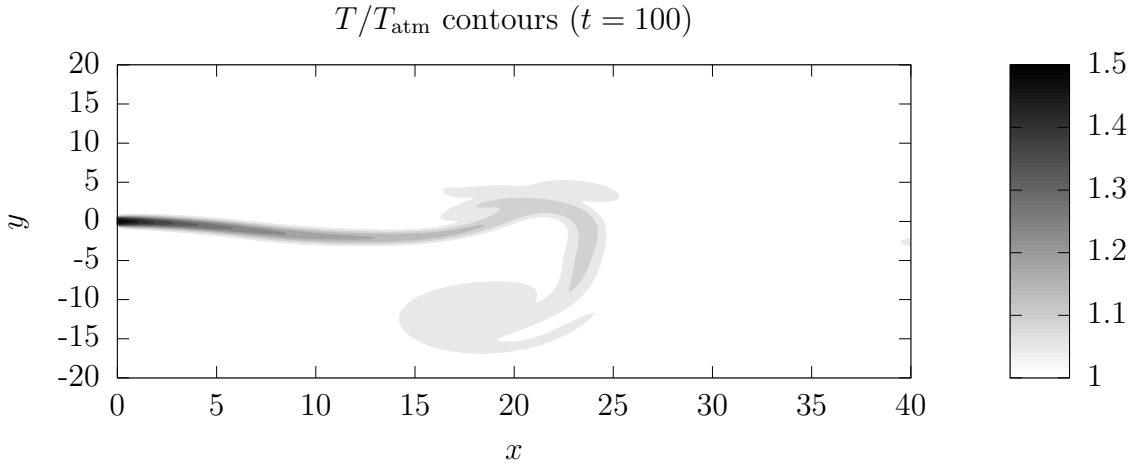

Figure 3.8: Temperature contours for long domain, no sponge-layer case.

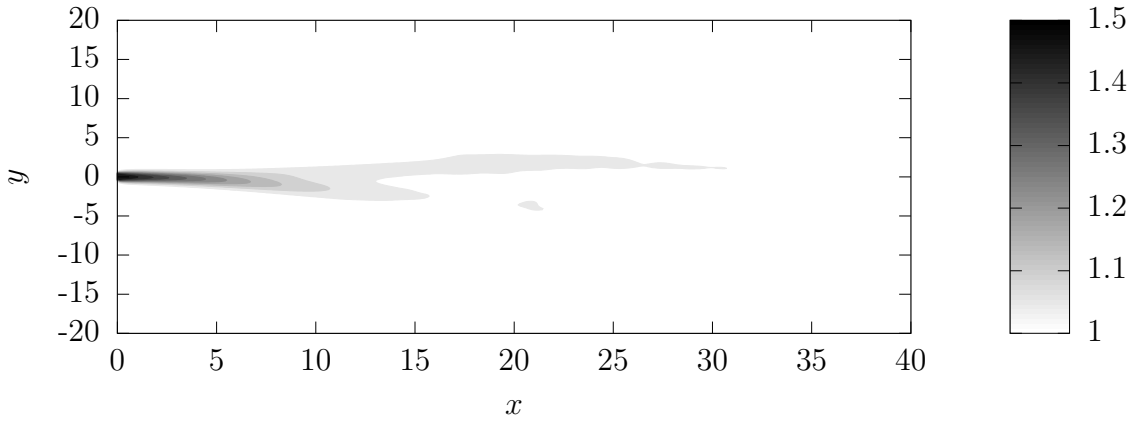

Figure 3.9: Temperature contours for long domain, no sponge-layer case.

Long-domain case

Long-domain temperature fields are shown in figures 4.21 and 4.51. The outflow in this configuration is placed so far from the inlet that the temperature differential there is negligible, and thus there is no noticeable build-up of hot gas near the outflow boundary, as shown in both the time-averaged and instantaneous fields.

Unfortunately, these cases have the clearest difficulty with statistical convergence for the time-averaged plots due to the long-domain being very computationally expensive.

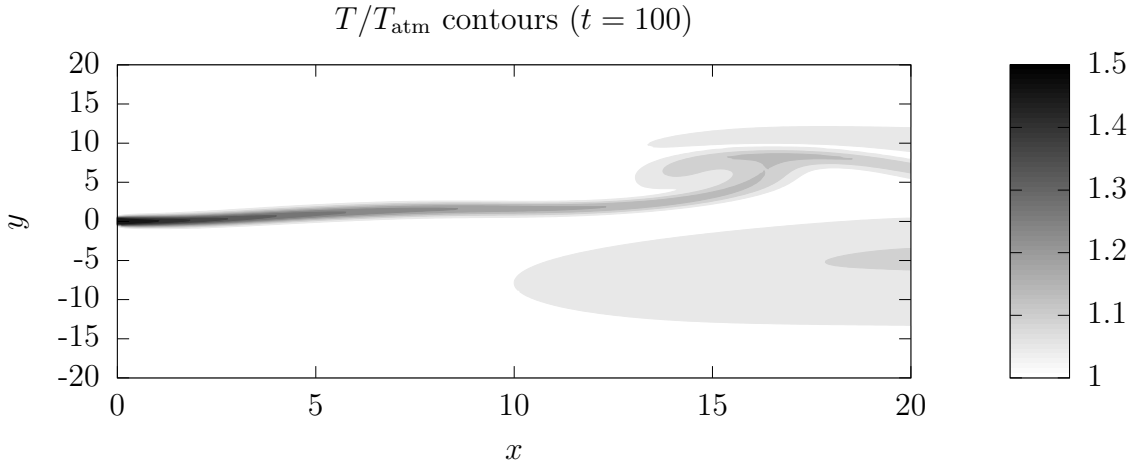

Figure 3.10: Temperature contours for short domain, no sponge-layer case.

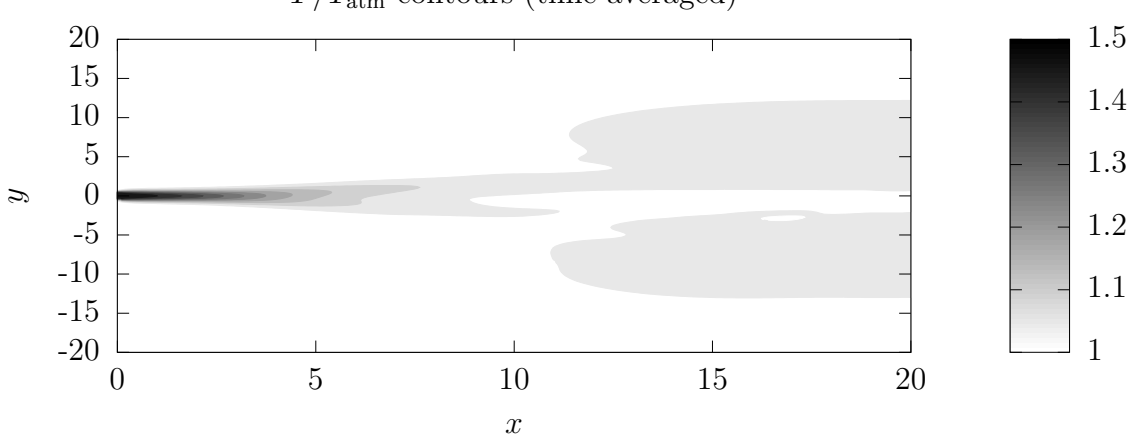

Figure 3.11: Temperature contours for short domain, no sponge-layer case.

Short-domain case

The short-domain case in figures 4.26 and 4.55 clearly shows a build-up of hot gas near the outlet. These problems are caused by large back-flow regions from the outlet as shown in figures 4.106 and 4.57.

Even the long-domain case has some time-averaged inflow at short-domain's outlet plane. This inflow is not physical; buoyant plume correlations show that the time-averaged inflow is zero [Hes02]. Still, if a shorter domain simulation can be shown to perform similarly to a long domain simulation, this is a major improvement.

The length of the domain appears to force the flow; much larger oscillations of temperature than should occur are seen in the probes as shown in figure 4.115.

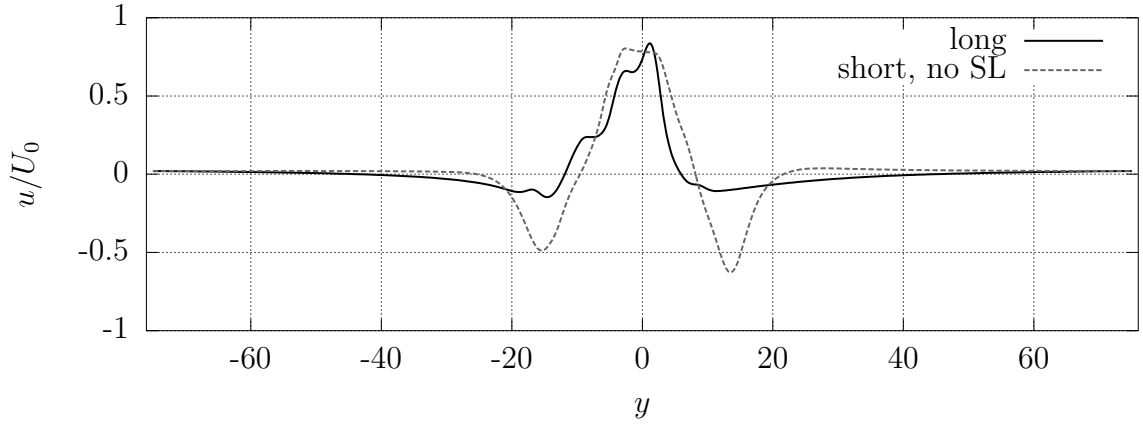

Figure 3.12: Time-averaged u-velocity at the outlet for short domain, no sponge-layer case.

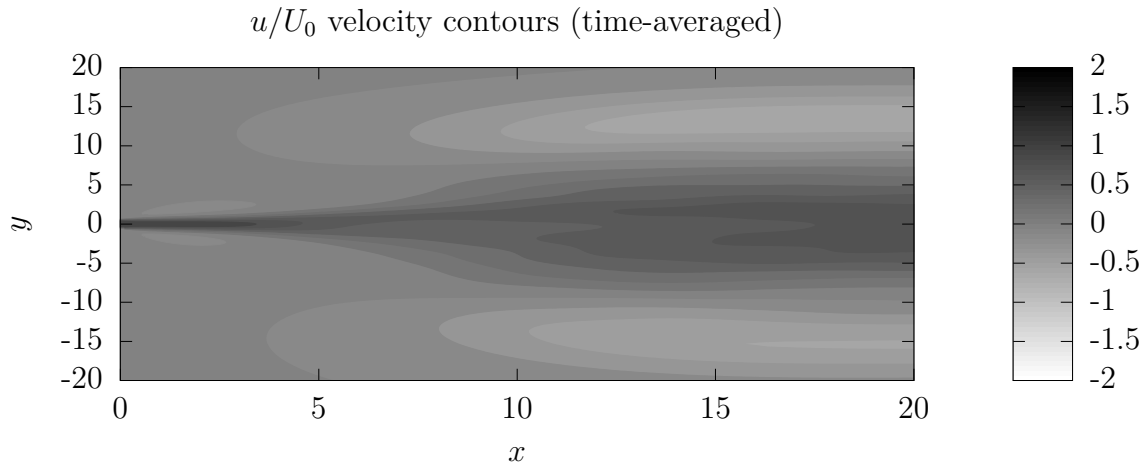

Figure 3.13: u-velocity contours for short domain, no sponge-layer case.

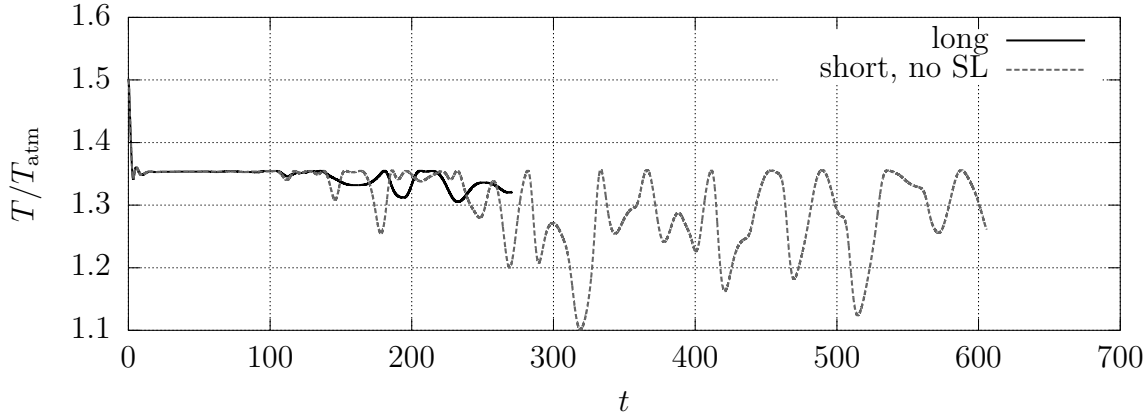

Figure 3.14: Centerline temperature probe one jet width from the inlet for short domain, no sponge-layer case.

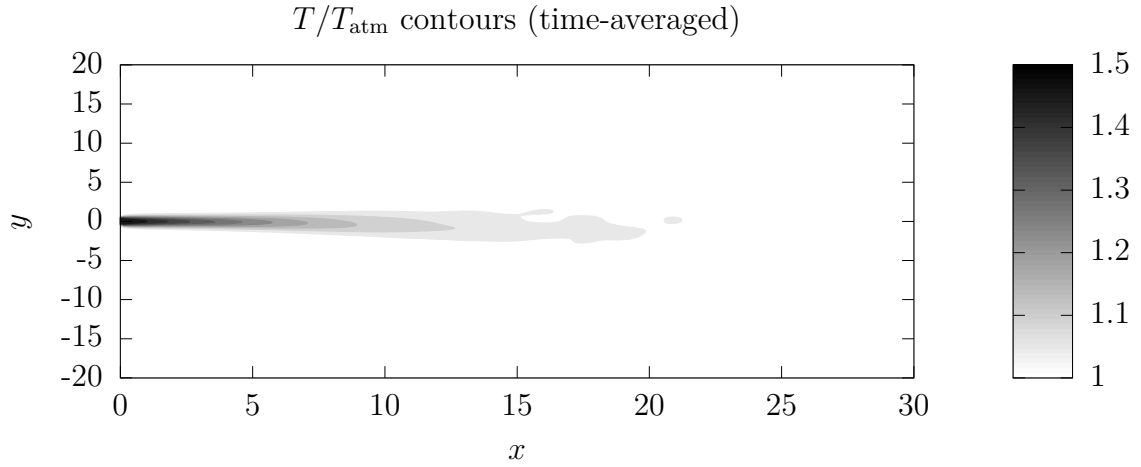

Figure 3.15: Temperature contours for short domain, 10 unit sponge-layer with 10-times viscosity increase case.

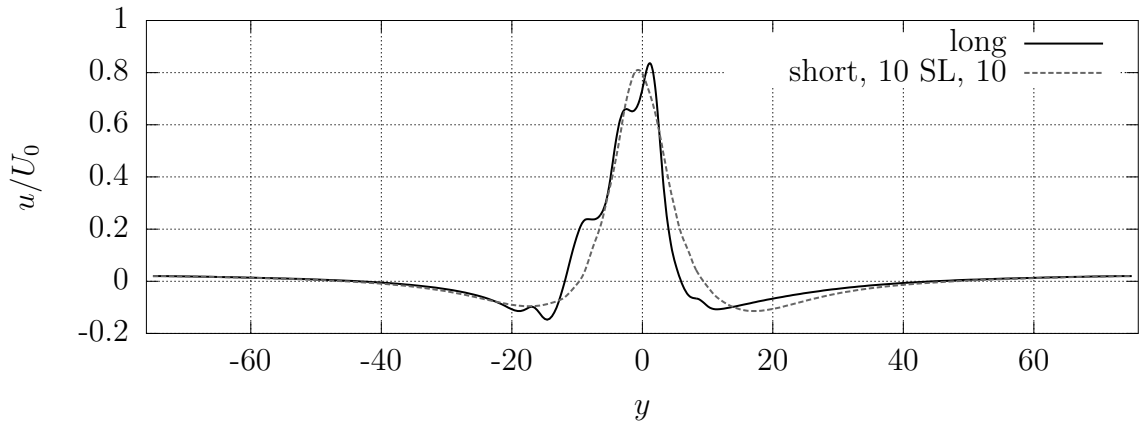

Figure 3.16: Time-averaged u-velocity at the outlet for short domain, 10 unit sponge-layer with 10-times viscosity increase case.

Sponge-layer case (10 unit long sponge layer, 10 times viscosity increase)

The inaccuracies seen earlier are minimized with a short sponge-layer. Figure 4.67 verifies that no hot fluid is building up near the boundary. As shown in figures 4.112 and 4.69, the outlet velocity profiles are similar between the long case and a short case with a sponge-layer. If the long-domain case were better statistically converged, the two would nearly overlap. The inflow velocity is seen to penetrate in much less deeply than the short domain case without a sponge layer as shown in figure 4.69. The forcing from the outflow is eliminated as shown in figure 4.121.

The sponge-layer could affect the upstream flow by damping out gradients. This

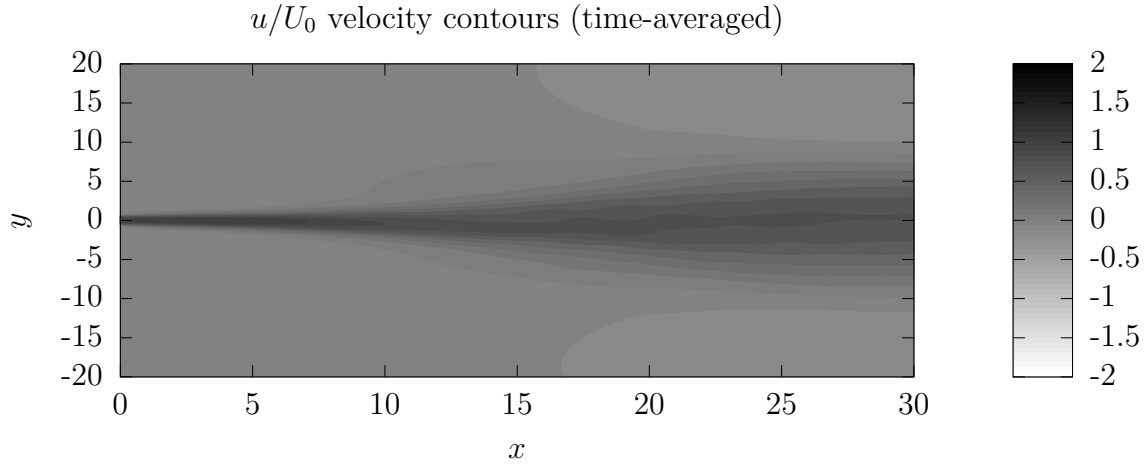

Figure 3.17: u-velocity contours for short domain, 10 unit sponge-layer with 10-times viscosity increase case.

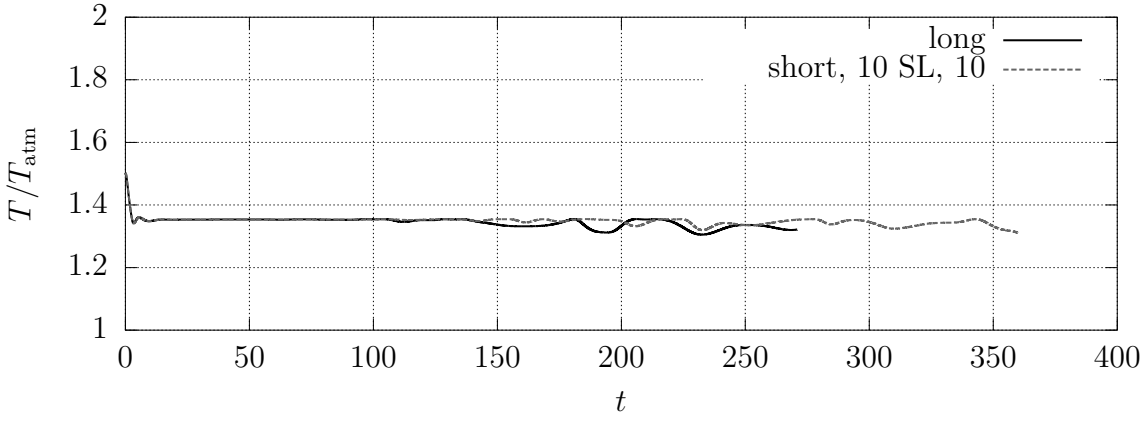

Figure 3.18: Centerline temperature probe one jet width from the inlet for short domain, 10 unit sponge-layer with 10-times viscosity increase case.

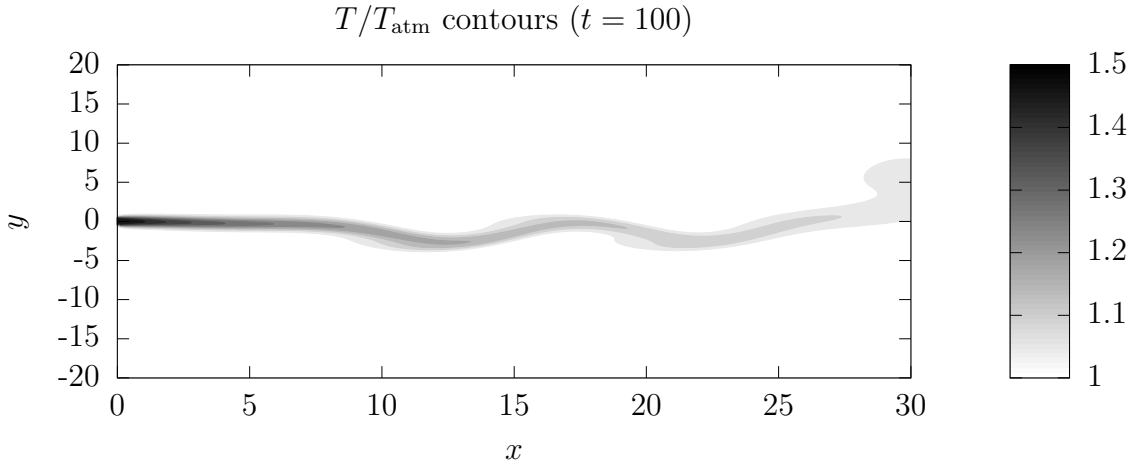

Figure 3.19: Temperature contours for the short domain, 10 unit sponge-layer with 10-times viscosity increase case.

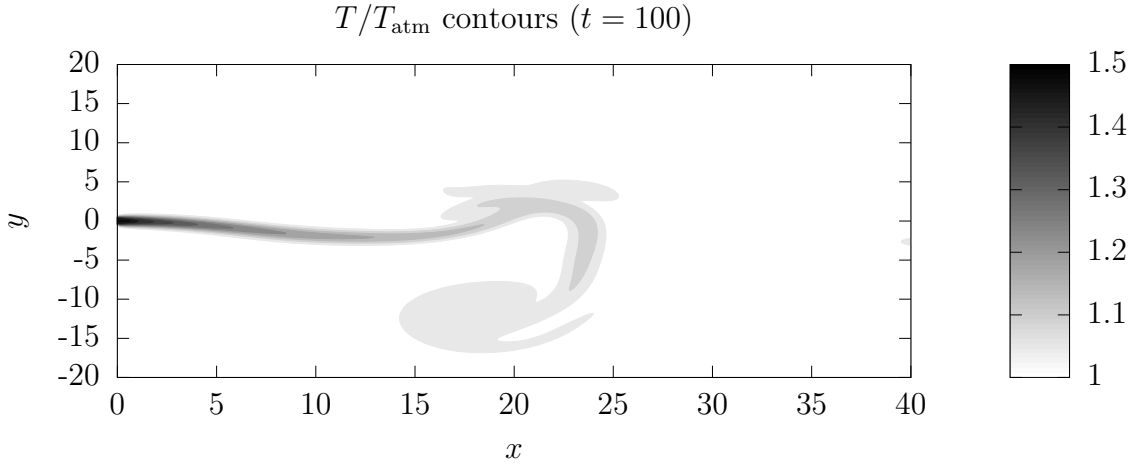

Figure 3.20: Temperature contours for long domain, no sponge-layer case.

may show up in the temperature contours by shrinking the size of the vortical structures seen. A comparison of the long-domain and short domain with sponge-layer cases show this does not appear to be the case, as seen in figures 4.41 and 4.21. Both figures show vortex structures with diameters of approximately 10.

3.4 Conclusion

The side boundary conditions appear to cause severe numerical instabilities. Extending the distance to these boundaries from the jet delays the development of the instability as shown in figure 3.7, however, the delay is not adequate to always obtain statistically converged time-averaged data. Future research into open boundary conditions for the far-field is worthwhile to fix this stability issue. A better evaluation of the outflow conditions is possible if the stability issue is fixed. It is also possible that improving the side boundary conditions will in turn improve the outflow accuracy because entrainment will be more realistic.

Adding sponge-layers at the side boundaries may eliminate this instability and is worth exploring, as also is examining more closely what occurs on the sides as the instability develops. Future research should also consider buoyant jets with better behaved boundaries such as walls, slip walls, or periodic boundaries.

Sponge-layers appear to improve accuracy near outflow boundaries for buoyancy-driven flows. This approach can be computationally inexpensive compared against large domains. This approach is not perfect, as it does not entirely eliminate unphysical inflows, however, it does eliminate unphysical build-up of how gas near the outflow plane.

Appendix: $T/T_{\mathbf{atm}} = 1.5$ plots

4.5 Instantaneous fields

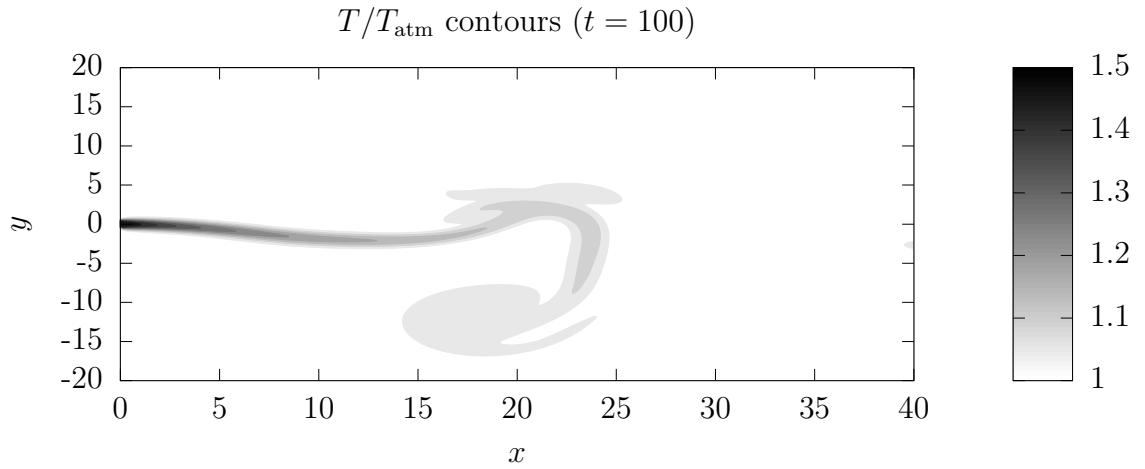

Figure 4.21: Temperature contours for the long domain, no sponge-layer case.

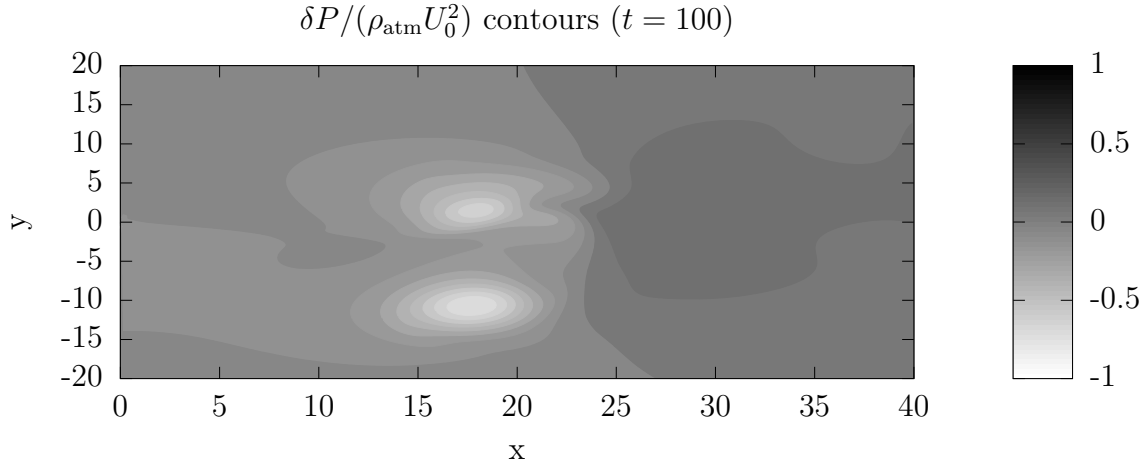

Figure 4.22: Pressure contours for the long domain, no sponge-layer case.

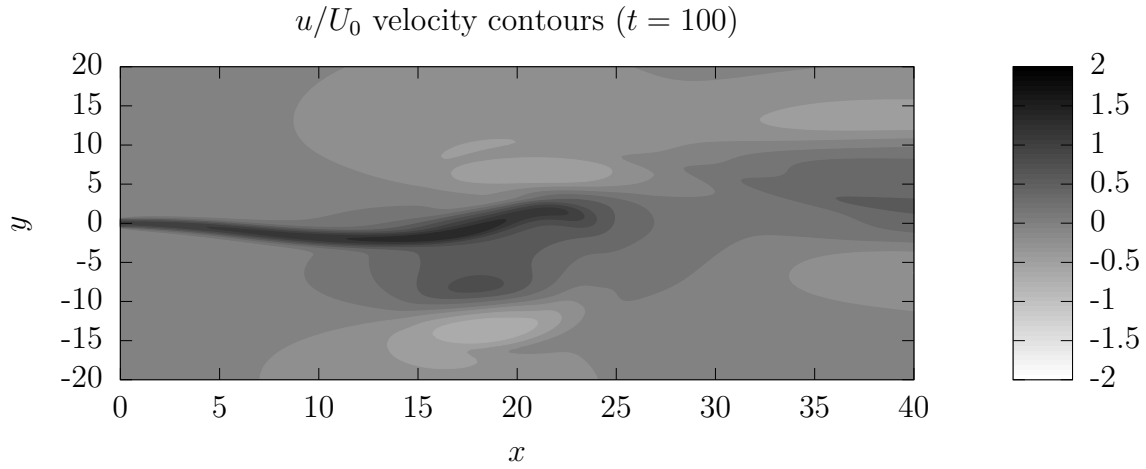

Figure 4.23: u-velocity contours for the long domain, no sponge-layer case.

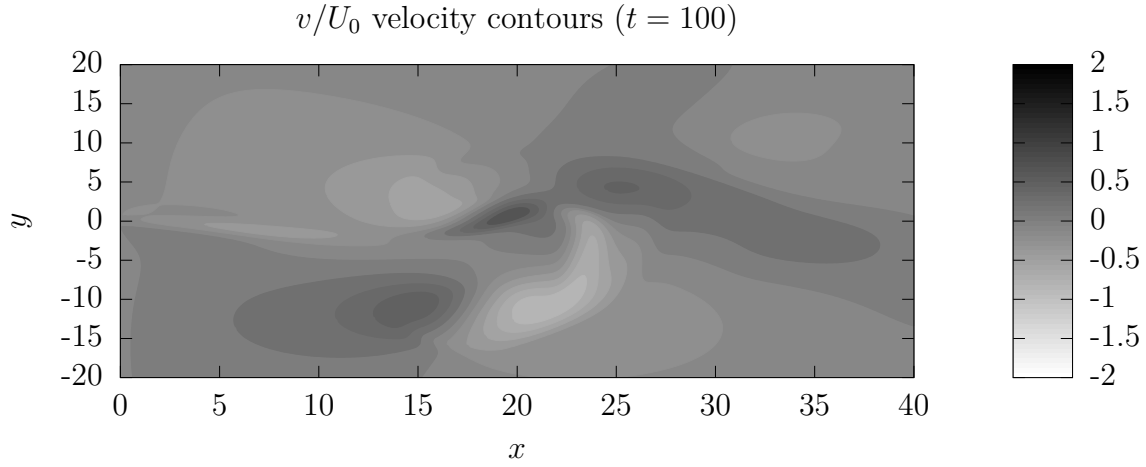

Figure 4.24: v-velocity contours for the long domain, no sponge-layer case.

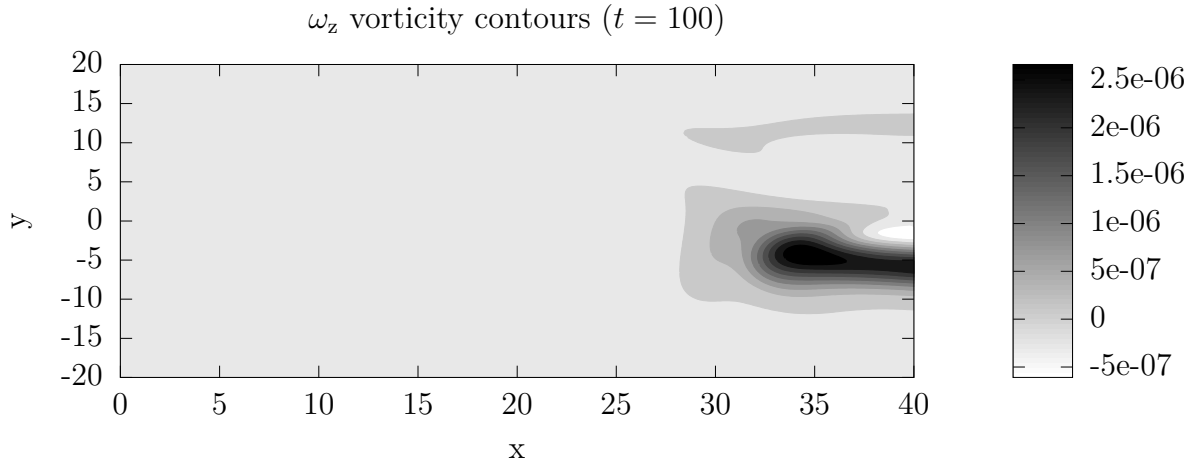

Figure 4.25: Vorticity contours for the long domain, no sponge-layer case.

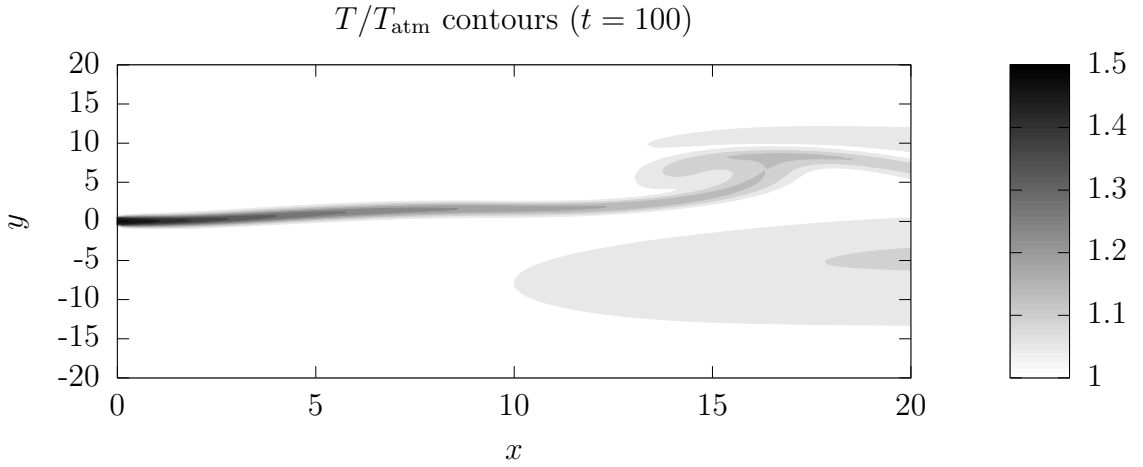

Figure 4.26: Temperature contours for the short domain, no sponge-layer case.

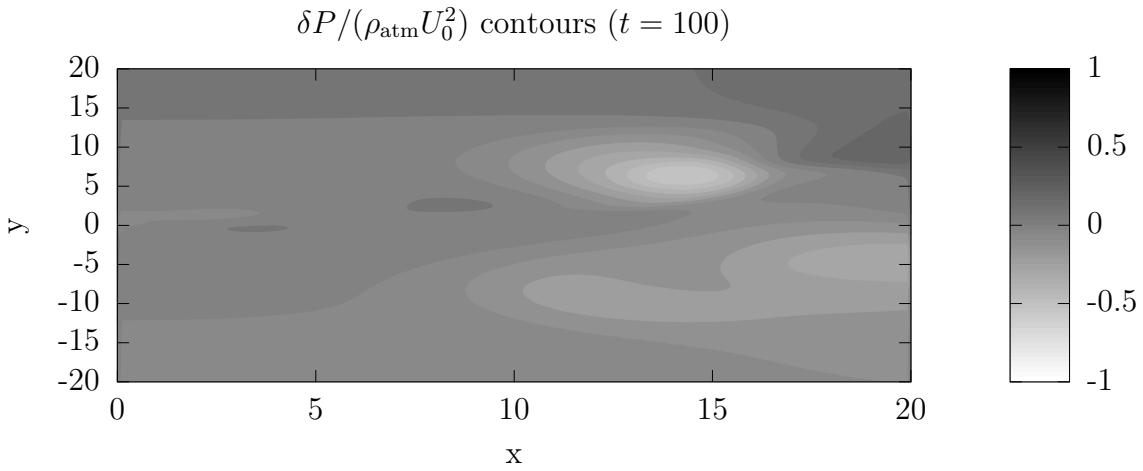

Figure 4.27: Pressure contours for the short domain, no sponge-layer case.

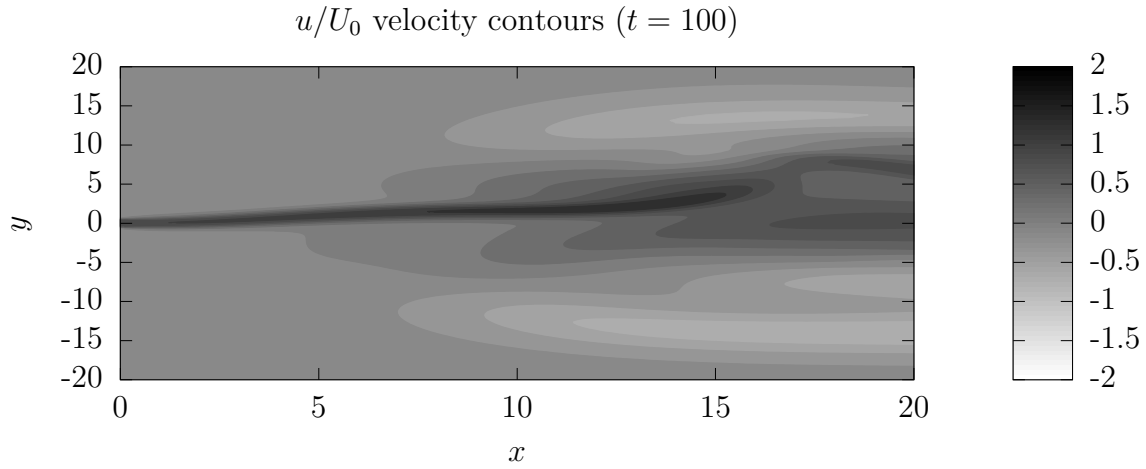

Figure 4.28: u-velocity contours for the short domain, no sponge-layer case.

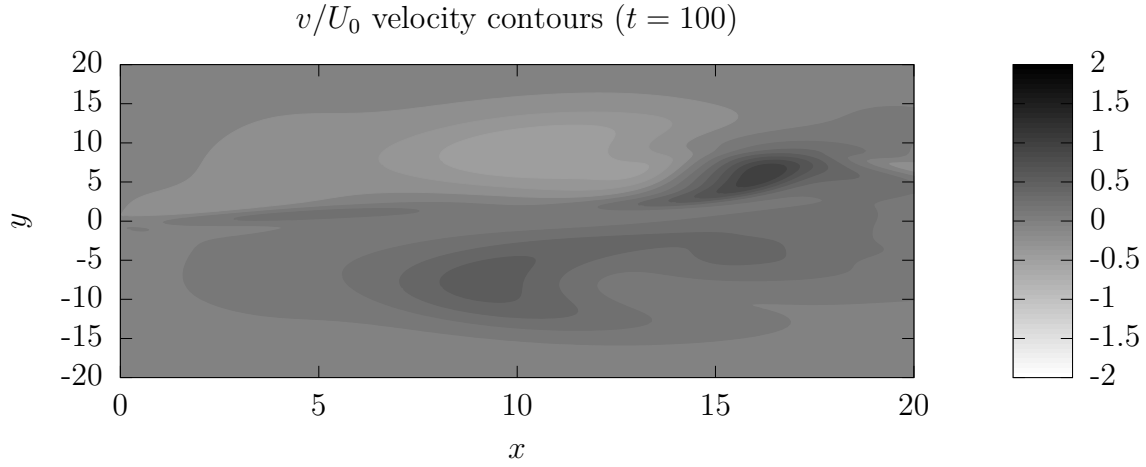

Figure 4.29: v-velocity contours for the short domain, no sponge-layer case.

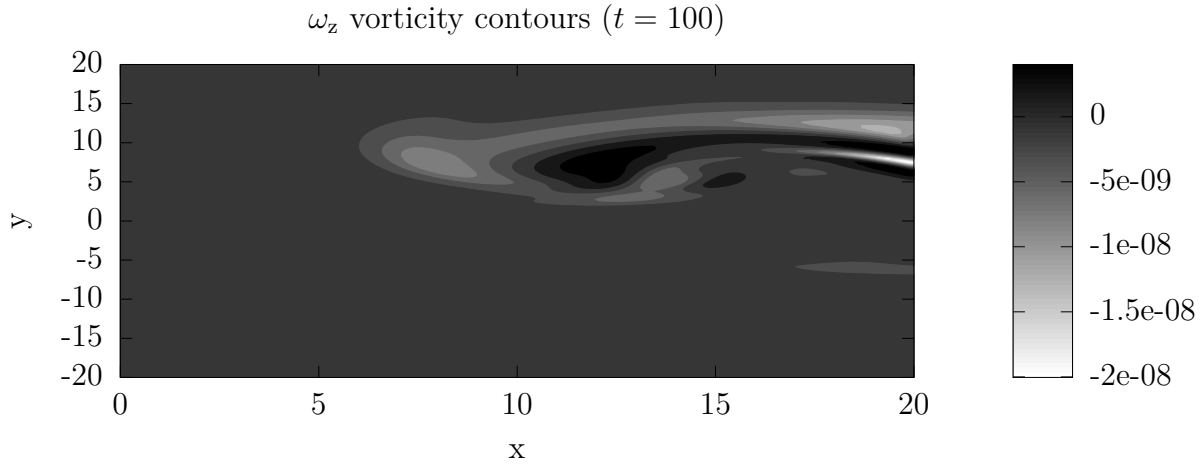

Figure 4.30: Vorticity contours for the short domain, no sponge-layer case.

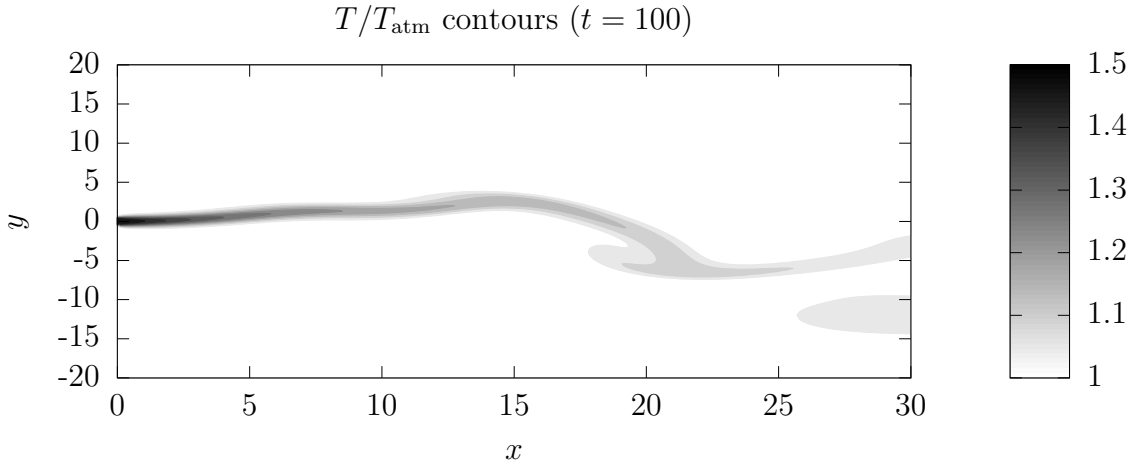

Figure 4.31: Temperature contours for the short domain, 10 unit sponge-layer with 5-times viscosity increase case.

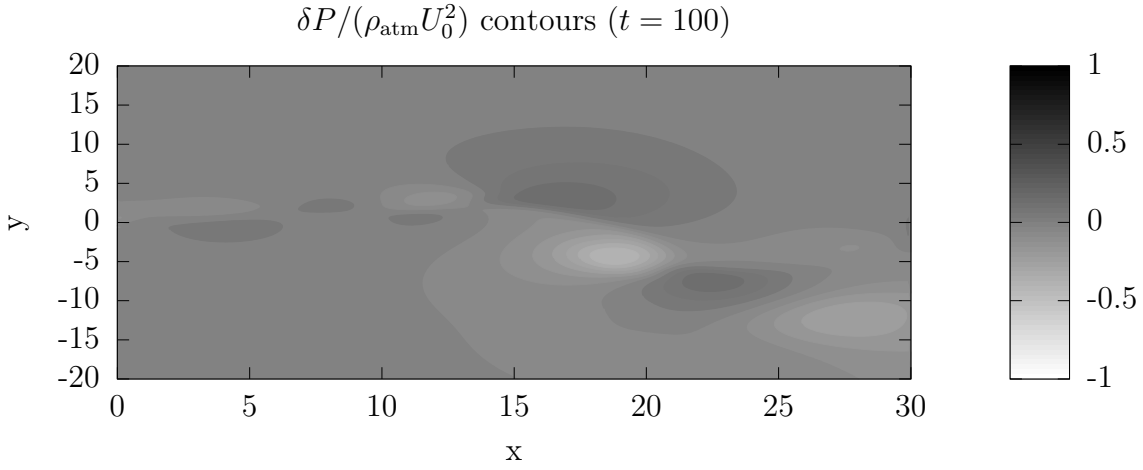

Figure 4.32: Pressure contours for the short domain, 10 unit sponge-layer with 5-times viscosity increase case.

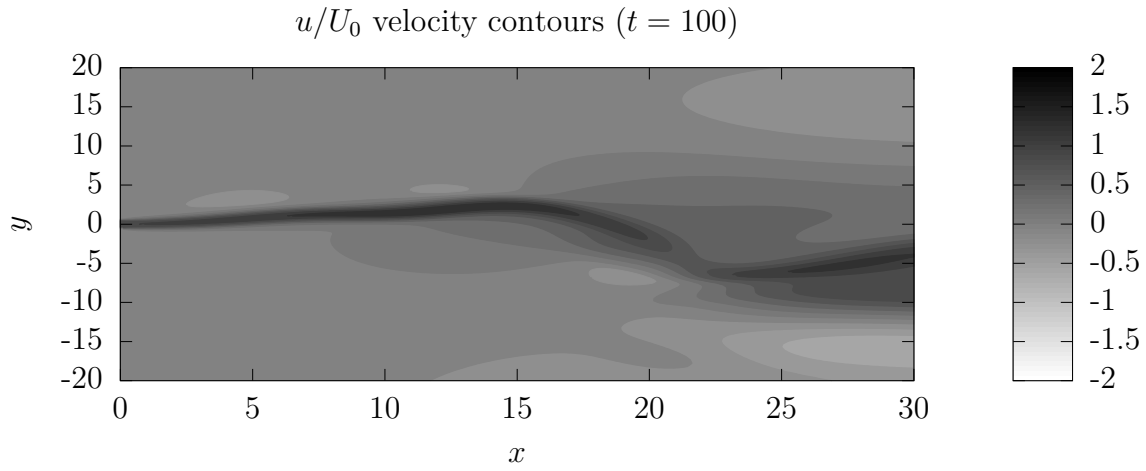

Figure 4.33: u-velocity contours for the short domain, 10 unit sponge-layer with 5-times viscosity increase case.

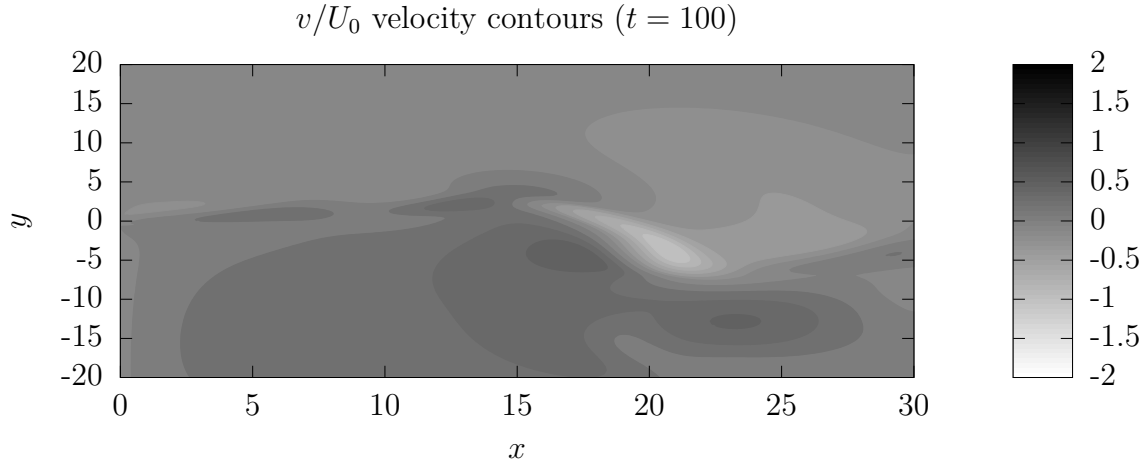

Figure 4.34: v-velocity contours for the short domain, 10 unit sponge-layer with 5-times viscosity increase case.

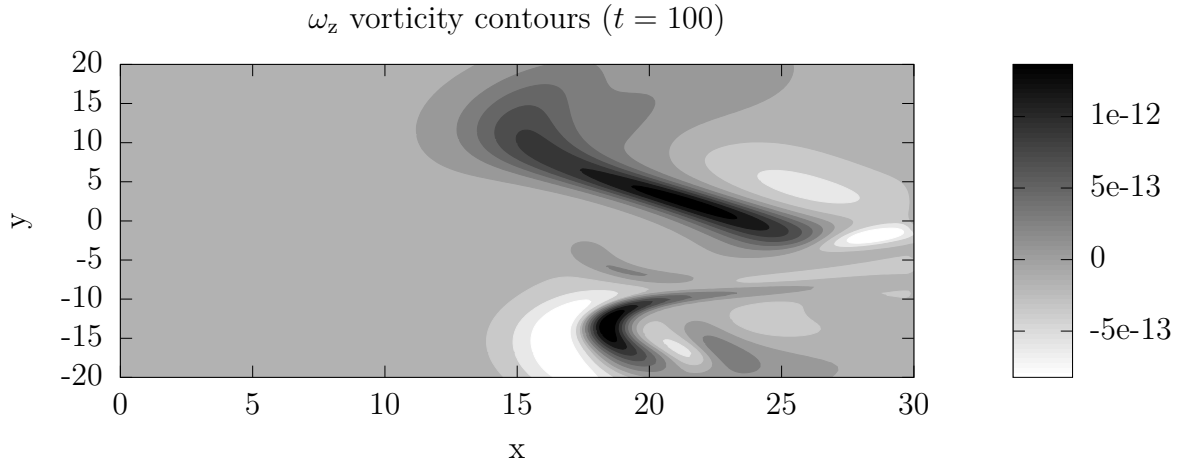

Figure 4.35: Vorticity contours for the short domain, 10 unit sponge-layer with 5-times viscosity increase case.

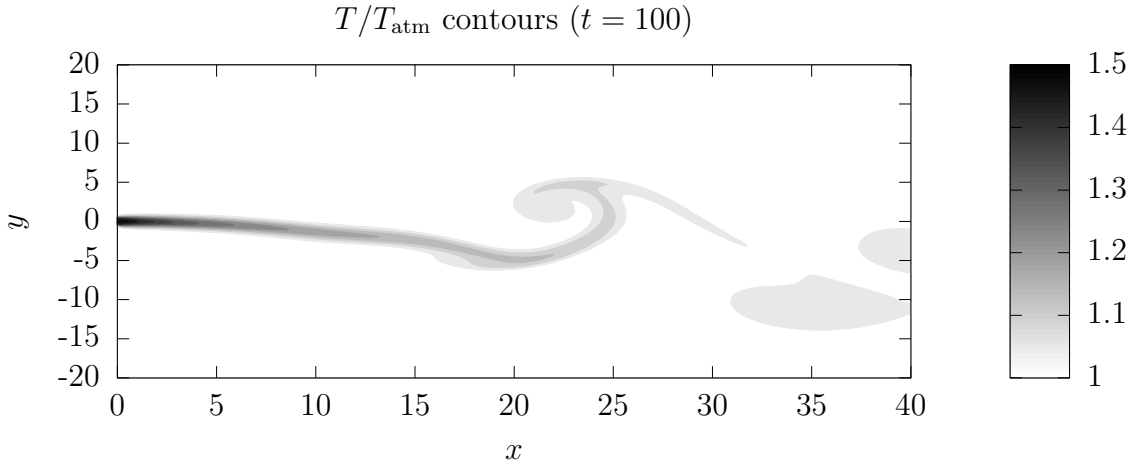

Figure 4.36: Temperature contours for the short domain, 20 unit sponge-layer with 5-times viscosity increase case.

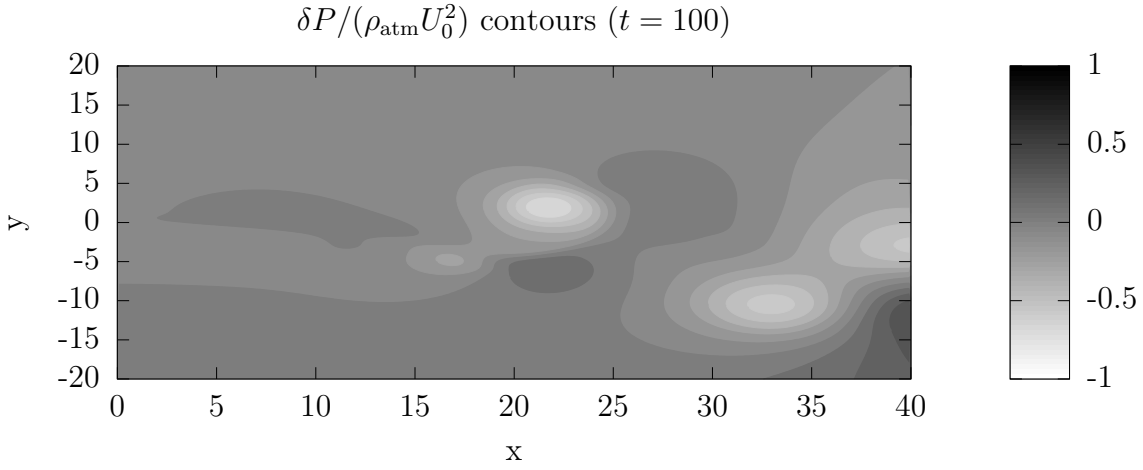

Figure 4.37: Pressure contours for the short domain, 20 unit sponge-layer with 5-times viscosity increase case.

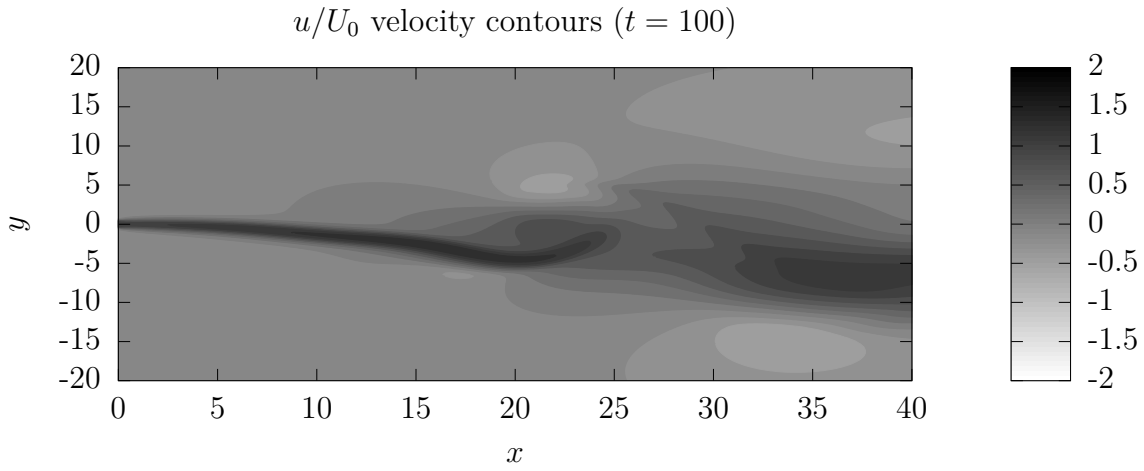

Figure 4.38: u-velocity contours for the short domain, 20 unit sponge-layer with 5-times viscosity increase case.

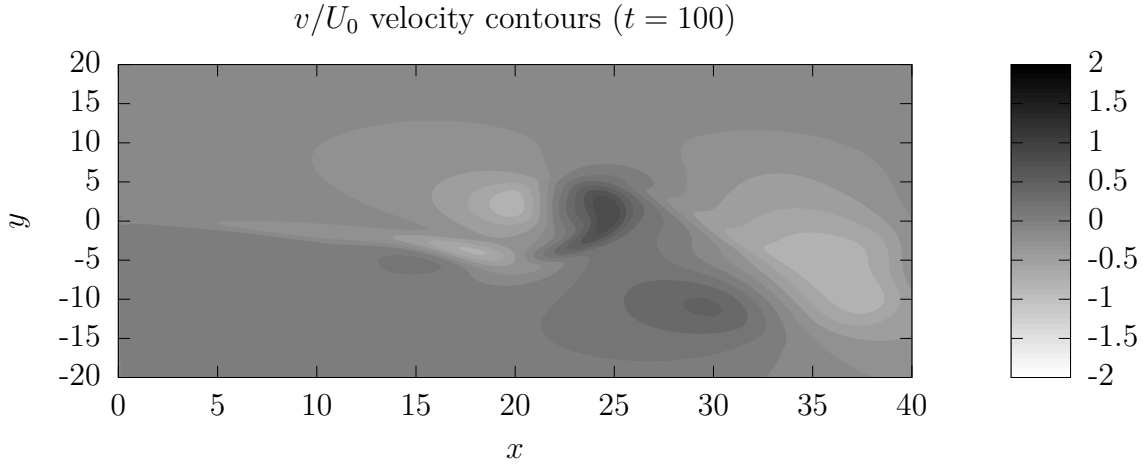

Figure 4.39: v-velocity contours for the short domain, 20 unit sponge-layer with 5-times viscosity increase case.

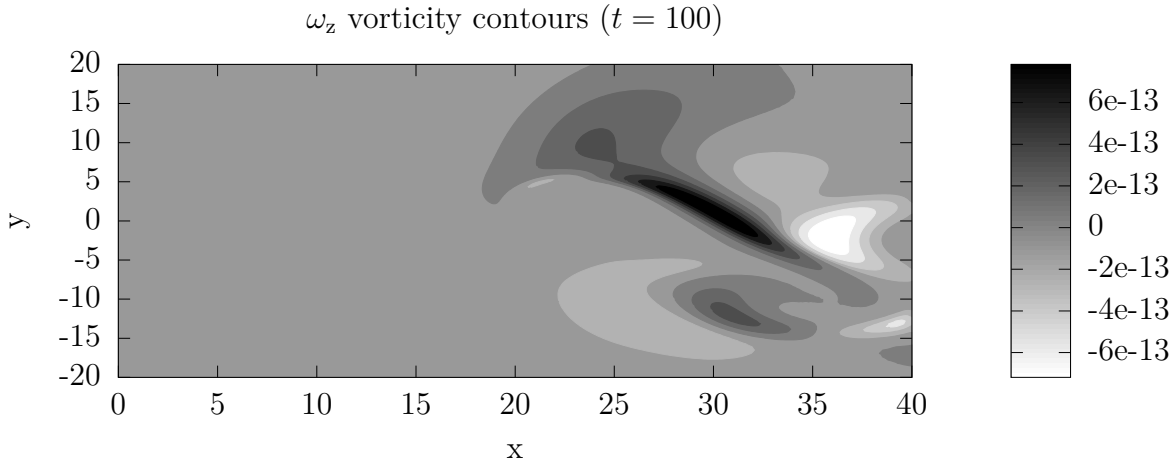

Figure 4.40: Vorticity contours for the short domain, 20 unit sponge-layer with 5-times viscosity increase case.

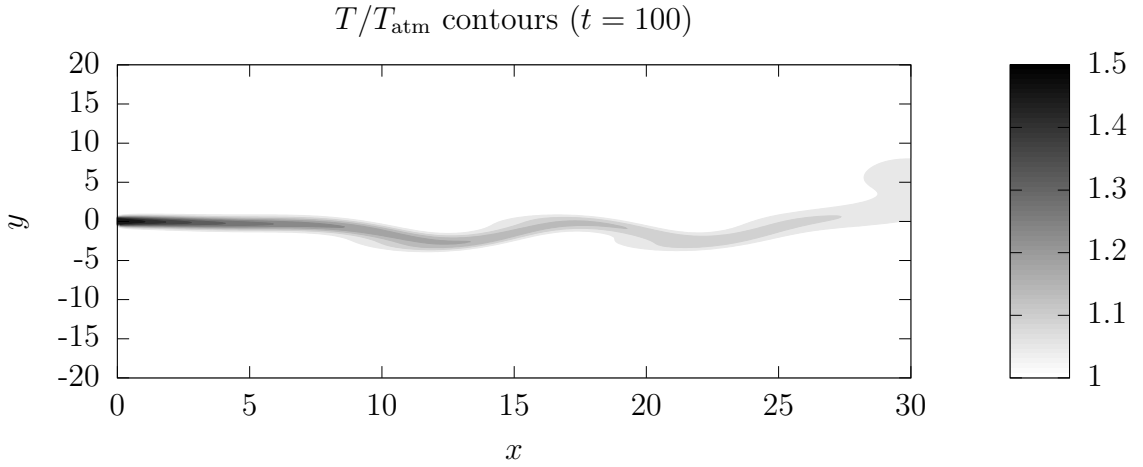

Figure 4.41: Temperature contours for the short domain, 10 unit sponge-layer with 10-times viscosity increase case.

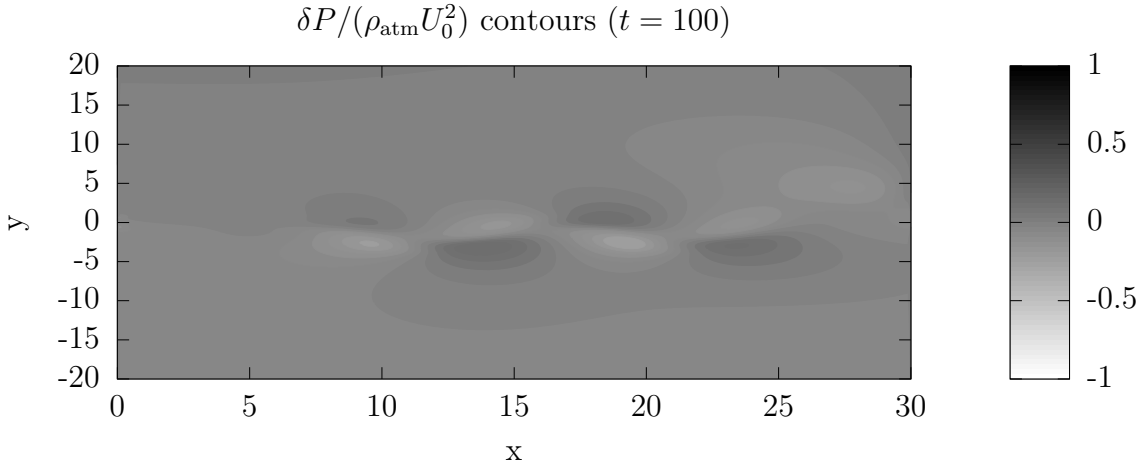

Figure 4.42: Pressure contours for the short domain, 10 unit sponge-layer with 10-times viscosity increase case.

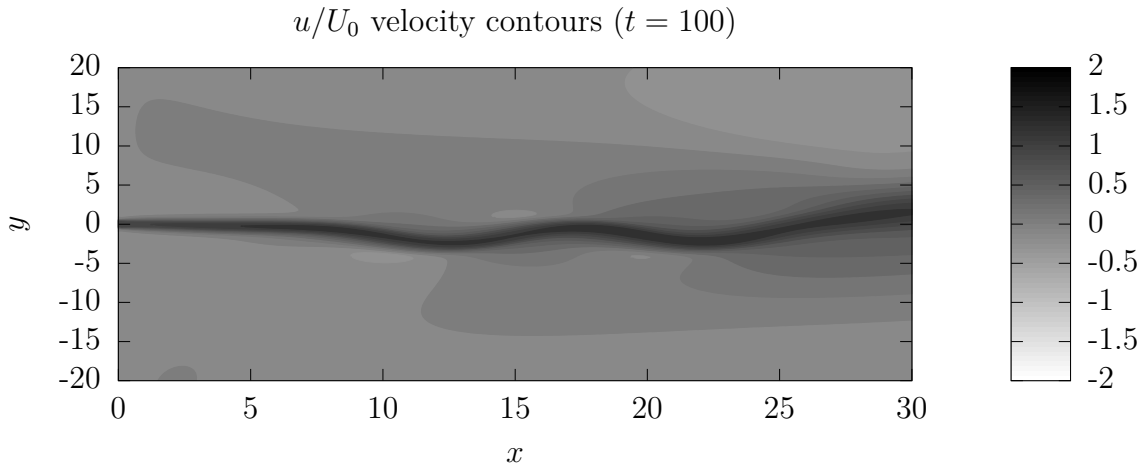

Figure 4.43: u-velocity contours for the short domain, 10 unit sponge-layer with 10-times viscosity increase case.

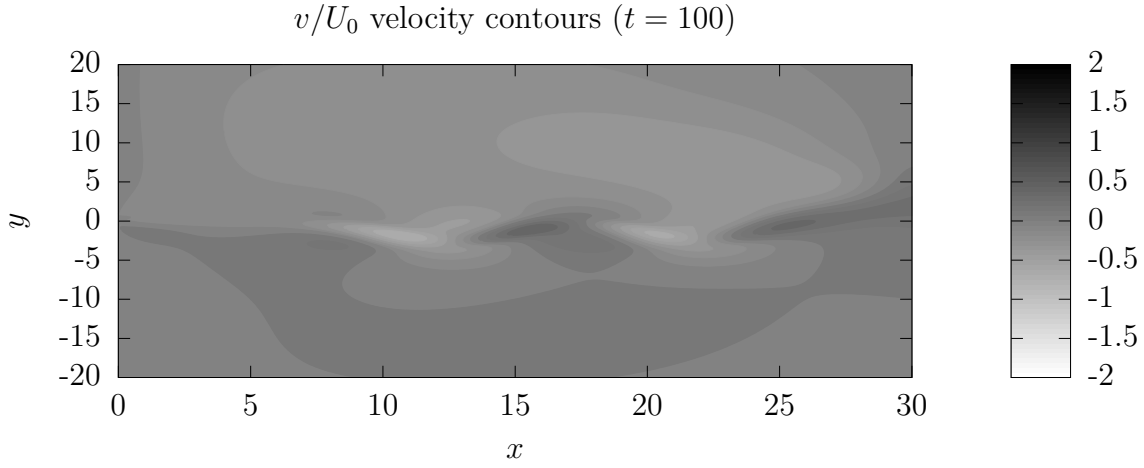

Figure 4.44: v-velocity contours for the short domain, 10 unit sponge-layer with 10-times viscosity increase case.

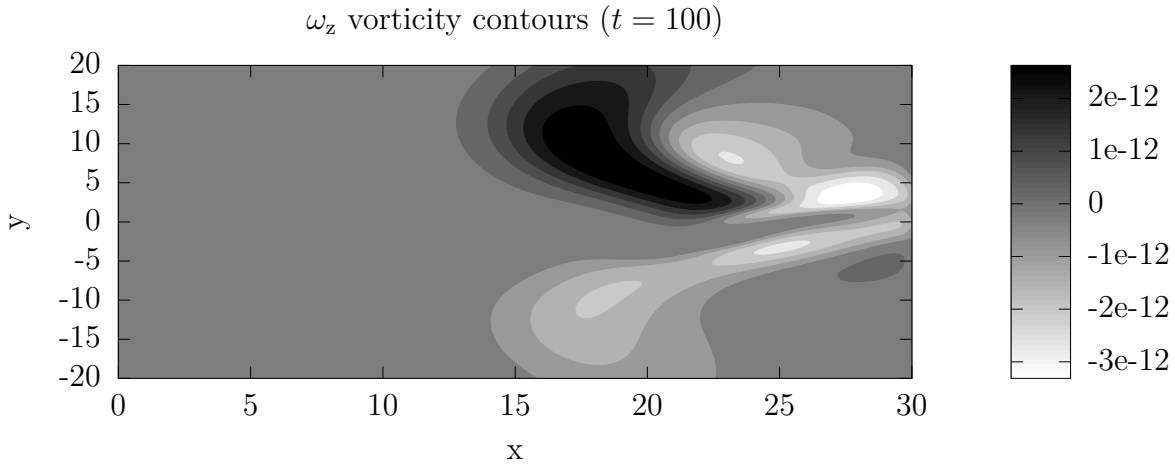

Figure 4.45: Vorticity contours for the short domain, 10 unit sponge-layer with 10-times viscosity increase case.

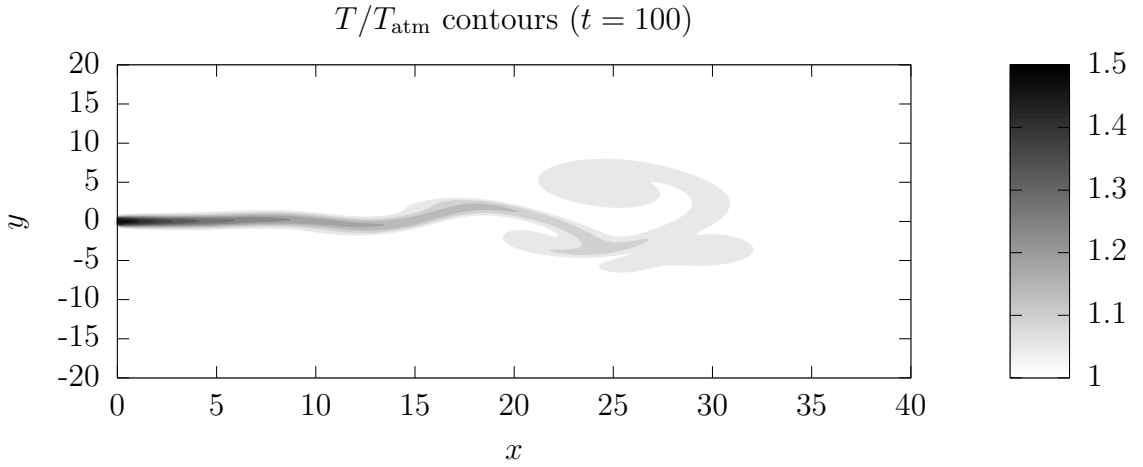

Figure 4.46: Temperature contours for the short domain, 20 unit sponge-layer with 10-times viscosity increase case.

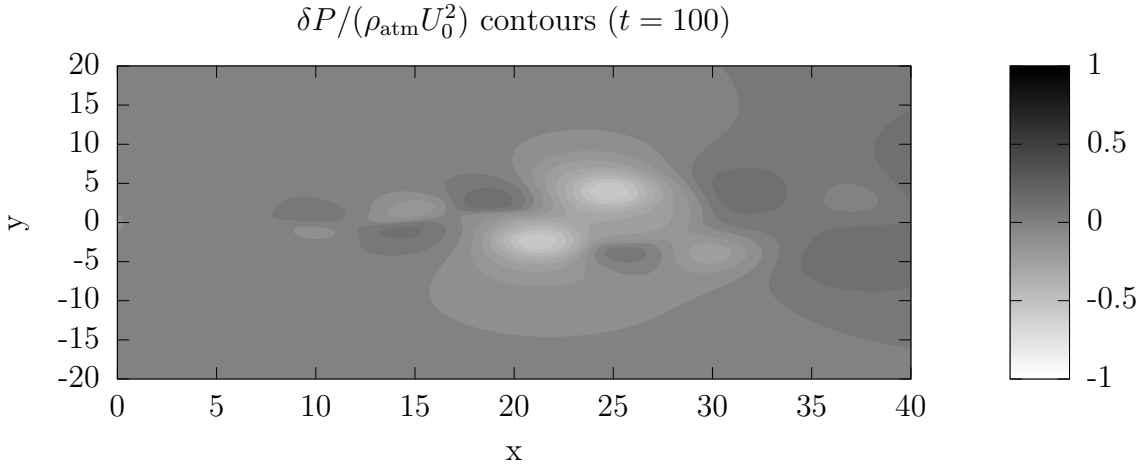

Figure 4.47: Pressure contours for the short domain, 20 unit sponge-layer with 10-times viscosity increase case.

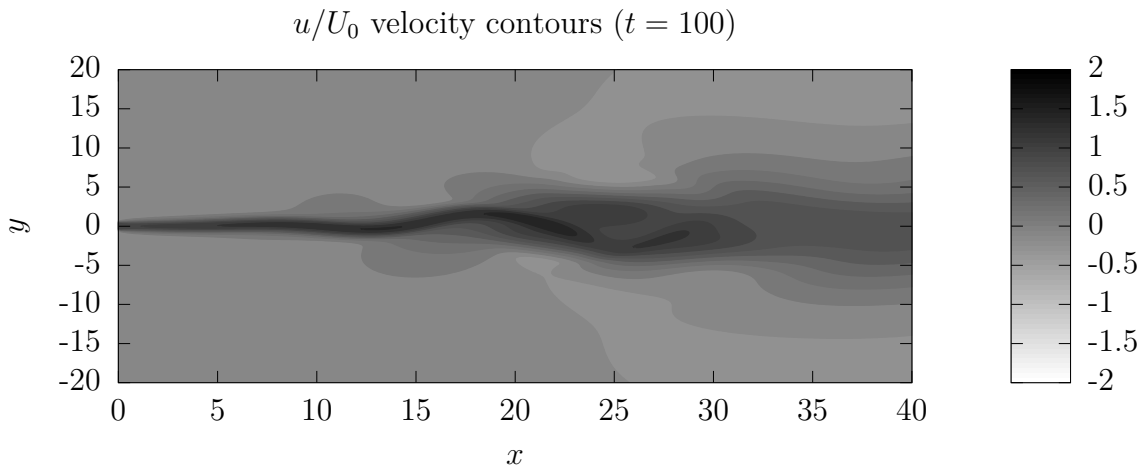

Figure 4.48: u-velocity contours for the short domain, 20 unit sponge-layer with 10-times viscosity increase case.

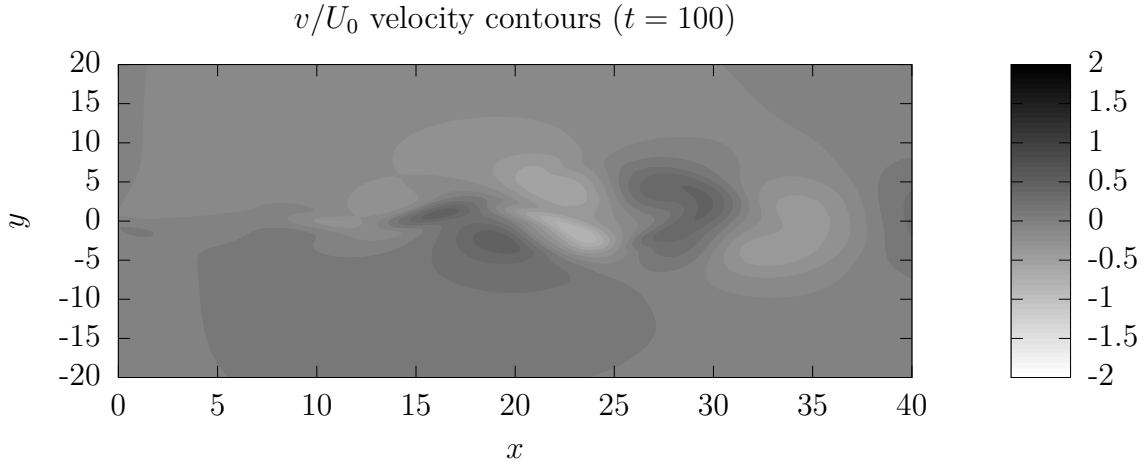

Figure 4.49: v-velocity contours for the short domain, 20 unit sponge-layer with 10-times viscosity increase case.

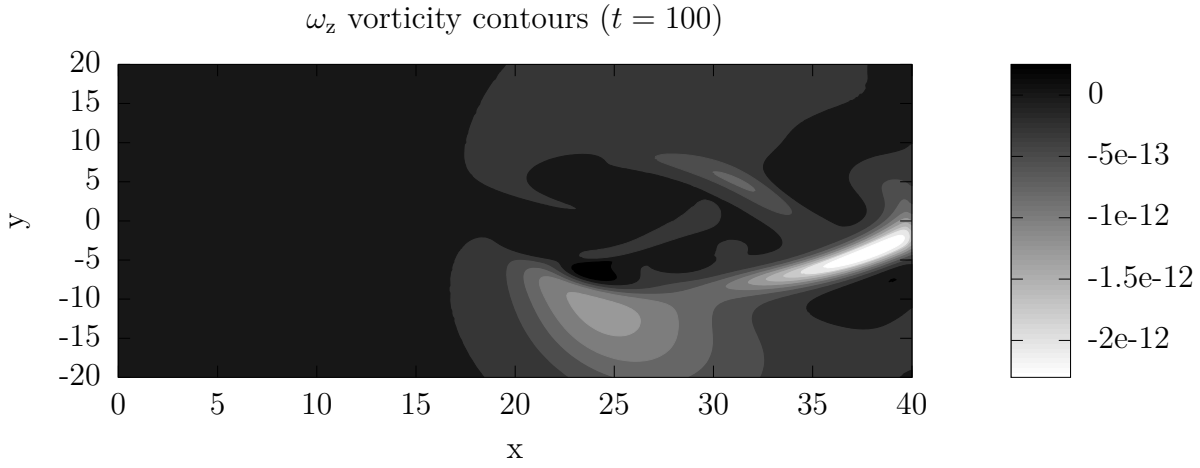

Figure 4.50: Vorticity contours for the short domain, 20 unit sponge-layer with 10-times viscosity increase case.

4.6 Time-averaged fields

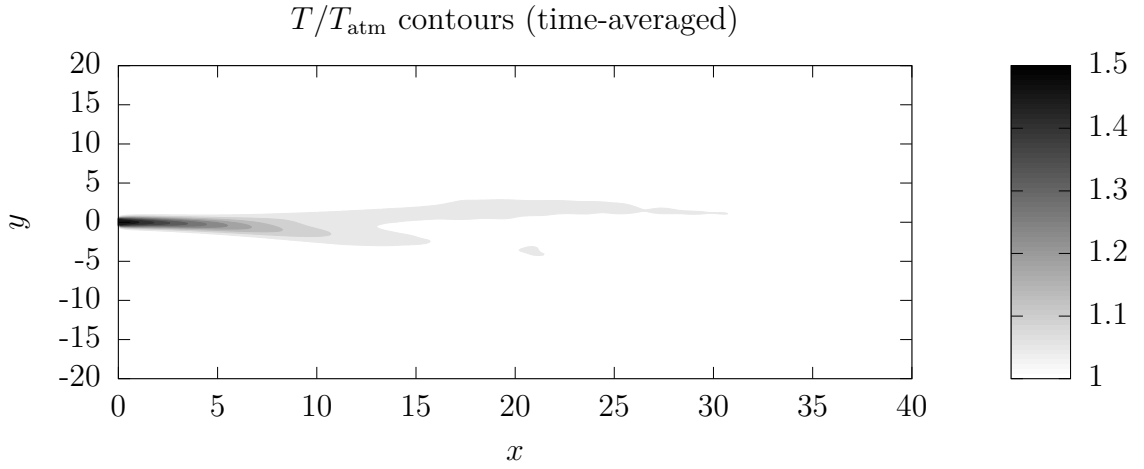

Figure 4.51: Temperature contours for the long domain, no sponge-layer case.

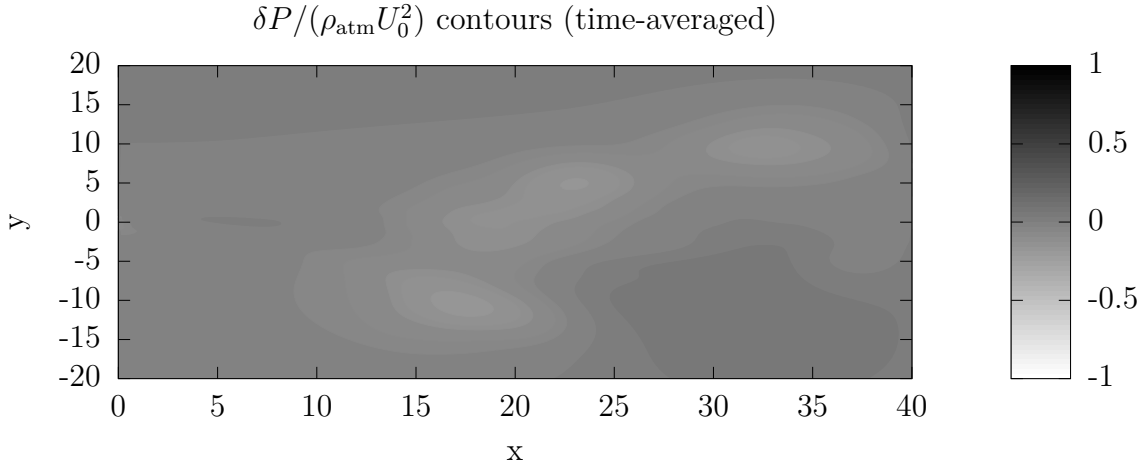

Figure 4.52: Pressure contours for the long domain, no sponge-layer case.

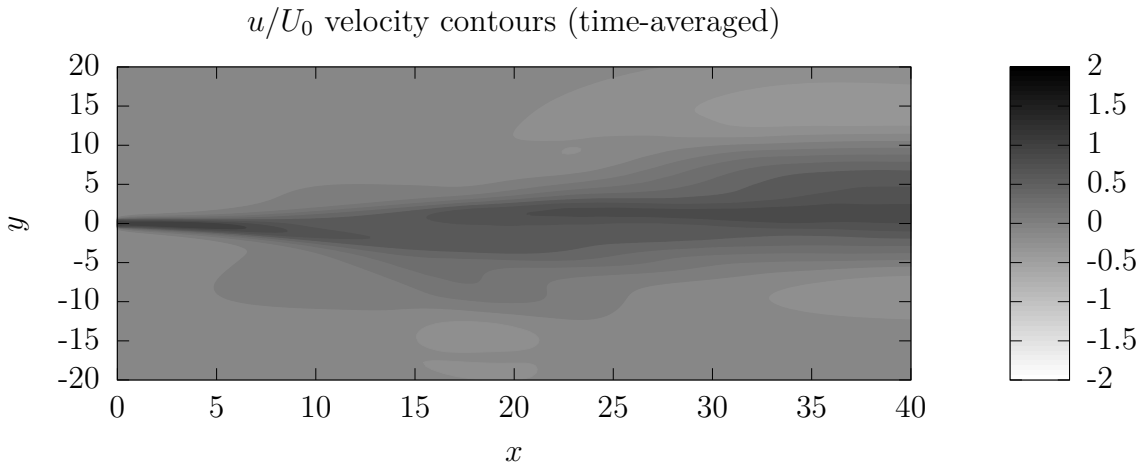

Figure 4.53: u-velocity contours for the long domain, no sponge-layer case.

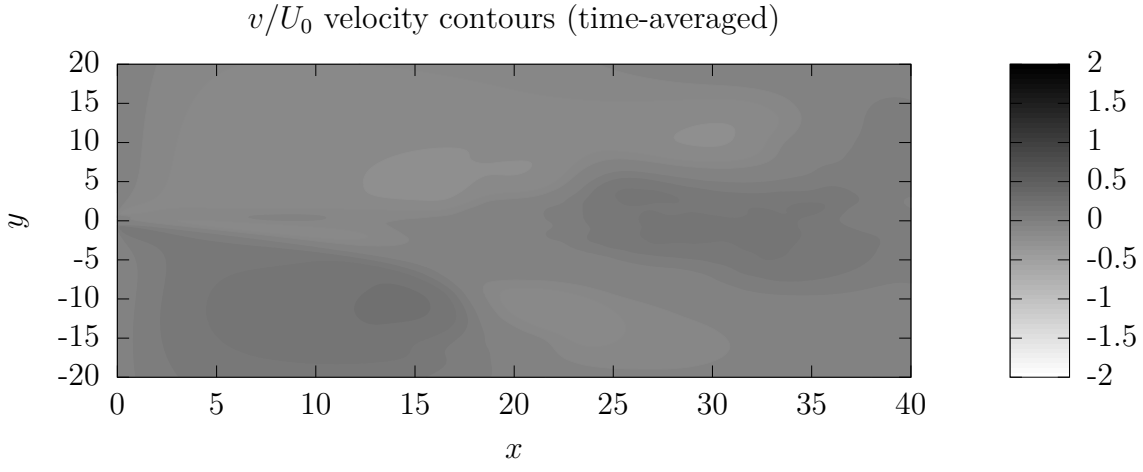

Figure 4.54: v-velocity contours for the long domain, no sponge-layer case.

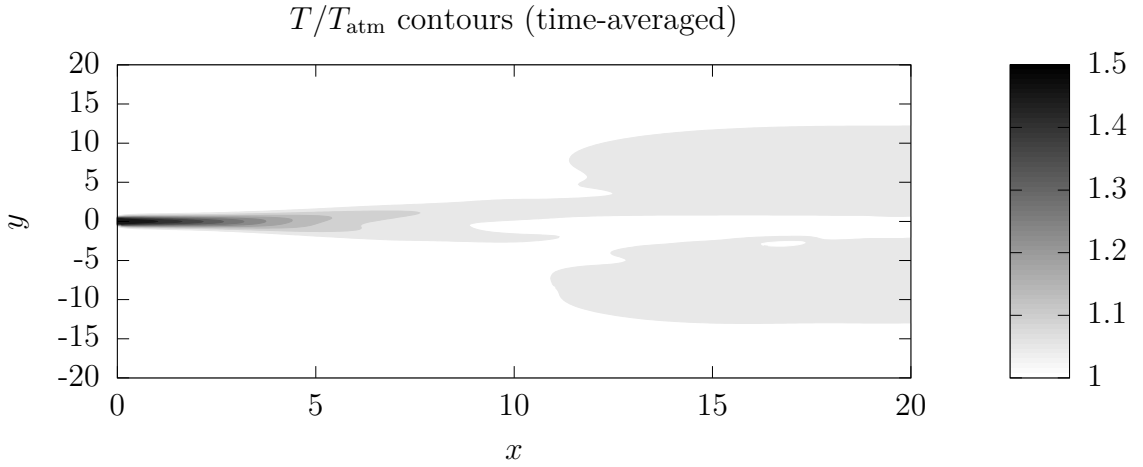

Figure 4.55: Temperature contours for the short domain, no sponge-layer case.

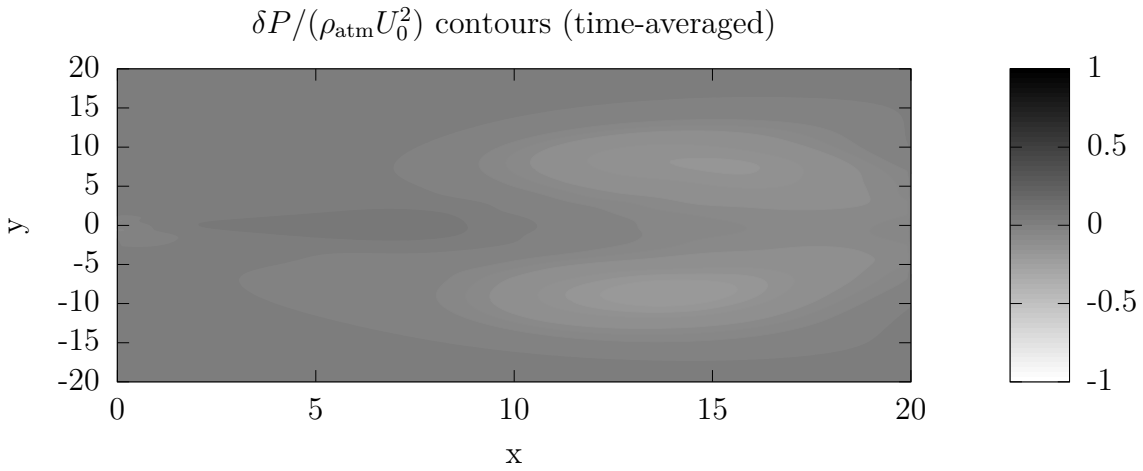

Figure 4.56: Pressure contours for the short domain, no sponge-layer case.

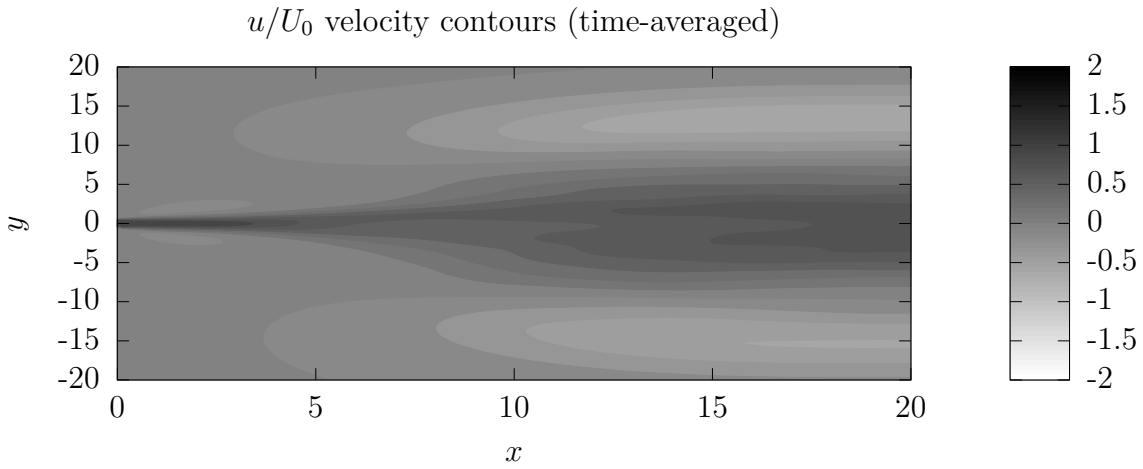

Figure 4.57: u-velocity contours for the short domain, no sponge-layer case.

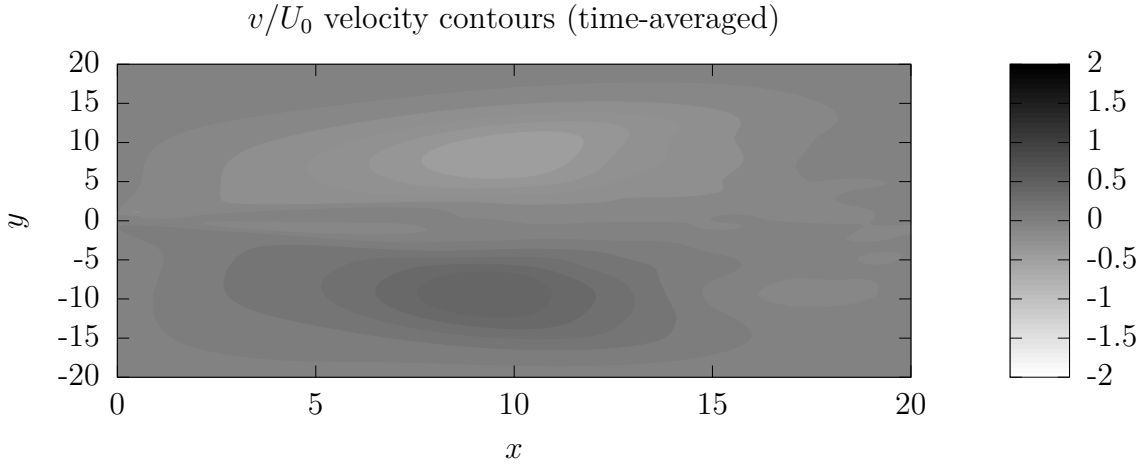

Figure 4.58: v-velocity contours for the short domain, no sponge-layer case.

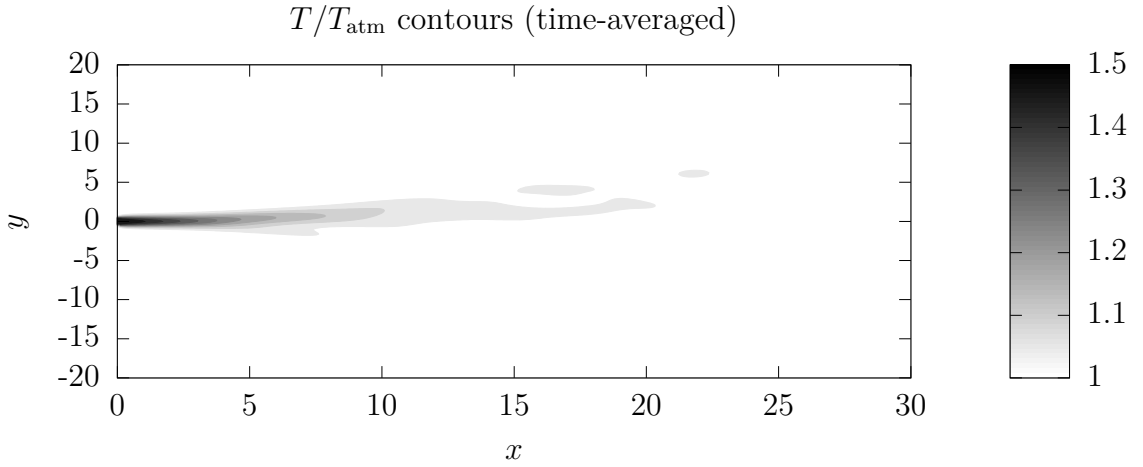

Figure 4.59: Temperature contours for the short domain, 10 unit sponge-layer with 5-times viscosity increase case.

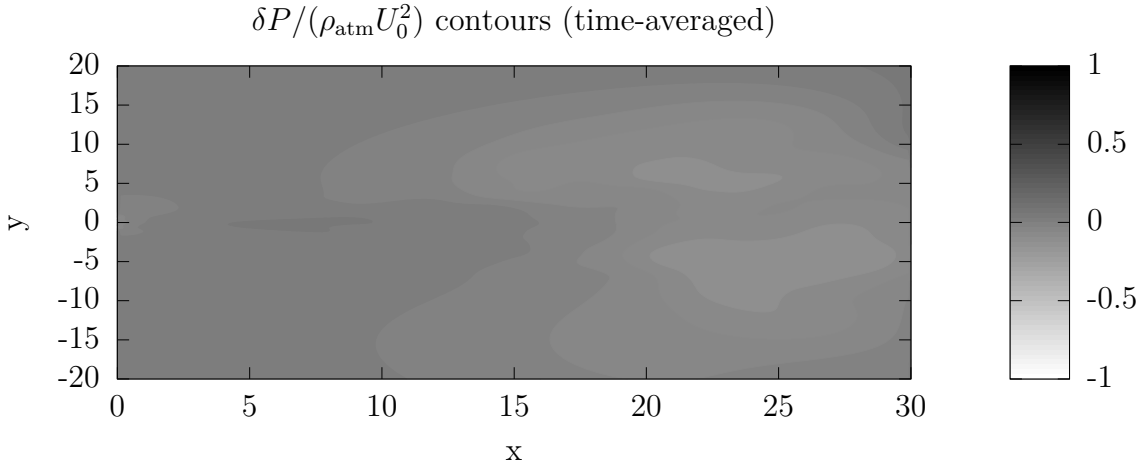

Figure 4.60: Pressure contours for the short domain, 10 unit sponge-layer with 5-times viscosity increase case.

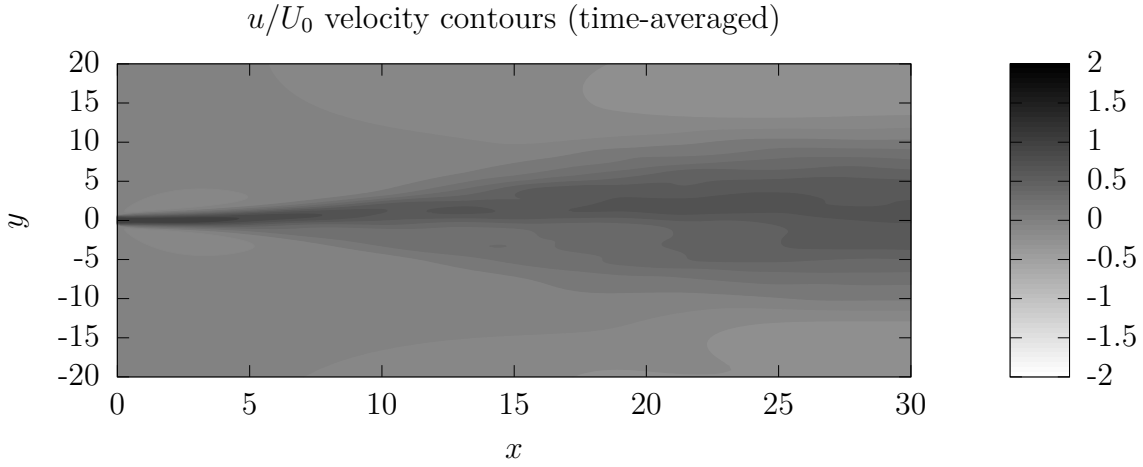

Figure 4.61: u-velocity contours for the short domain, 10 unit sponge-layer with 5-times viscosity increase case.

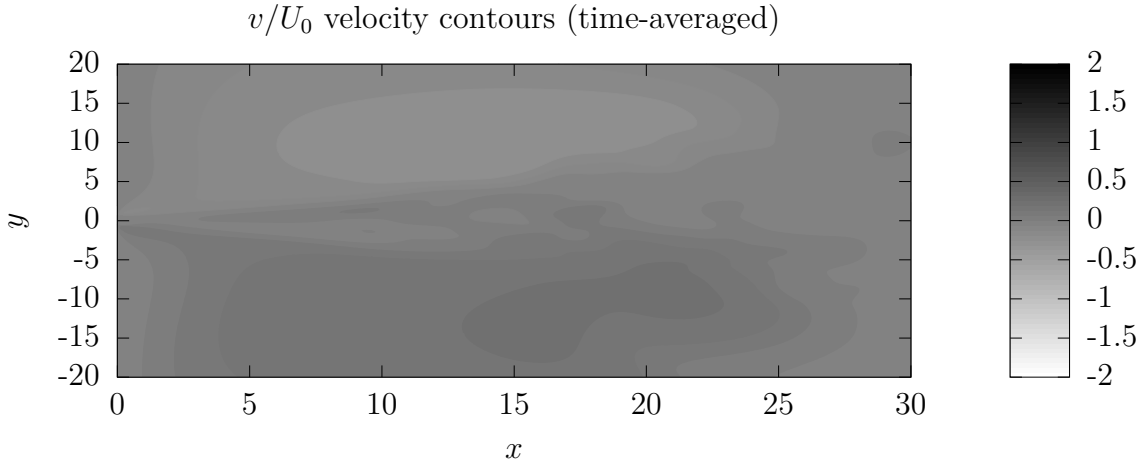

Figure 4.62: v-velocity contours for the short domain, 10 unit sponge-layer with 5-times viscosity increase case.

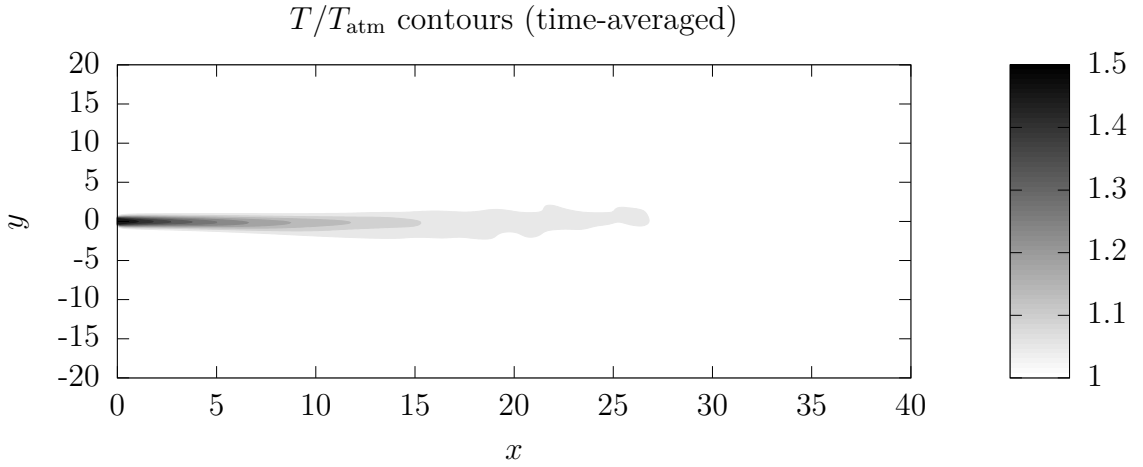

Figure 4.63: Temperature contours for the short domain, 20 unit sponge-layer with 5-times viscosity increase case.

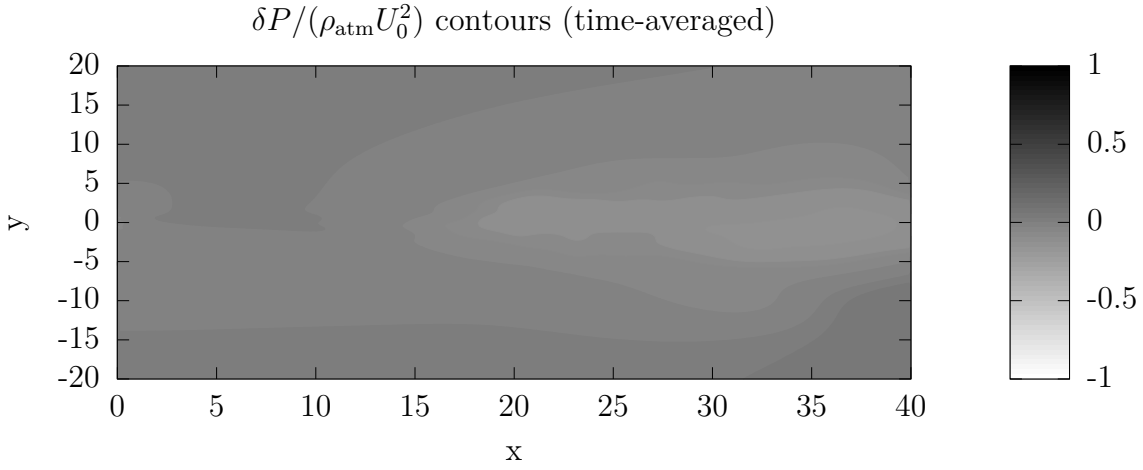

Figure 4.64: Pressure contours for the short domain, 20 unit sponge-layer with 5-times viscosity increase case.

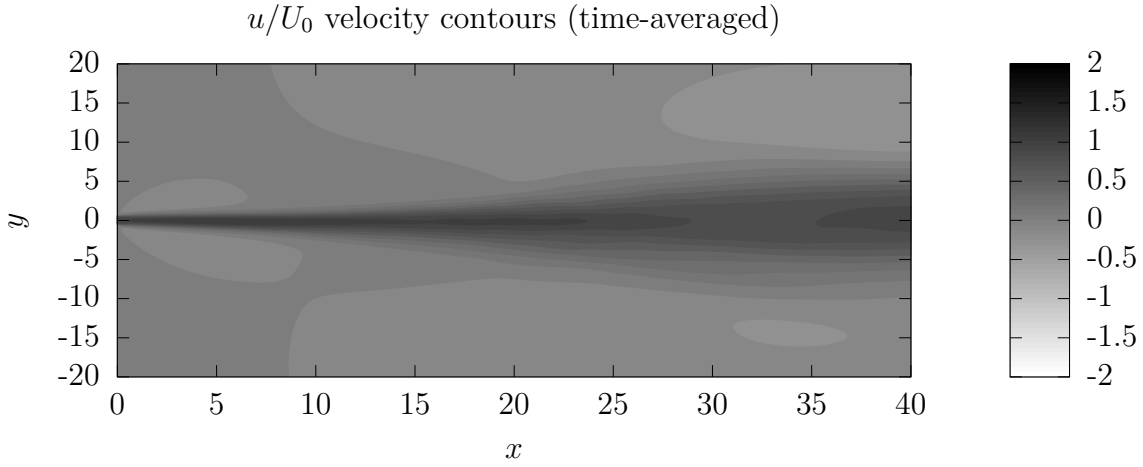

Figure 4.65: u-velocity contours for the short domain, 20 unit sponge-layer with 5-times viscosity increase case.

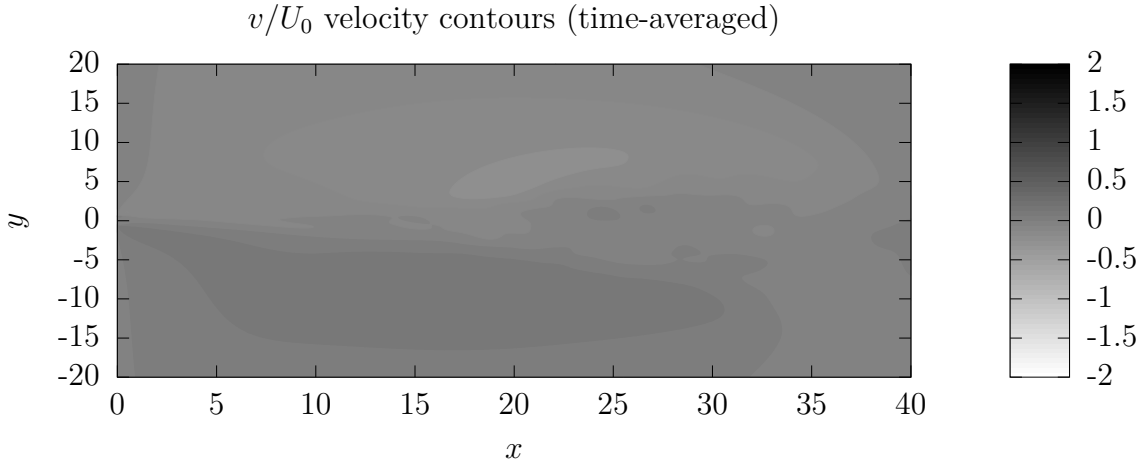

Figure 4.66: v-velocity contours for the short domain, 20 unit sponge-layer with 5-times viscosity increase case.

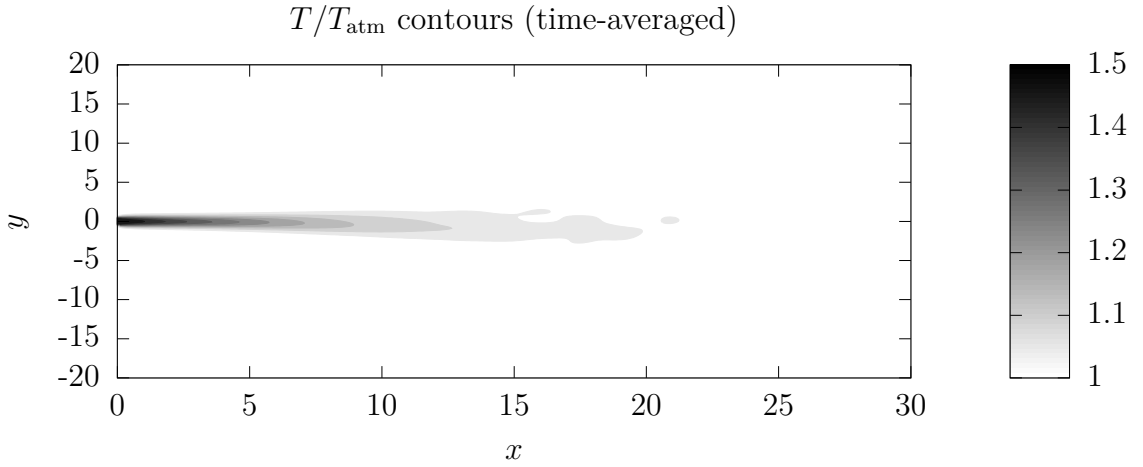

Figure 4.67: Temperature contours for the short domain, 10 unit sponge-layer with 10-times viscosity increase case.

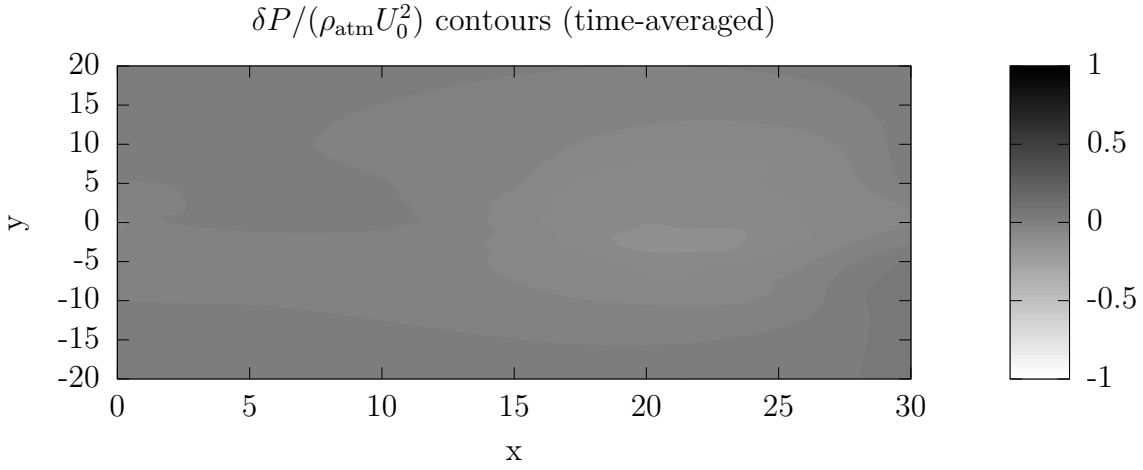

Figure 4.68: Pressure contours for the short domain, 10 unit sponge-layer with 10-times viscosity increase case.

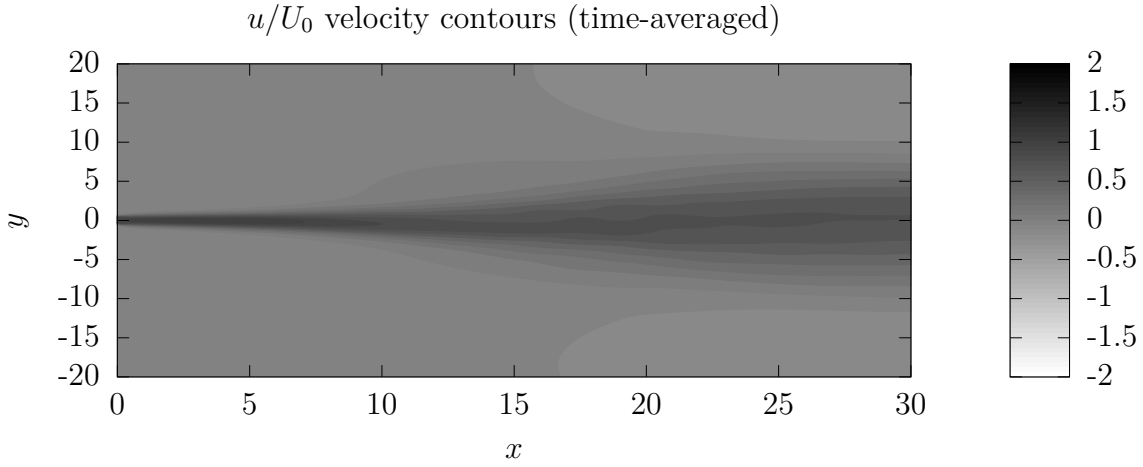

Figure 4.69: u-velocity contours for the short domain, 10 unit sponge-layer with 10-times viscosity increase case.

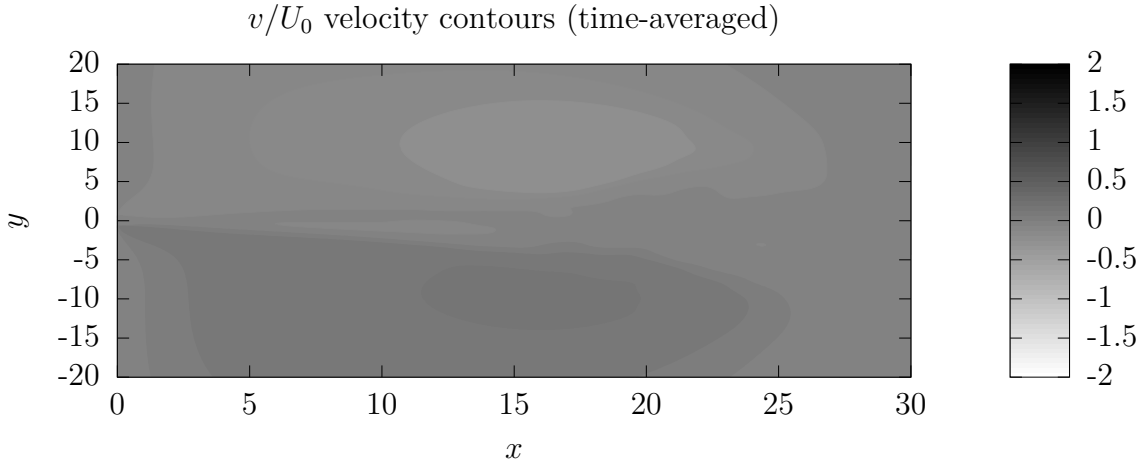

Figure 4.70: v-velocity contours for the short domain, 10 unit sponge-layer with 10-times viscosity increase case.

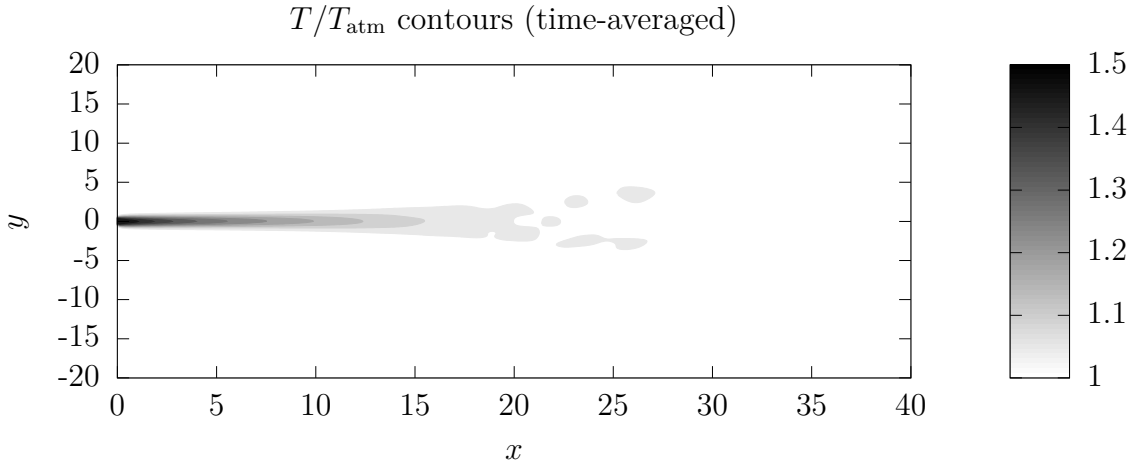

Figure 4.71: Temperature contours for the short domain, 20 unit sponge-layer with 10-times viscosity increase case.

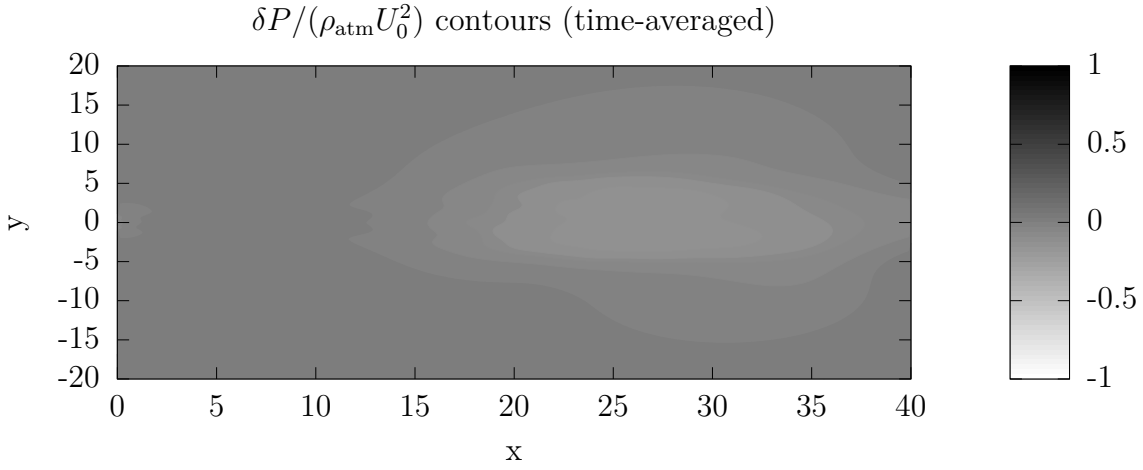

Figure 4.72: Pressure contours for the short domain, 20 unit sponge-layer with 10-times viscosity increase case.

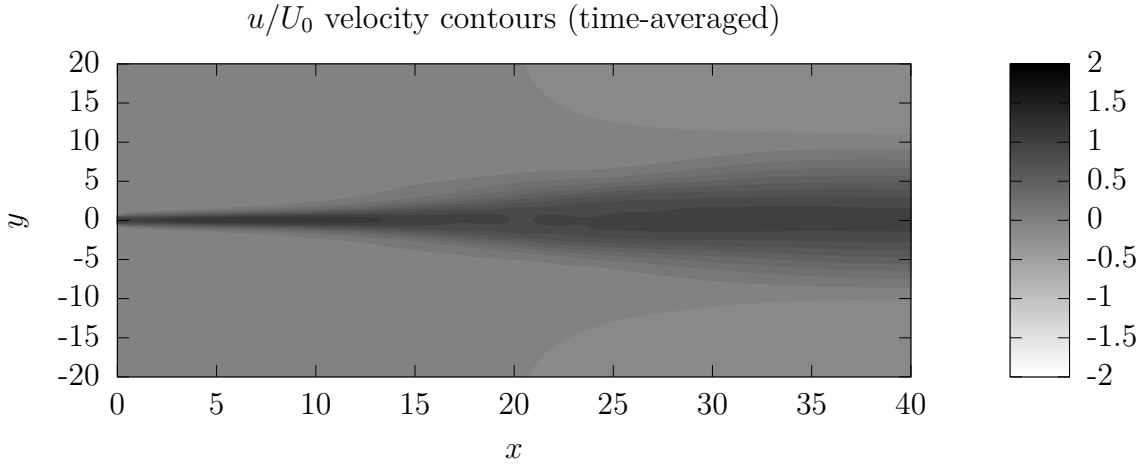

Figure 4.73: u-velocity contours for the short domain, 20 unit sponge-layer with 10-times viscosity increase case.

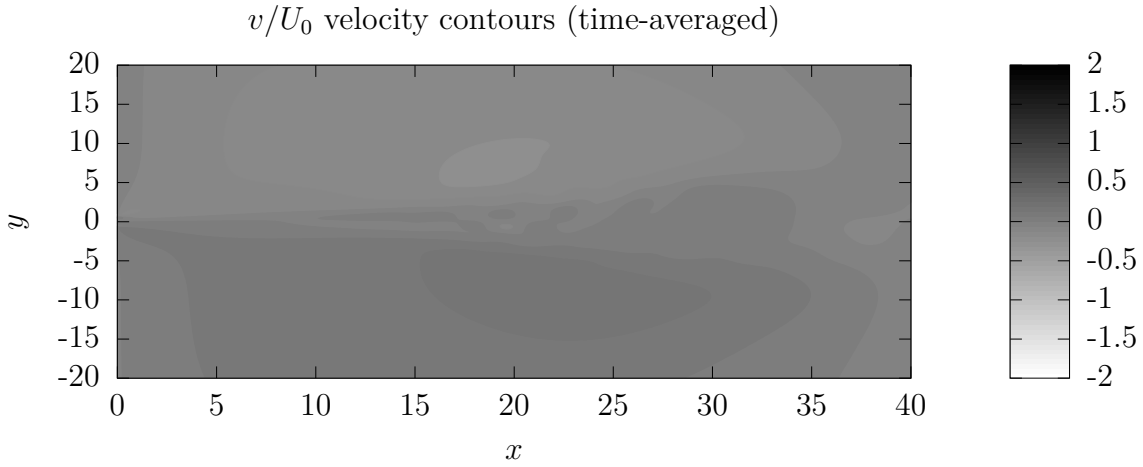

Figure 4.74: v-velocity contours for the short domain, 20 unit sponge-layer with 10-times viscosity increase case.

4.7 Instantaneous centerlines

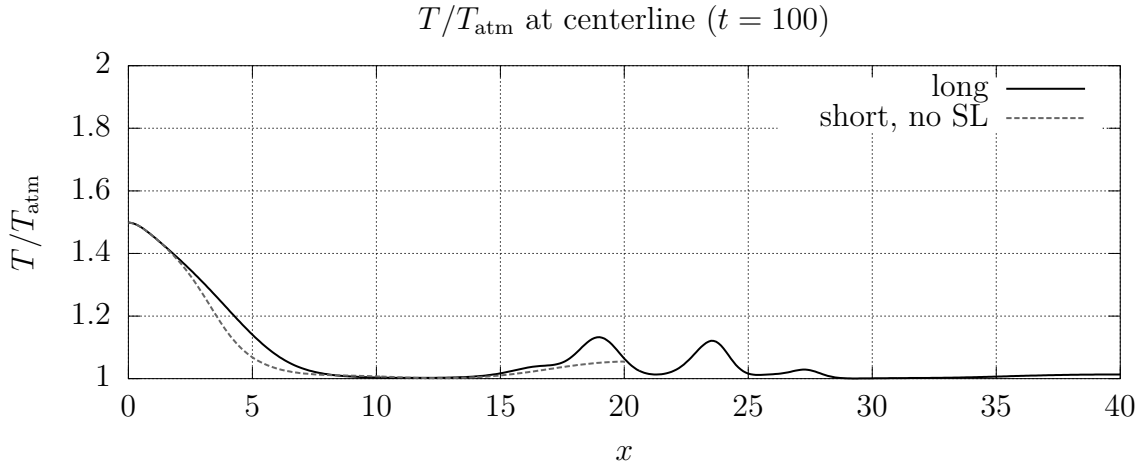

Figure 4.75: Comparison of long-domain temperatures with short domain, no sponge-layer temperatures at the centerline.

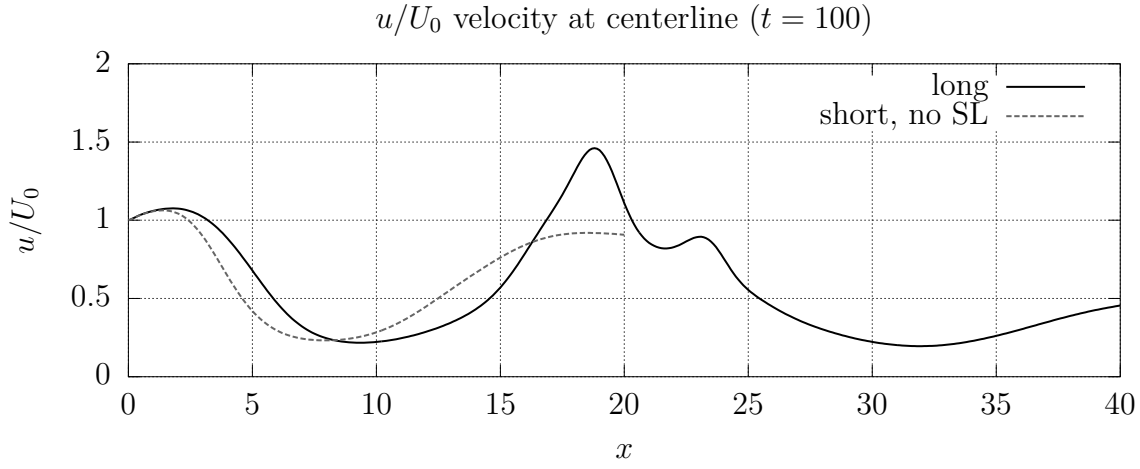

Figure 4.76: Comparison of long-domain u-velocity with short domain, no sponge-layer u-velocity at the centerline.

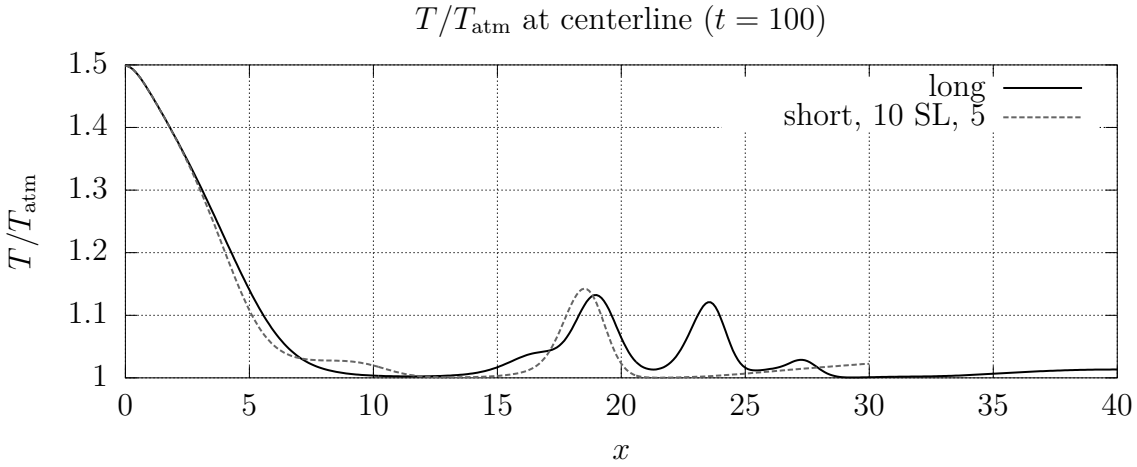

Figure 4.77: Comparison of long-domain temperatures with short domain, 10 unit sponge-layer with 5-times viscosity increase temperatures at the centerline.

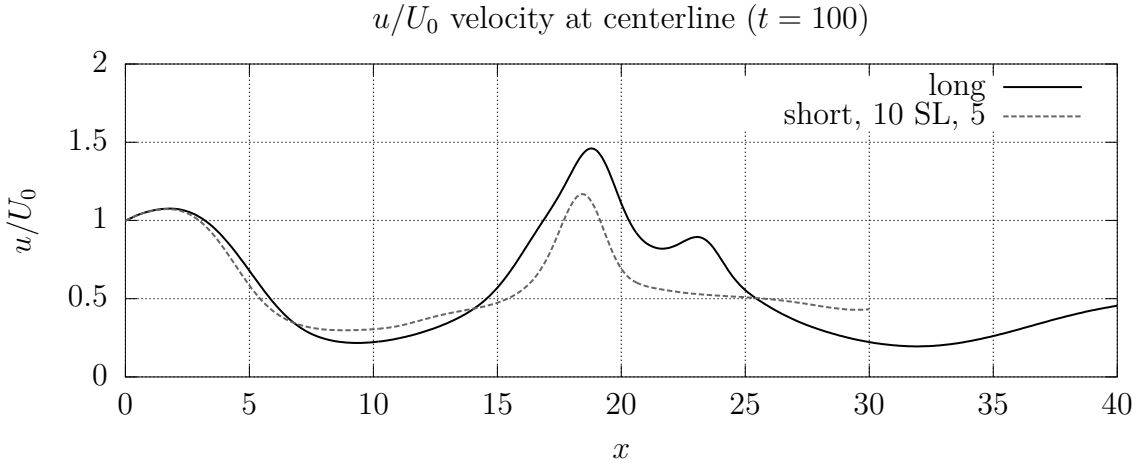

Figure 4.78: Comparison of long-domain u-velocity with short domain, 10 unit sponge-layer with 5-times viscosity increase u-velocity at the centerline.

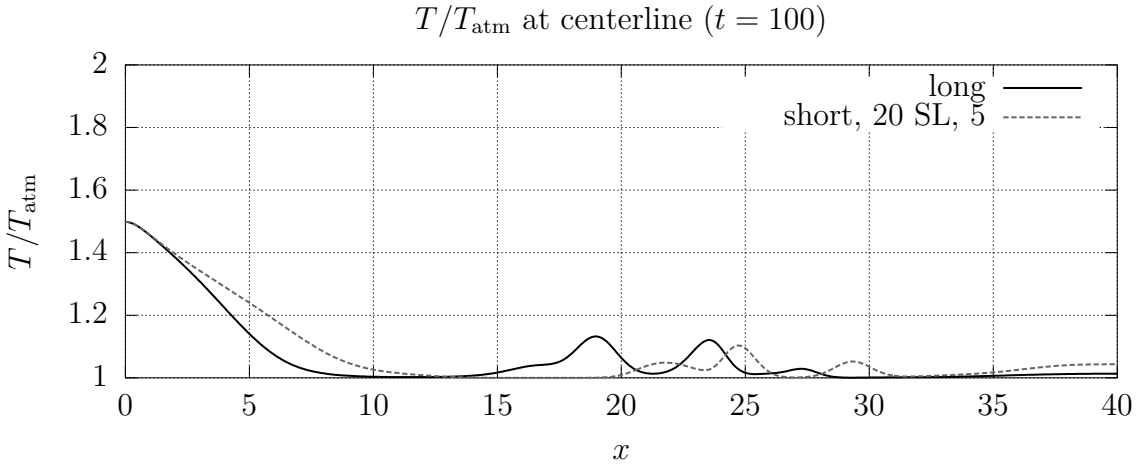

Figure 4.79: Comparison of long-domain temperatures with short domain, 20 unit sponge-layer with 5-times viscosity increase temperatures at the centerline.

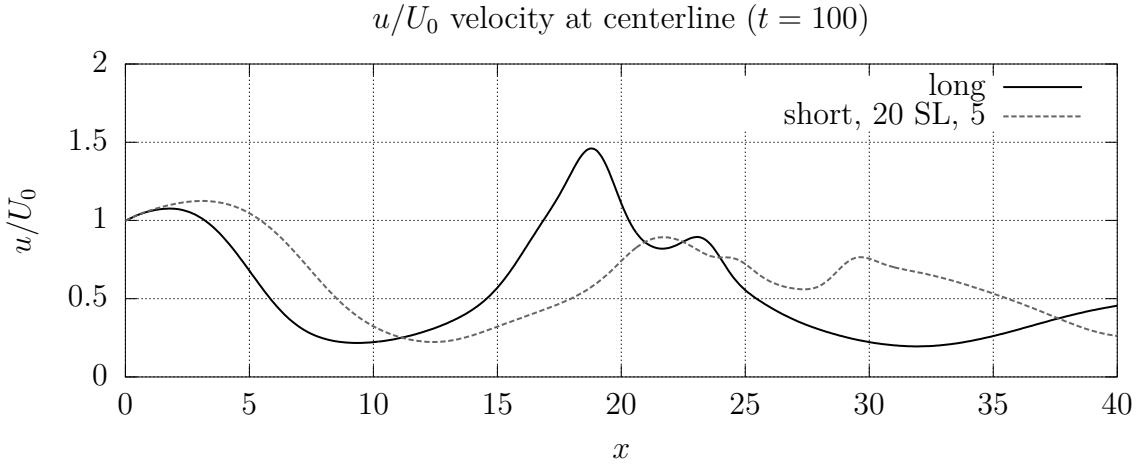

Figure 4.80: Comparison of long-domain u-velocity with short domain, 20 unit sponge-layer with 5-times viscosity increase u-velocity at the centerline.

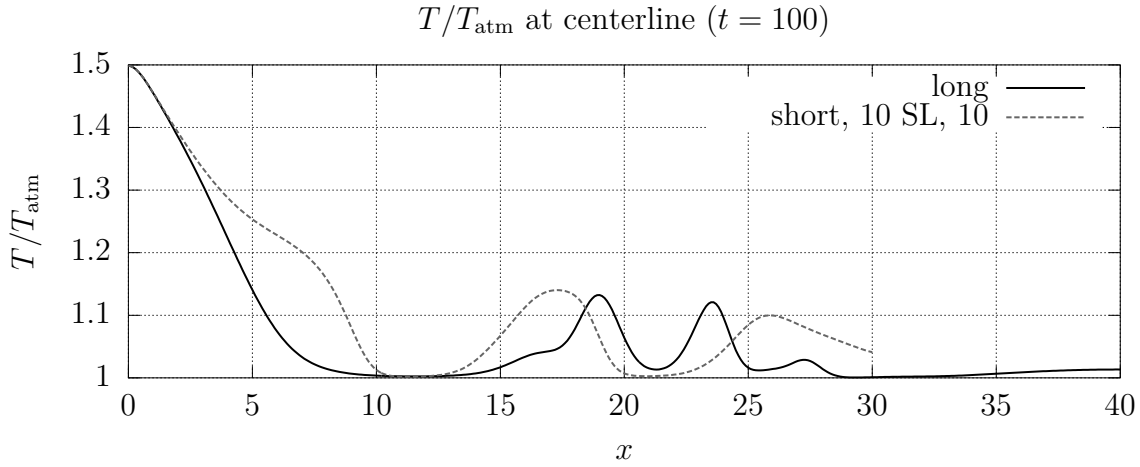

Figure 4.81: Comparison of long-domain temperatures with short domain, 10 unit sponge-layer with 10-times viscosity increase temperatures at the centerline.

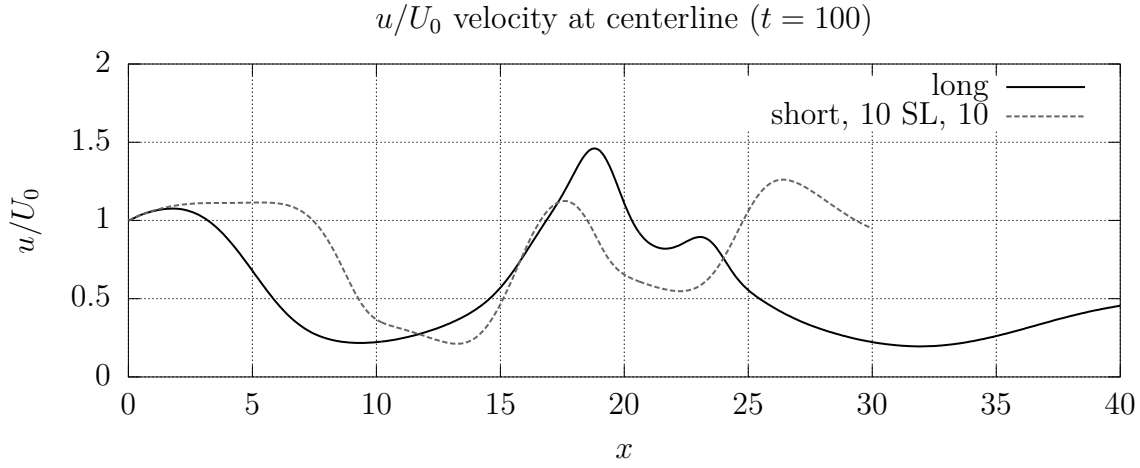

Figure 4.82: Comparison of long-domain u-velocity with short domain, 10 unit sponge-layer with 10-times viscosity increase u-velocity at the centerline.

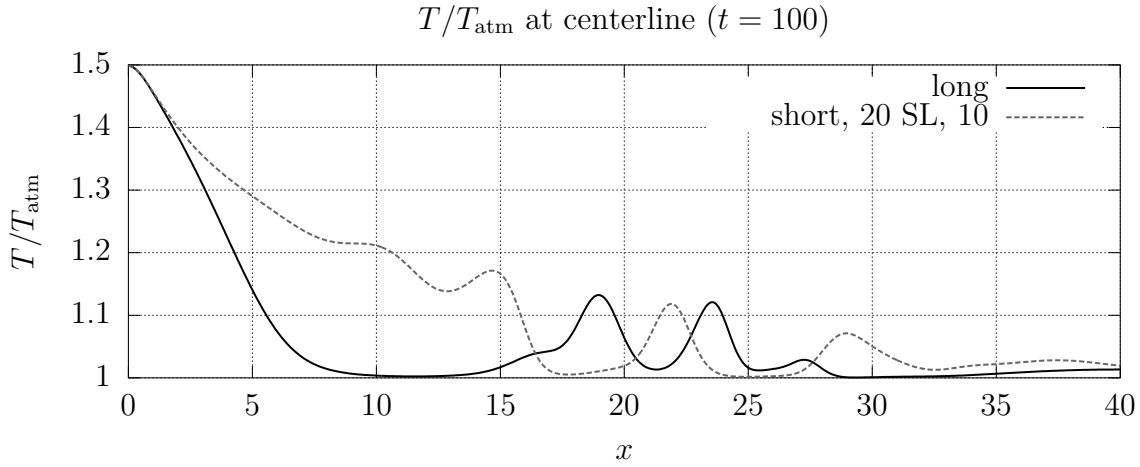

Figure 4.83: Comparison of long-domain temperatures with short domain, 20 unit sponge-layer with 10-times viscosity increase temperatures at the centerline.

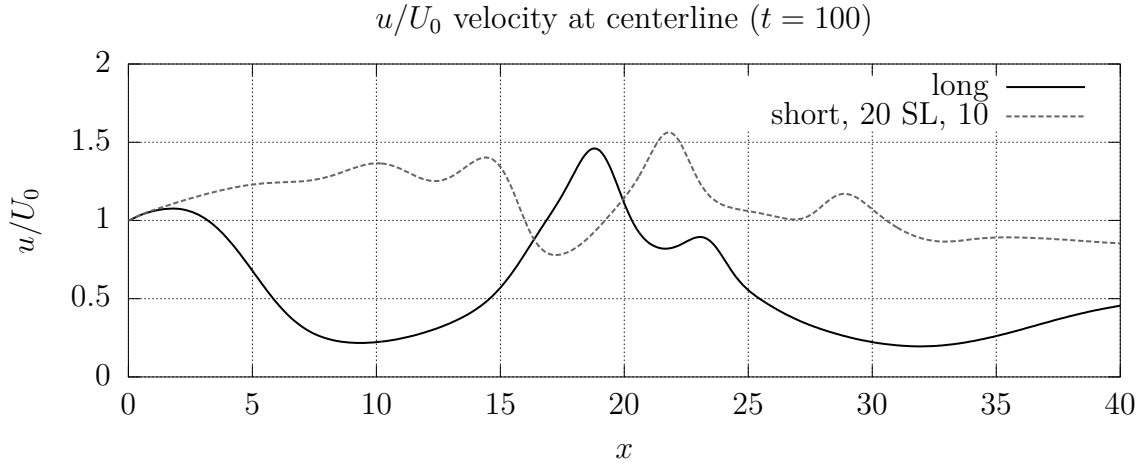

Figure 4.84: Comparison of long-domain u-velocity with short domain, 20 unit sponge-layer with 10-times viscosity increase u-velocity at the centerline.

4.8 Time-averaged centerlines

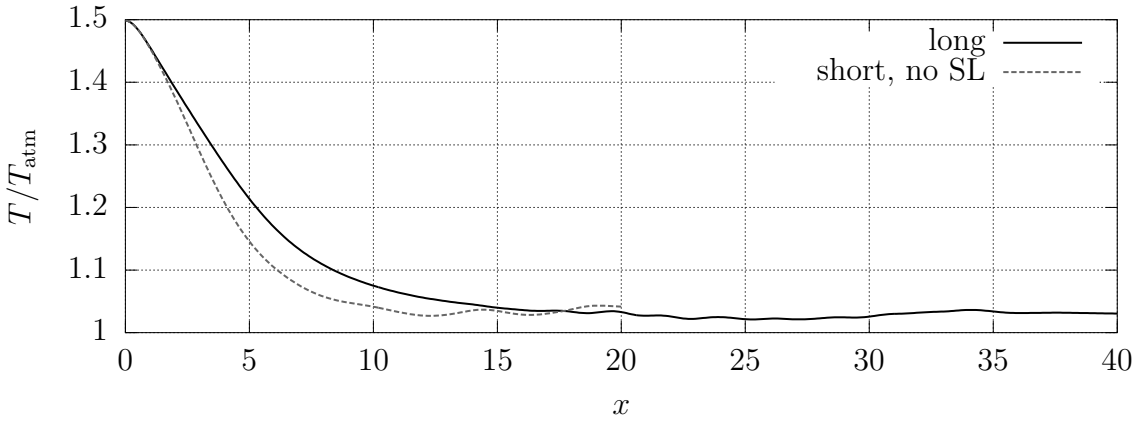

Figure 4.85: Comparison of long-domain time-averaged temperatures with short domain, no sponge-layer time-averaged temperatures at the centerline.

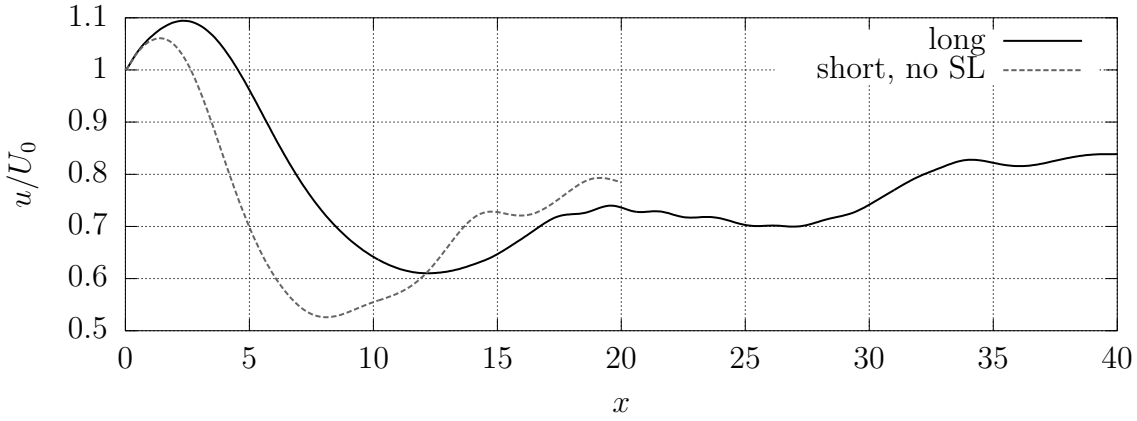

Figure 4.86: Comparison of long-domain time-averaged u-velocity with short domain, no sponge-layer time-averaged u-velocity at the centerline.

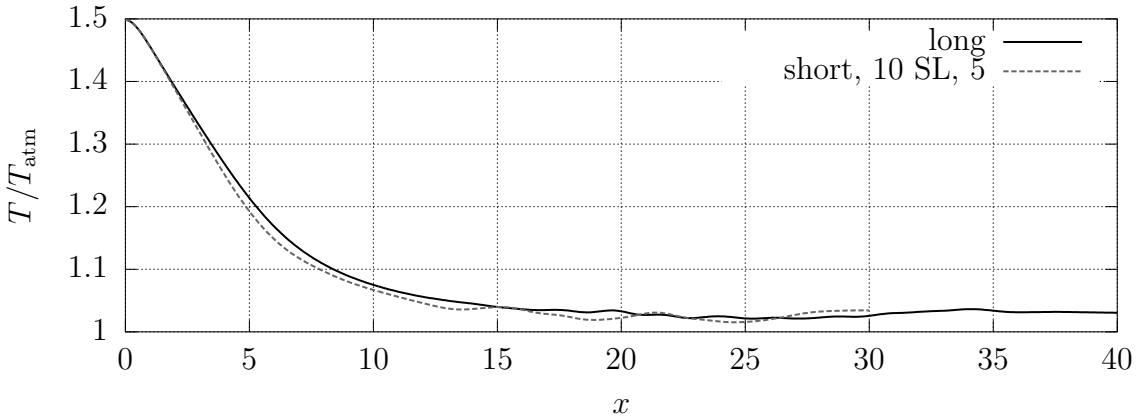

Figure 4.87: Comparison of long-domain time-averaged temperatures with short domain, 10 unit sponge-layer with 5-times viscosity increase time-averaged temperatures at the centerline.

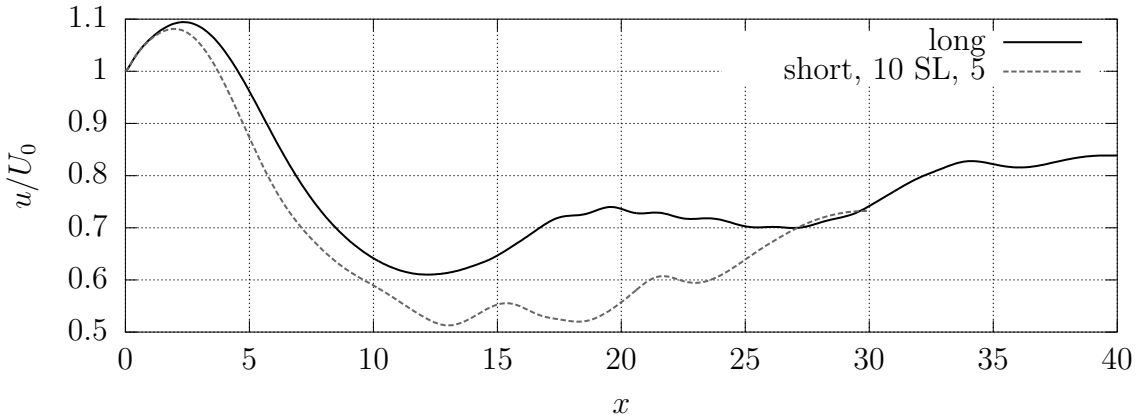

Figure 4.88: Comparison of long-domain time-averaged u-velocity with short domain, 10 unit sponge-layer with 5-times viscosity increase time-averaged u-velocity at the centerline.

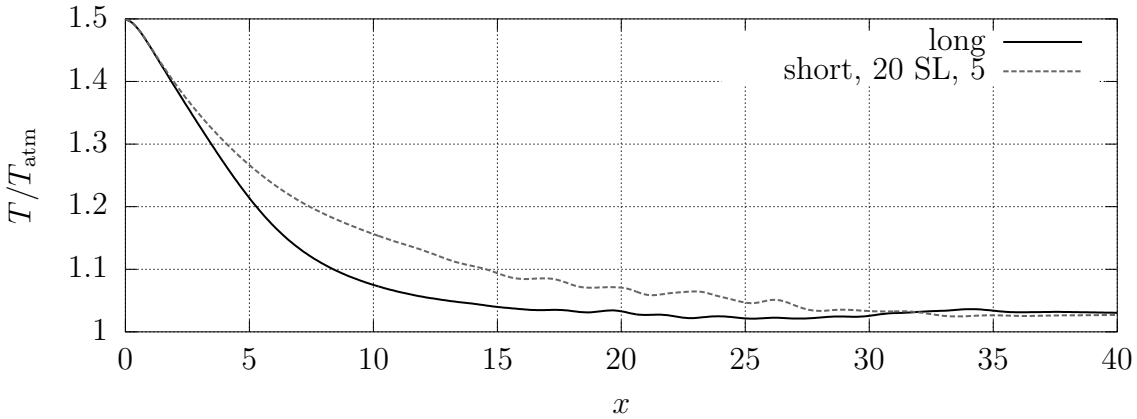

Figure 4.89: Comparison of long-domain time-averaged temperatures with short domain, 20 unit sponge-layer with 5-times viscosity increase time-averaged temperatures at the centerline.

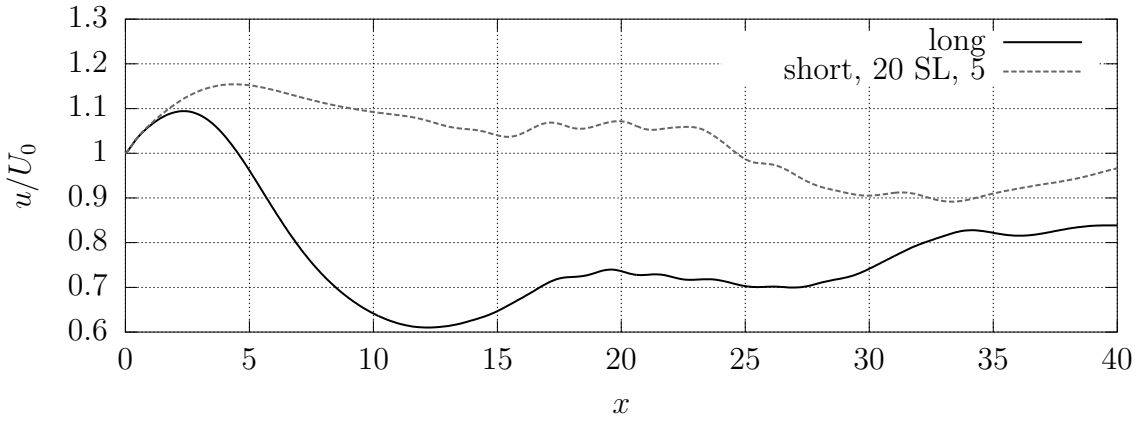

Figure 4.90: Comparison of long-domain time-averaged u-velocity with short domain, 20 unit sponge-layer with 5-times viscosity increase time-averaged u-velocity at the centerline.

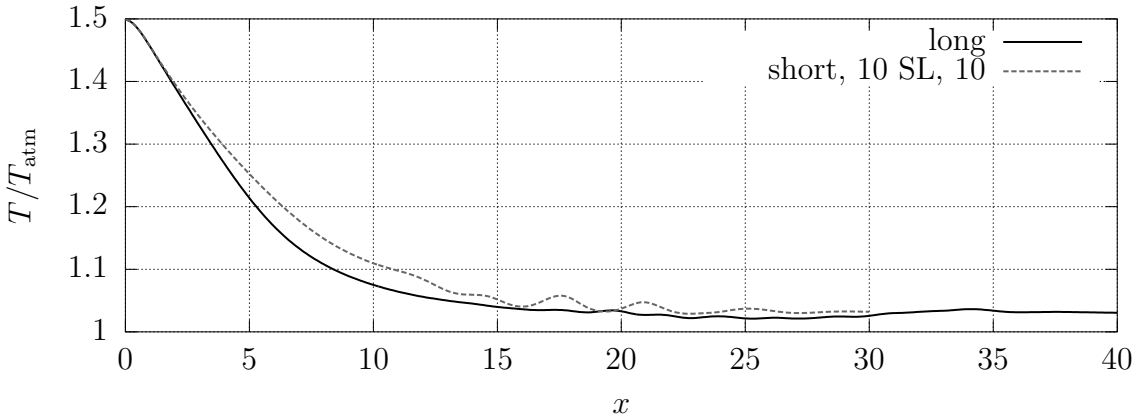

Figure 4.91: Comparison of long-domain time-averaged temperatures with short domain, 10 unit sponge-layer with 10-times viscosity increase time-averaged temperatures at the centerline.

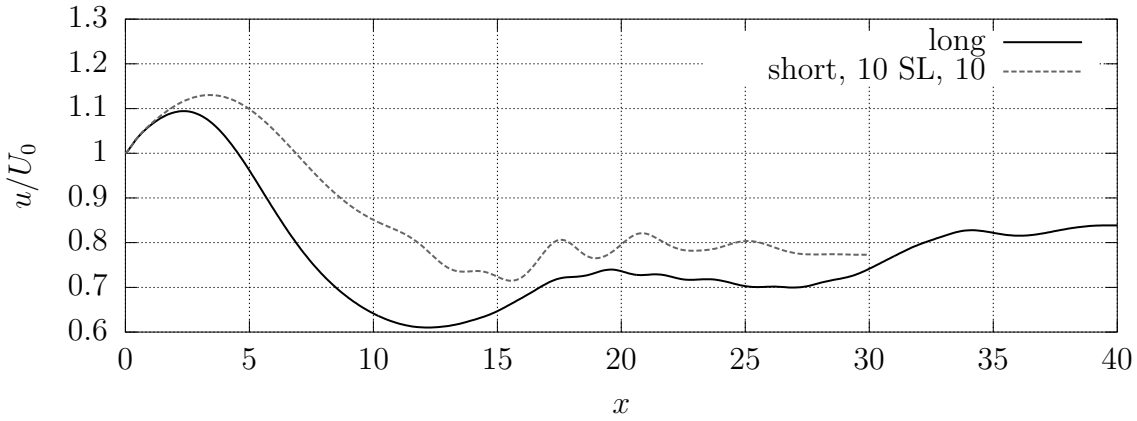

Figure 4.92: Comparison of long-domain time-averaged u-velocity with short domain, 10 unit sponge-layer with 10-times viscosity increase time-averaged u-velocity at the centerline.

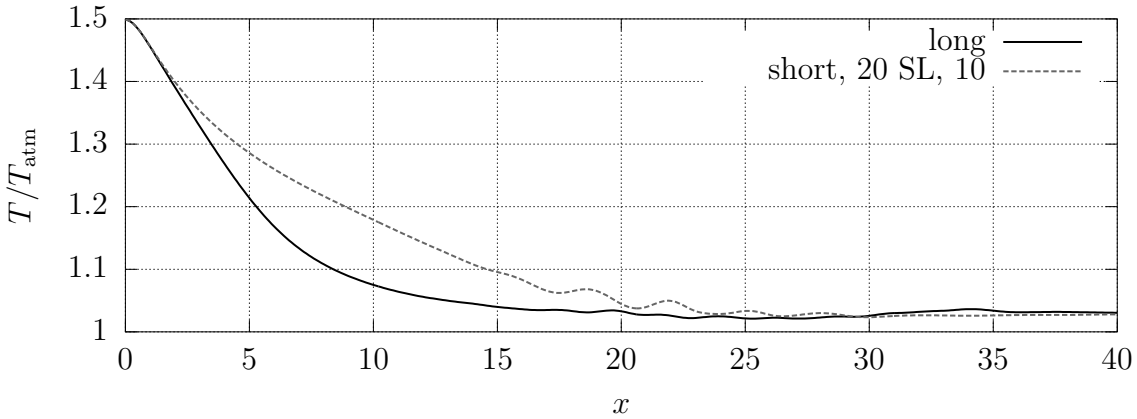

Figure 4.93: Comparison of long-domain time-averaged temperatures with short domain, 20 unit sponge-layer with 10-times viscosity increase time-averaged temperatures at the centerline.

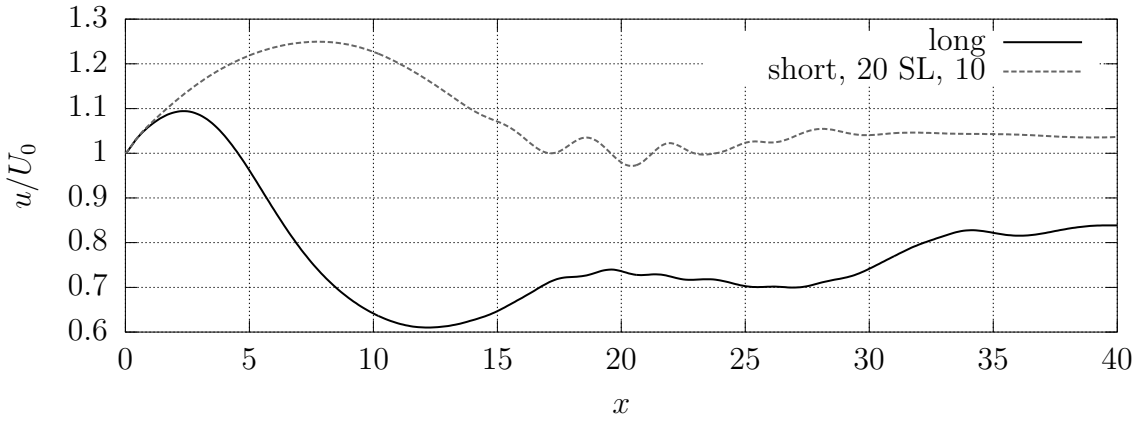

Figure 4.94: Comparison of long-domain time-averaged u-velocity with short domain, 20 unit sponge-layer with 10-times viscosity increase time-averaged u-velocity at the centerline.

4.9 Instantaneous outflow profiles

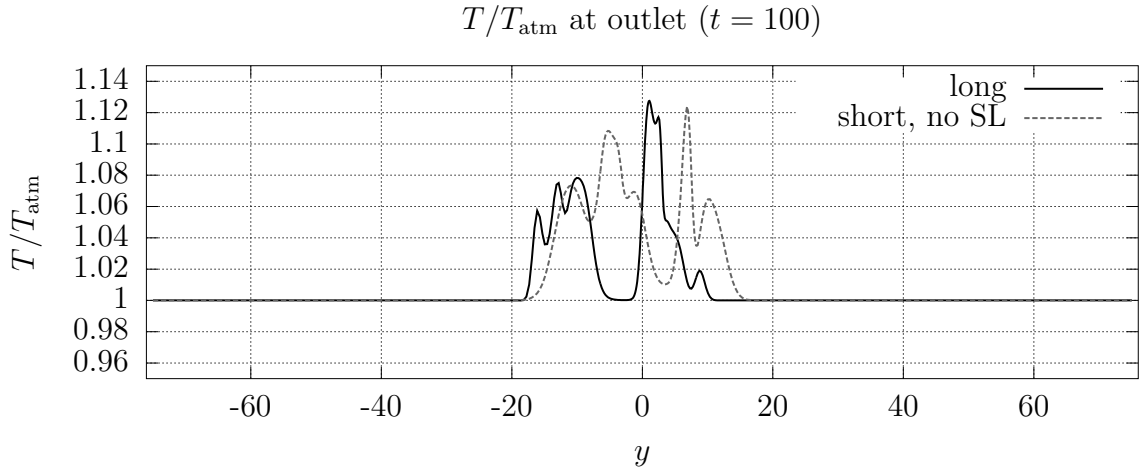

Figure 4.95: Temperature at the outlet for short domain, no sponge-layer case.

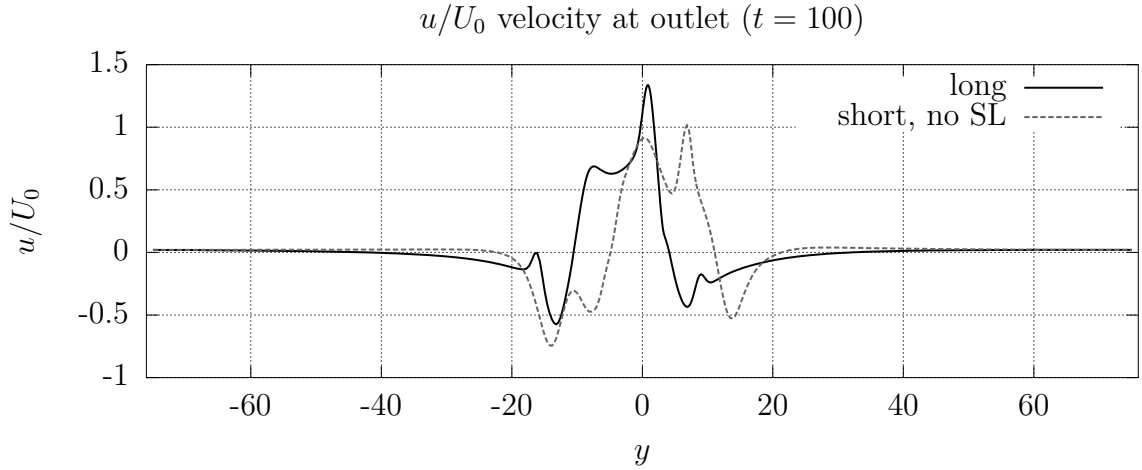

Figure 4.96: u-velocity at the outlet for short domain, no sponge-layer case.

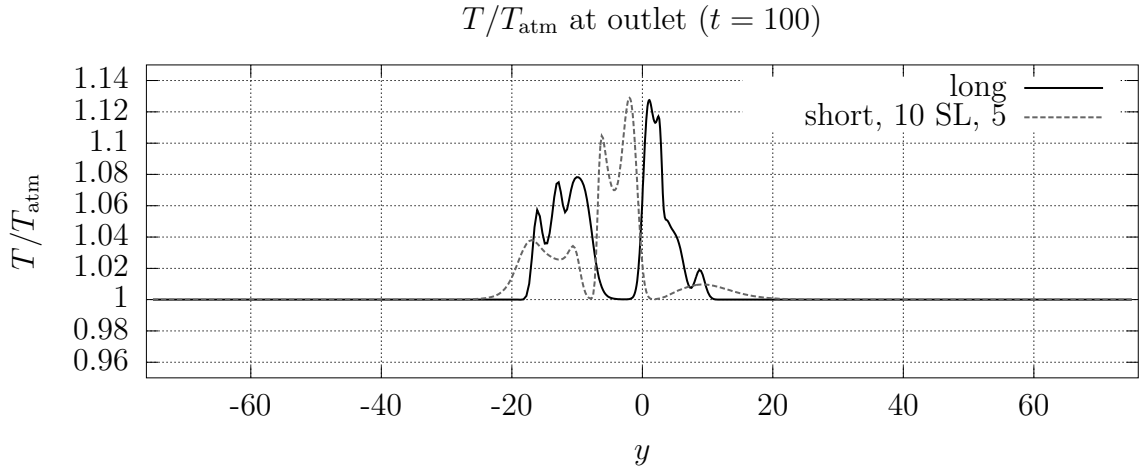

Figure 4.97: Temperature at the outlet for short domain, 10 unit sponge-layer with 5-times viscosity increase case.

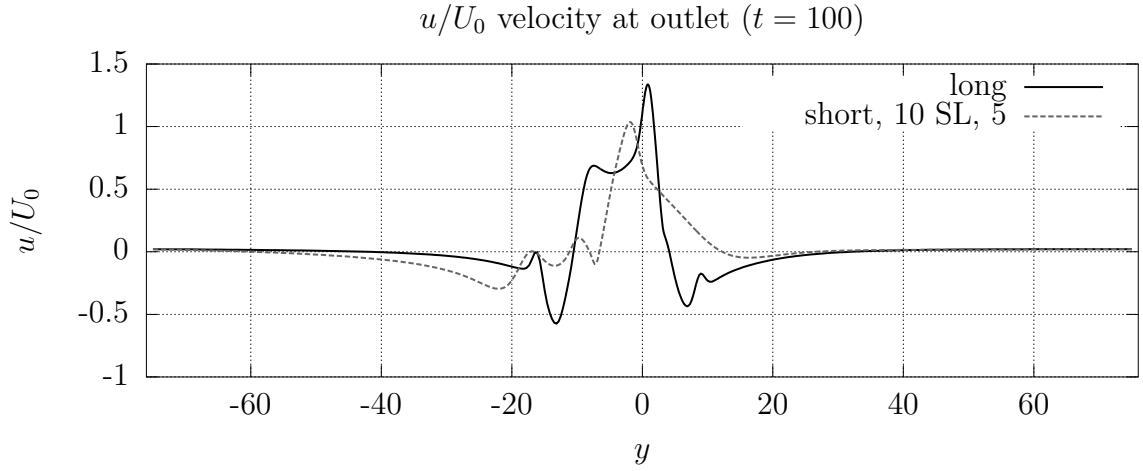

Figure 4.98: u-velocity at the outlet for short domain, 10 unit sponge-layer with 5-times viscosity increase case.

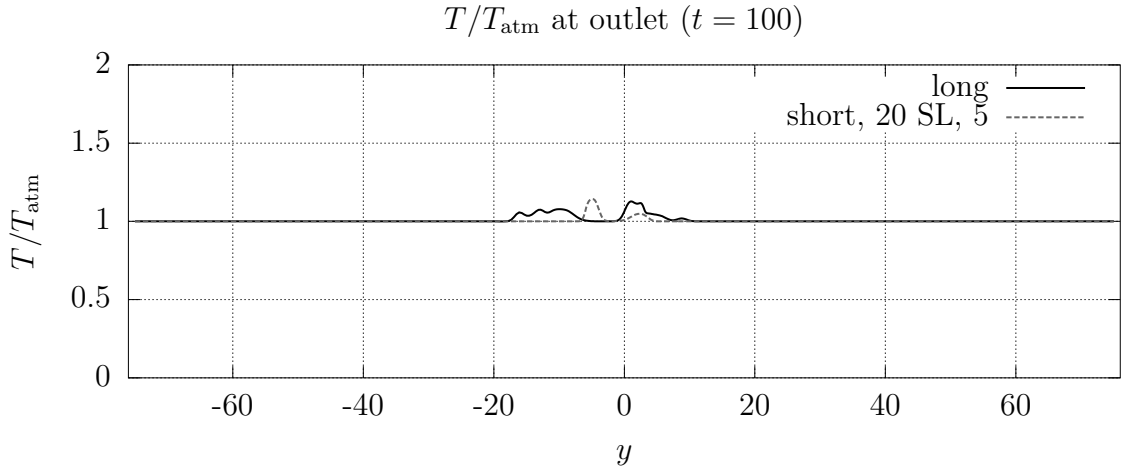

Figure 4.99: Temperature at the outlet for short domain, 20 unit sponge-layer with 5-times viscosity increase case.

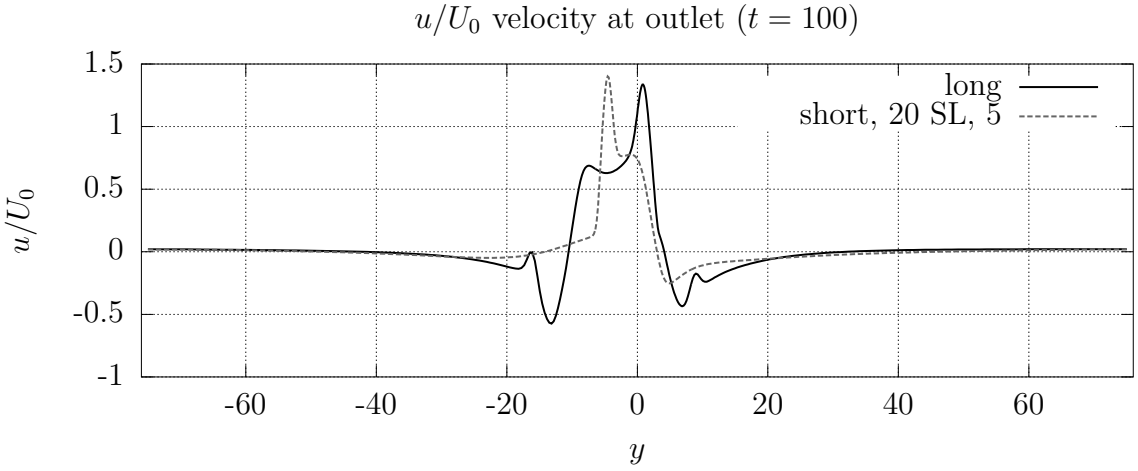

Figure 4.100: u-velocity at the outlet for short domain, 20 unit sponge-layer with 5-times viscosity increase case.

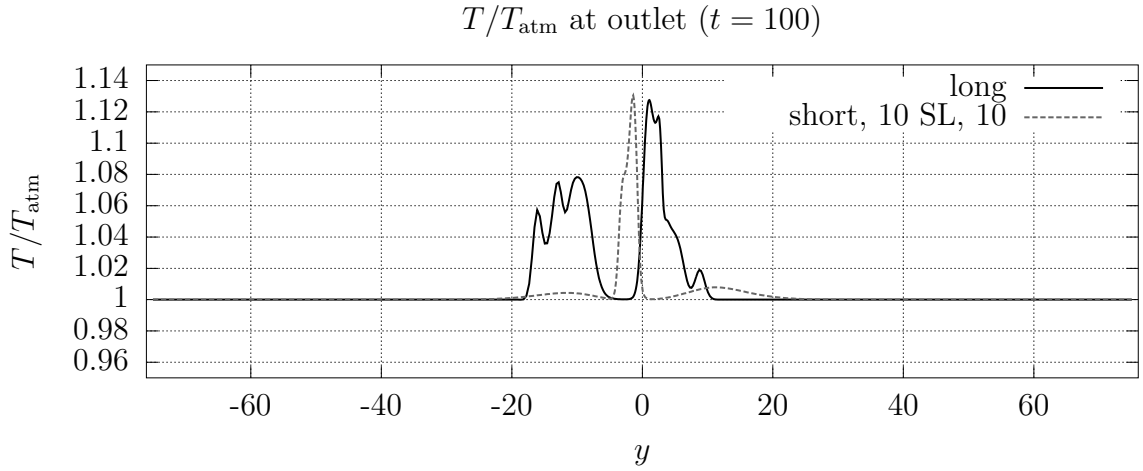

Figure 4.101: Temperature at the outlet for short domain, 10 unit sponge-layer with 10-times viscosity increase case.

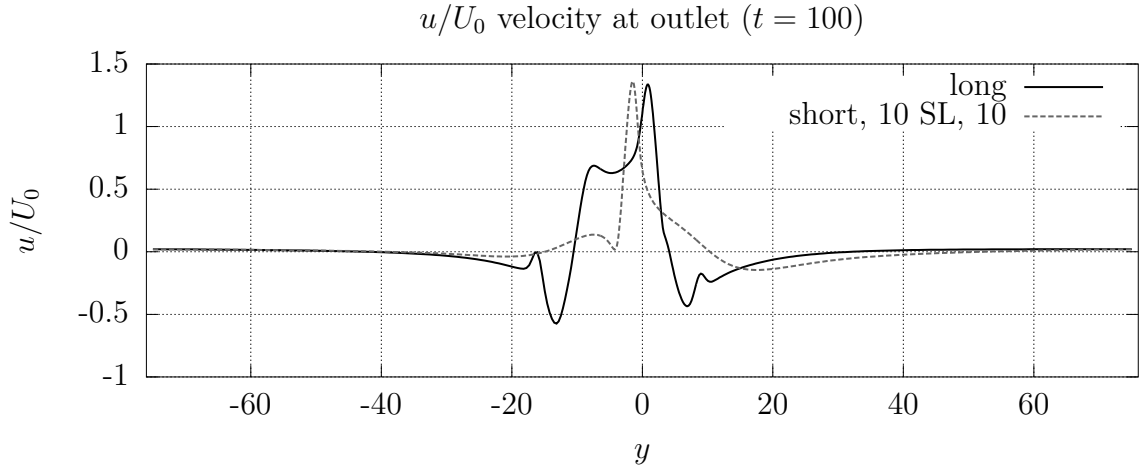

Figure 4.102: u-velocity at the outlet for short domain, 10 unit sponge-layer with 10-times viscosity increase case.

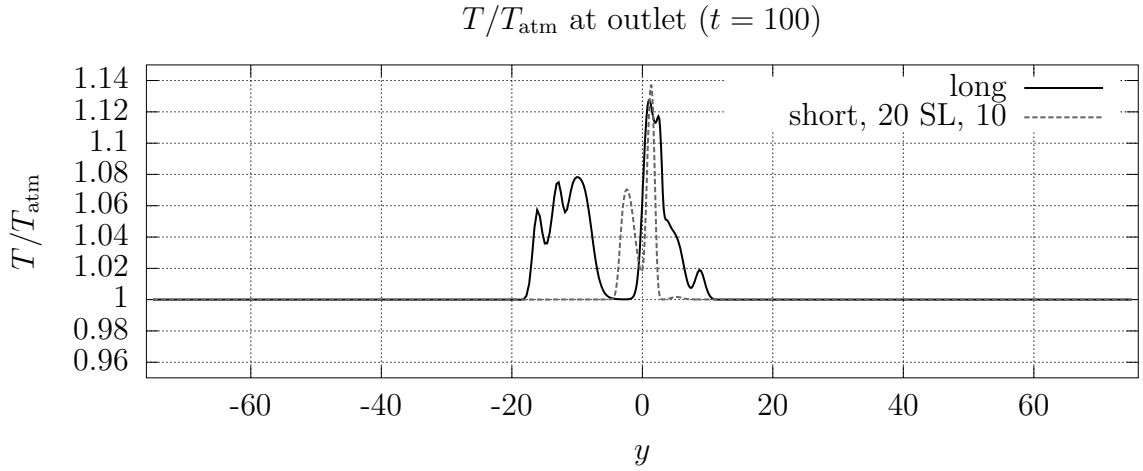

Figure 4.103: Temperature at the outlet for short domain, 20 unit sponge-layer with 10-times viscosity increase case.

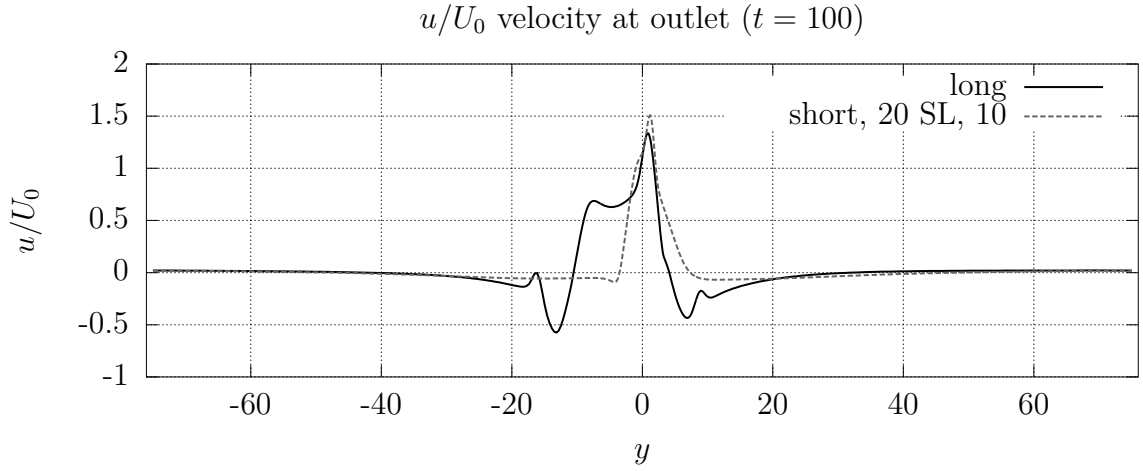

Figure 4.104: u-velocity at the outlet for short domain, 20 unit sponge-layer with 10-times viscosity increase case.

4.10 Time-averaged outflow profiles

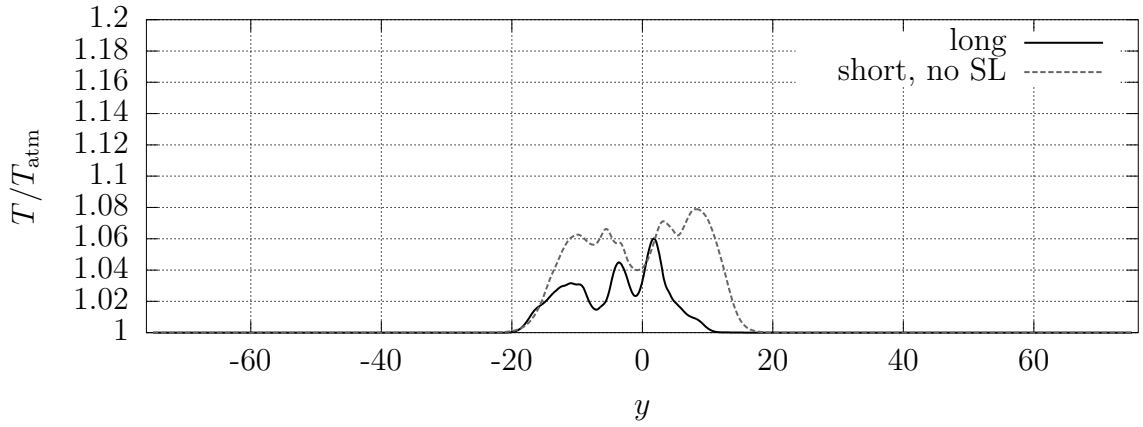

Figure 4.105: Time-averaged temperature at the outlet for short domain, no sponge-layer case.

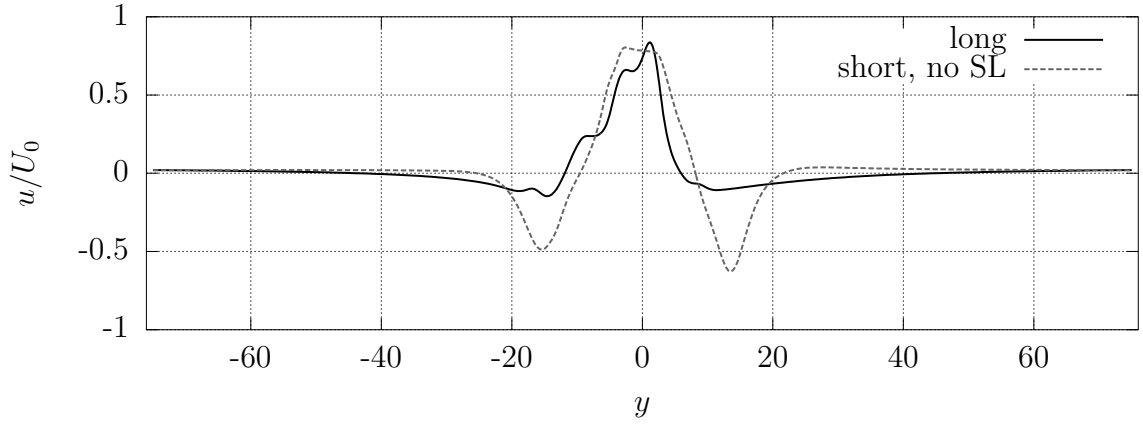

Figure 4.106: Time-averaged u-velocity at the outlet for short domain, no sponge-layer case.

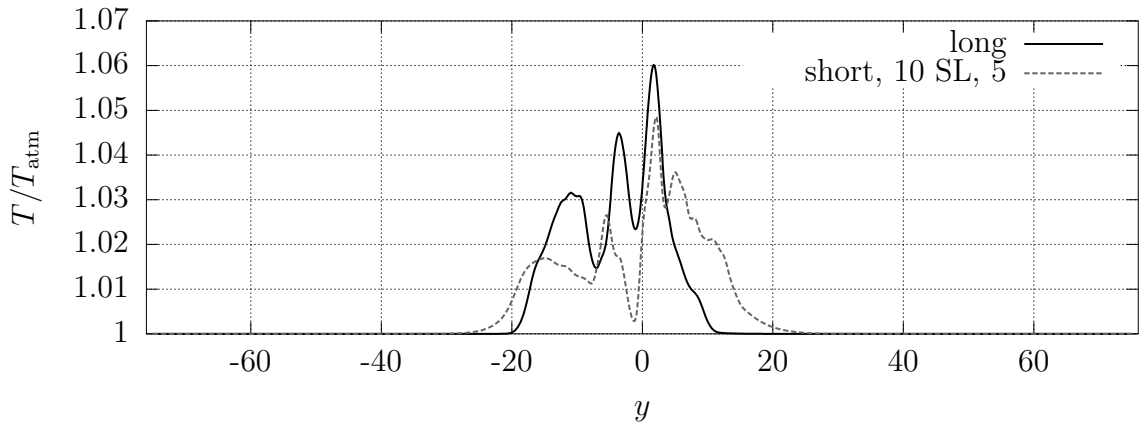

Figure 4.107: Time-averaged temperature at the outlet for short domain, 10 unit sponge-layer with 5-times viscosity increase case.

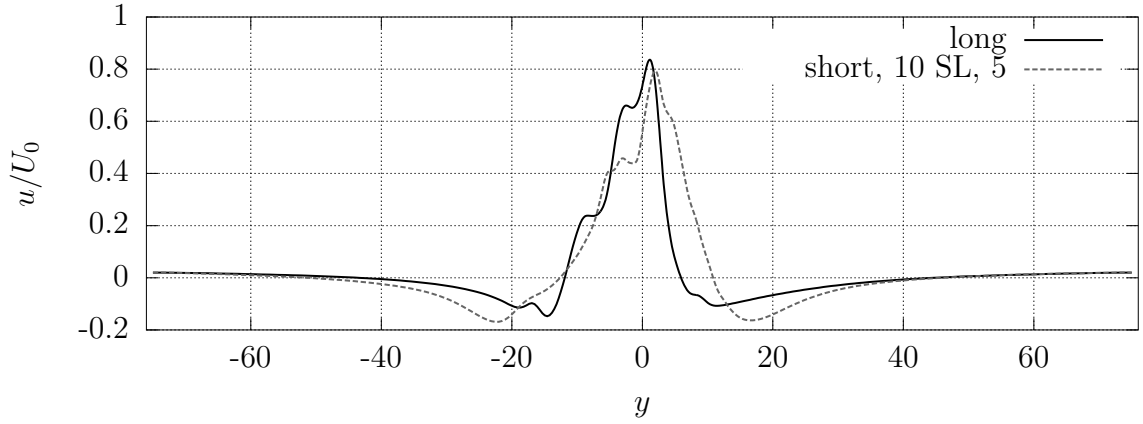

Figure 4.108: Time-averaged u-velocity at the outlet for short domain, 10 unit sponge-layer with 5-times viscosity increase case.

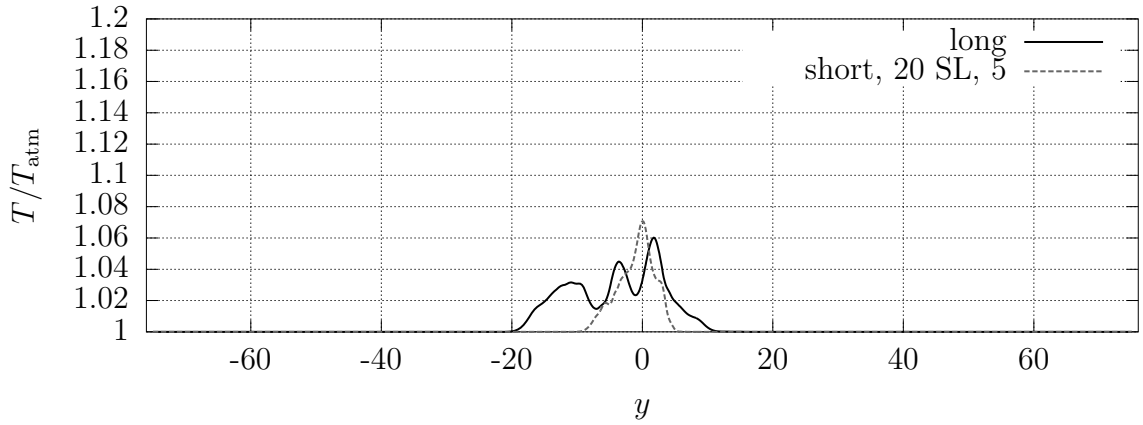

Figure 4.109: Time-averaged temperature at the outlet for short domain, 20 unit sponge-layer with 5-times viscosity increase case.

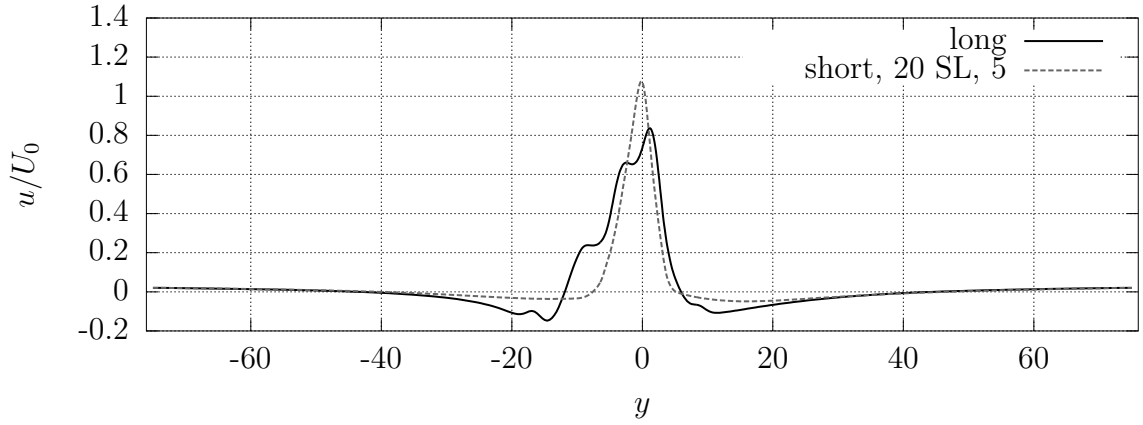

Figure 4.110: Time-averaged u-velocity at the outlet for short domain, 20 unit sponge-layer with 5-times viscosity increase case.

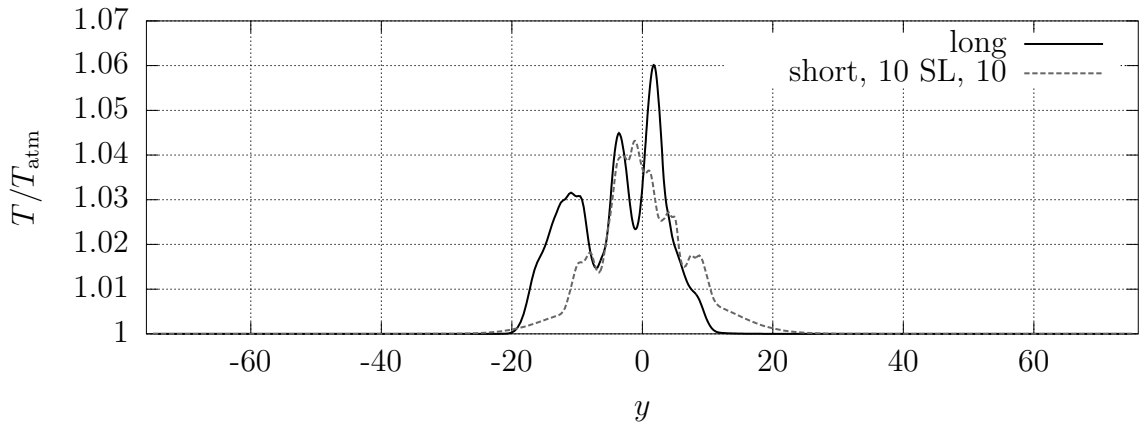

Figure 4.111: Time-averaged temperature at the outlet for short domain, 10 unit sponge-layer with 10-times viscosity increase case.

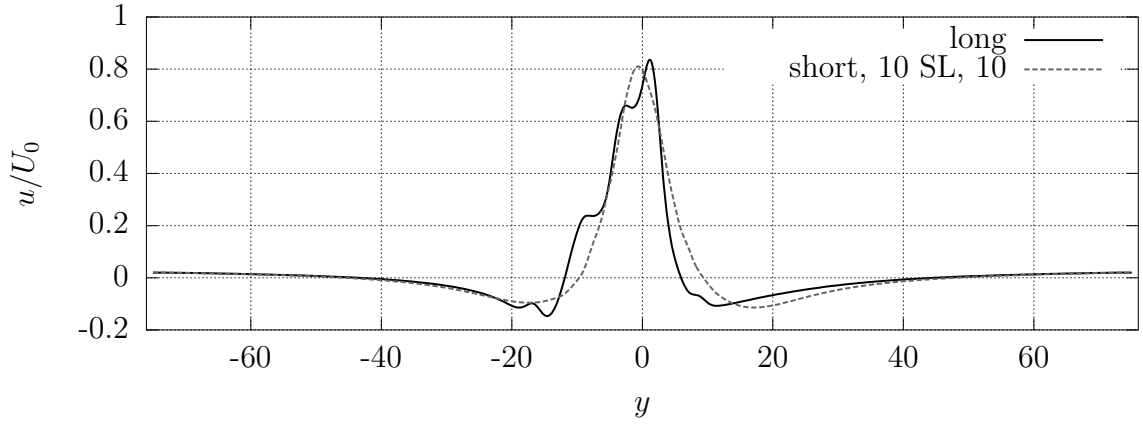

Figure 4.112: Time-averaged u-velocity at the outlet for short domain, 10 unit sponge-layer with 10-times viscosity increase case.

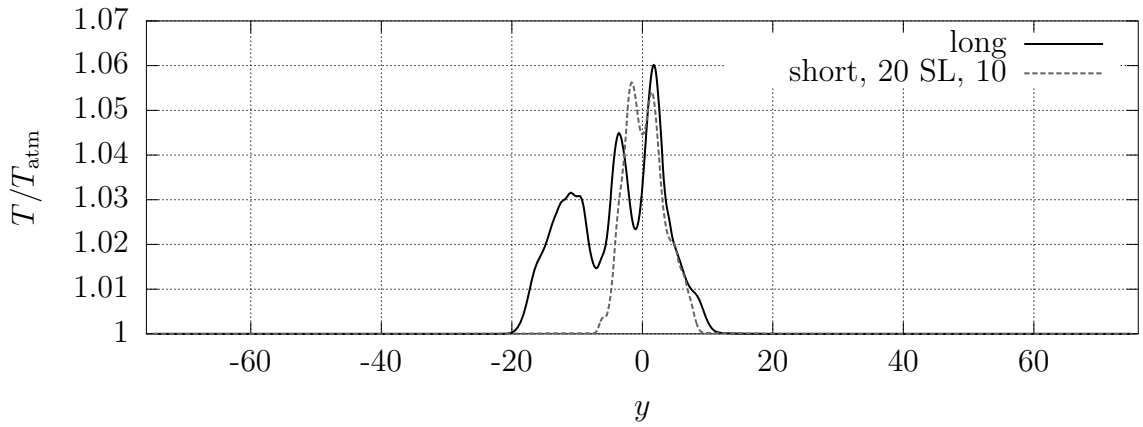

Figure 4.113: Time-averaged temperature at the outlet for short domain, 20 unit sponge-layer with 10-times viscosity increase case.

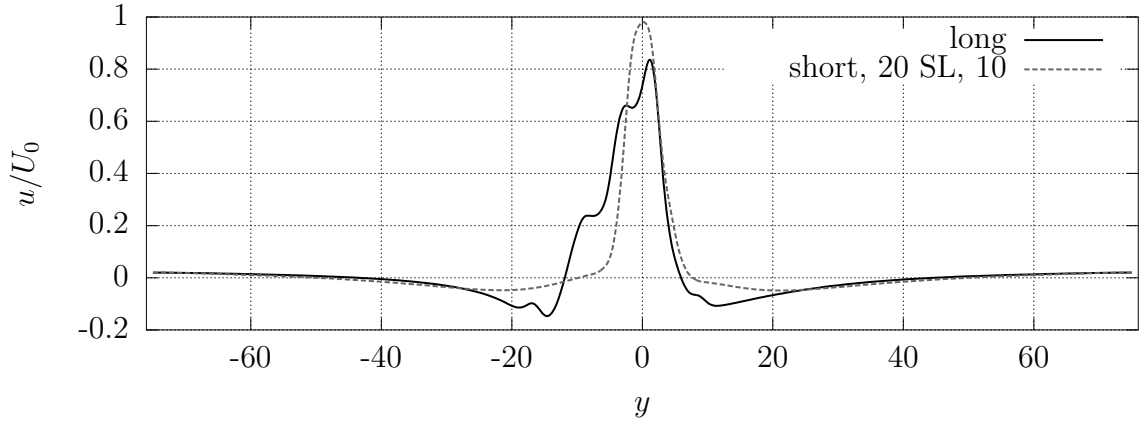

Figure 4.114: Time-averaged u-velocity at the outlet for short domain, 20 unit sponge-layer with 10-times viscosity increase case.

4.11 Probes

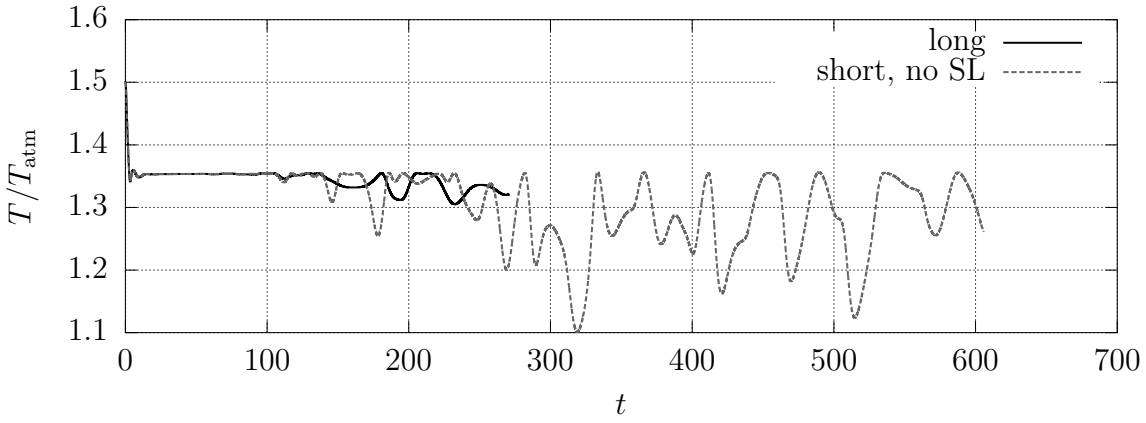

Figure 4.115: Centerline temperature probe one jet width from the inlet for short domain, no sponge-layer case.

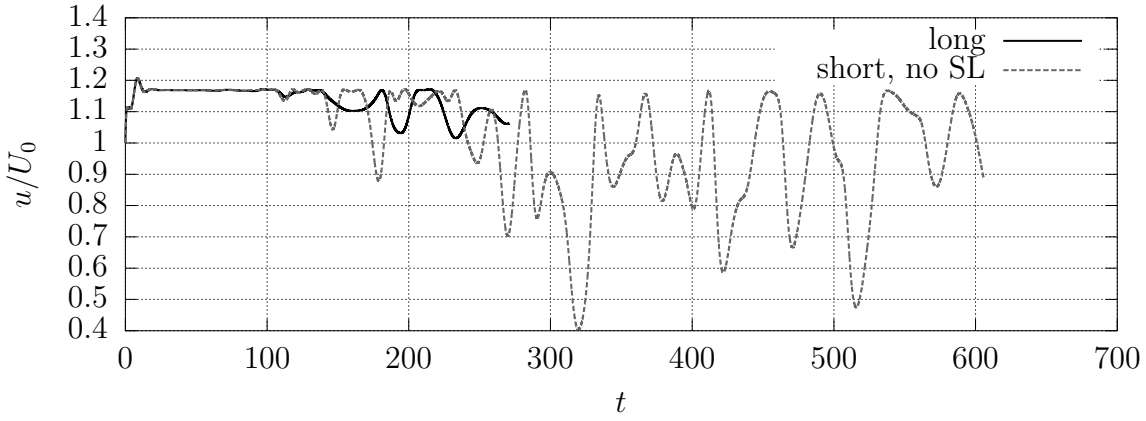

Figure 4.116: Centerline u-velocity probe one jet width from the inlet for short domain, no sponge-layer case.

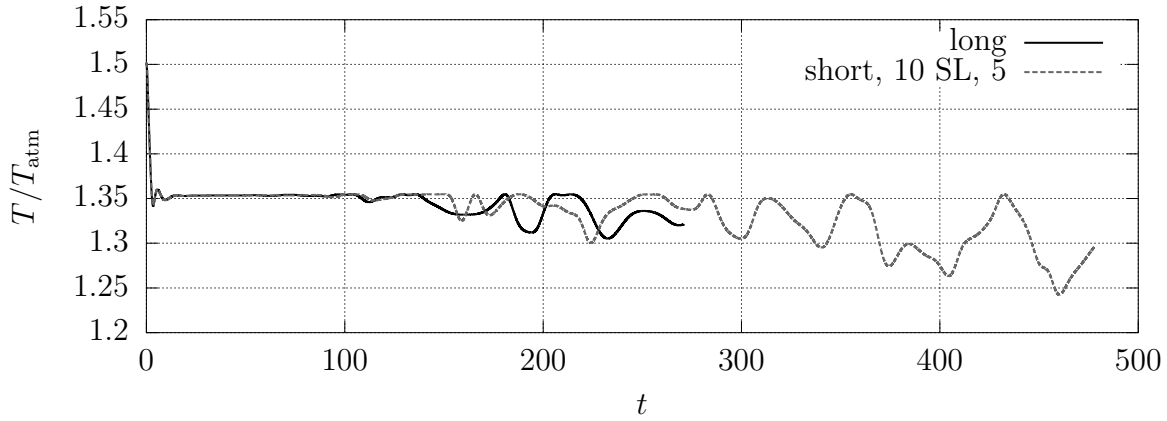

Figure 4.117: Centerline temperature probe one jet width from the inlet for short domain, 10 unit sponge-layer with 5-times viscosity increase case.

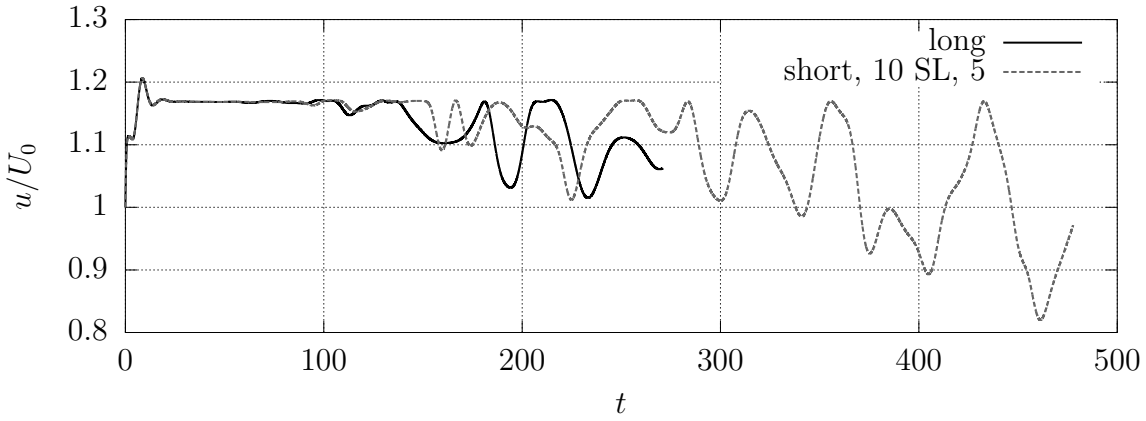

Figure 4.118: Centerline u-velocity probe one jet width from the inlet for short domain, 10 unit sponge-layer with 5-times viscosity increase case.

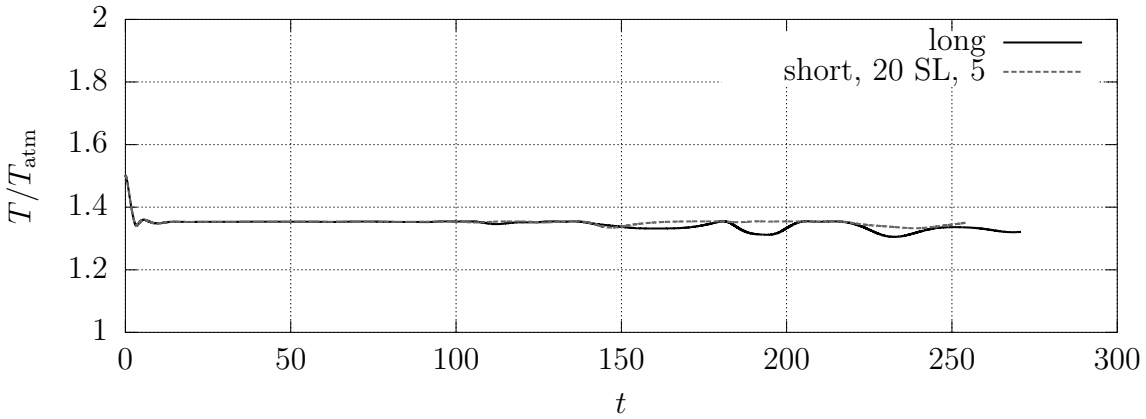

Figure 4.119: Centerline temperature probe one jet width from the inlet for short domain, 20 unit sponge-layer with 5-times viscosity increase case.

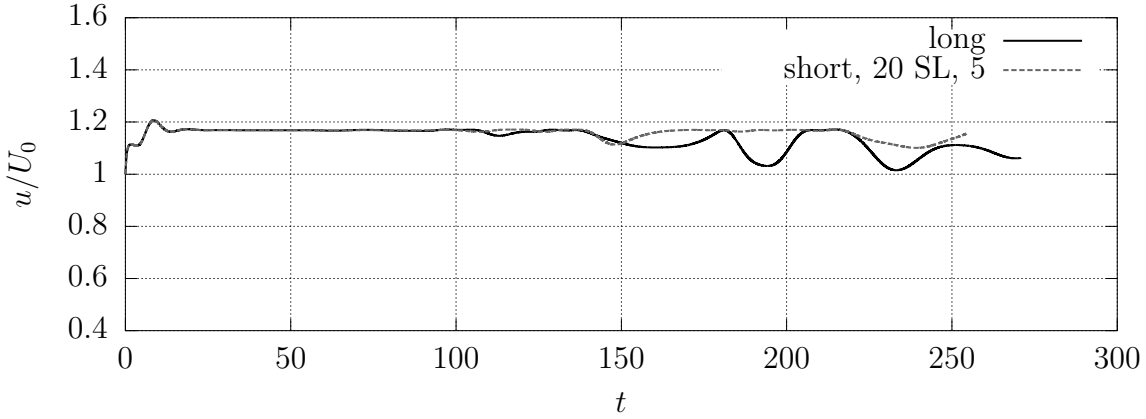

Figure 4.120: Centerline u-velocity probe one jet width from the inlet for short domain, 20 unit sponge-layer with 5-times viscosity increase case.

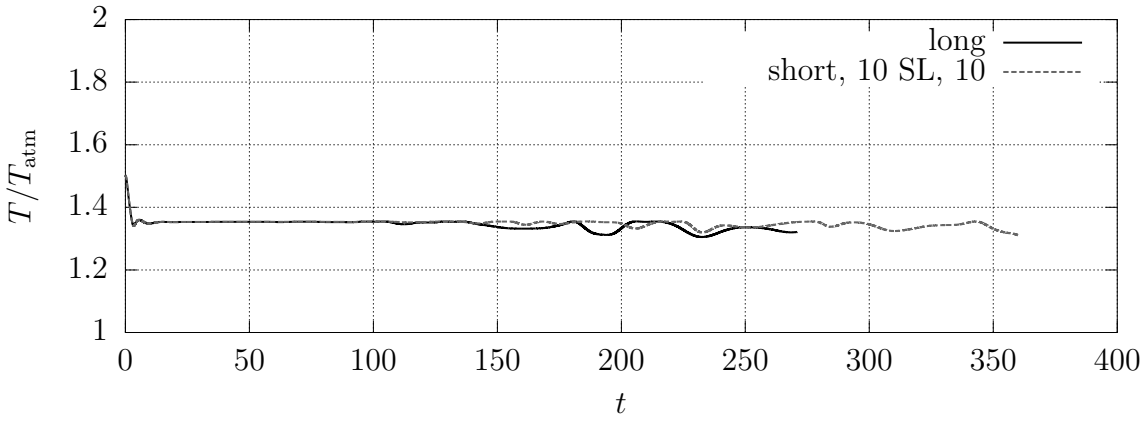

Figure 4.121: Centerline temperature probe one jet width from the inlet for short domain, 10 unit sponge-layer with 10-times viscosity increase case.

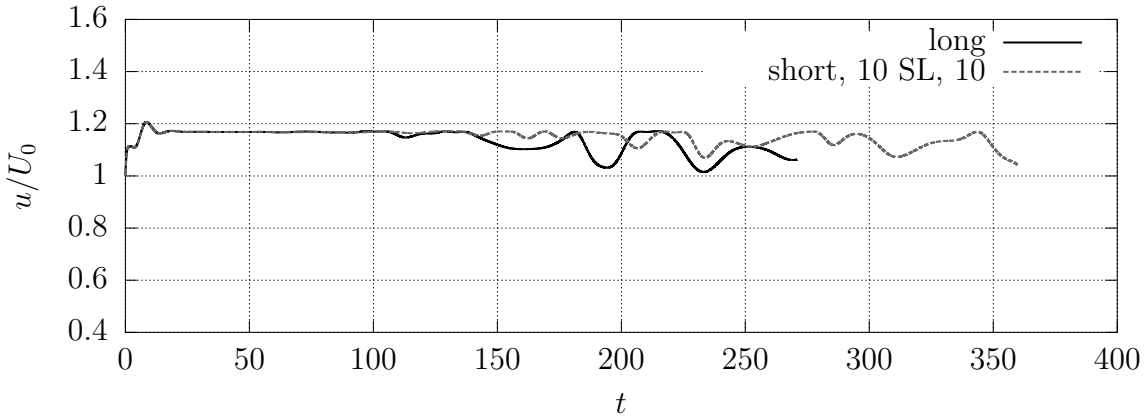

Figure 4.122: Centerline u-velocity probe one jet width from the inlet for short domain, 10 unit sponge-layer with 10-times viscosity increase case.

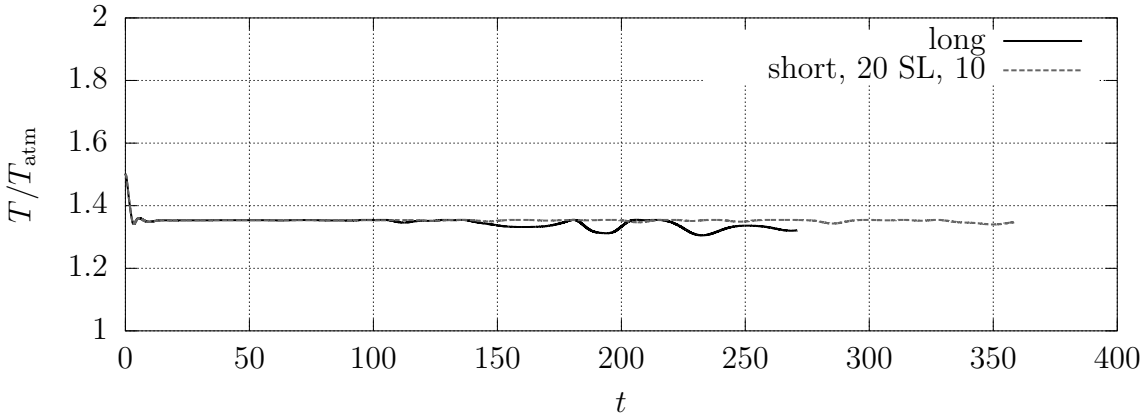

Figure 4.123: Centerline temperature probe one jet width from the inlet for short domain, 20 unit sponge-layer with 10-times viscosity increase case.

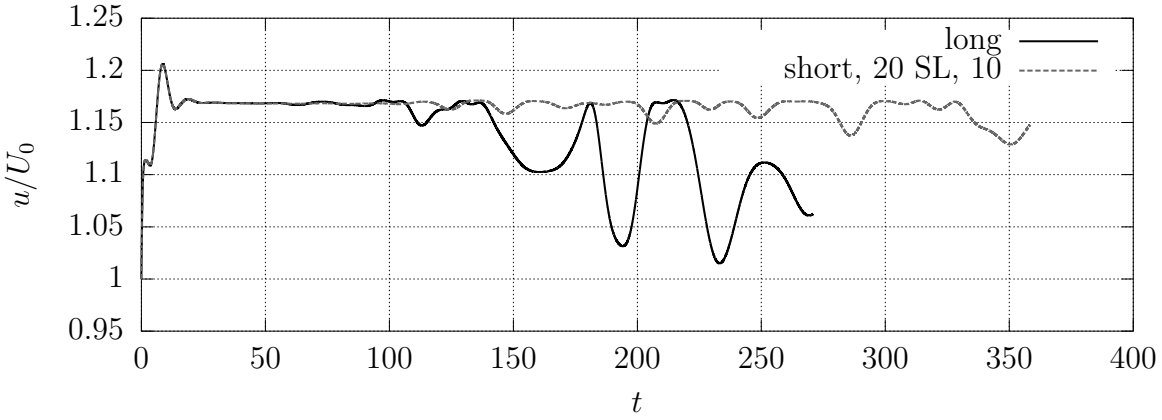

Figure 4.124: Centerline u-velocity probe one jet width from the inlet for short domain, 20 unit sponge-layer with 10-times viscosity increase case.

Appendix: $T/T_{\mathbf{atm}} = 2$ plots

5.12 Instantaneous fields

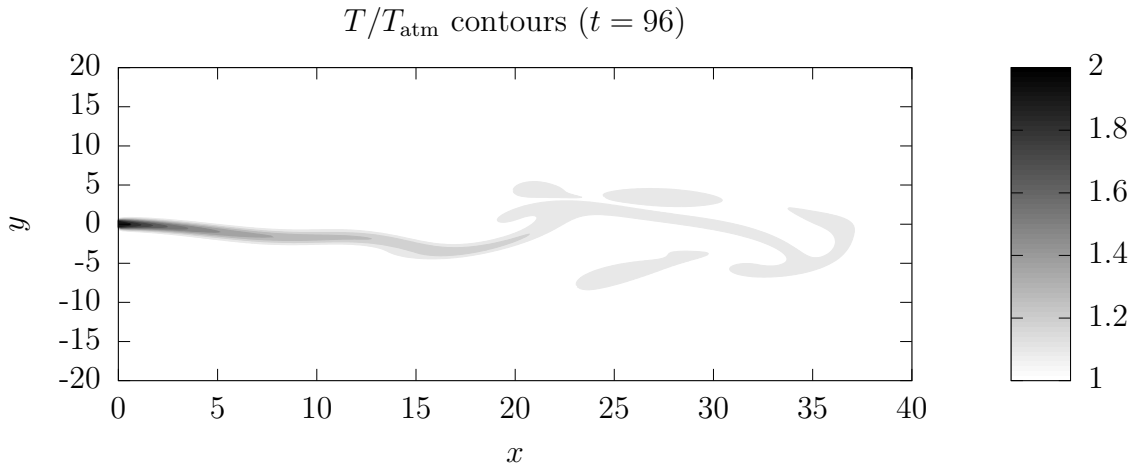

Figure 5.125: Temperature contours for the long domain, no sponge-layer case.

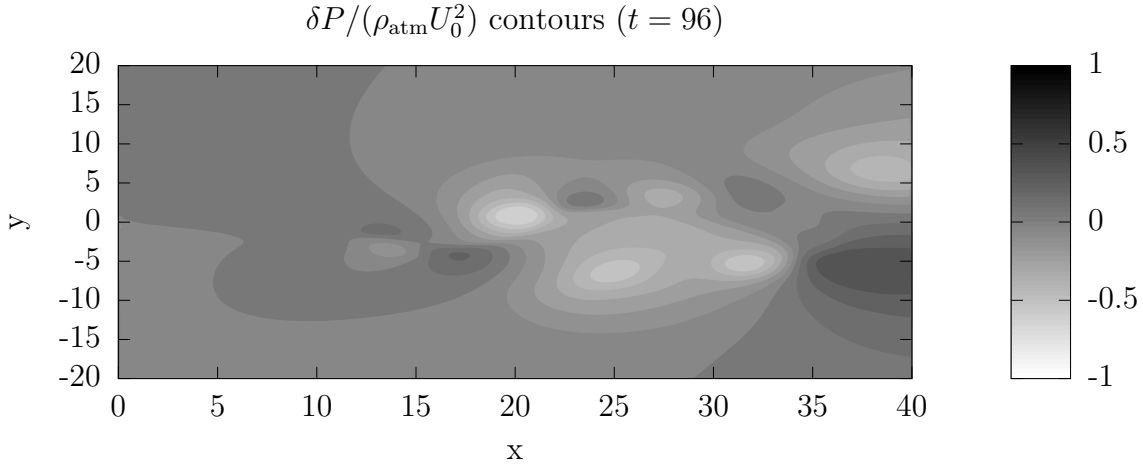

Figure 5.126: Pressure contours for the long domain, no sponge-layer case.

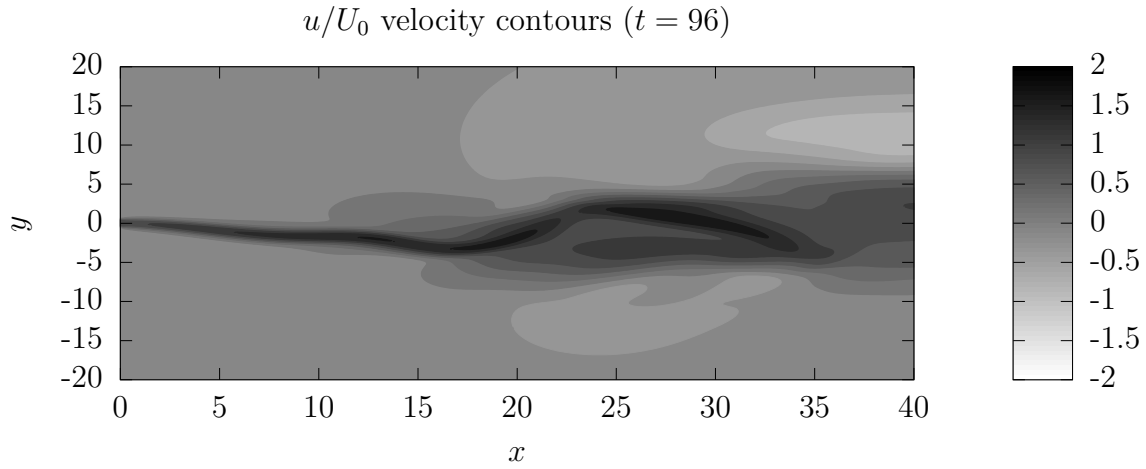

Figure 5.127: u-velocity contours for the long domain, no sponge-layer case.

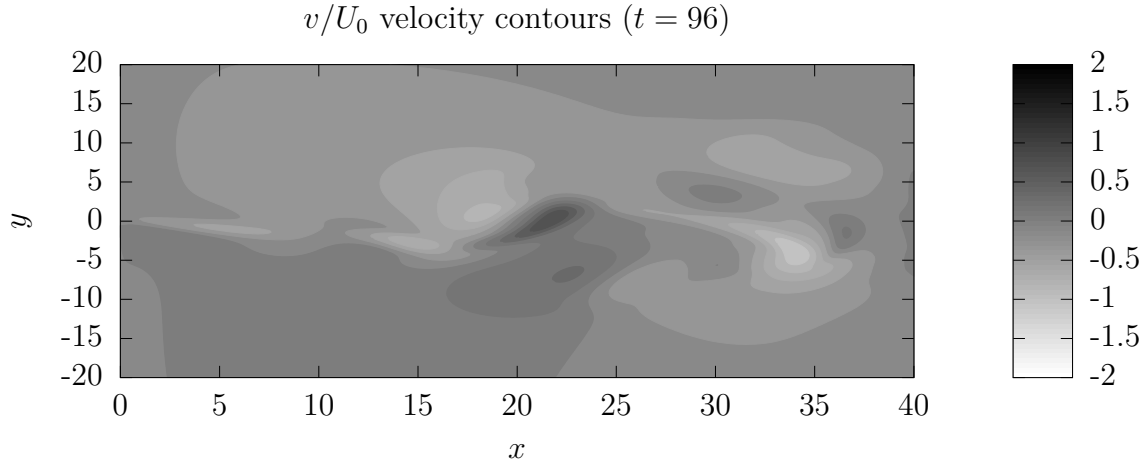

Figure 5.128: v-velocity contours for the long domain, no sponge-layer case.

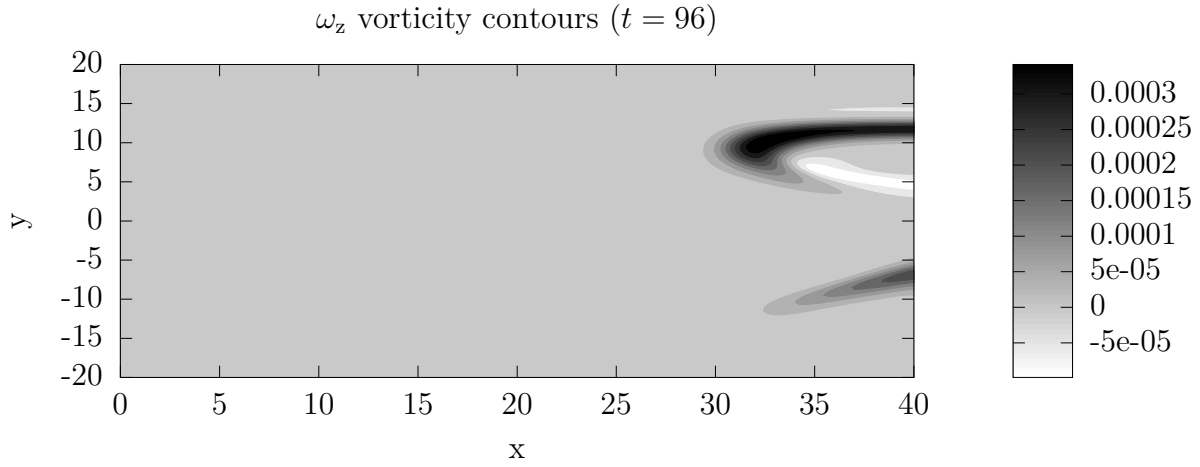

Figure 5.129: Vorticity contours for the long domain, no sponge-layer case.

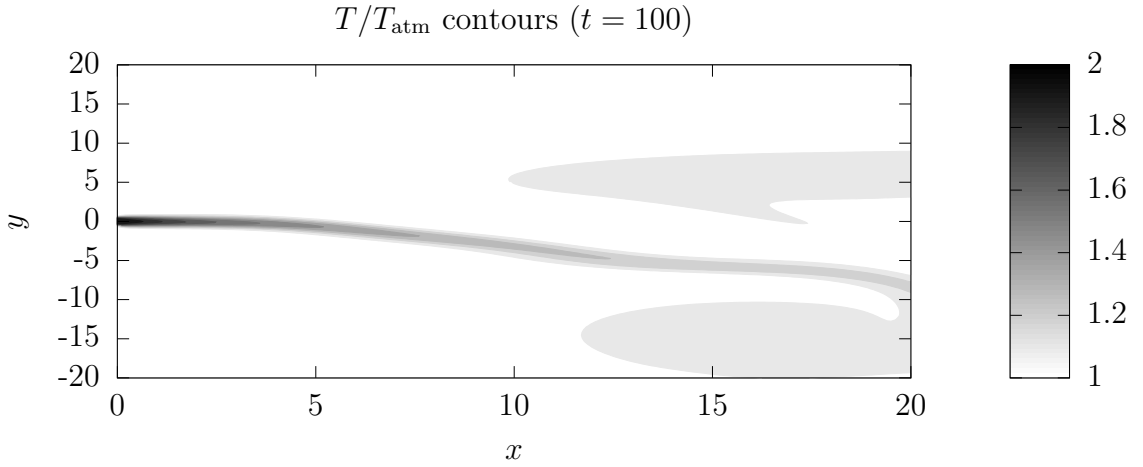

Figure 5.130: Temperature contours for the short domain, no sponge-layer case.

Figure 5.131: Pressure contours for the short domain, no sponge-layer case.

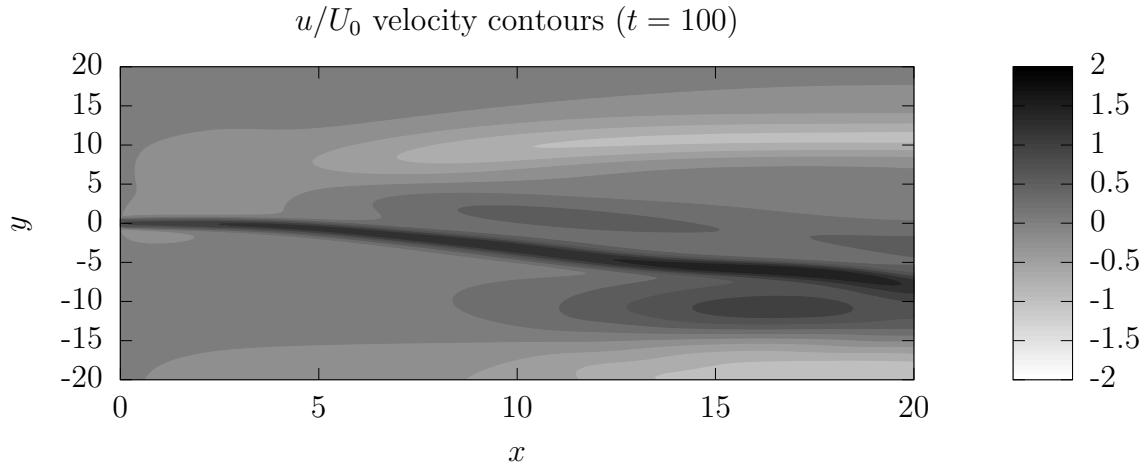

Figure 5.132: u-velocity contours for the short domain, no sponge-layer case.

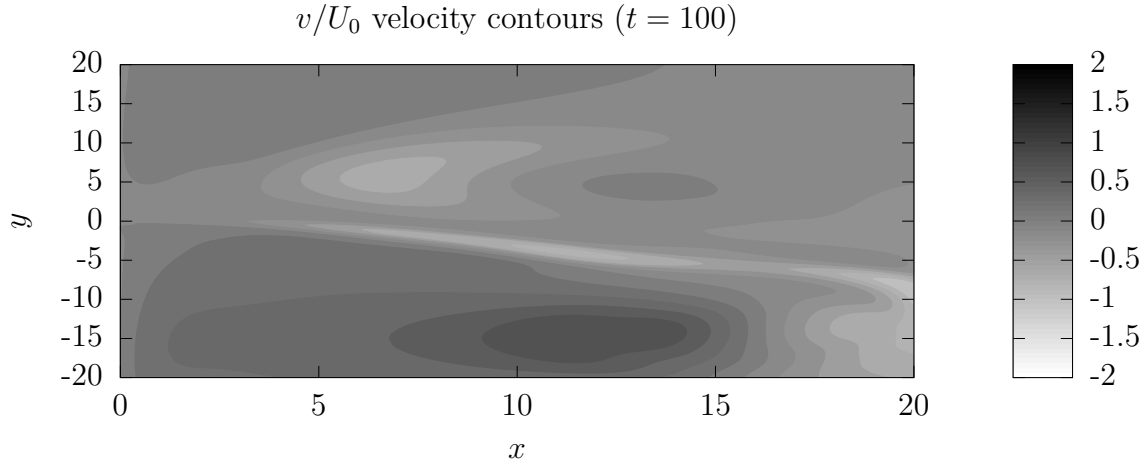

Figure 5.133: v-velocity contours for the short domain, no sponge-layer case.

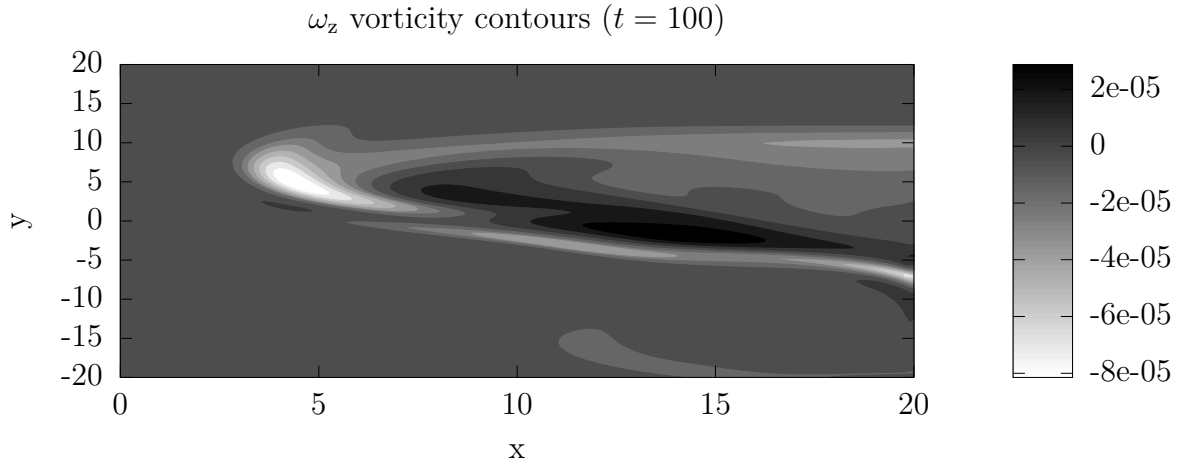

Figure 5.134: Vorticity contours for the short domain, no sponge-layer case.

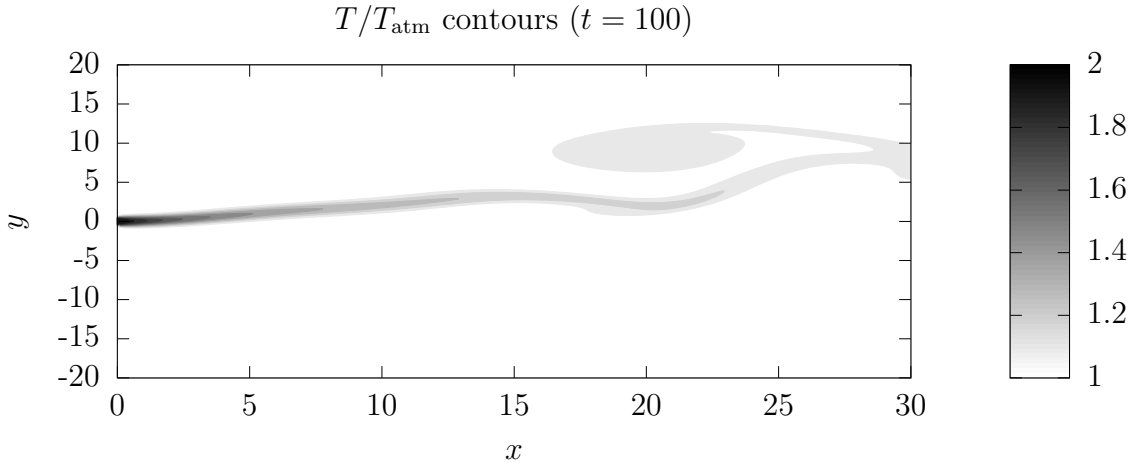

Figure 5.135: Temperature contours for the short domain, 10 unit sponge-layer with 5-times viscosity increase case.

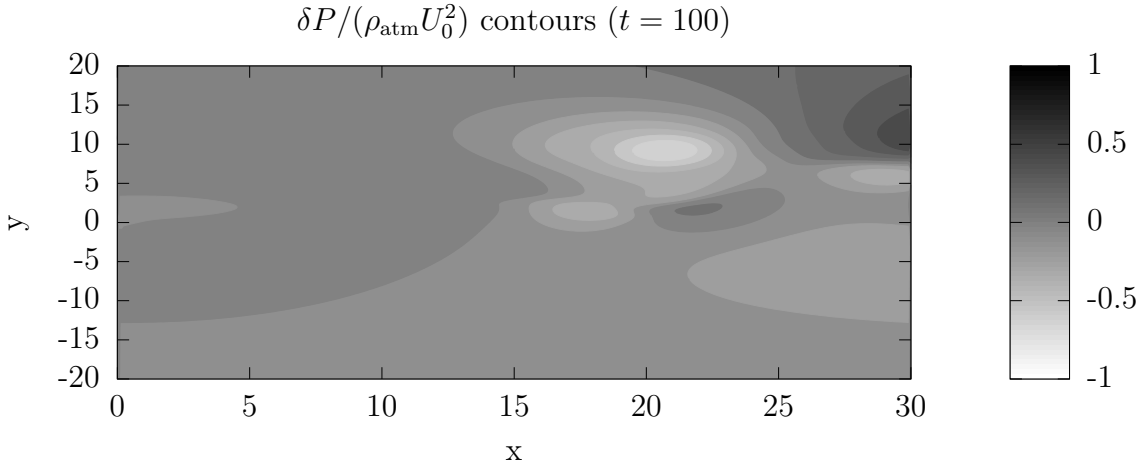

Figure 5.136: Pressure contours for the short domain, 10 unit sponge-layer with 5-times viscosity increase case.

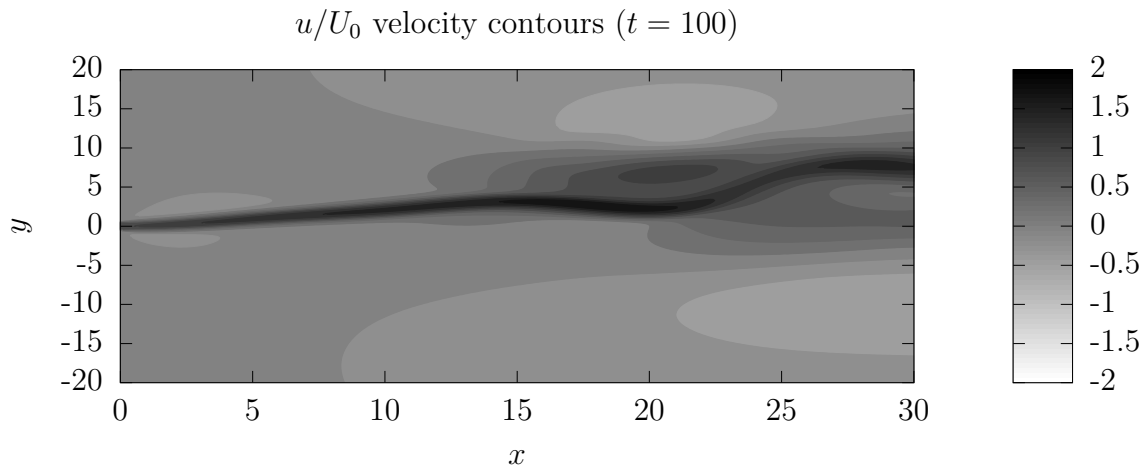

Figure 5.137: u-velocity contours for the short domain, 10 unit sponge-layer with 5-times viscosity increase case.

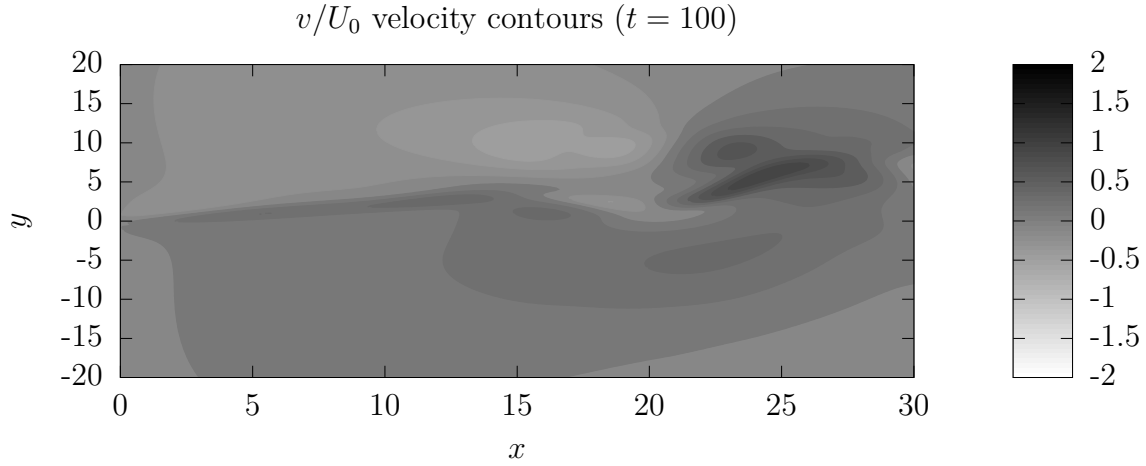

Figure 5.138: v-velocity contours for the short domain, 10 unit sponge-layer with 5-times viscosity increase case.

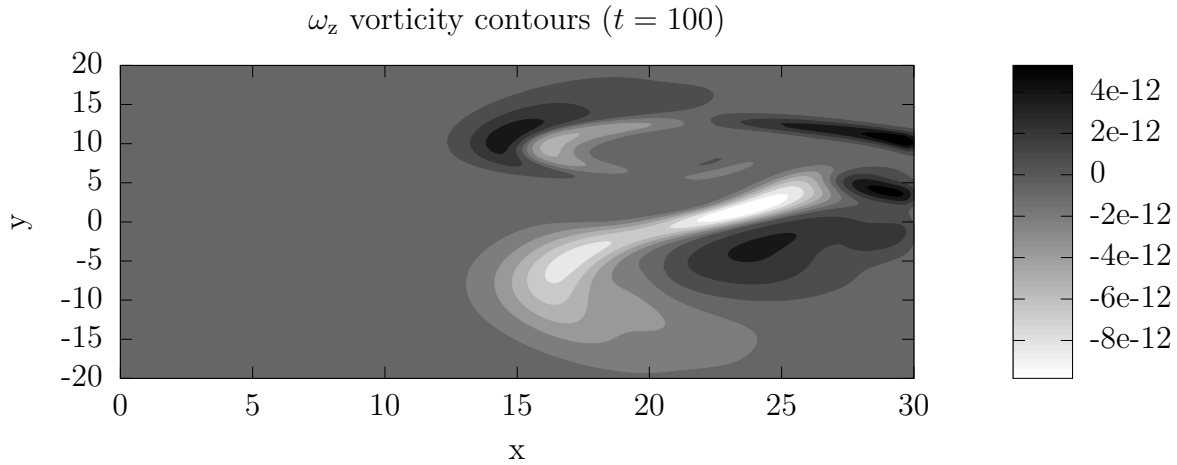

Figure 5.139: Vorticity contours for the short domain, 10 unit sponge-layer with 5-times viscosity increase case.

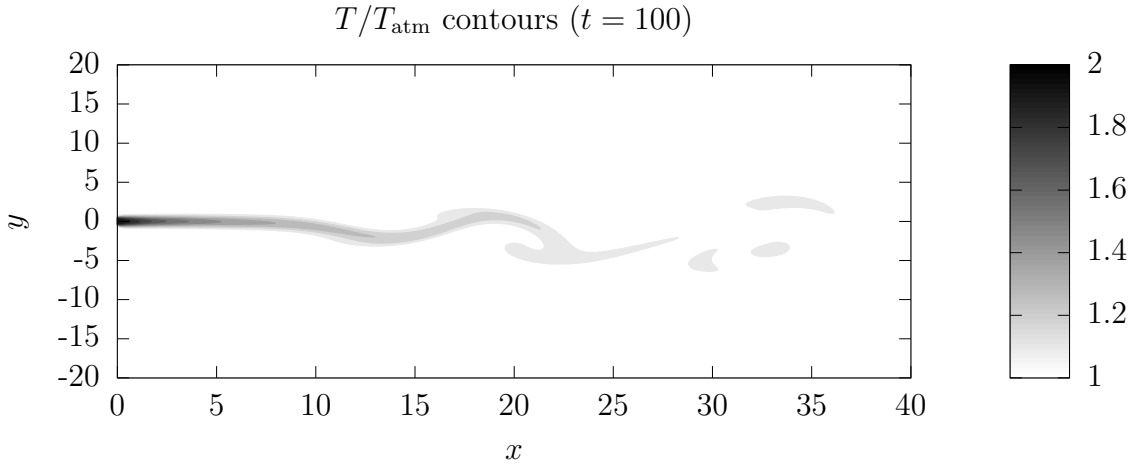

Figure 5.140: Temperature contours for the short domain, 20 unit sponge-layer with 5-times viscosity increase case.

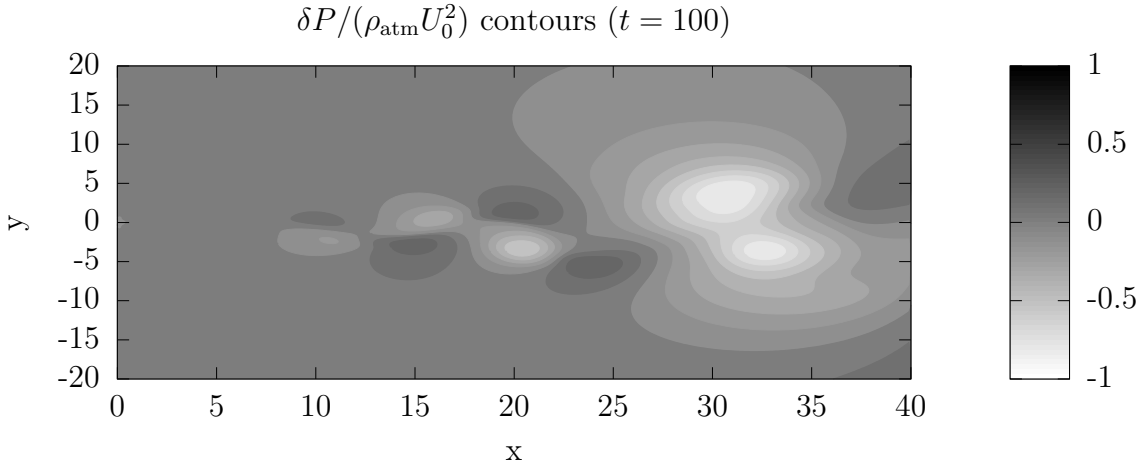

Figure 5.141: Pressure contours for the short domain, 20 unit sponge-layer with 5-times viscosity increase case.

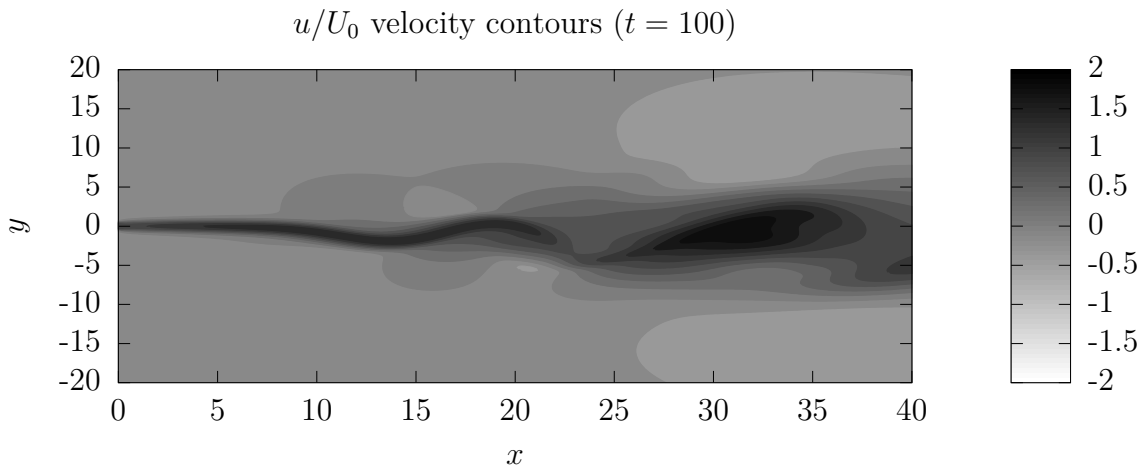

Figure 5.142: u-velocity contours for the short domain, 20 unit sponge-layer with 5-times viscosity increase case.

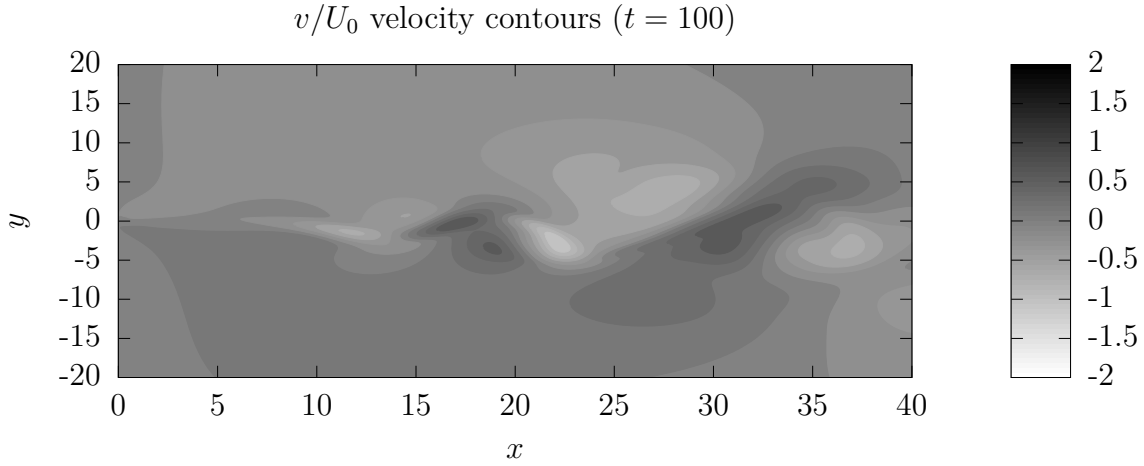

Figure 5.143: v-velocity contours for the short domain, 20 unit sponge-layer with 5-times viscosity increase case.

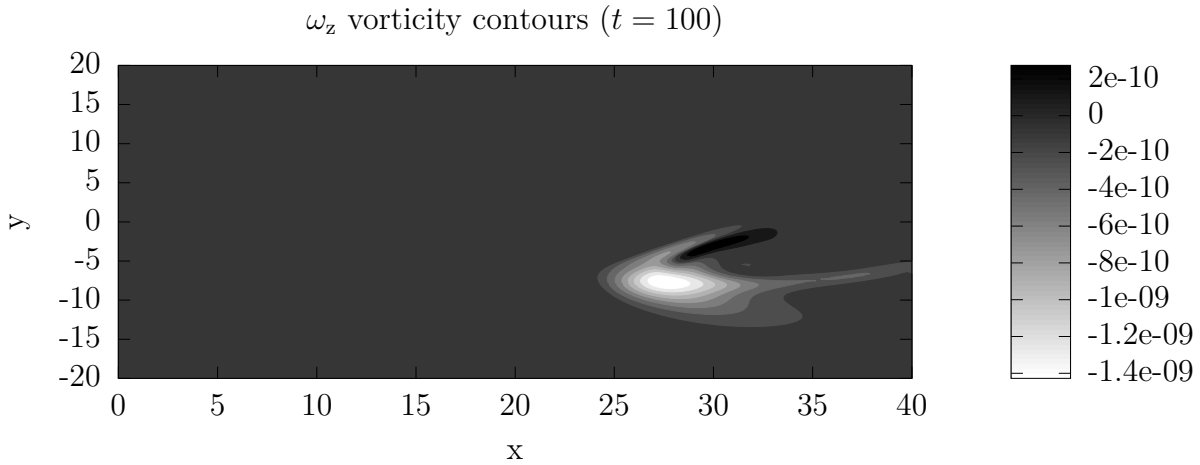

Figure 5.144: Vorticity contours for the short domain, 20 unit sponge-layer with 5-times viscosity increase case.

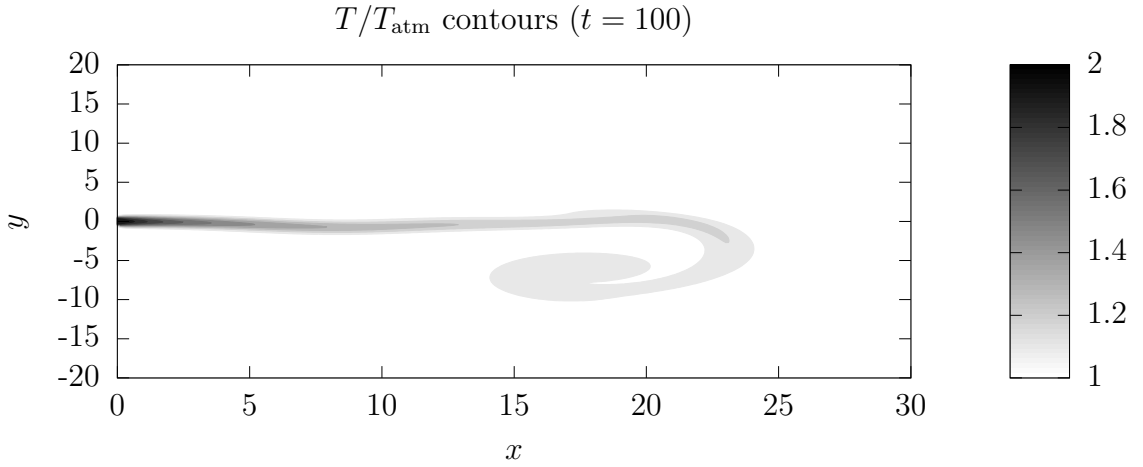

Figure 5.145: Temperature contours for the short domain, 10 unit sponge-layer with 10-times viscosity increase case.

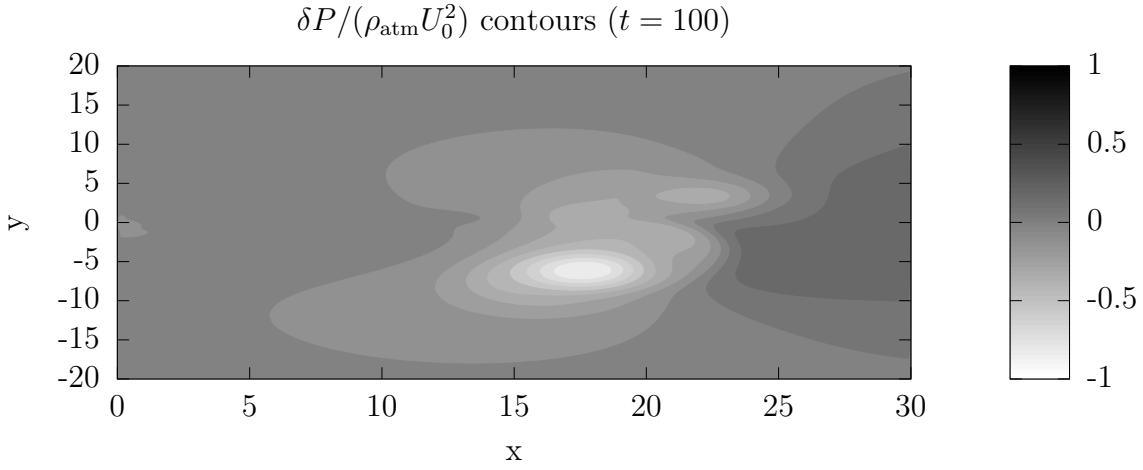

Figure 5.146: Pressure contours for the short domain, 10 unit sponge-layer with 10-times viscosity increase case.

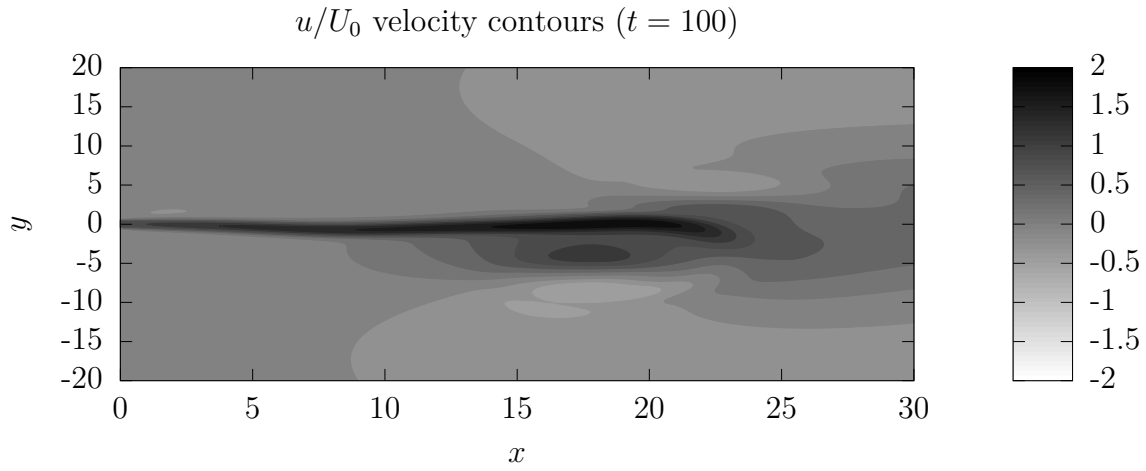

Figure 5.147: u-velocity contours for the short domain, 10 unit sponge-layer with 10-times viscosity increase case.

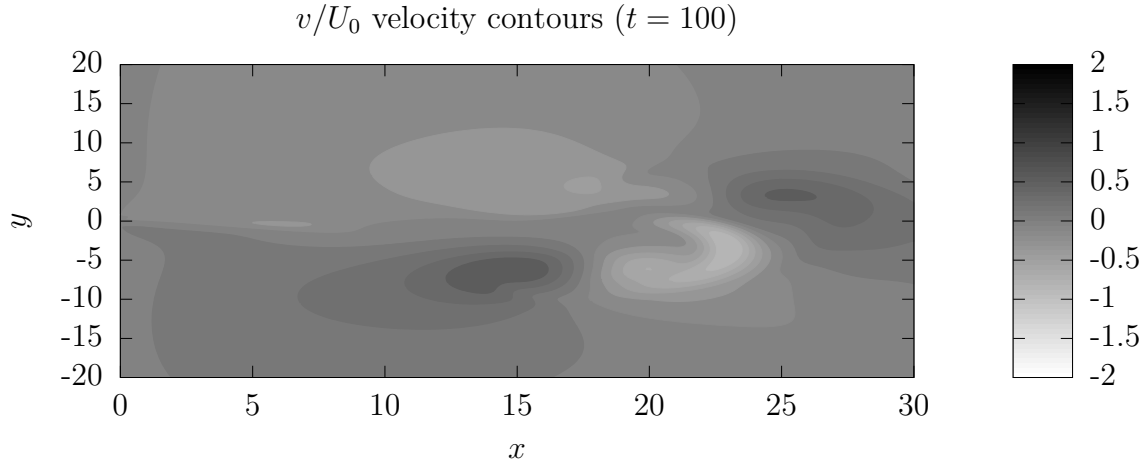

Figure 5.148: v-velocity contours for the short domain, 10 unit sponge-layer with 10-times viscosity increase case.

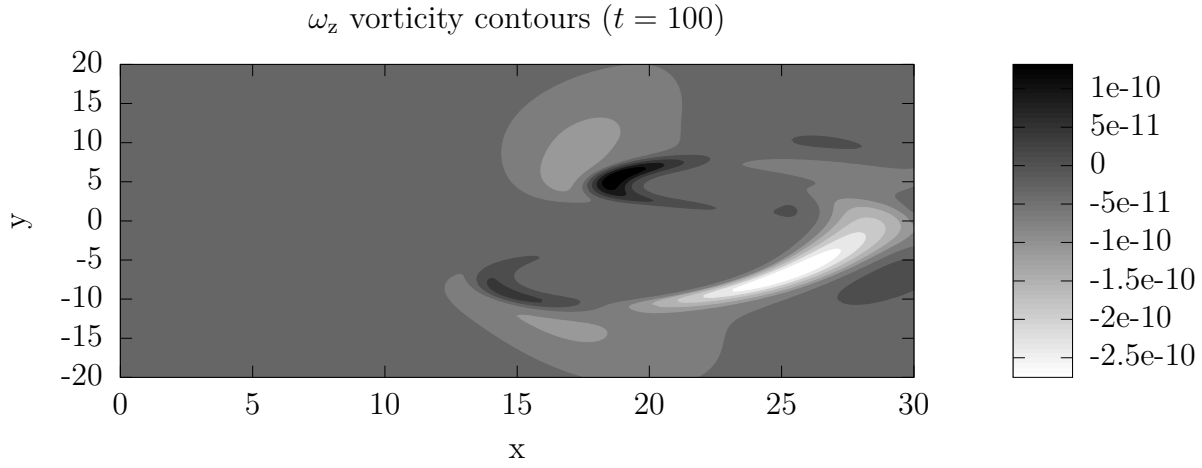

Figure 5.149: Vorticity contours for the short domain, 10 unit sponge-layer with 10-times viscosity increase case.

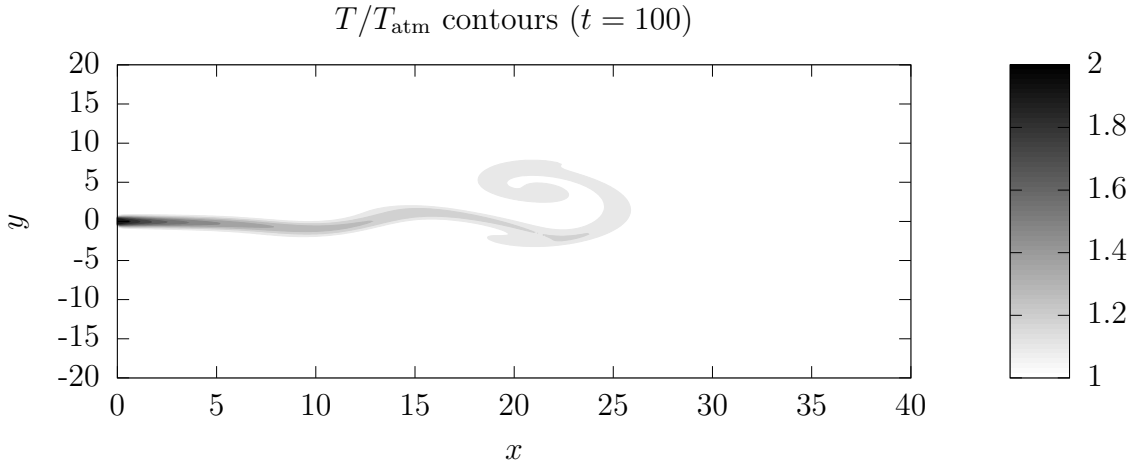

Figure 5.150: Temperature contours for the short domain, 20 unit sponge-layer with 10-times viscosity increase case.

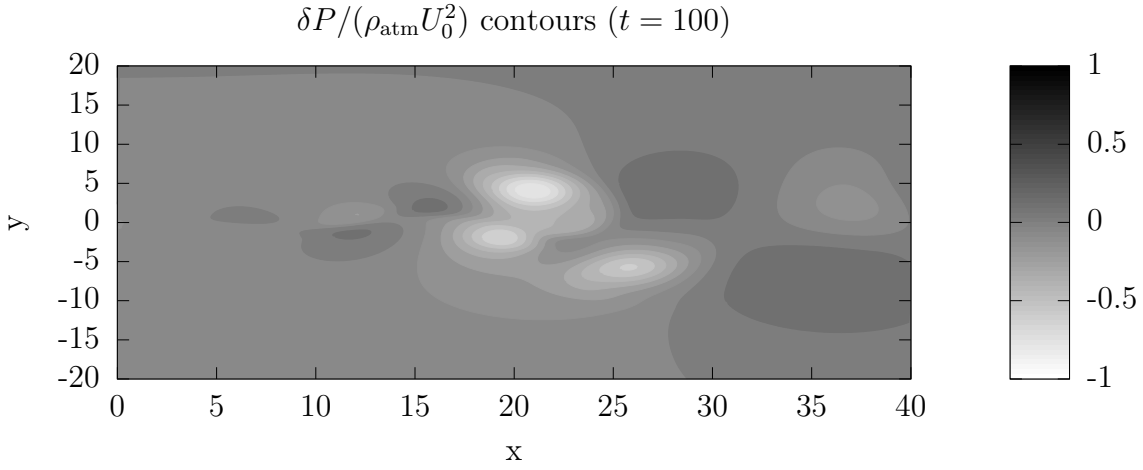

Figure 5.151: Pressure contours for the short domain, 20 unit sponge-layer with 10-times viscosity increase case.

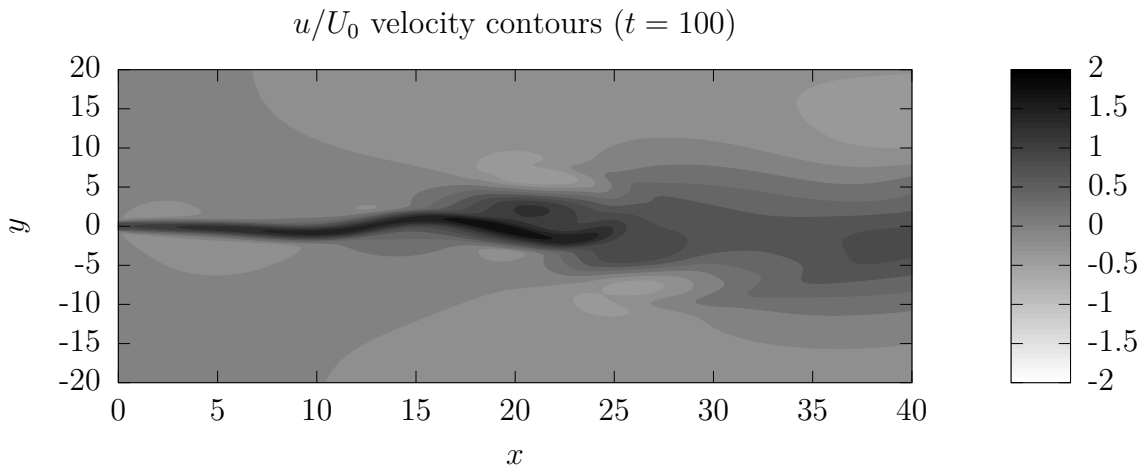

Figure 5.152: u-velocity contours for the short domain, 20 unit sponge-layer with 10-times viscosity increase case.

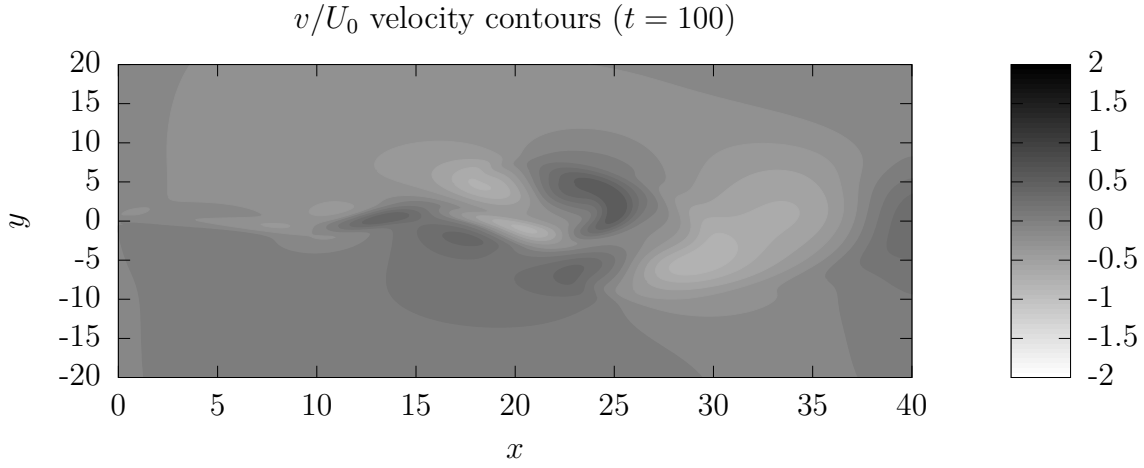

Figure 5.153: v-velocity contours for the short domain, 20 unit sponge-layer with 10-times viscosity increase case.

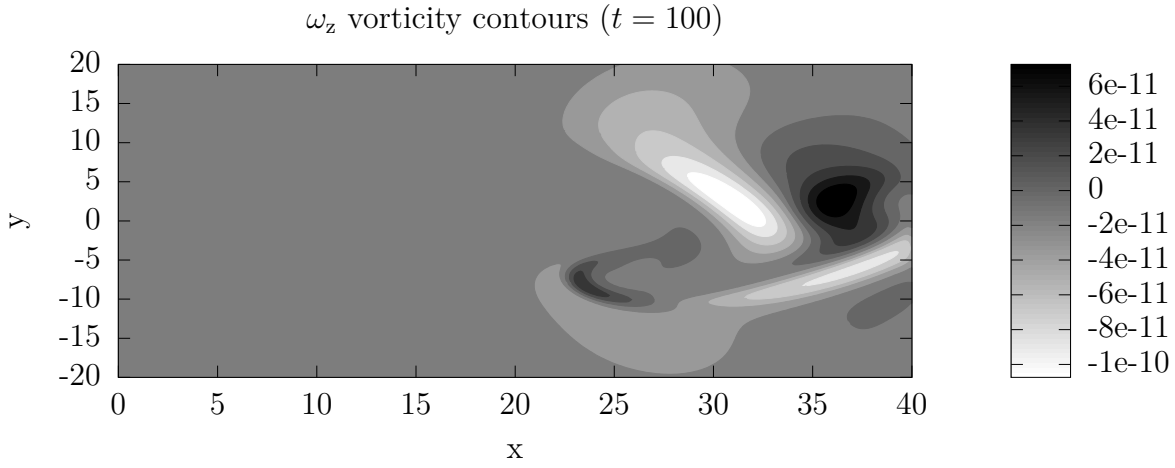

Figure 5.154: Vorticity contours for the short domain, 20 unit sponge-layer with 10-times viscosity increase case.

5.13 Time-averaged fields

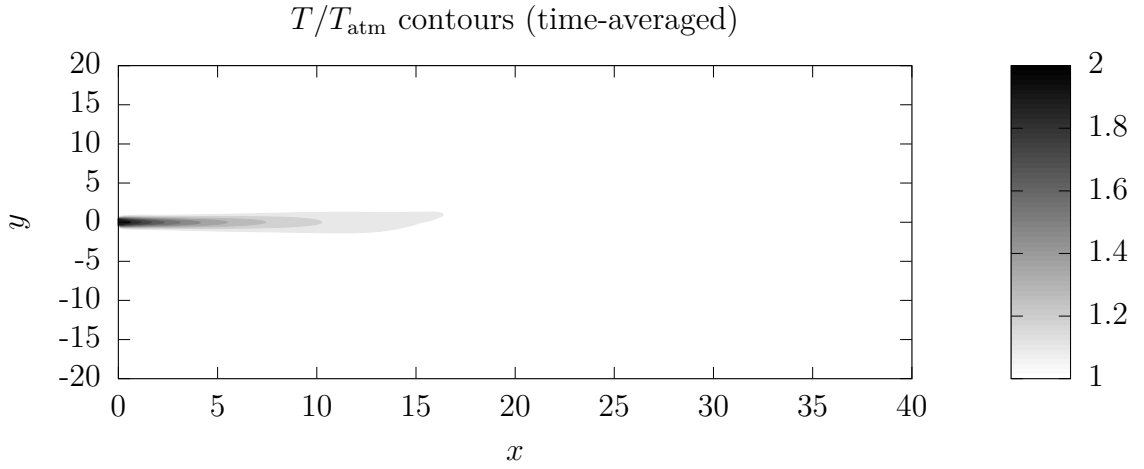

Figure 5.155: Temperature contours for the long domain, no sponge-layer case.

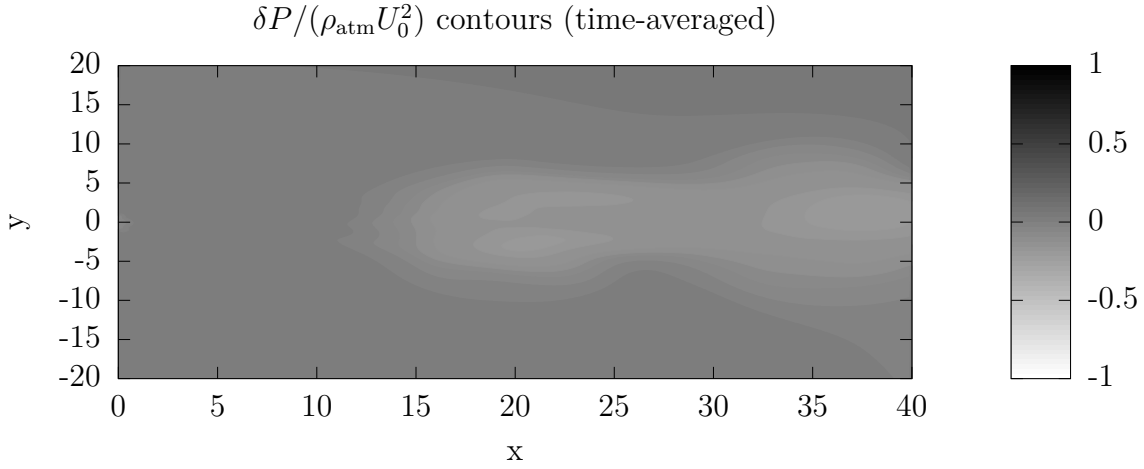

Figure 5.156: Pressure contours for the long domain, no sponge-layer case.

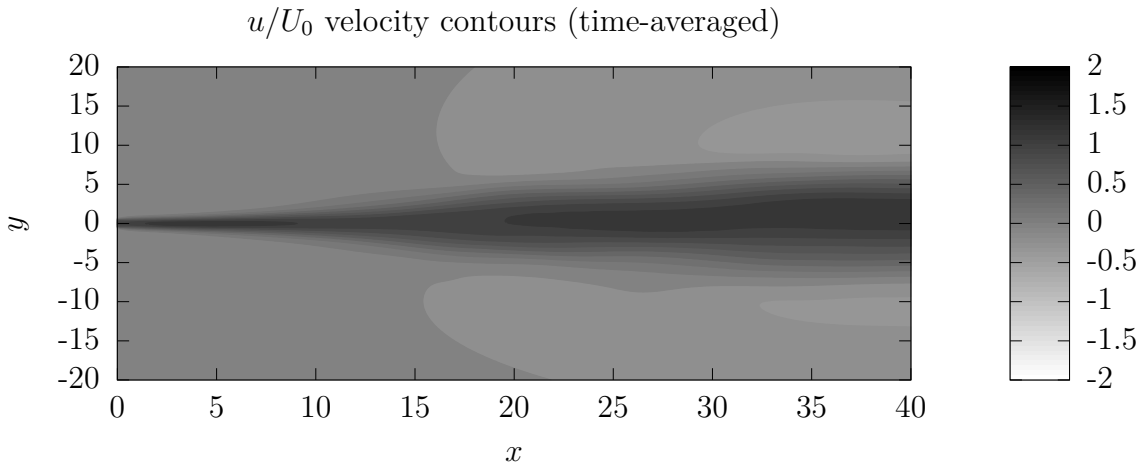

Figure 5.157: u-velocity contours for the long domain, no sponge-layer case.

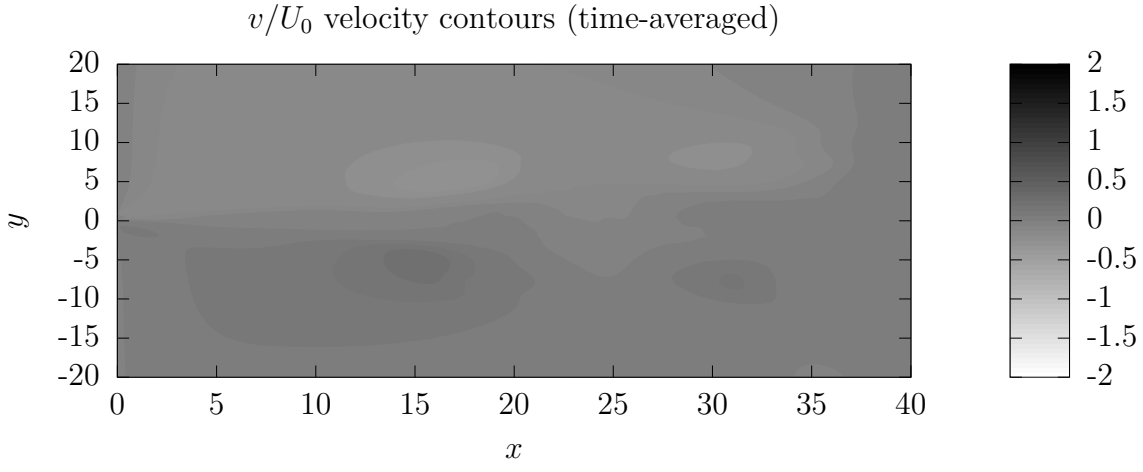

Figure 5.158: v-velocity contours for the long domain, no sponge-layer case.

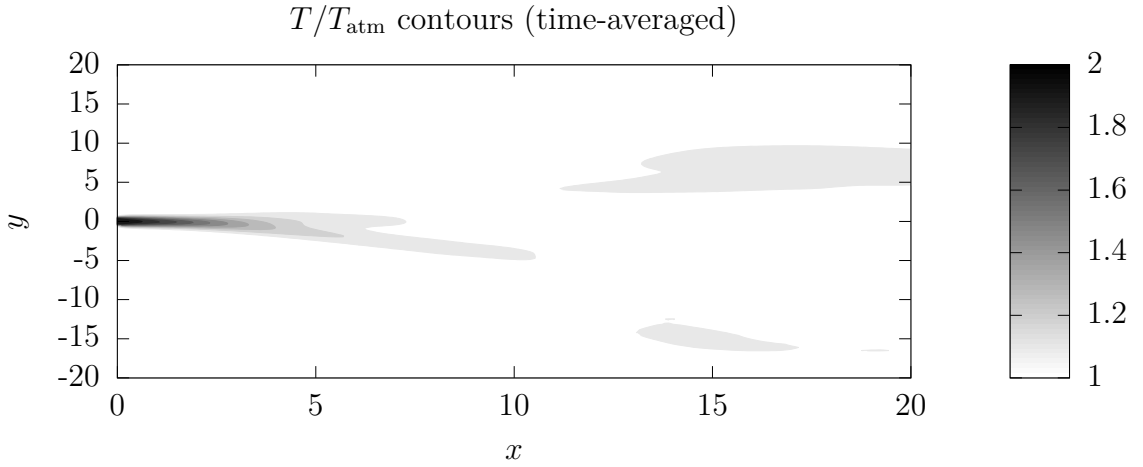

Figure 5.159: Temperature contours for the short domain, no sponge-layer case.

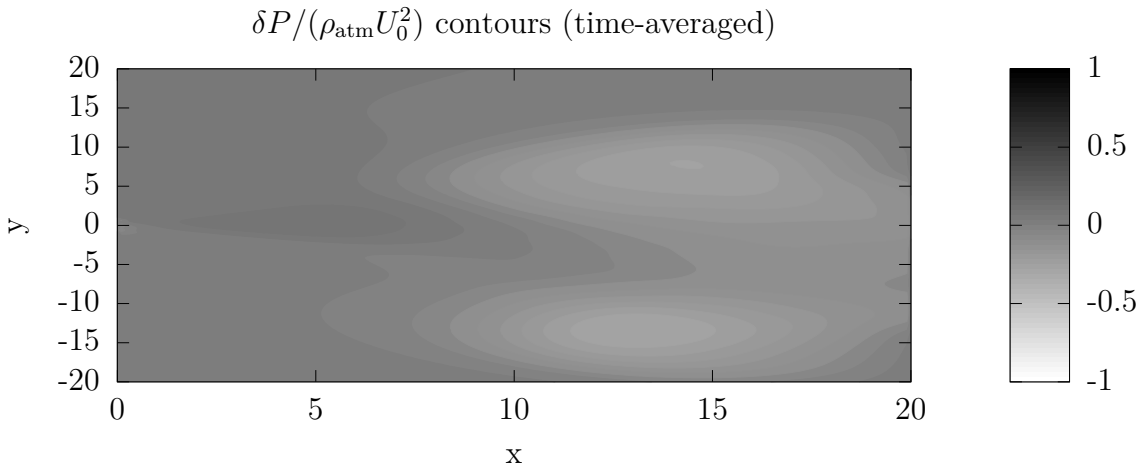

Figure 5.160: Pressure contours for the short domain, no sponge-layer case.

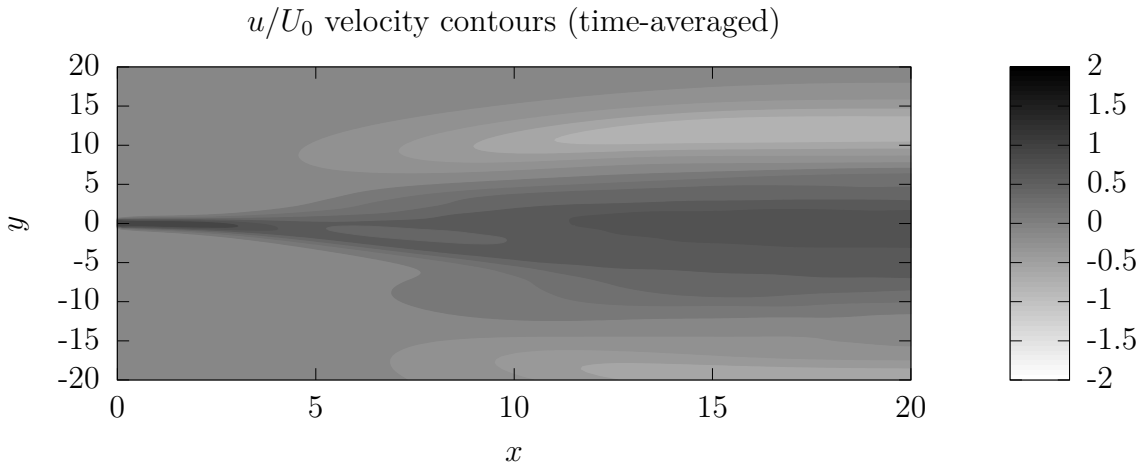

Figure 5.161: u-velocity contours for the short domain, no sponge-layer case.

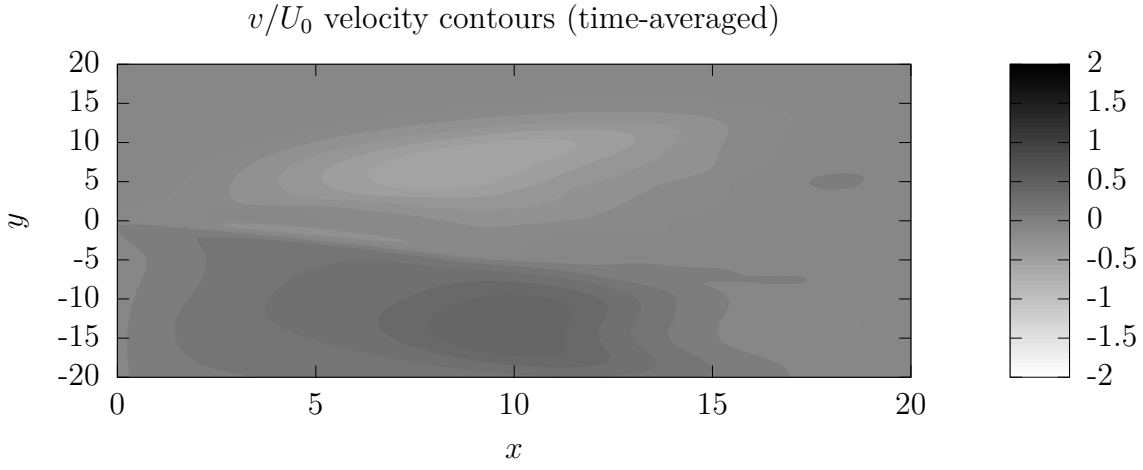

Figure 5.162: v-velocity contours for the short domain, no sponge-layer case.

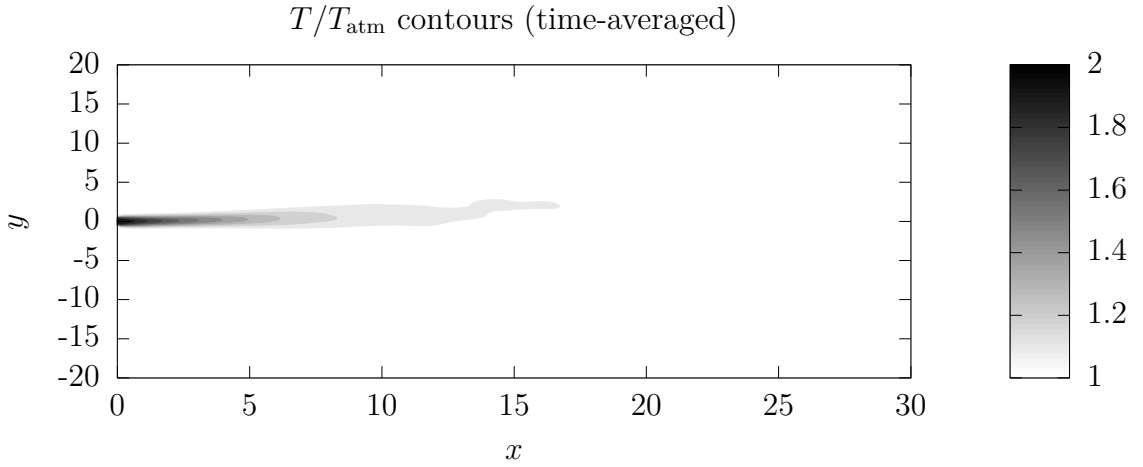

Figure 5.163: Temperature contours for the short domain, 10 unit sponge-layer with 5-times viscosity increase case.

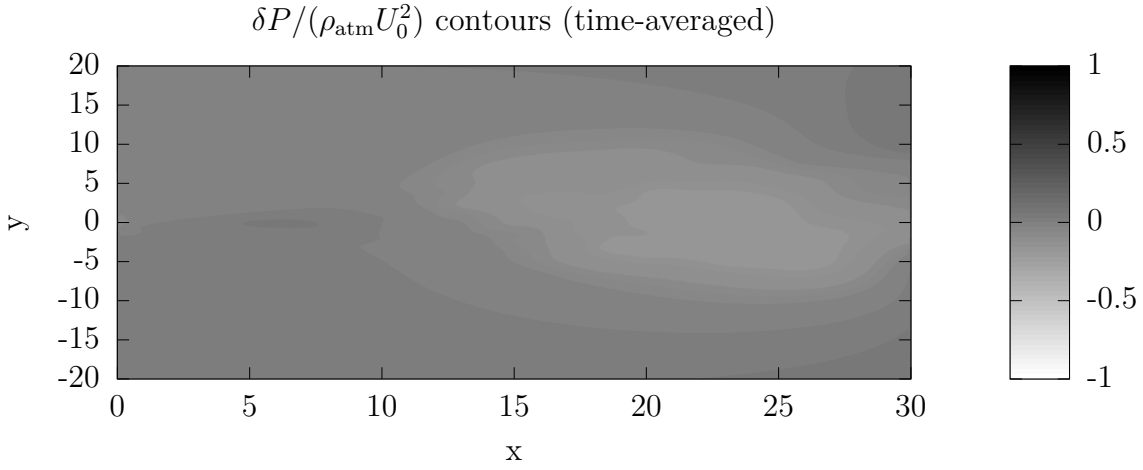

Figure 5.164: Pressure contours for the short domain, 10 unit sponge-layer with 5-times viscosity increase case.

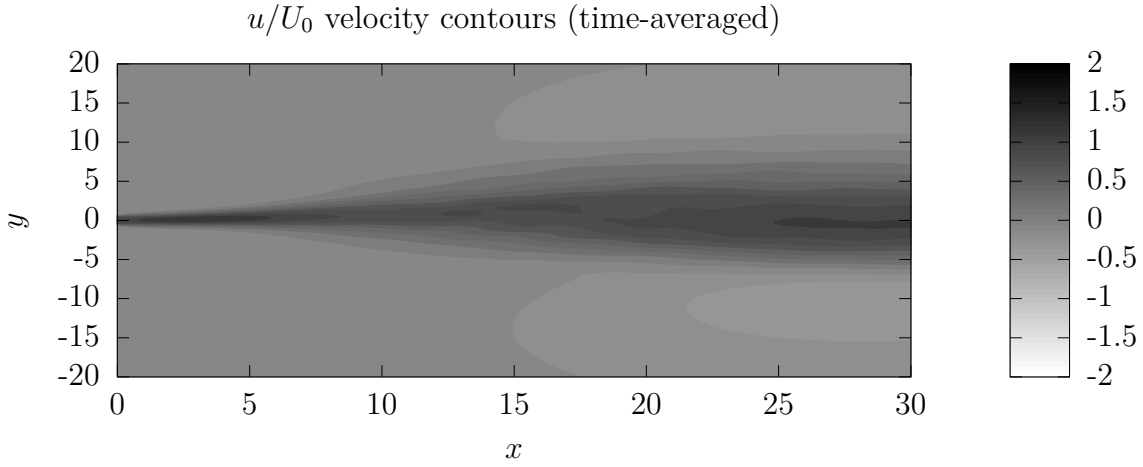

Figure 5.165: u-velocity contours for the short domain, 10 unit sponge-layer with 5-times viscosity increase case.

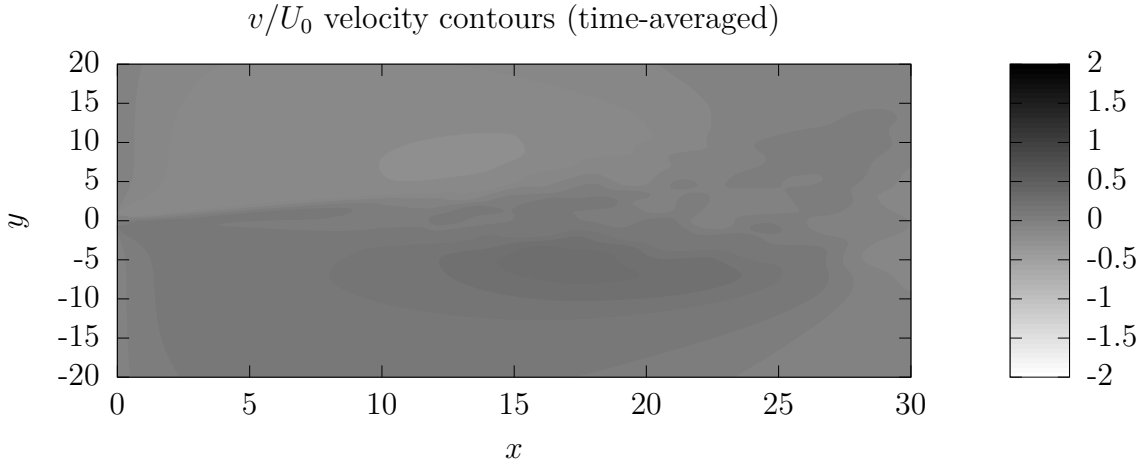

Figure 5.166: v-velocity contours for the short domain, 10 unit sponge-layer with 5-times viscosity increase case.

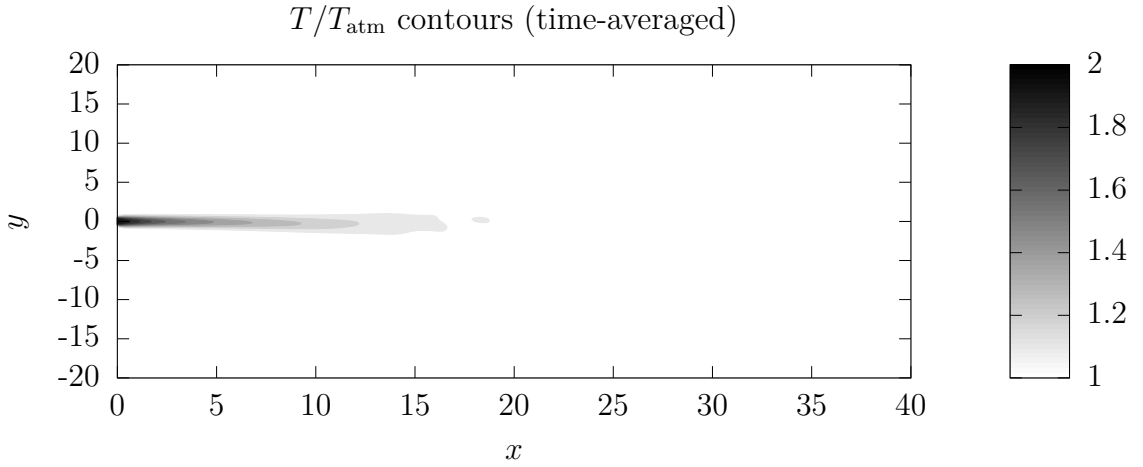

Figure 5.167: Temperature contours for the short domain, 20 unit sponge-layer with 5-times viscosity increase case.

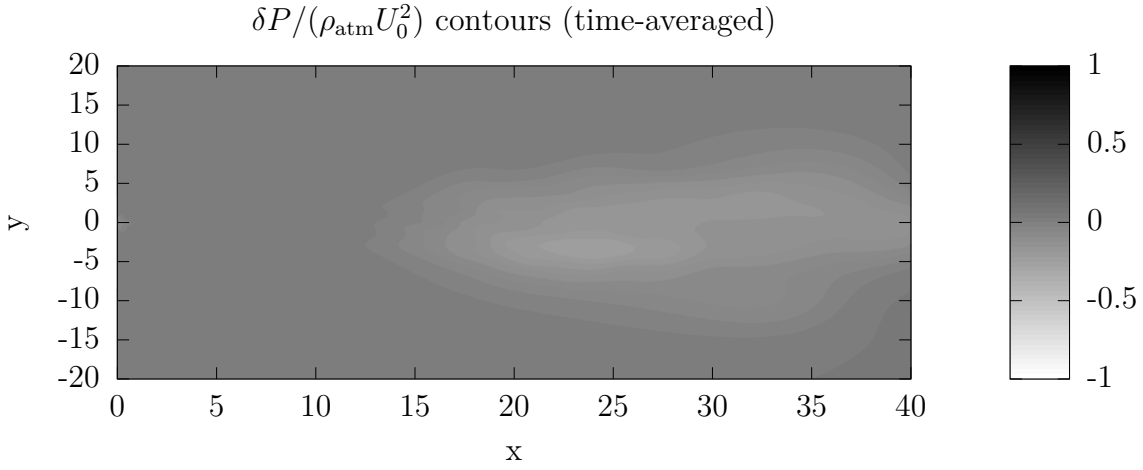

Figure 5.168: Pressure contours for the short domain, 20 unit sponge-layer with 5-times viscosity increase case.

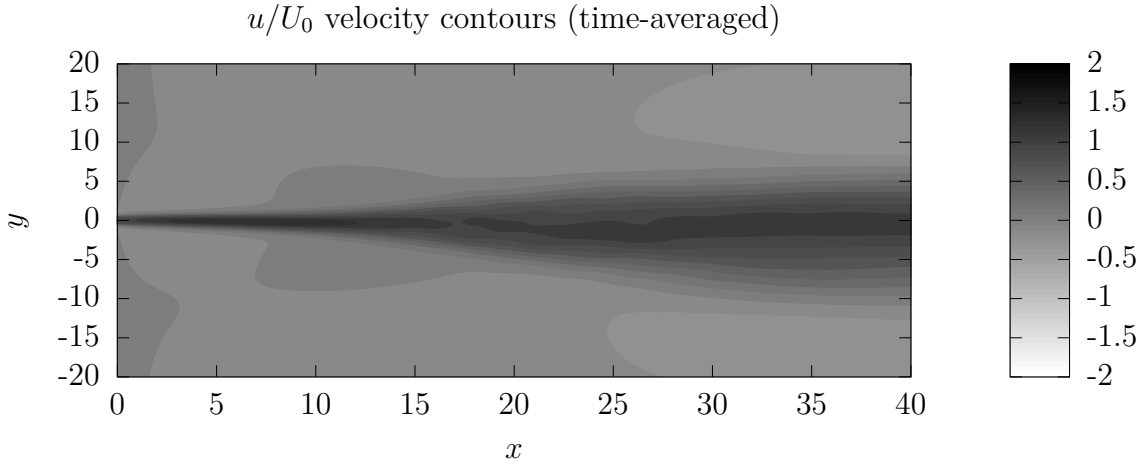

Figure 5.169: u-velocity contours for the short domain, 20 unit sponge-layer with 5-times viscosity increase case.

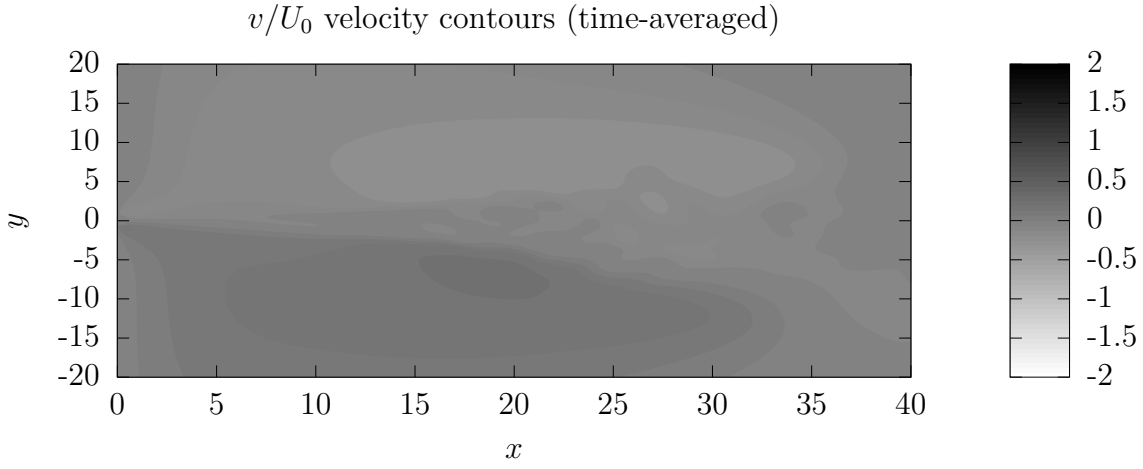

Figure 5.170: v-velocity contours for the short domain, 20 unit sponge-layer with 5-times viscosity increase case.

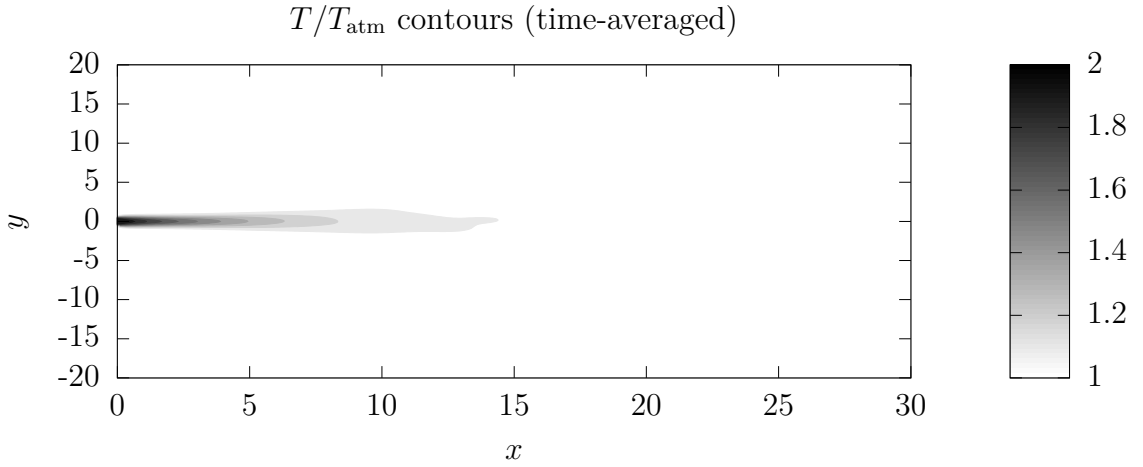

Figure 5.171: Temperature contours for the short domain, 10 unit sponge-layer with 10-times viscosity increase case.

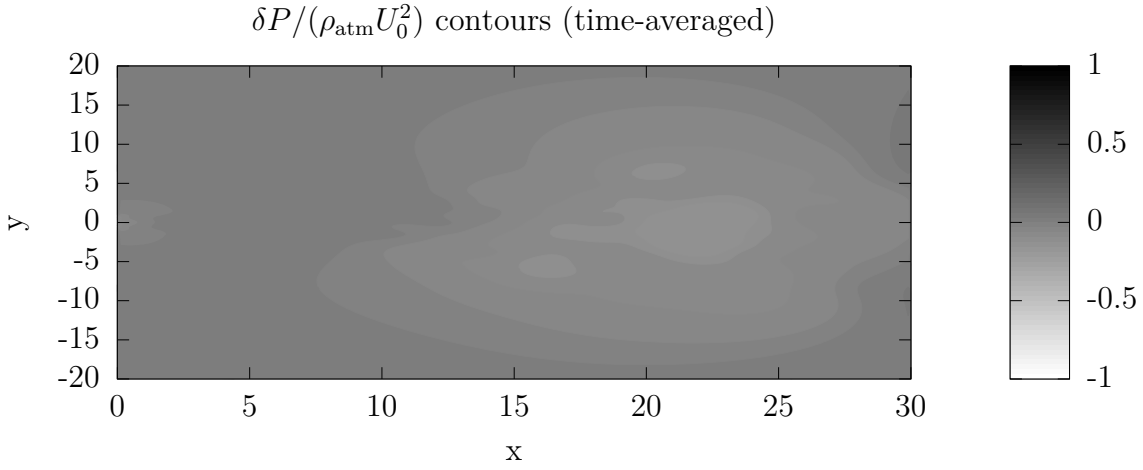

Figure 5.172: Pressure contours for the short domain, 10 unit sponge-layer with 10-times viscosity increase case.

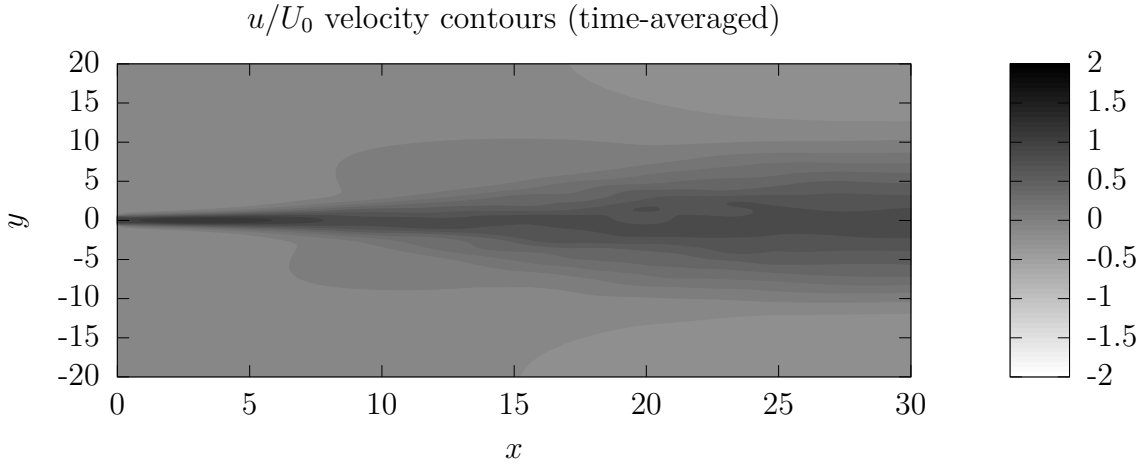

Figure 5.173: u-velocity contours for the short domain, 10 unit sponge-layer with 10-times viscosity increase case.

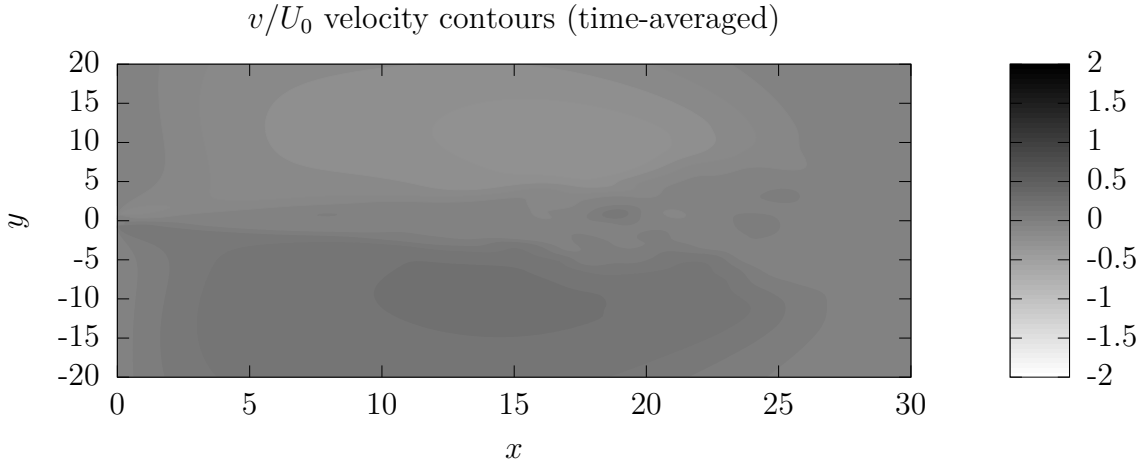

Figure 5.174: v-velocity contours for the short domain, 10 unit sponge-layer with 10-times viscosity increase case.

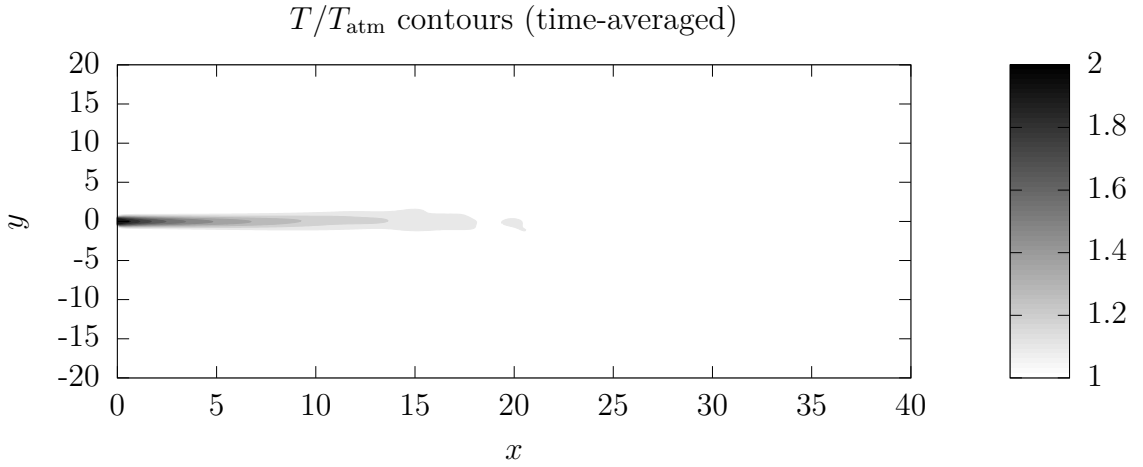

Figure 5.175: Temperature contours for the short domain, 20 unit sponge-layer with 10-times viscosity increase case.

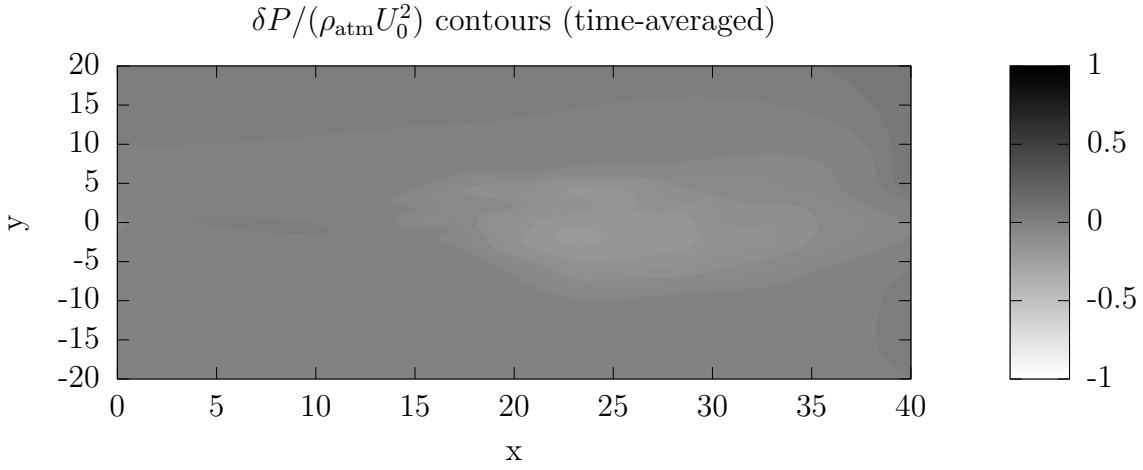

Figure 5.176: Pressure contours for the short domain, 20 unit sponge-layer with 10-times viscosity increase case.

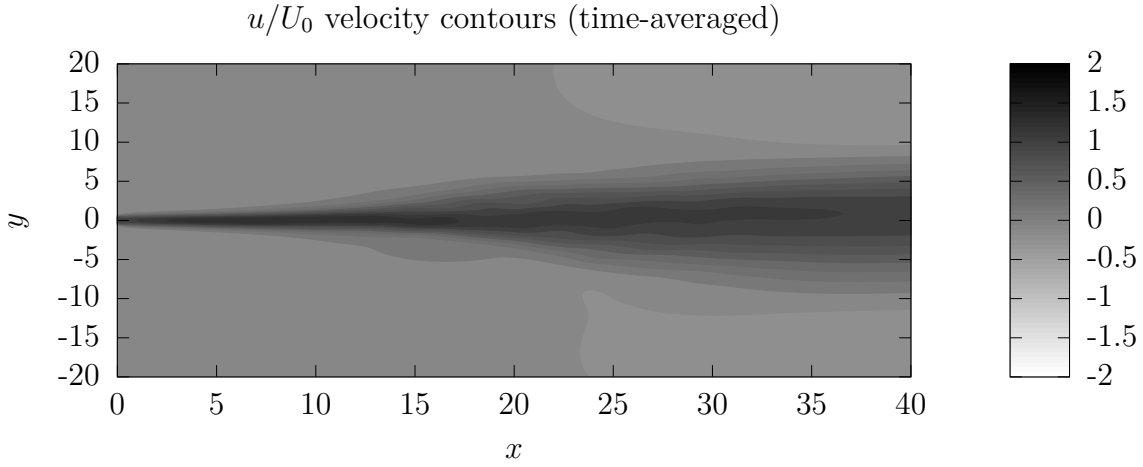

Figure 5.177: u-velocity contours for the short domain, 20 unit sponge-layer with 10-times viscosity increase case.

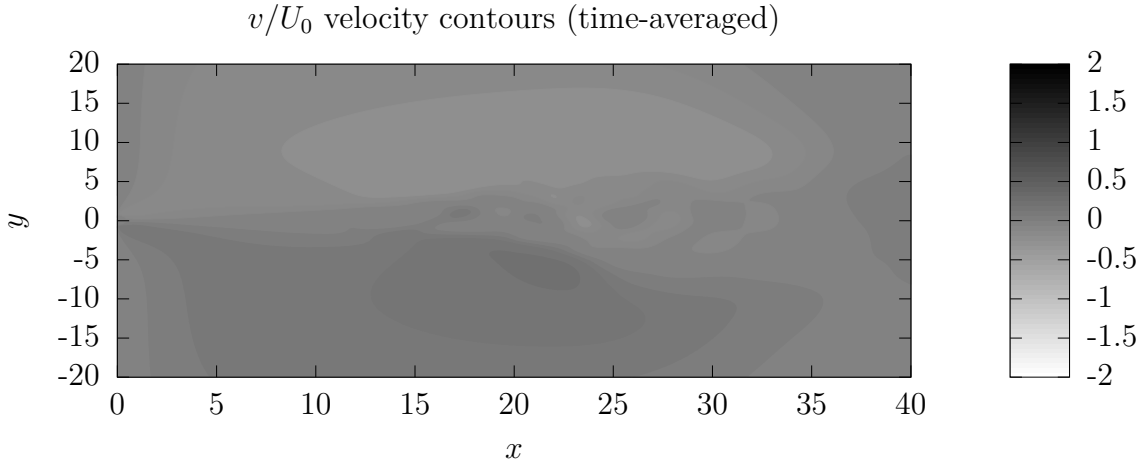

Figure 5.178: v-velocity contours for the short domain, 20 unit sponge-layer with 10-times viscosity increase case.

5.14 Instantaneous centerlines

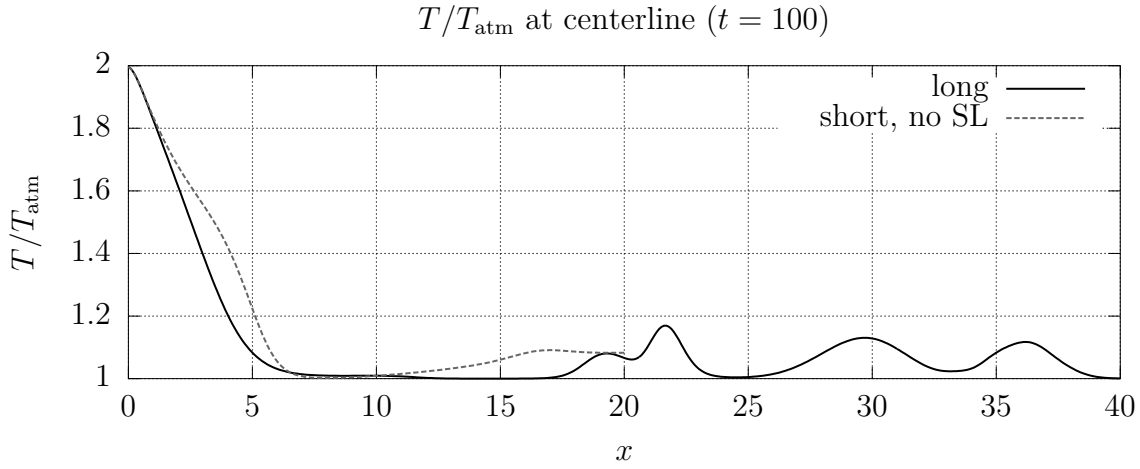

Figure 5.179: Comparison of long-domain temperatures with short domain, no sponge-layer temperatures at the centerline.

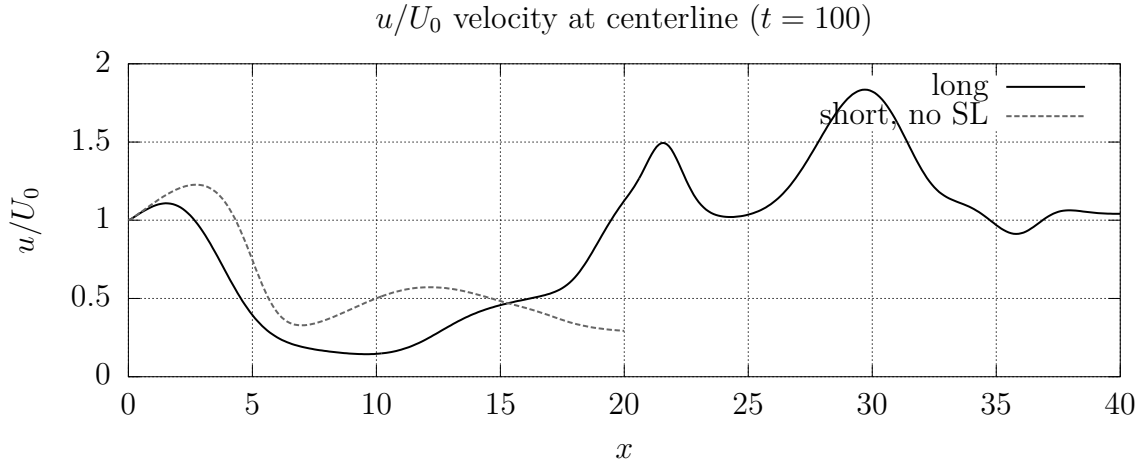

Figure 5.180: Comparison of long-domain u-velocity with short domain, no sponge-layer u-velocity at the centerline.

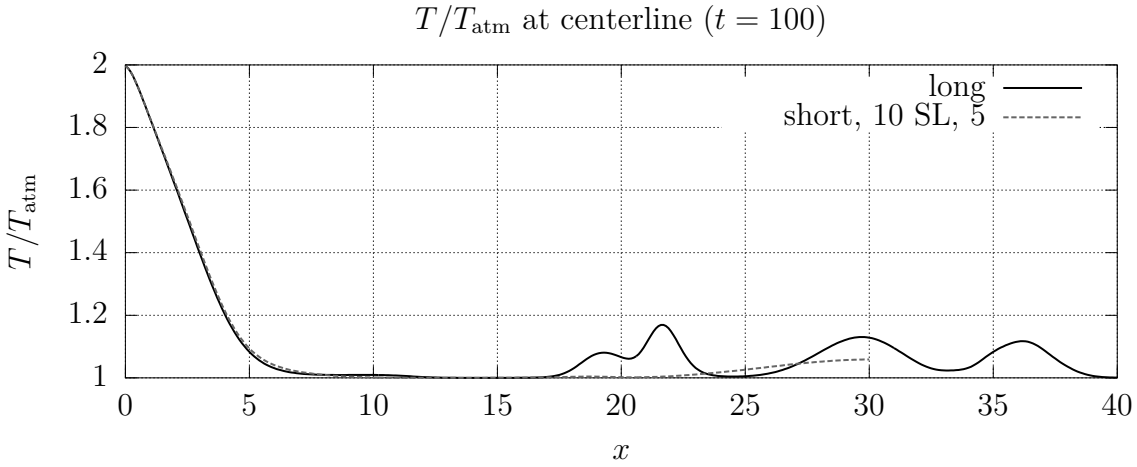

Figure 5.181: Comparison of long-domain temperatures with short domain, 10 unit sponge-layer with 5-times viscosity increase temperatures at the centerline.

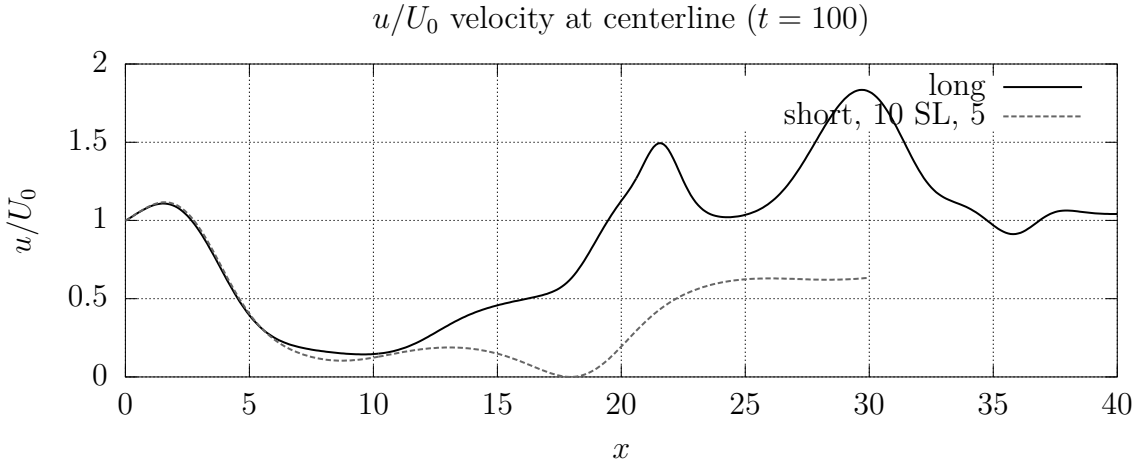

Figure 5.182: Comparison of long-domain u-velocity with short domain, 10 unit sponge-layer with 5-times viscosity increase u-velocity at the centerline.

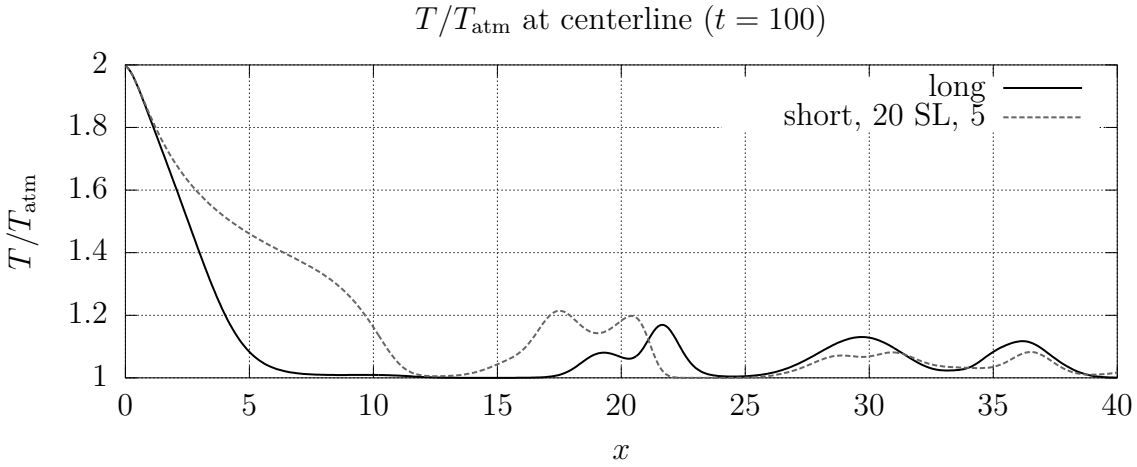

Figure 5.183: Comparison of long-domain temperatures with short domain, 20 unit sponge-layer with 5-times viscosity increase temperatures at the centerline.

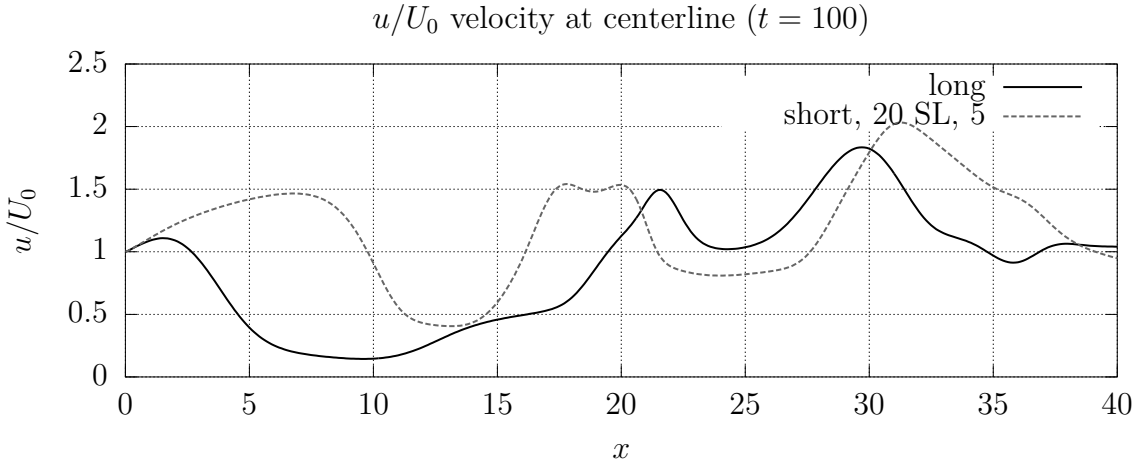

Figure 5.184: Comparison of long-domain u-velocity with short domain, 20 unit sponge-layer with 5-times viscosity increase u-velocity at the centerline.

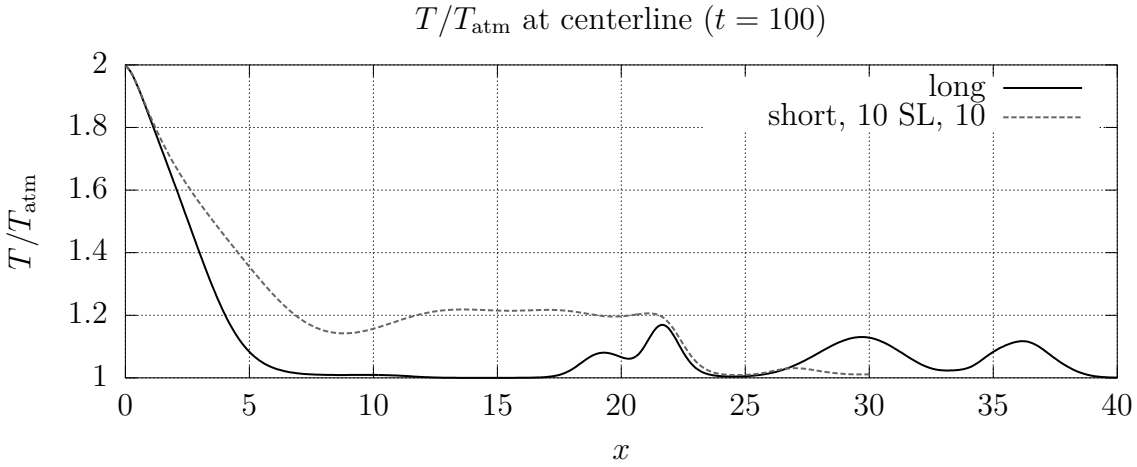

Figure 5.185: Comparison of long-domain temperatures with short domain, 10 unit sponge-layer with 10-times viscosity increase temperatures at the centerline.

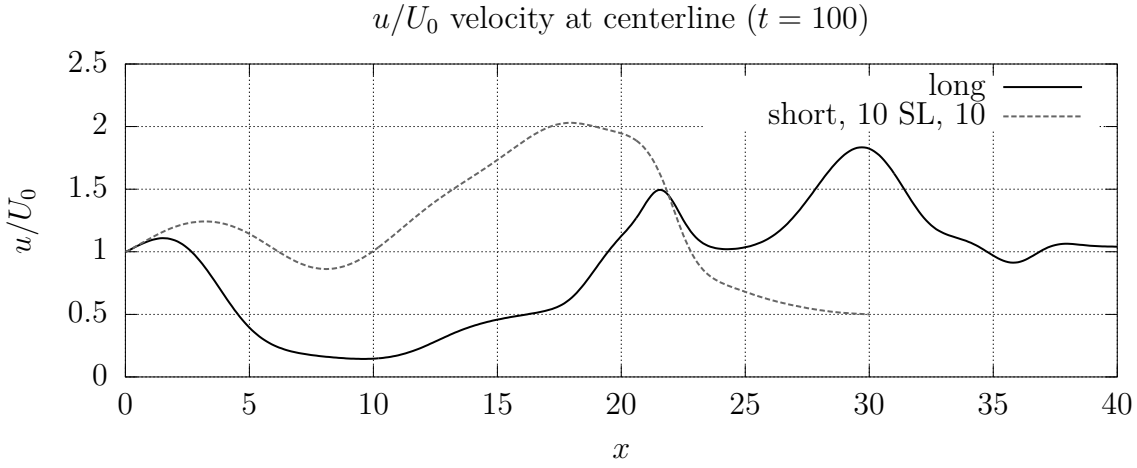

Figure 5.186: Comparison of long-domain u-velocity with short domain, 10 unit sponge-layer with 10-times viscosity increase u-velocity at the centerline.

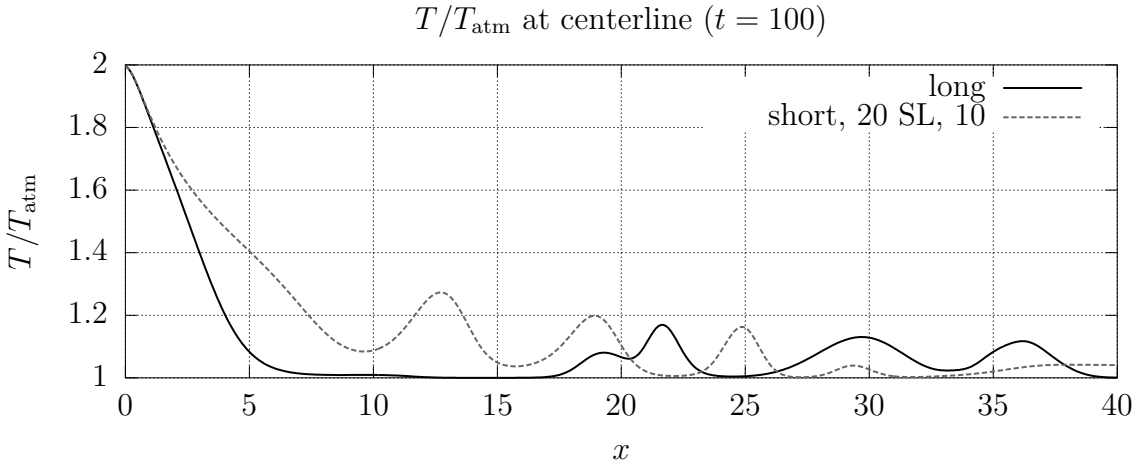

Figure 5.187: Comparison of long-domain temperatures with short domain, 20 unit sponge-layer with 10-times viscosity increase temperatures at the centerline.

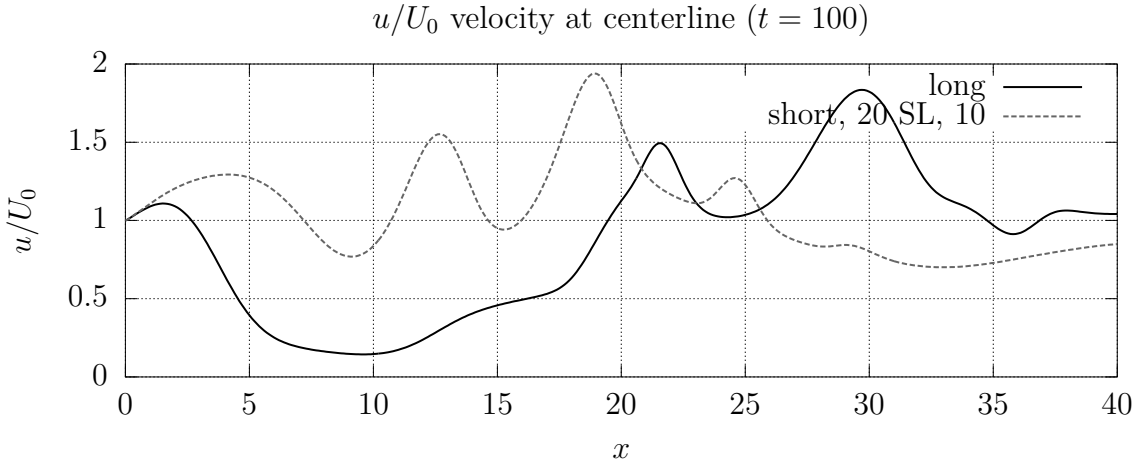

Figure 5.188: Comparison of long-domain u-velocity with short domain, 20 unit sponge-layer with 10-times viscosity increase u-velocity at the centerline.

5.15 Time-averaged centerlines

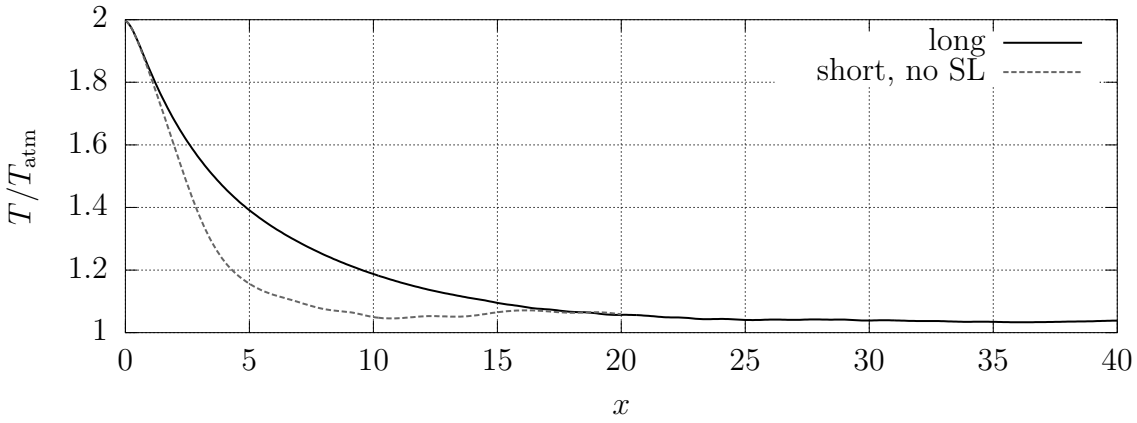

Figure 5.189: Comparison of long-domain time-averaged temperatures with short domain, no sponge-layer time-averaged temperatures at the centerline.

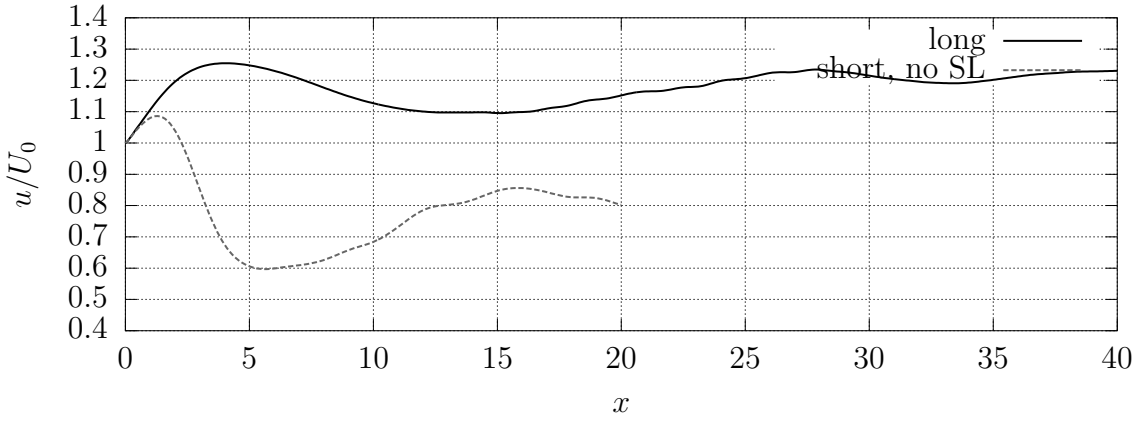

Figure 5.190: Comparison of long-domain time-averaged u-velocity with short domain, no sponge-layer time-averaged u-velocity at the centerline.

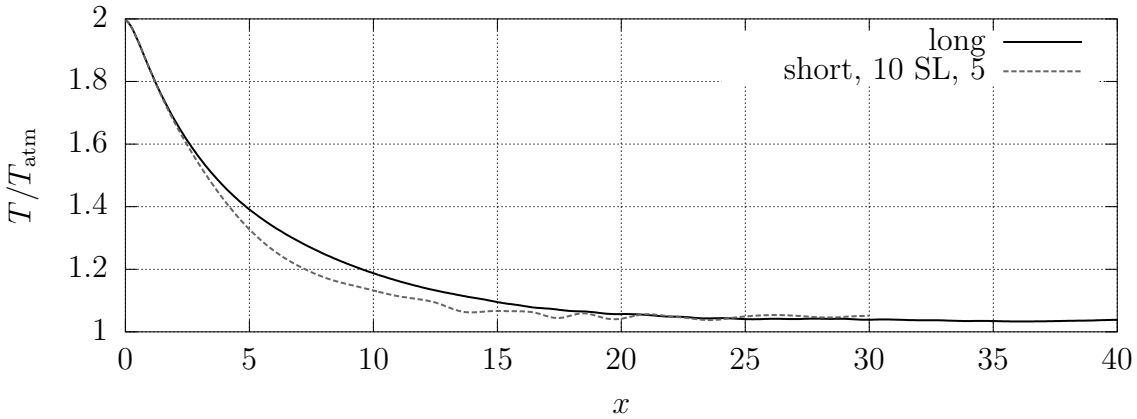

Figure 5.191: Comparison of long-domain time-averaged temperatures with short domain, 10 unit sponge-layer with 5-times viscosity increase time-averaged temperatures at the centerline.

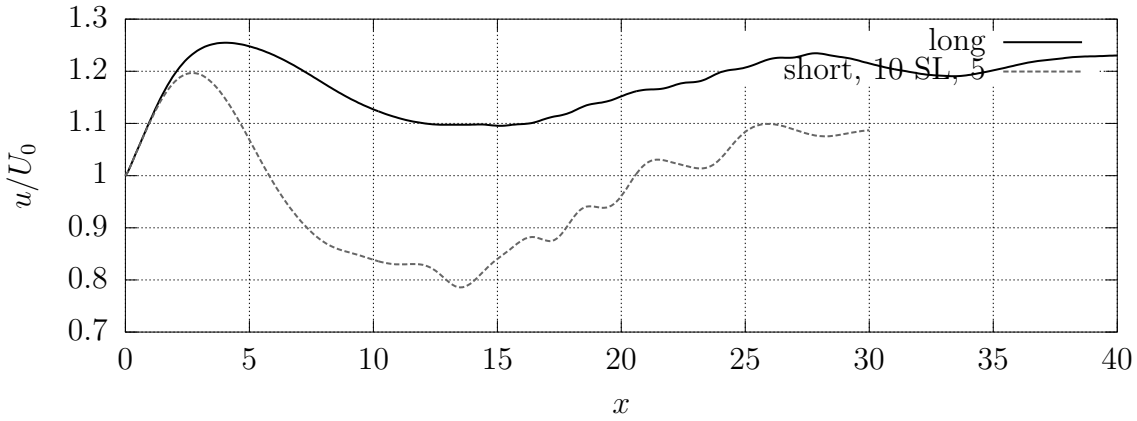

Figure 5.192: Comparison of long-domain time-averaged u-velocity with short domain, 10 unit sponge-layer with 5-times viscosity increase time-averaged u-velocity at the centerline.

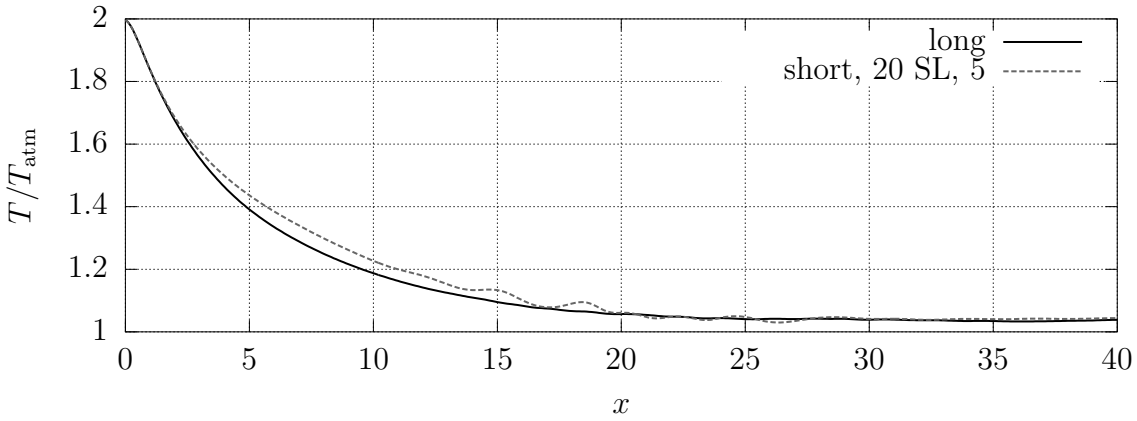

Figure 5.193: Comparison of long-domain time-averaged temperatures with short domain, 20 unit sponge-layer with 5-times viscosity increase time-averaged temperatures at the centerline.

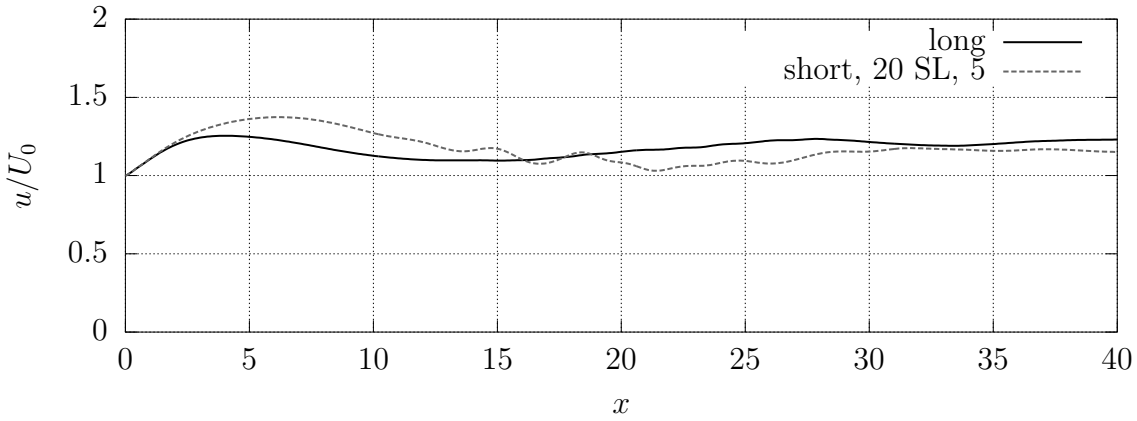

Figure 5.194: Comparison of long-domain time-averaged u-velocity with short domain, 20 unit sponge-layer with 5-times viscosity increase time-averaged u-velocity at the centerline.

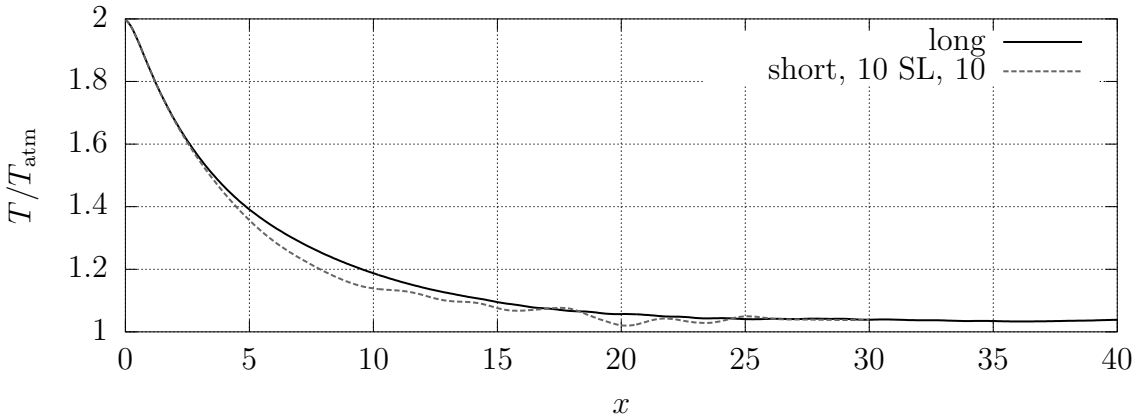

Figure 5.195: Comparison of long-domain time-averaged temperatures with short domain, 10 unit sponge-layer with 10-times viscosity increase time-averaged temperatures at the centerline.

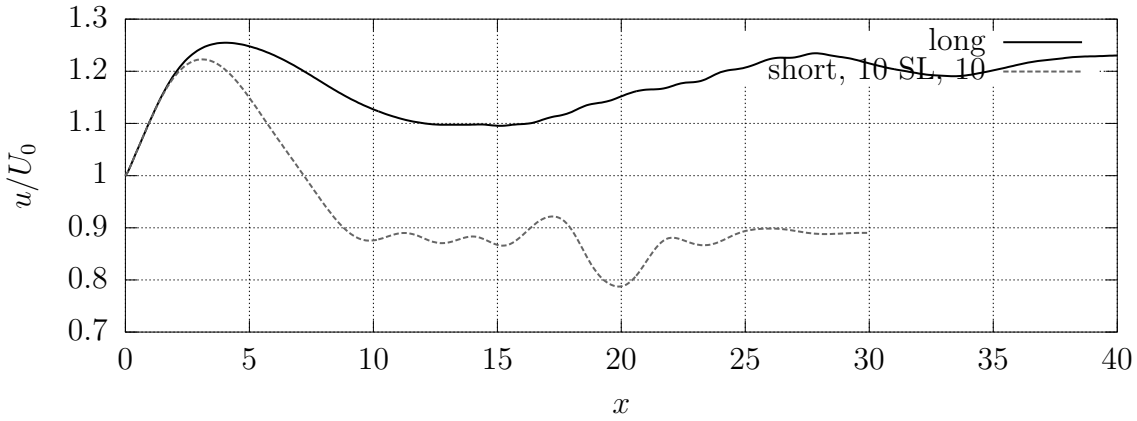

Figure 5.196: Comparison of long-domain time-averaged u-velocity with short domain, 10 unit sponge-layer with 10-times viscosity increase time-averaged u-velocity at the centerline.

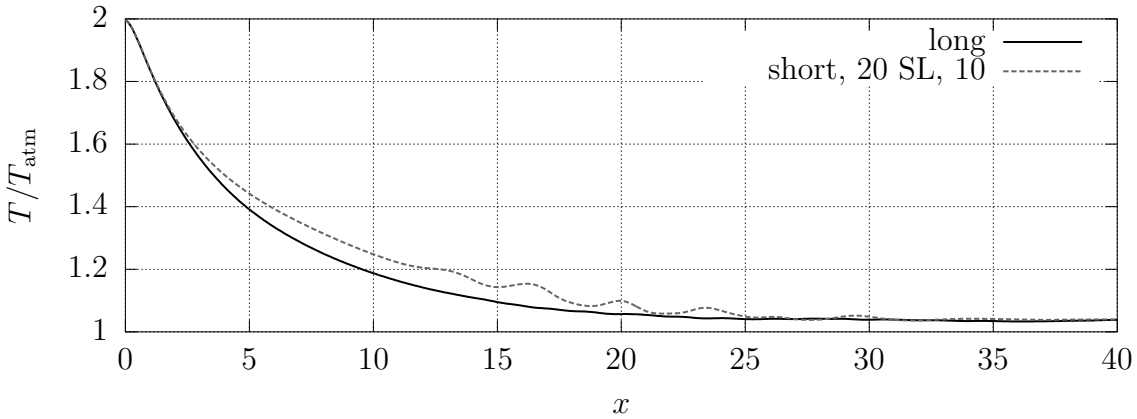

Figure 5.197: Comparison of long-domain time-averaged temperatures with short domain, 20 unit sponge-layer with 10-times viscosity increase time-averaged temperatures at the centerline.

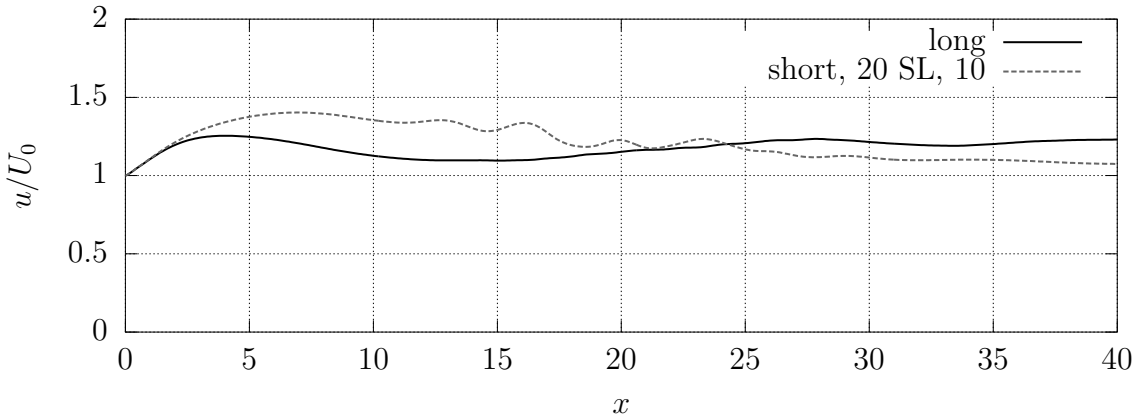

Figure 5.198: Comparison of long-domain time-averaged u-velocity with short domain, 20 unit sponge-layer with 10-times viscosity increase time-averaged u-velocity at the centerline.

5.16 Instantaneous outflow profiles

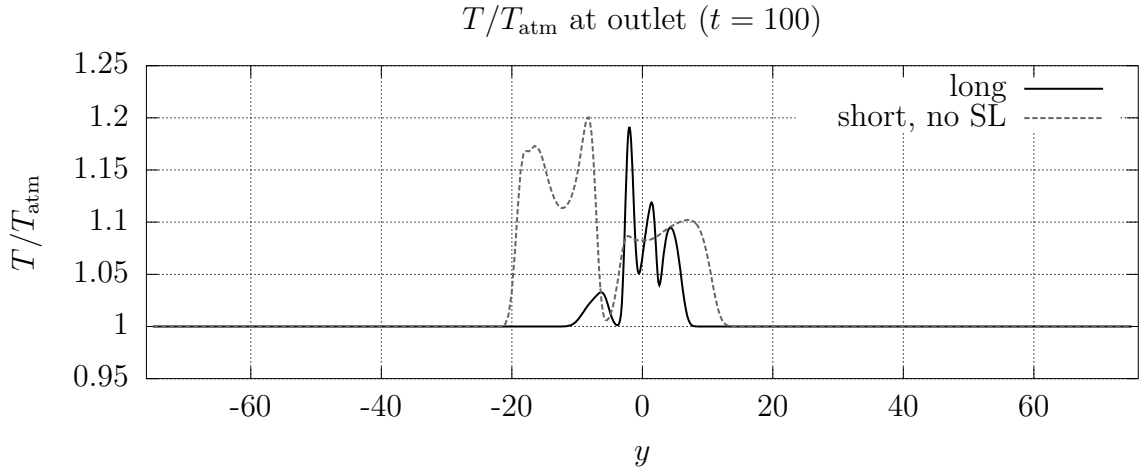

Figure 5.199: Temperature at the outlet for short domain, no sponge-layer case.

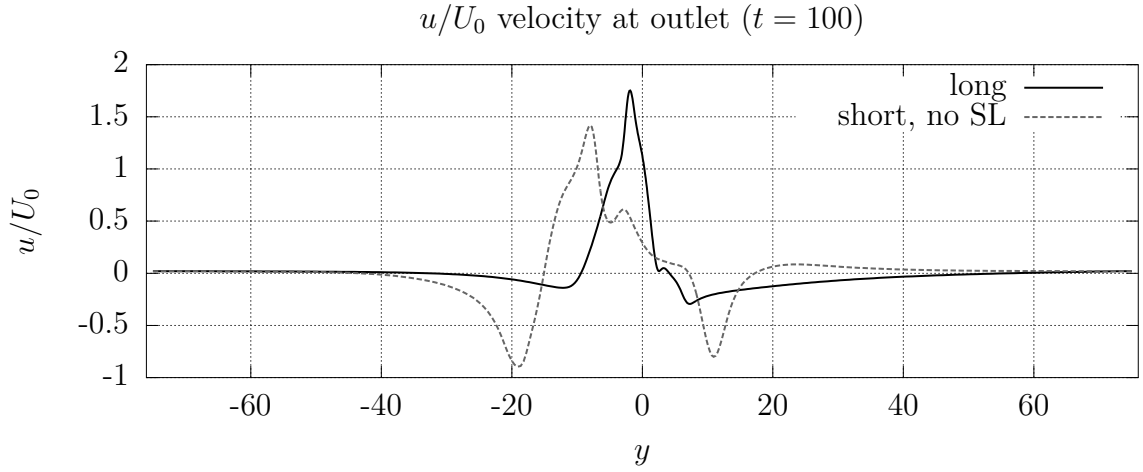

Figure 5.200: u-velocity at the outlet for short domain, no sponge-layer case.

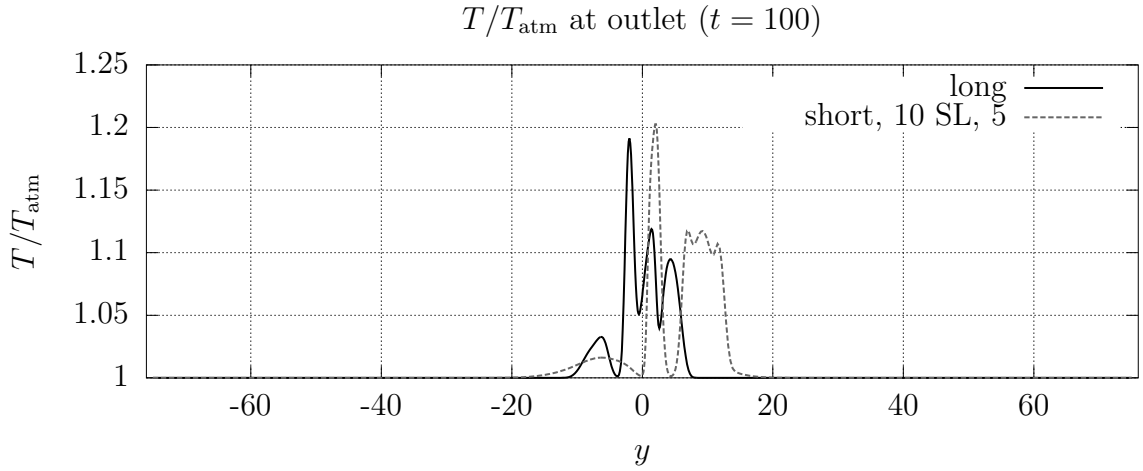

Figure 5.201: Temperature at the outlet for short domain, 10 unit sponge-layer with 5-times viscosity increase case.

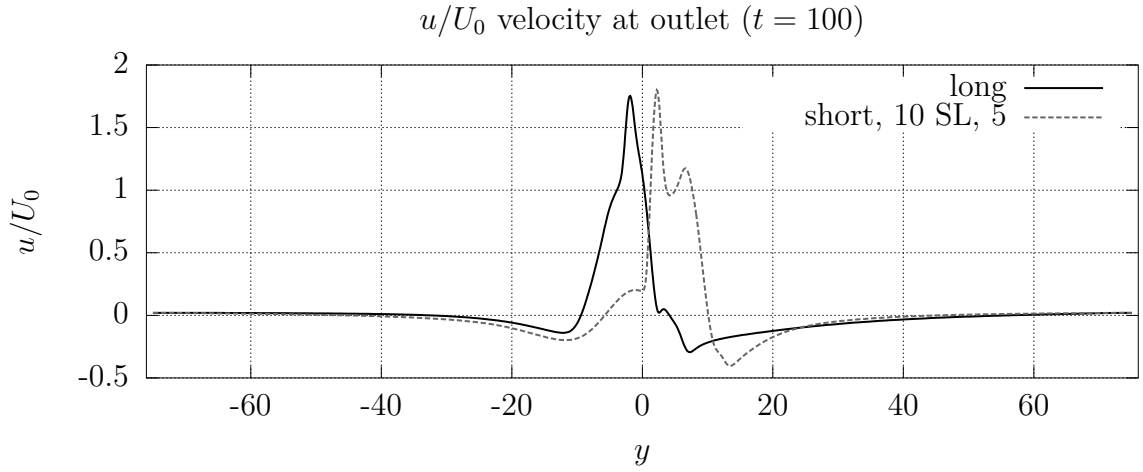

Figure 5.202: u-velocity at the outlet for short domain, 10 unit sponge-layer with 5-times viscosity increase case.

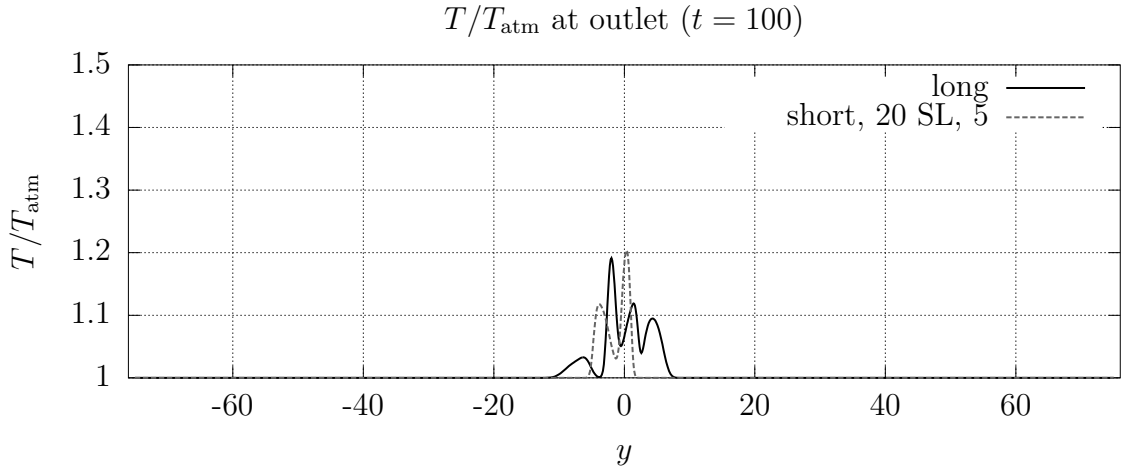

Figure 5.203: Temperature at the outlet for short domain, 20 unit sponge-layer with 5-times viscosity increase case.

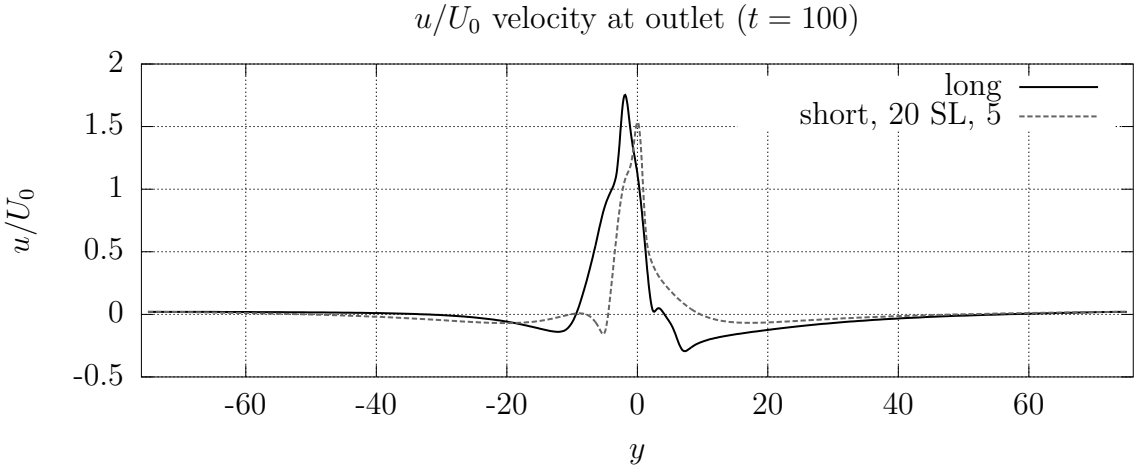

Figure 5.204: u-velocity at the outlet for short domain, 20 unit sponge-layer with 5-times viscosity increase case.

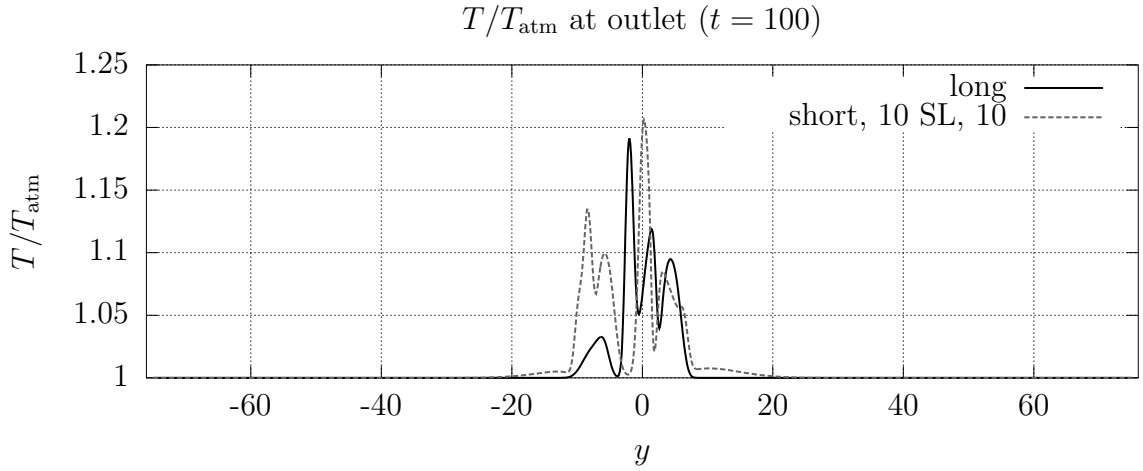

Figure 5.205: Temperature at the outlet for short domain, 10 unit sponge-layer with 10-times viscosity increase case.

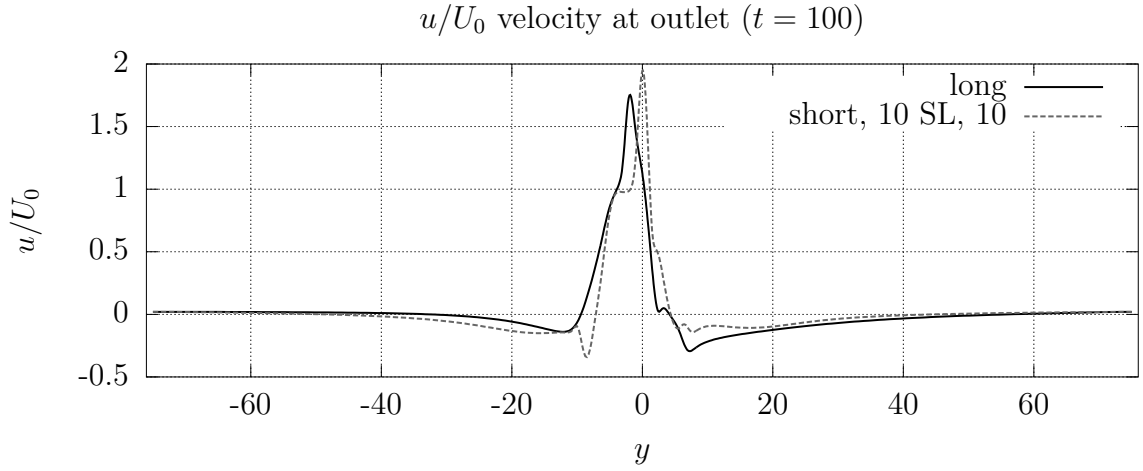

Figure 5.206: u-velocity at the outlet for short domain, 10 unit sponge-layer with 10-times viscosity increase case.

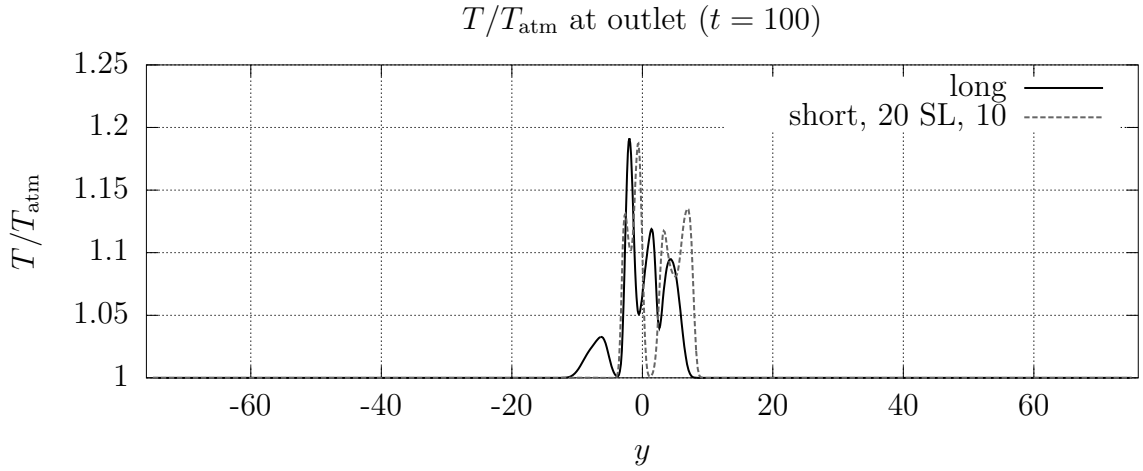

Figure 5.207: Temperature at the outlet for short domain, 20 unit sponge-layer with 10-times viscosity increase case.

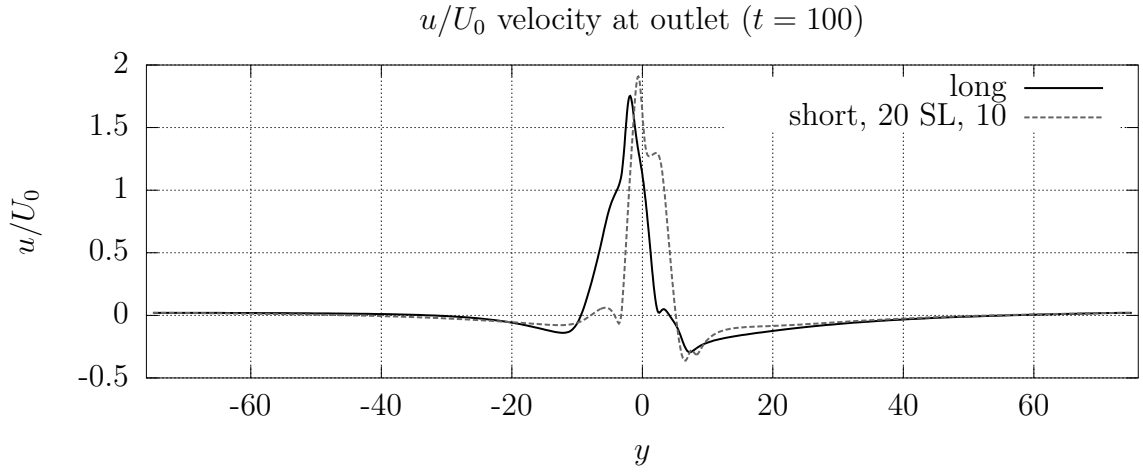

Figure 5.208: u-velocity at the outlet for short domain, 20 unit sponge-layer with 10-times viscosity increase case.

5.17 Time-averaged outflow profiles

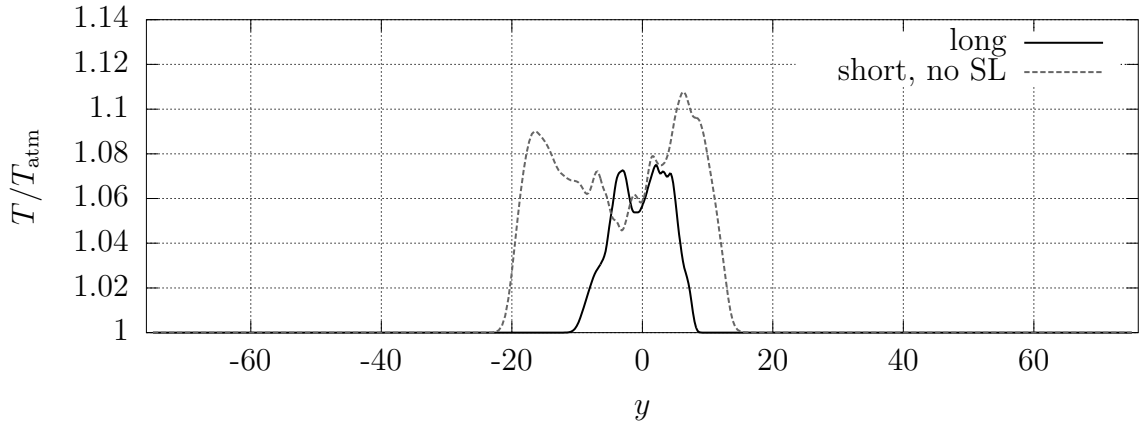

Figure 5.209: Time-averaged temperature at the outlet for short domain, no sponge-layer case.

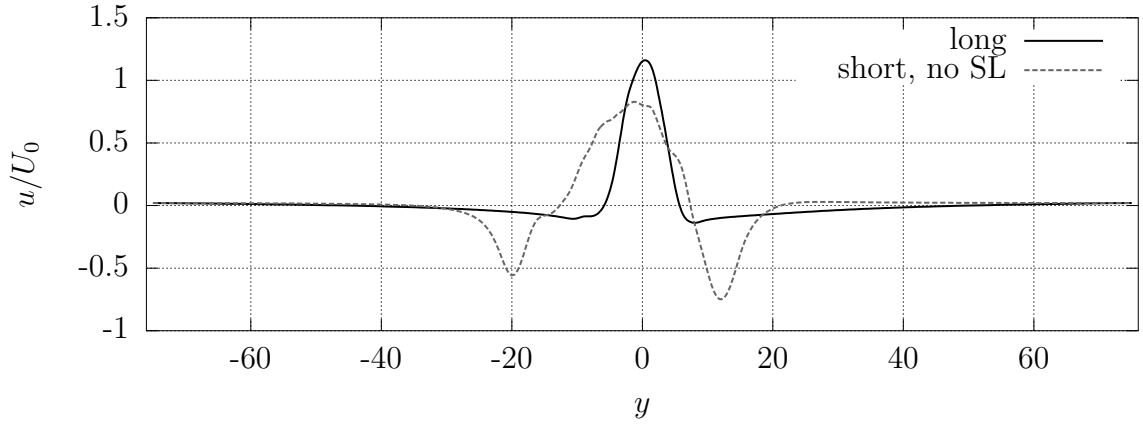

Figure 5.210: Time-averaged u-velocity at the outlet for short domain, no sponge-layer case.

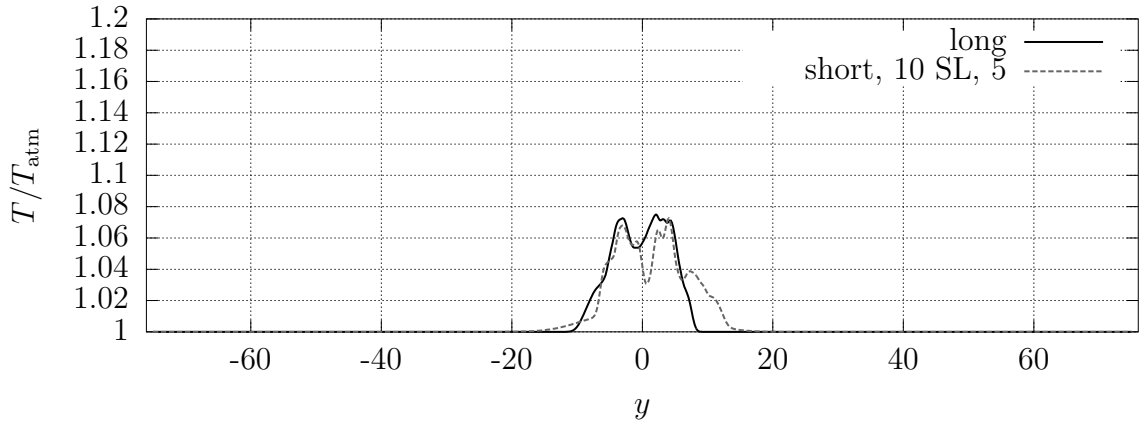

Figure 5.211: Time-averaged temperature at the outlet for short domain, 10 unit sponge-layer with 5-times viscosity increase case.

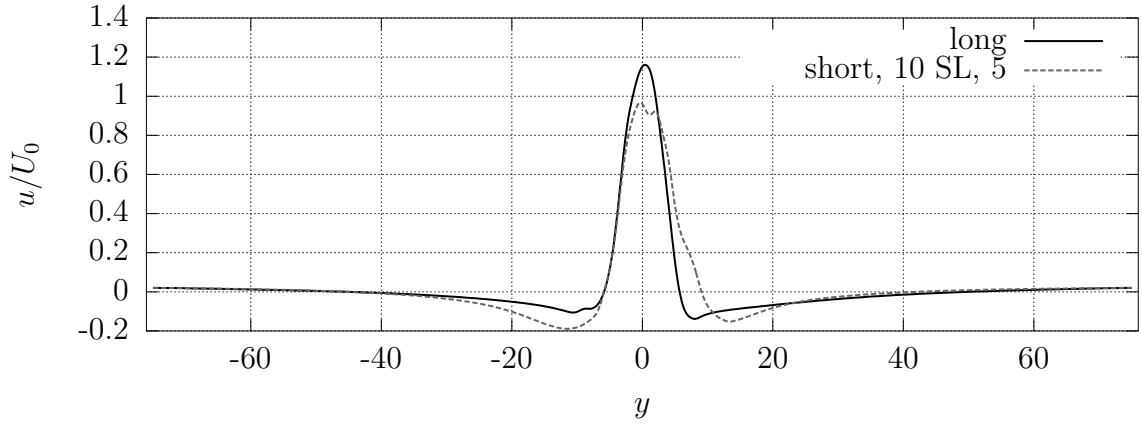

Figure 5.212: Time-averaged u-velocity at the outlet for short domain, 10 unit sponge-layer with 5-times viscosity increase case.

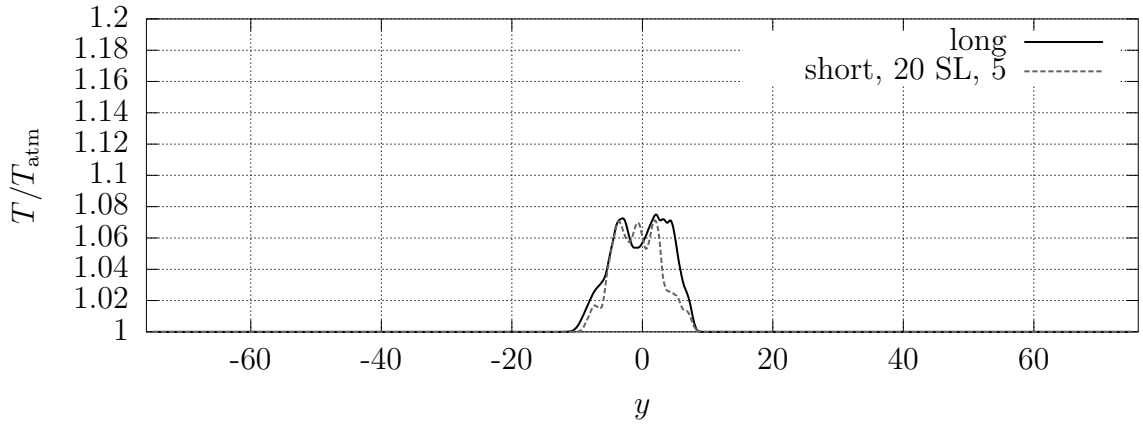

Figure 5.213: Time-averaged temperature at the outlet for short domain, 20 unit sponge-layer with 5-times viscosity increase case.

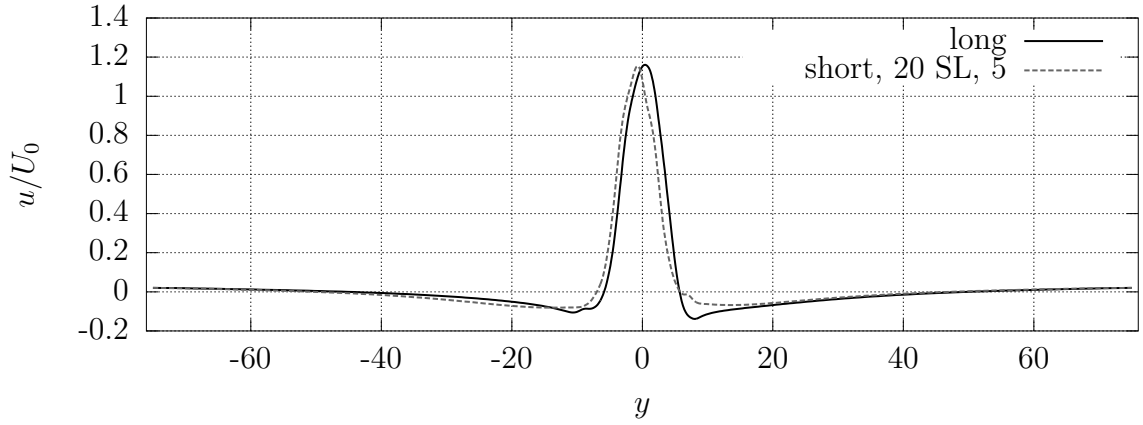

Figure 5.214: Time-averaged u-velocity at the outlet for short domain, 20 unit sponge-layer with 5-times viscosity increase case.

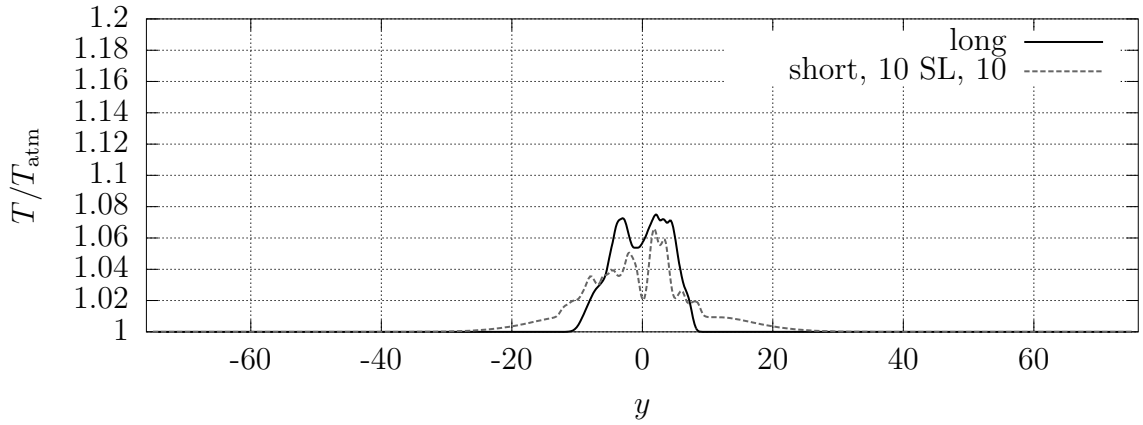

Figure 5.215: Time-averaged temperature at the outlet for short domain, 10 unit sponge-layer with 10-times viscosity increase case.

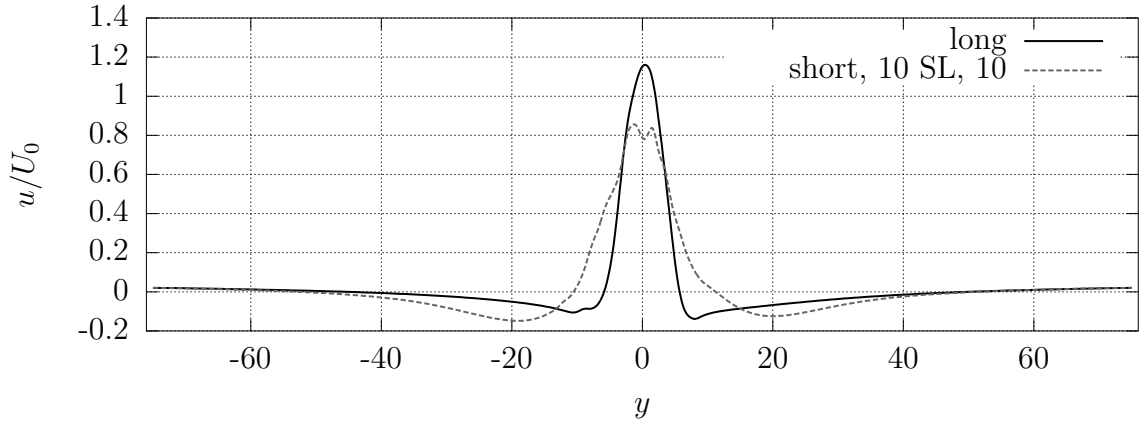

Figure 5.216: Time-averaged u-velocity at the outlet for short domain, 10 unit sponge-layer with 10-times viscosity increase case.

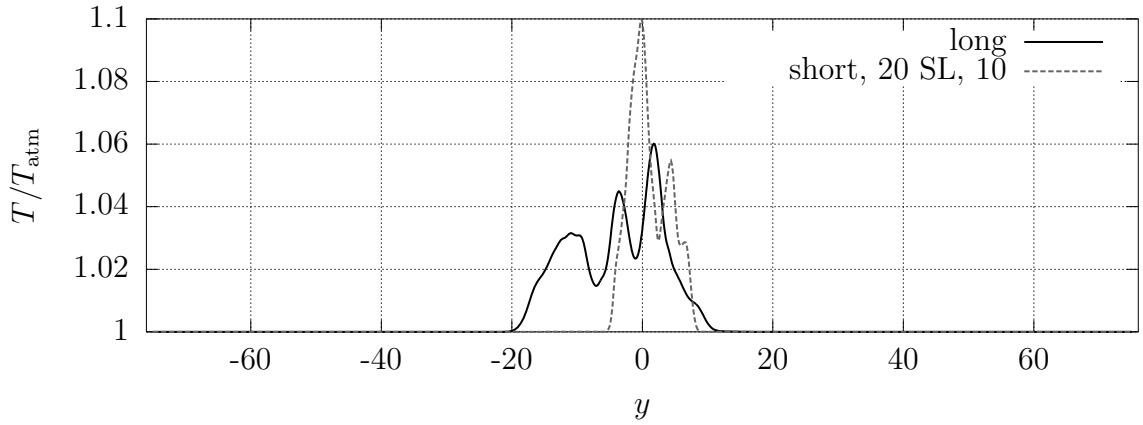

Figure 5.217: Time-averaged temperature at the outlet for short domain, 20 unit sponge-layer with 10-times viscosity increase case.

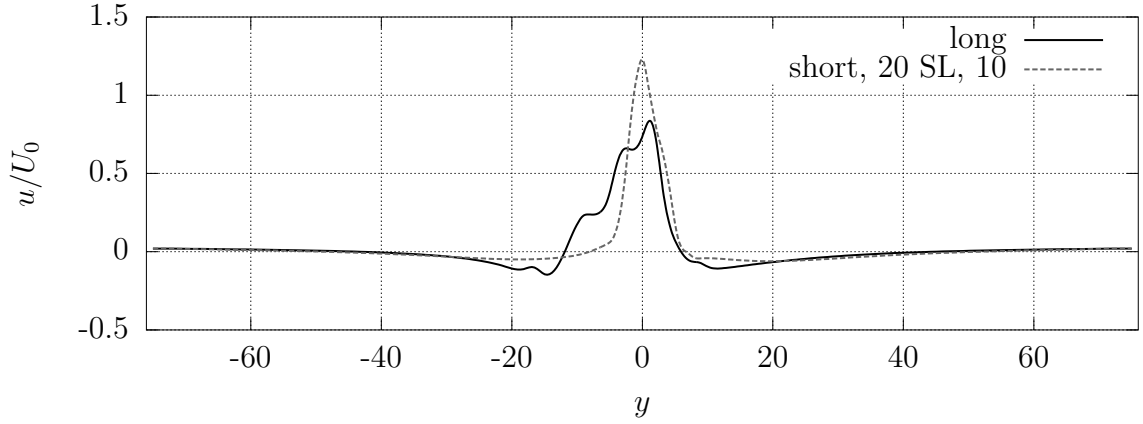

Figure 5.218: Time-averaged u-velocity at the outlet for short domain, 20 unit sponge-layer with 10-times viscosity increase case.

5.18 Probes

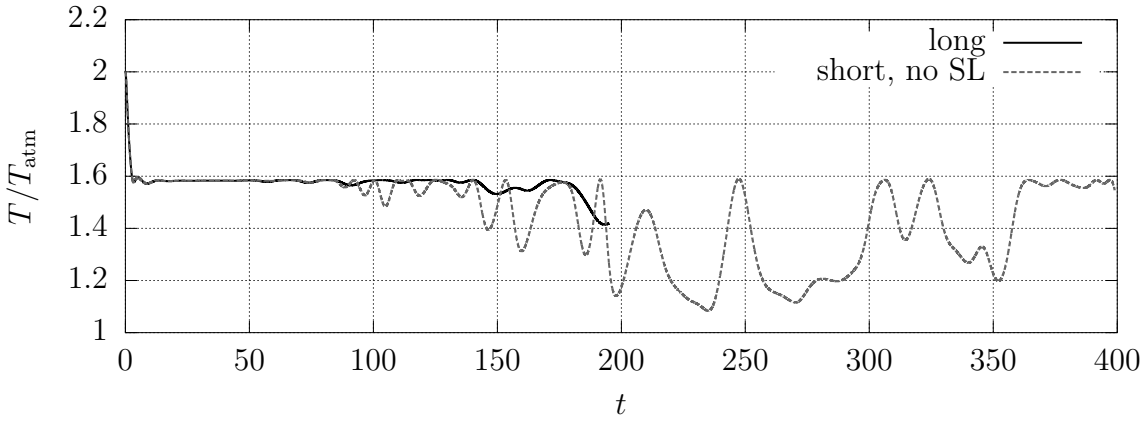

Figure 5.219: Centerline temperature probe one jet width from the inlet for short domain, no sponge-layer case.

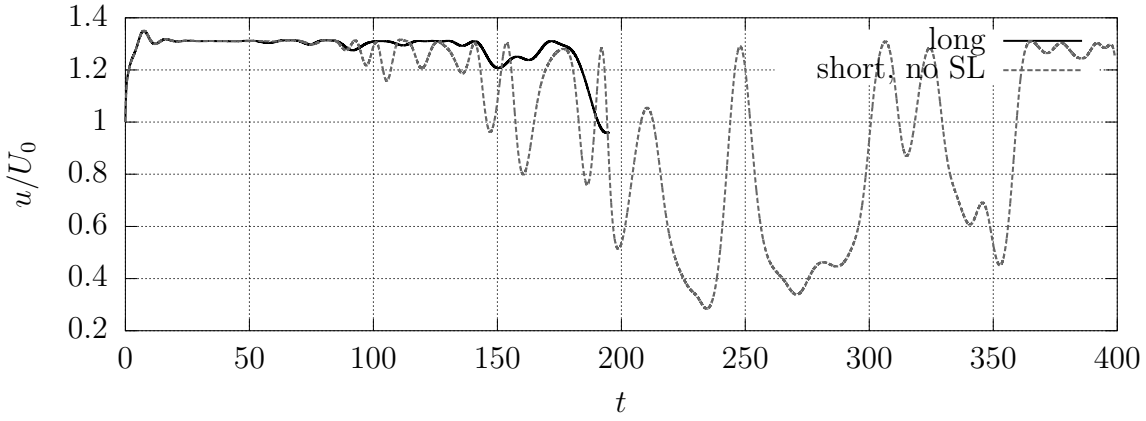

Figure 5.220: Centerline u-velocity probe one jet width from the inlet for short domain, no sponge-layer case.

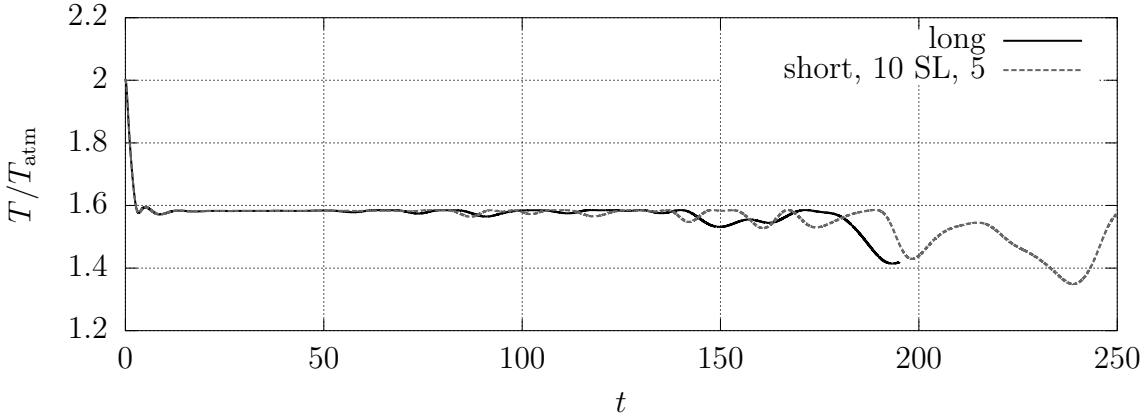

Figure 5.221: Centerline temperature probe one jet width from the inlet for short domain, 10 unit sponge-layer with 5-times viscosity increase case.

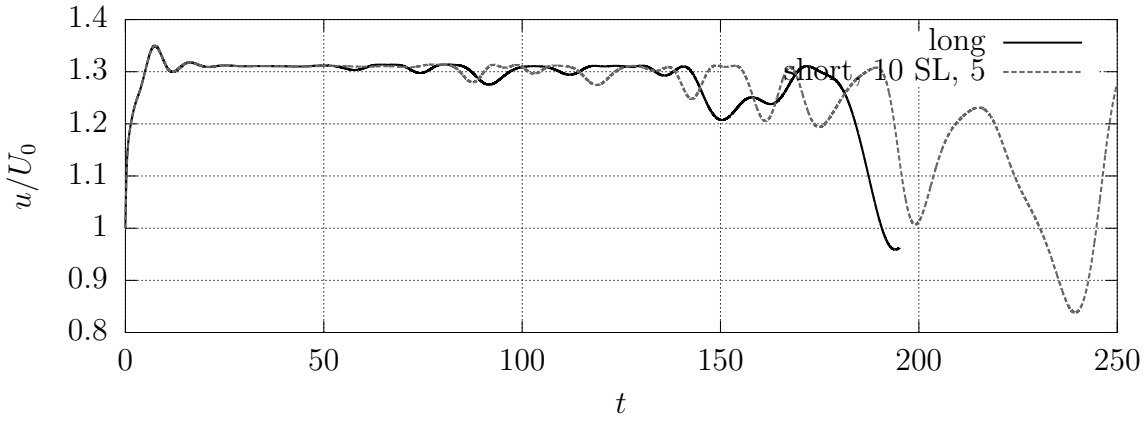

Figure 5.222: Centerline u-velocity probe one jet width from the inlet for short domain, 10 unit sponge-layer with 5-times viscosity increase case.

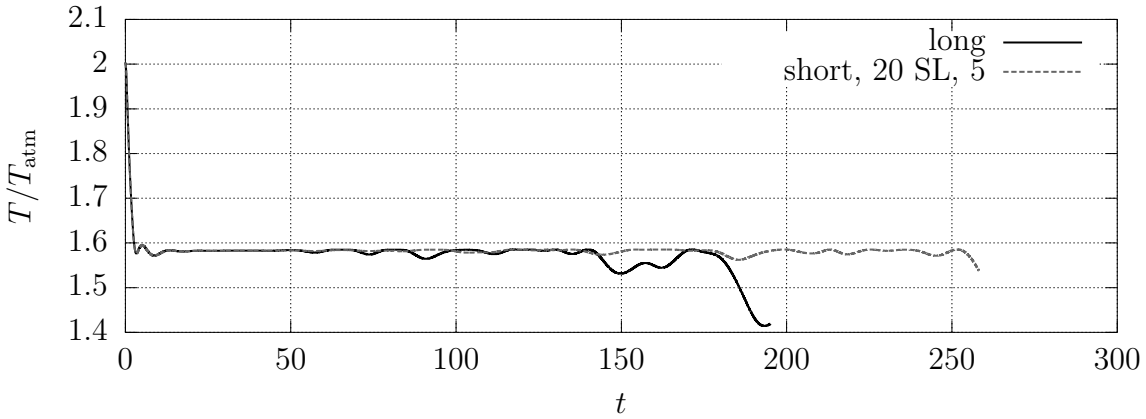

Figure 5.223: Centerline temperature probe one jet width from the inlet for short domain, 20 unit sponge-layer with 5-times viscosity increase case.

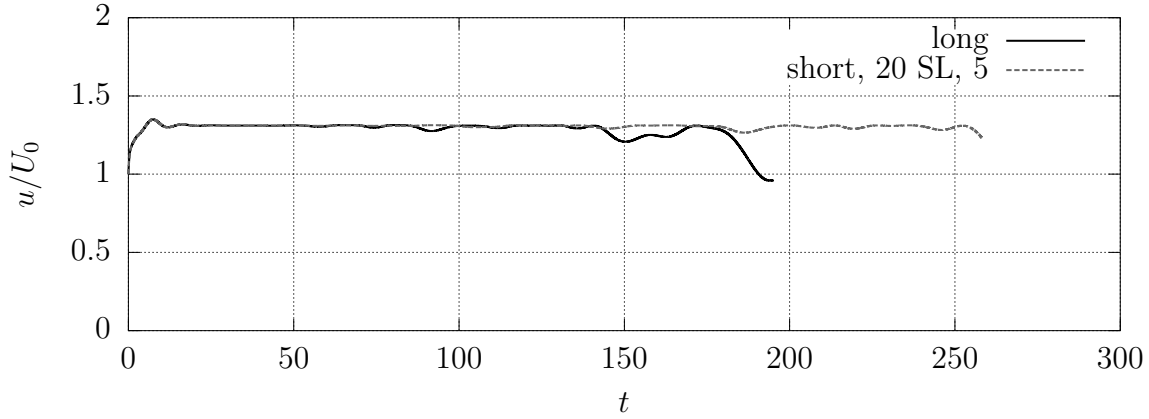

Figure 5.224: Centerline u-velocity probe one jet width from the inlet for short domain, 20 unit sponge-layer with 5-times viscosity increase case.

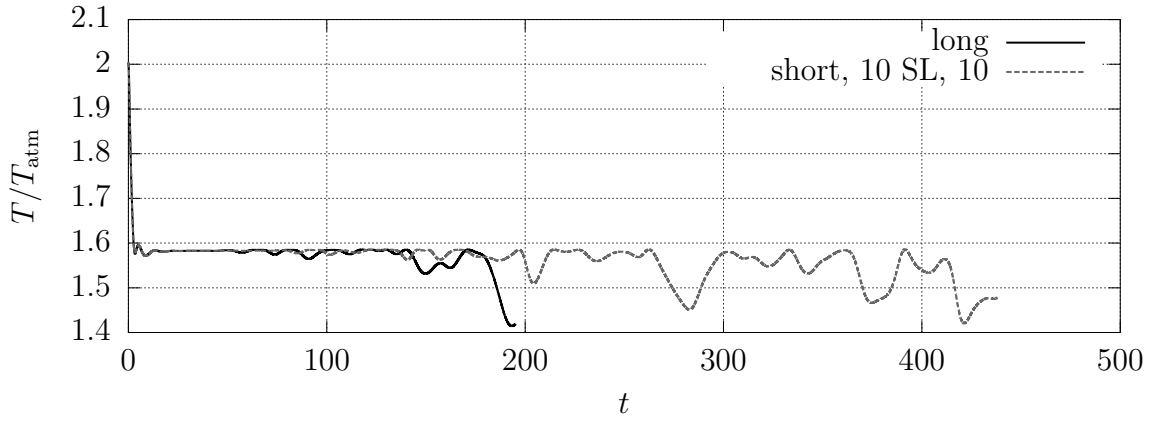

Figure 5.225: Centerline temperature probe one jet width from the inlet for short domain, 10 unit sponge-layer with 10-times viscosity increase case.

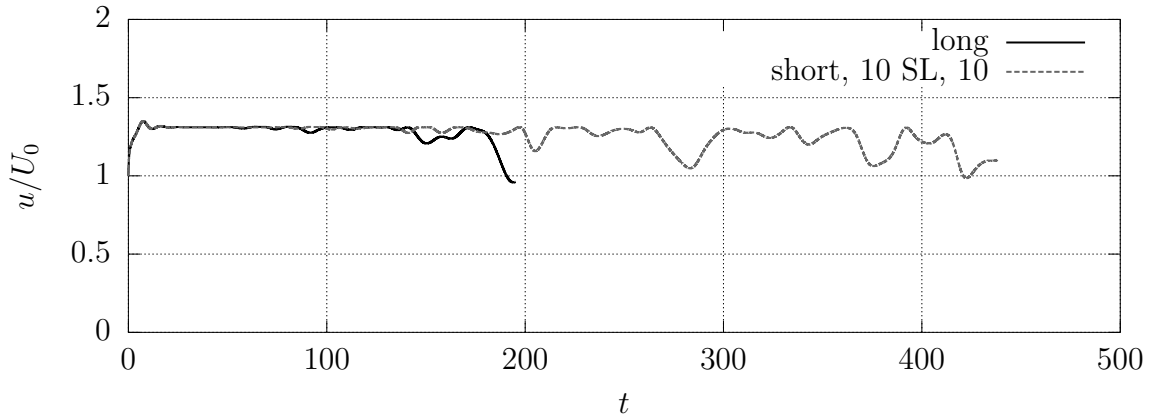

Figure 5.226: Centerline u-velocity probe one jet width from the inlet for short domain, 10 unit sponge-layer with 10-times viscosity increase case.

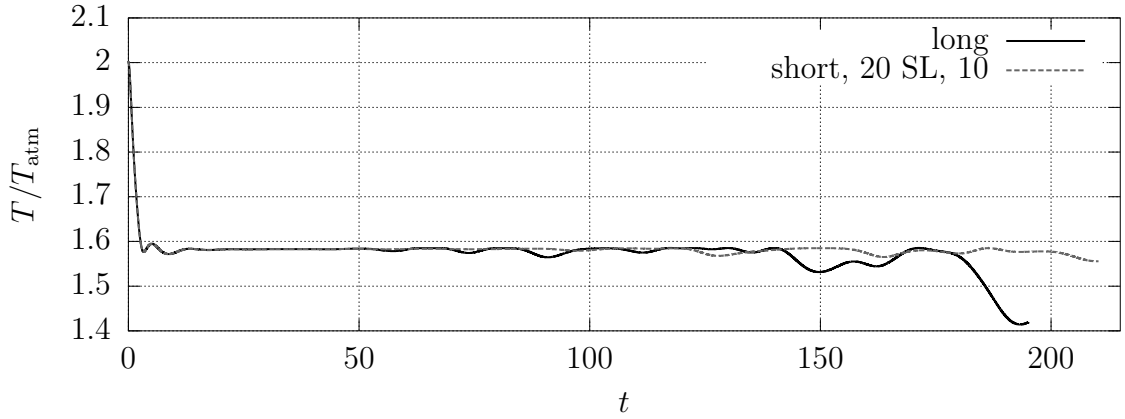

Figure 5.227: Centerline temperature probe one jet width from the inlet for short domain, 20 unit sponge-layer with 10-times viscosity increase case.

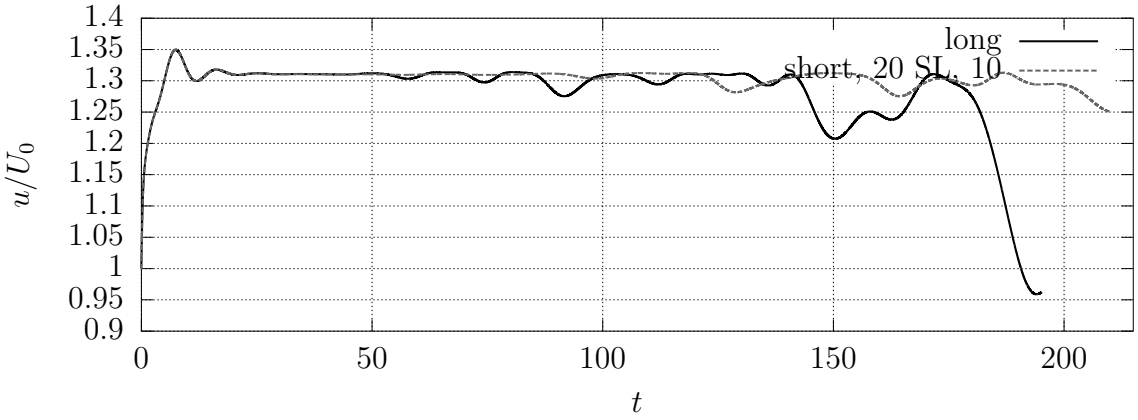

Figure 5.228: Centerline u-velocity probe one jet width from the inlet for short domain, 20 unit sponge-layer with 10-times viscosity increase case.

Appendix: $T/T_{\mathbf{atm}} = 4$ plots

6.19 Instantaneous fields

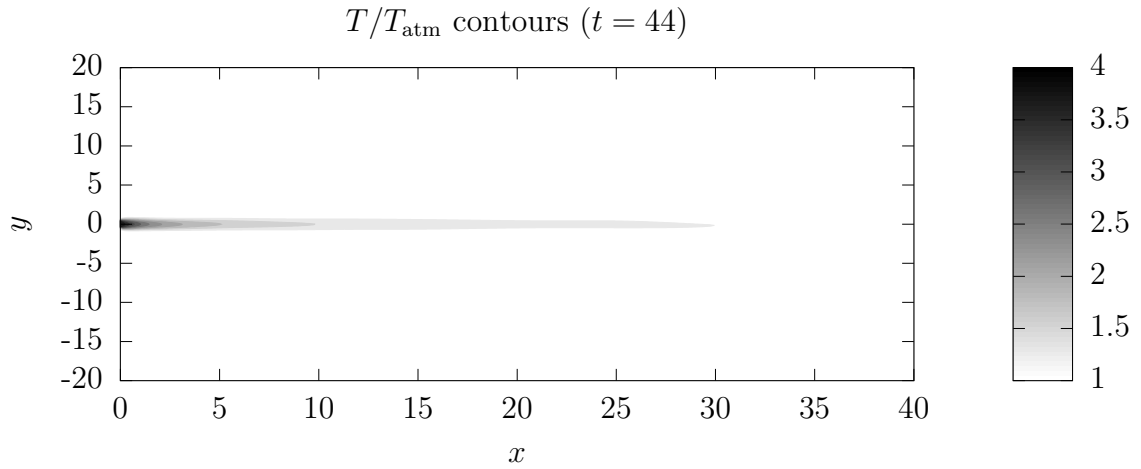

Figure 6.229: Temperature contours for the long domain, no sponge-layer case.

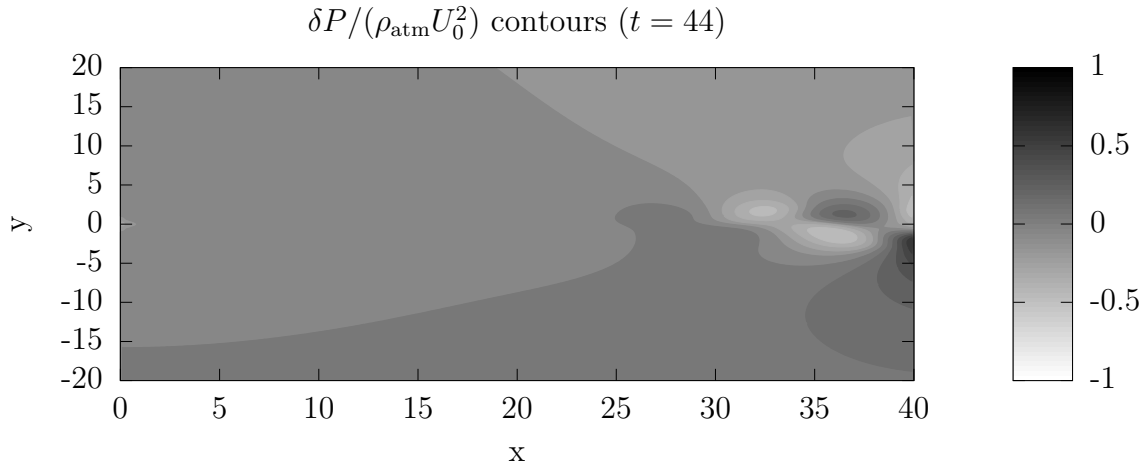

Figure 6.230: Pressure contours for the long domain, no sponge-layer case.

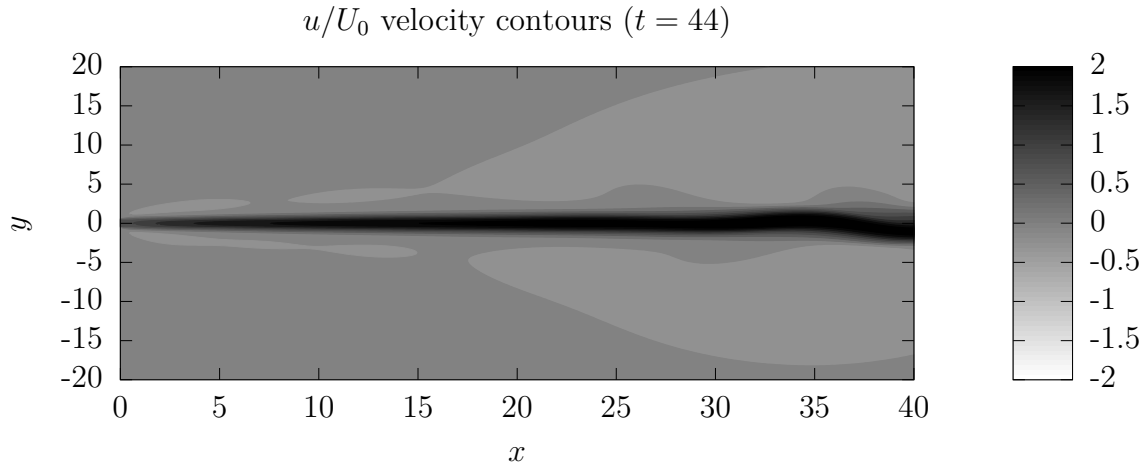

Figure 6.231: u-velocity contours for the long domain, no sponge-layer case.

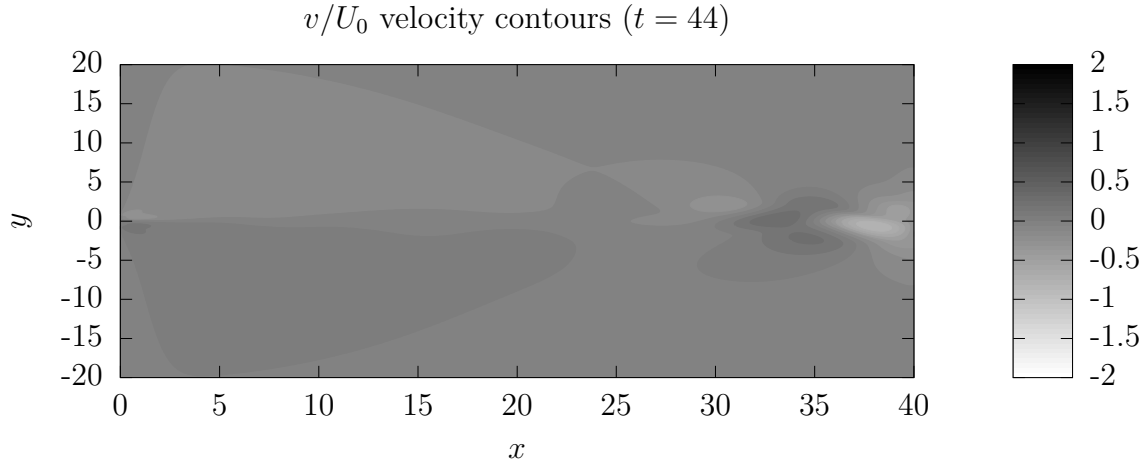

Figure 6.232: v-velocity contours for the long domain, no sponge-layer case.

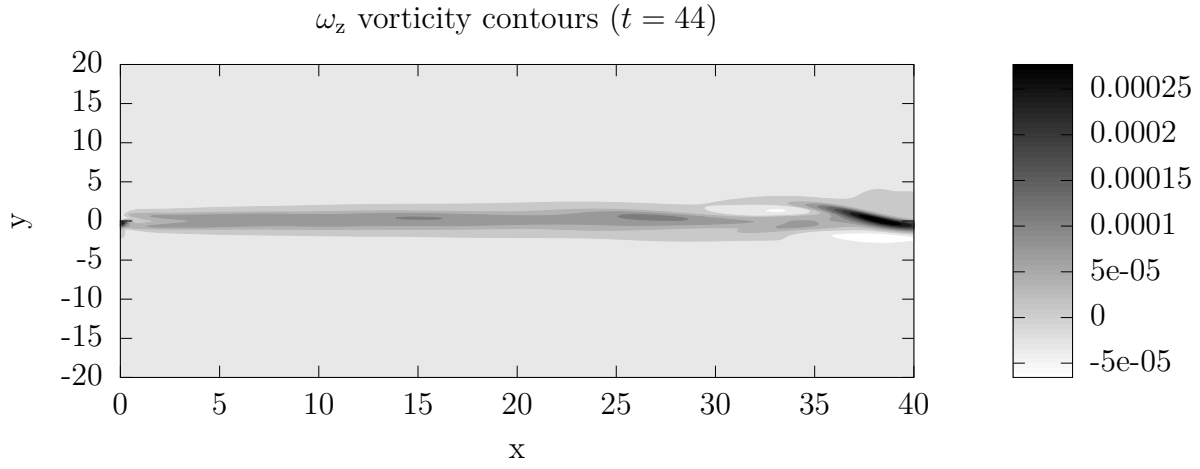

Figure 6.233: Vorticity contours for the long domain, no sponge-layer case.

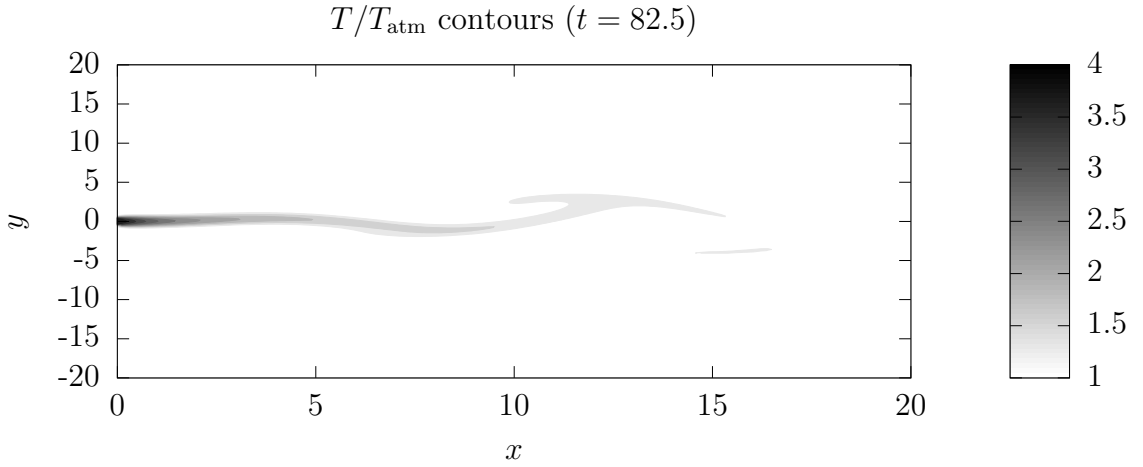

Figure 6.234: Temperature contours for the short domain, no sponge-layer case.

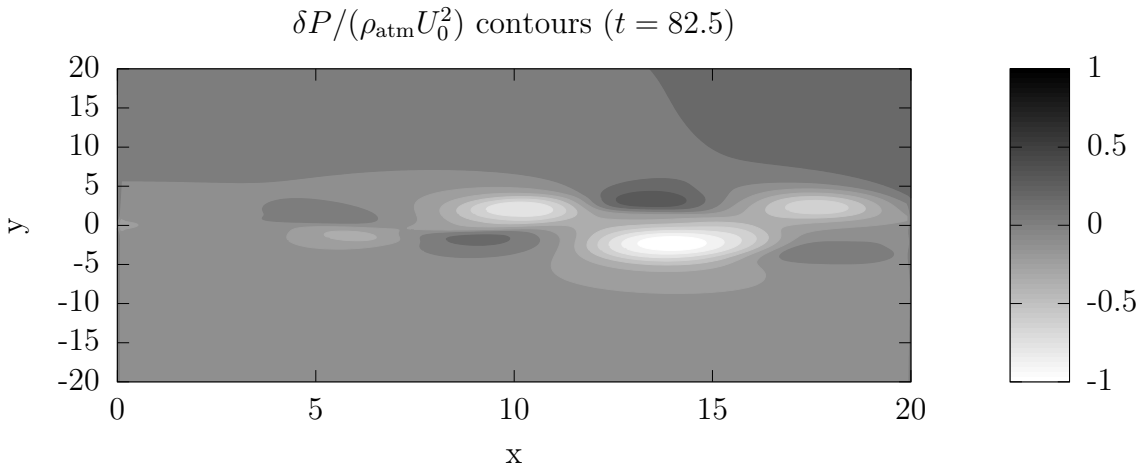

Figure 6.235: Pressure contours for the short domain, no sponge-layer case.

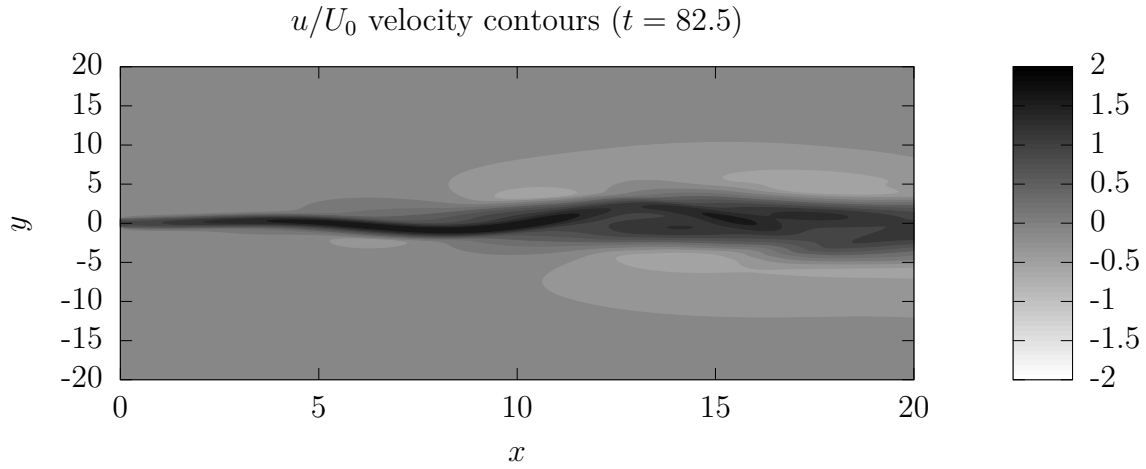

Figure 6.236: u-velocity contours for the short domain, no sponge-layer case.

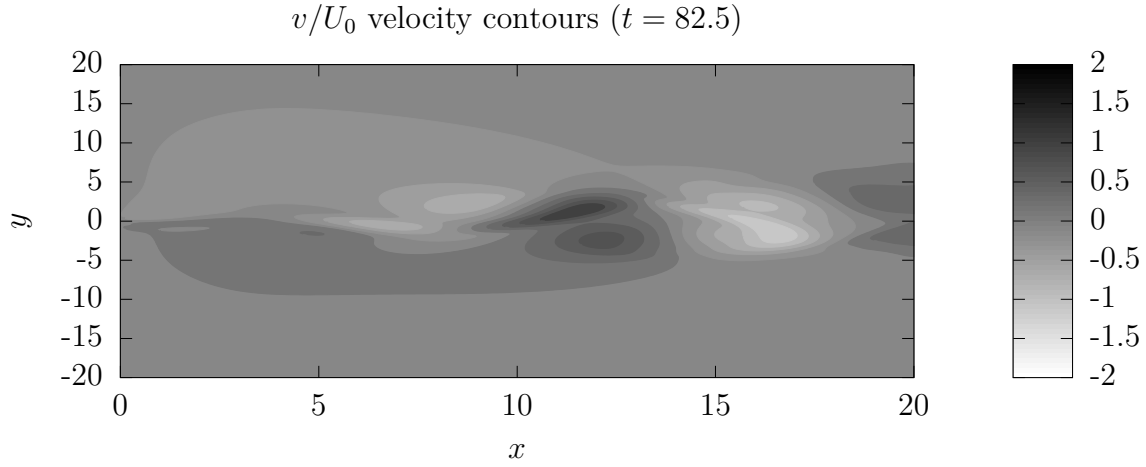

Figure 6.237: v-velocity contours for the short domain, no sponge-layer case.

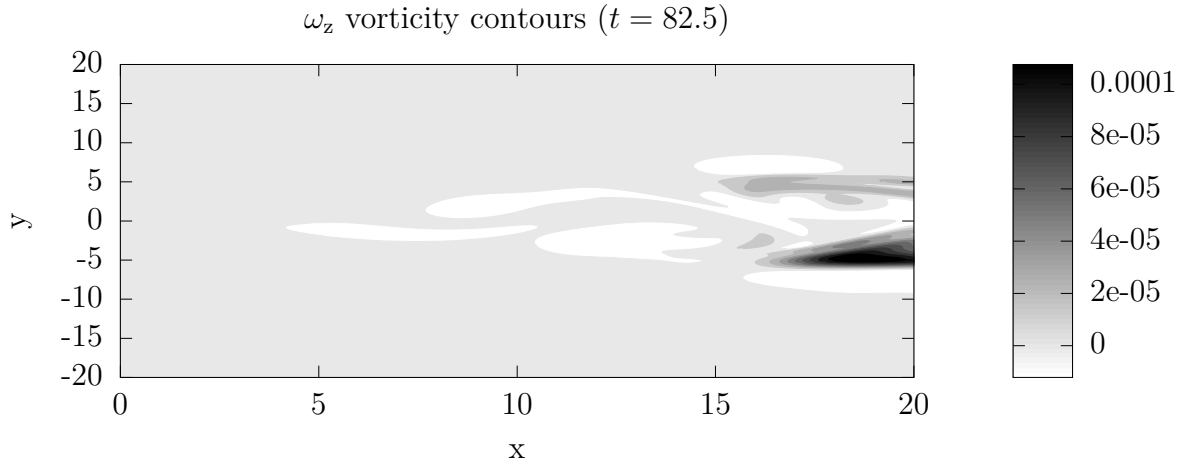

Figure 6.238: Vorticity contours for the short domain, no sponge-layer case.

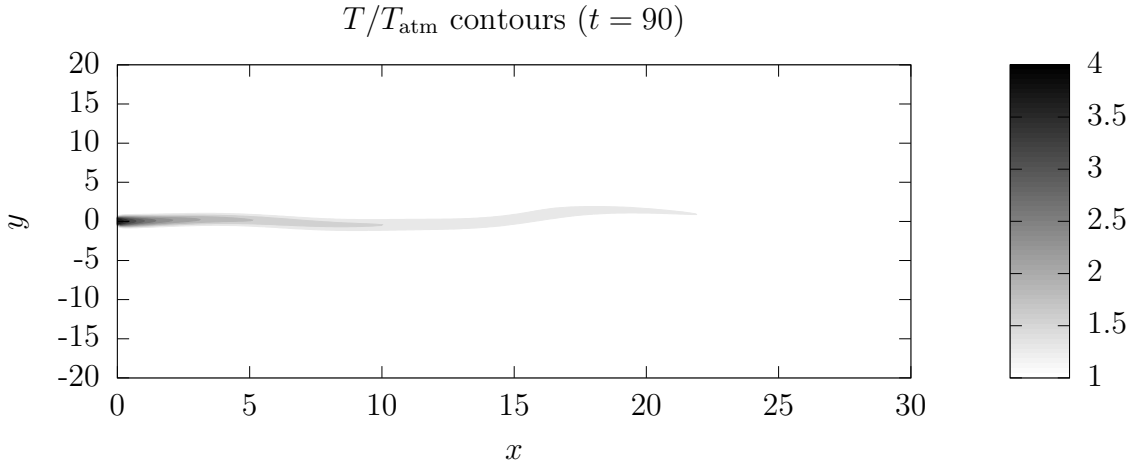

Figure 6.239: Temperature contours for the short domain, 10 unit sponge-layer with 5-times viscosity increase case.

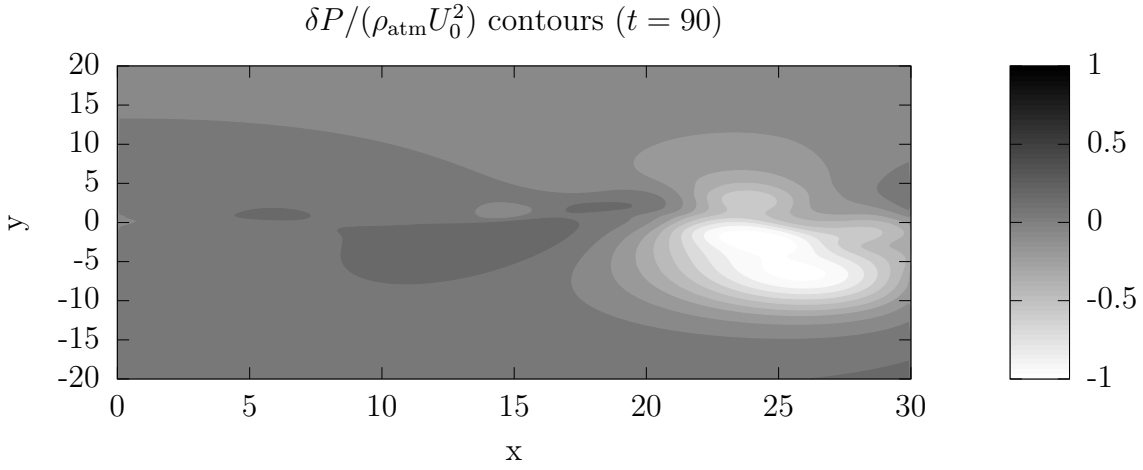

Figure 6.240: Pressure contours for the short domain, 10 unit sponge-layer with 5-times viscosity increase case.

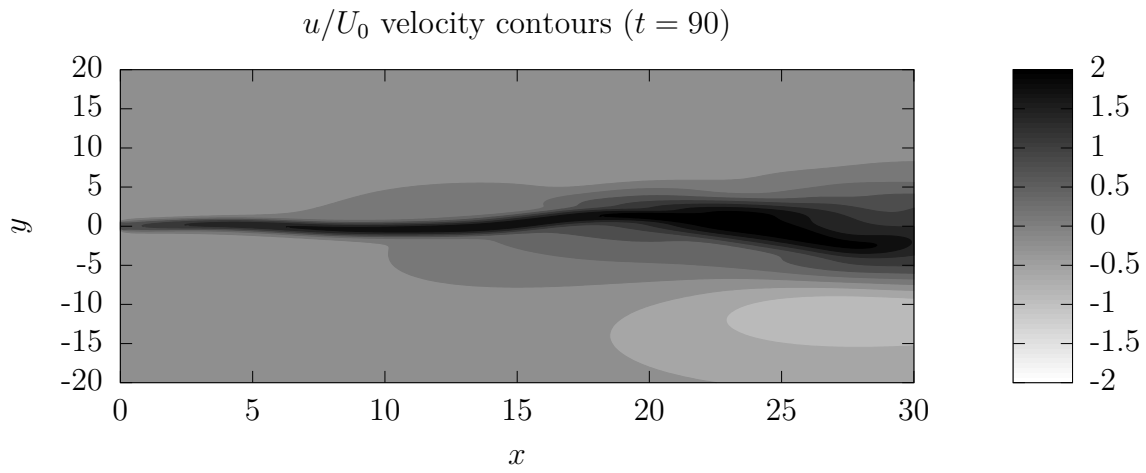

Figure 6.241: u-velocity contours for the short domain, 10 unit sponge-layer with 5-times viscosity increase case.

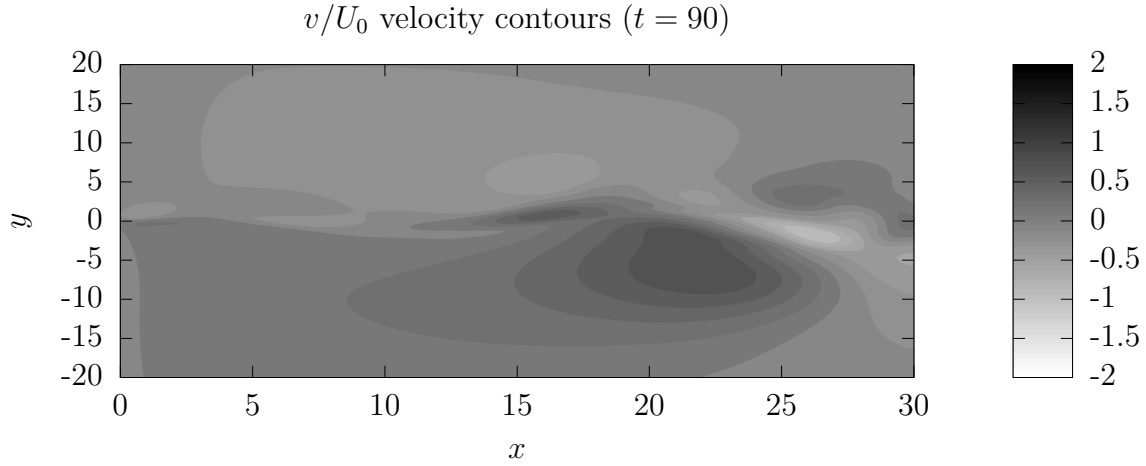

Figure 6.242: v-velocity contours for the short domain, 10 unit sponge-layer with 5-times viscosity increase case.

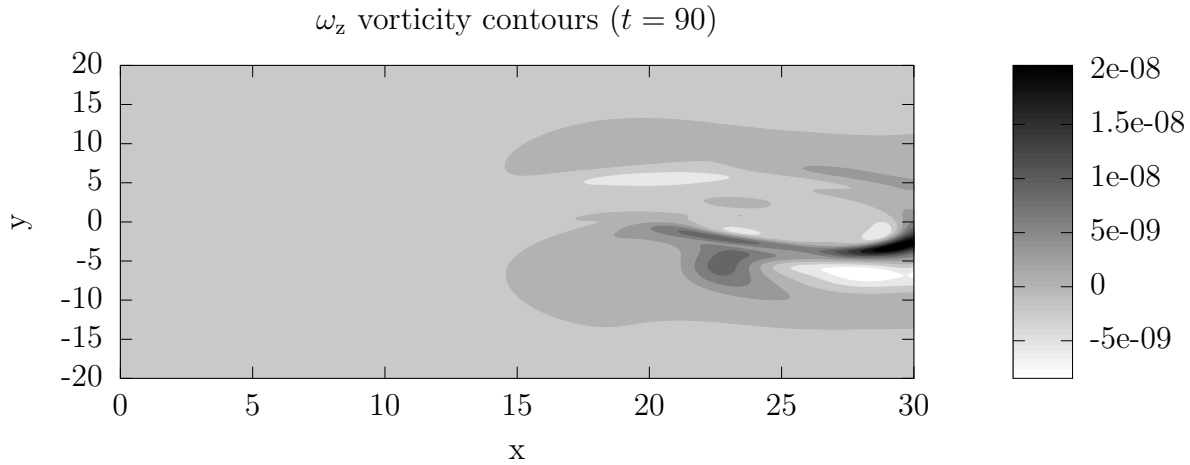

Figure 6.243: Vorticity contours for the short domain, 10 unit sponge-layer with 5-times viscosity increase case.

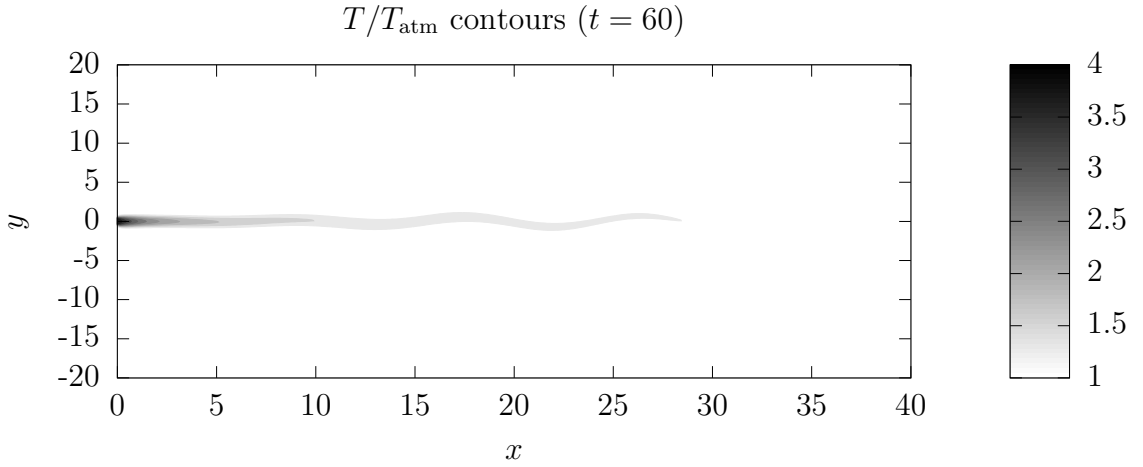

Figure 6.244: Temperature contours for the short domain, 20 unit sponge-layer with 5-times viscosity increase case.

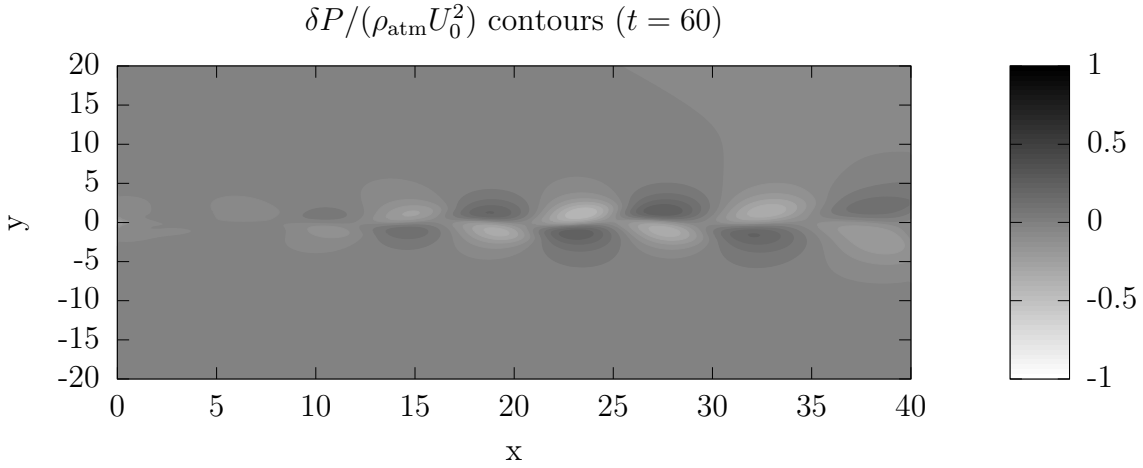

Figure 6.245: Pressure contours for the short domain, 20 unit sponge-layer with 5-times viscosity increase case.

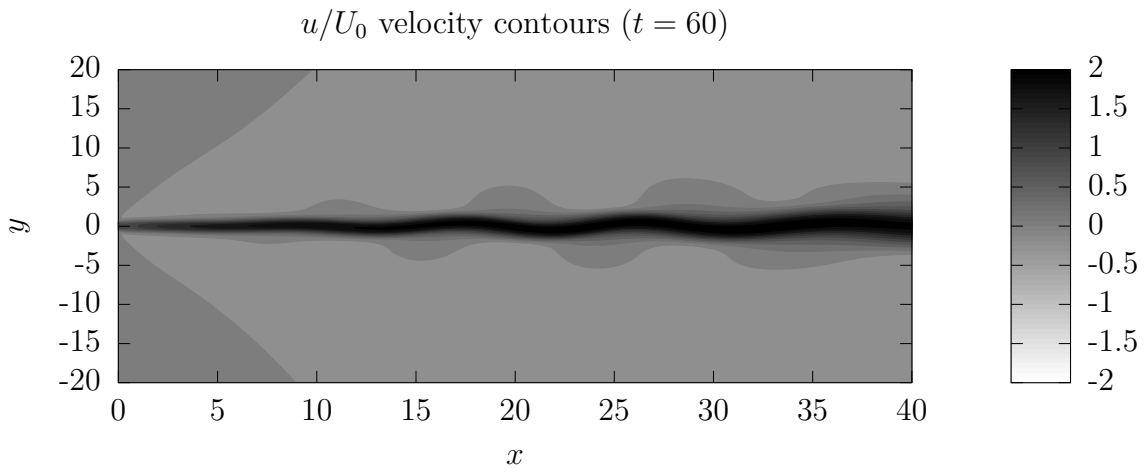

Figure 6.246: u-velocity contours for the short domain, 20 unit sponge-layer with 5-times viscosity increase case.

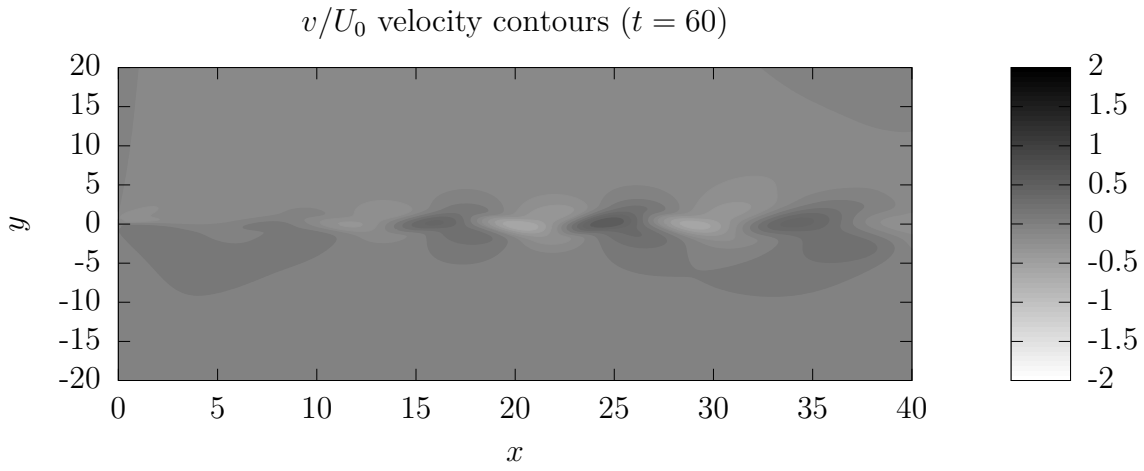

Figure 6.247: v-velocity contours for the short domain, 20 unit sponge-layer with 5-times viscosity increase case.

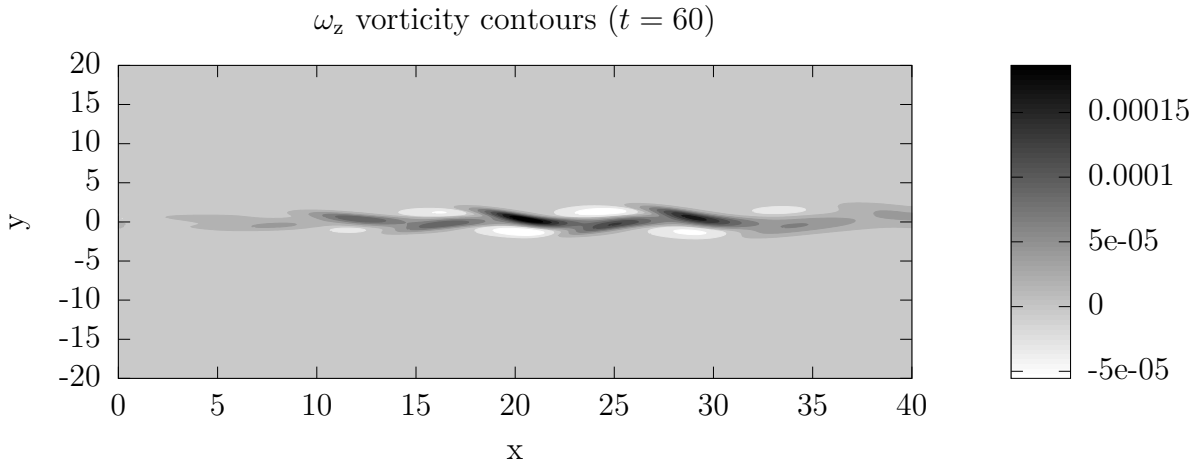

Figure 6.248: Vorticity contours for the short domain, 20 unit sponge-layer with 5-times viscosity increase case.

6.20 Time-averaged fields

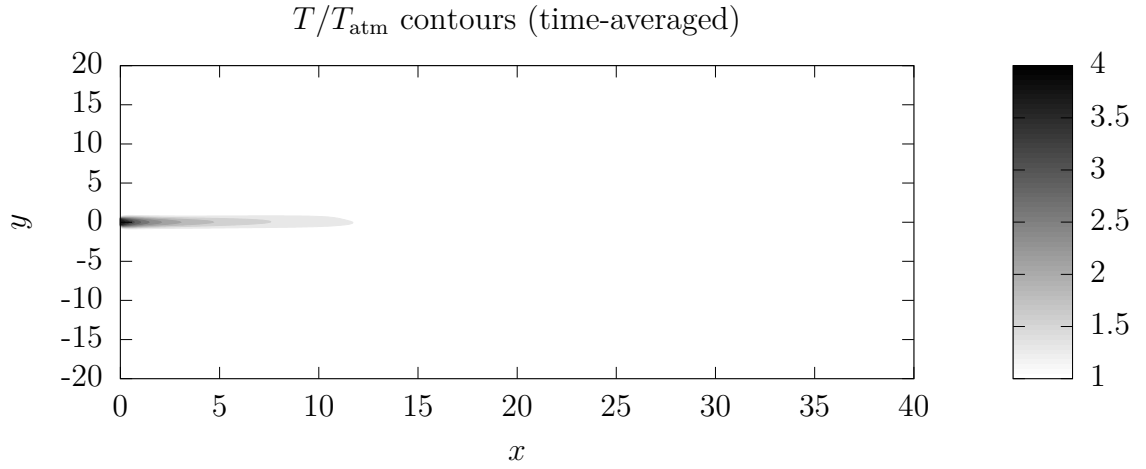

Figure 6.249: Temperature contours for the long domain, no sponge-layer case.

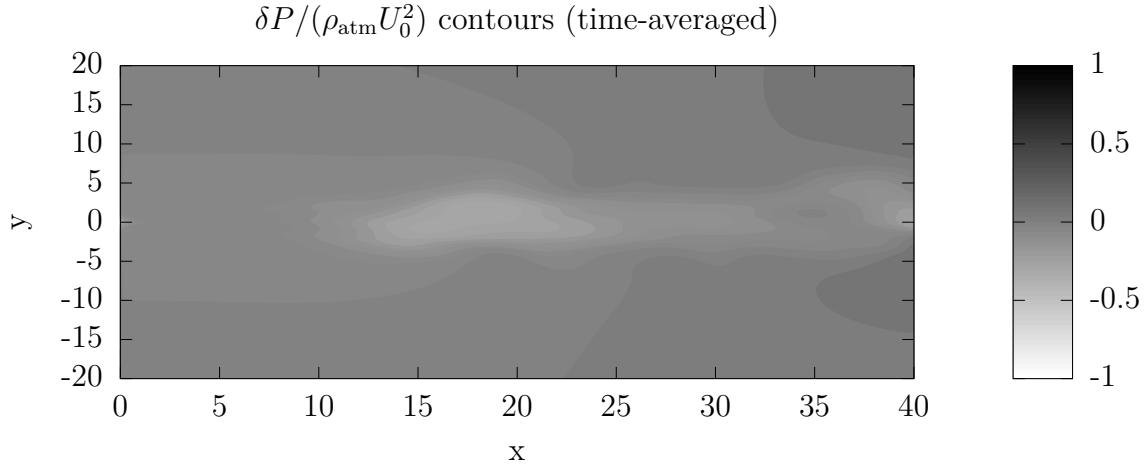

Figure 6.250: Pressure contours for the long domain, no sponge-layer case.

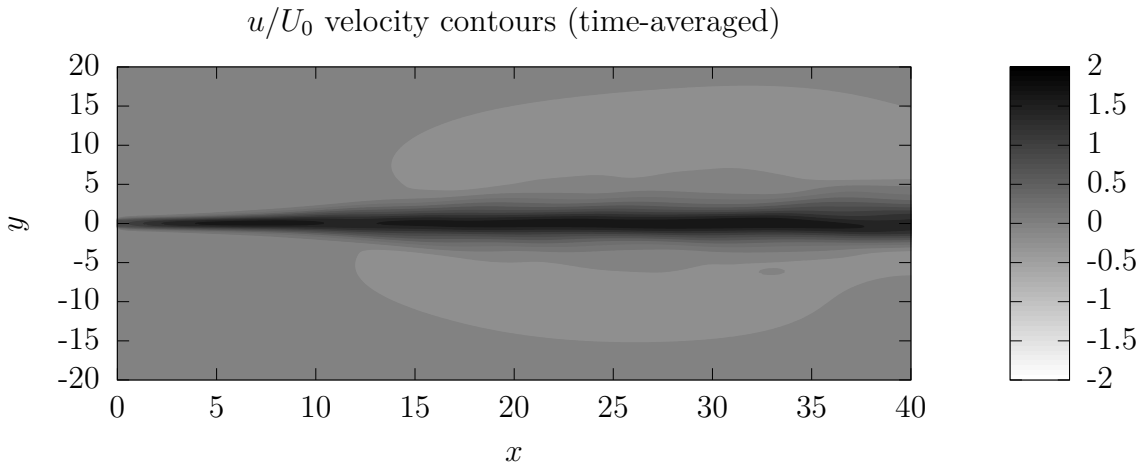

Figure 6.251: u-velocity contours for the long domain, no sponge-layer case.

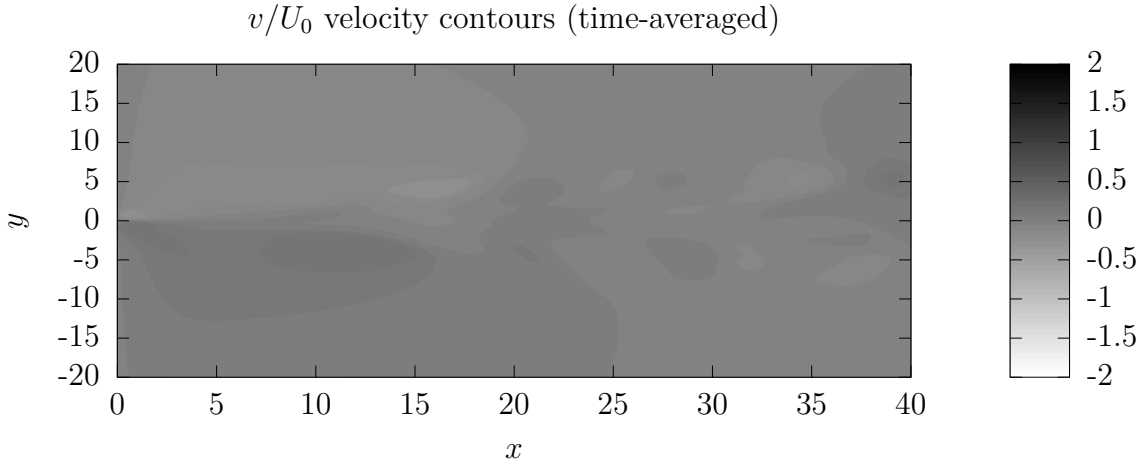

Figure 6.252: v-velocity contours for the long domain, no sponge-layer case.

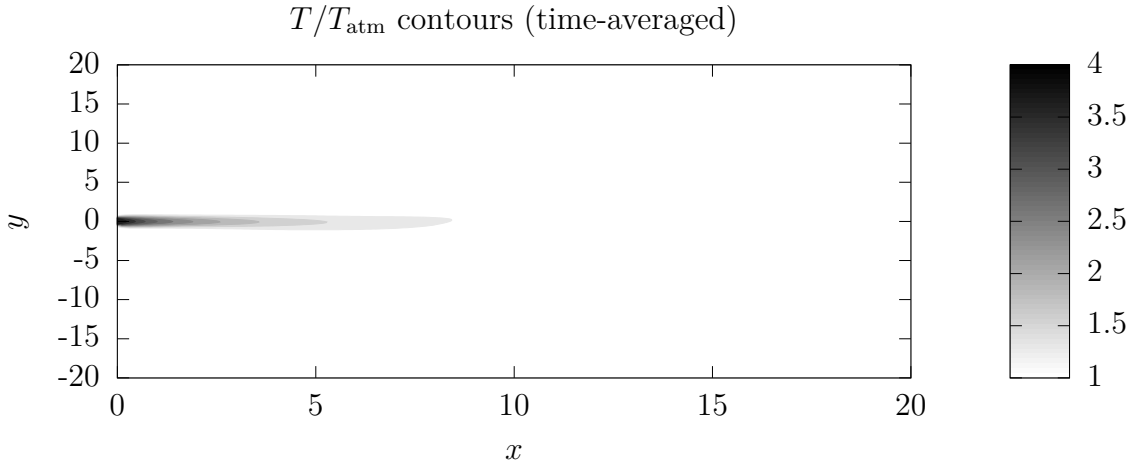

Figure 6.253: Temperature contours for the short domain, no sponge-layer case.

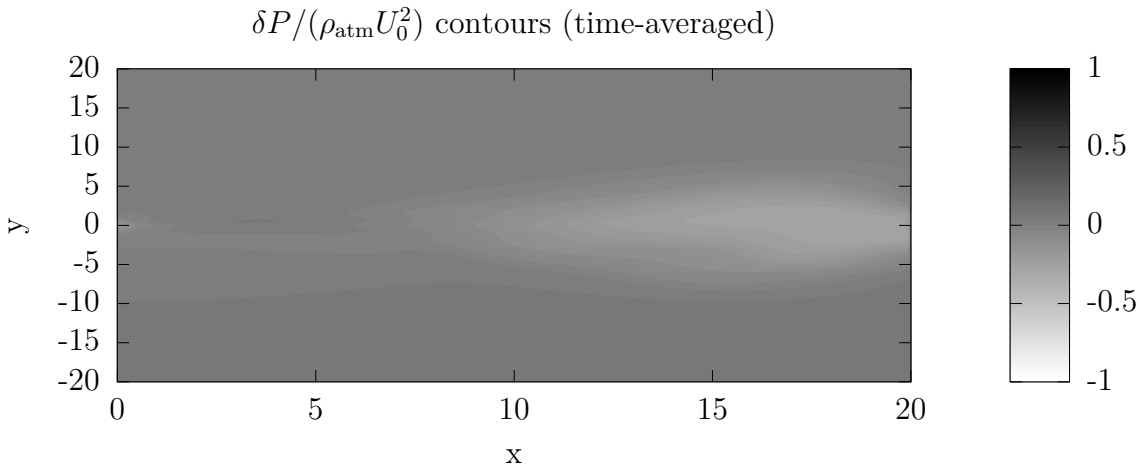

Figure 6.254: Pressure contours for the short domain, no sponge-layer case.

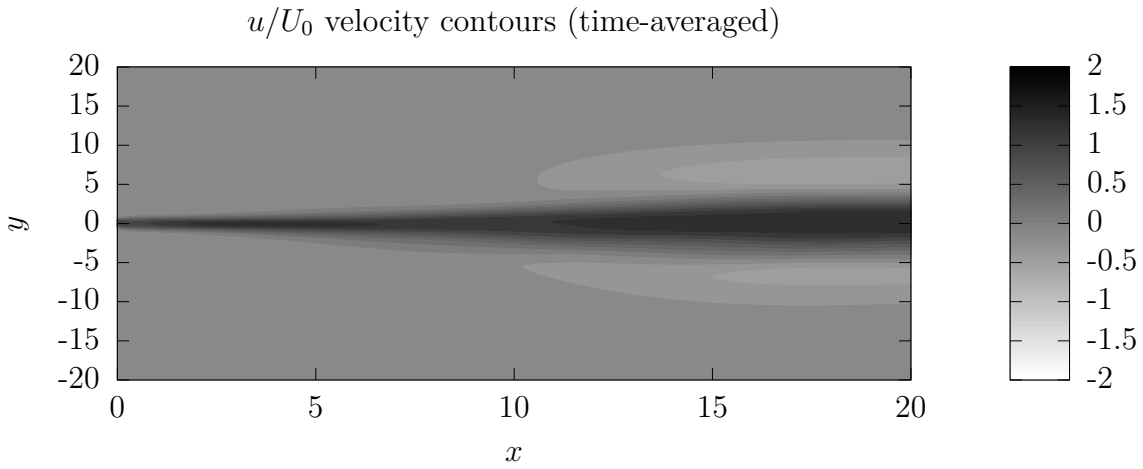

Figure 6.255: u-velocity contours for the short domain, no sponge-layer case.

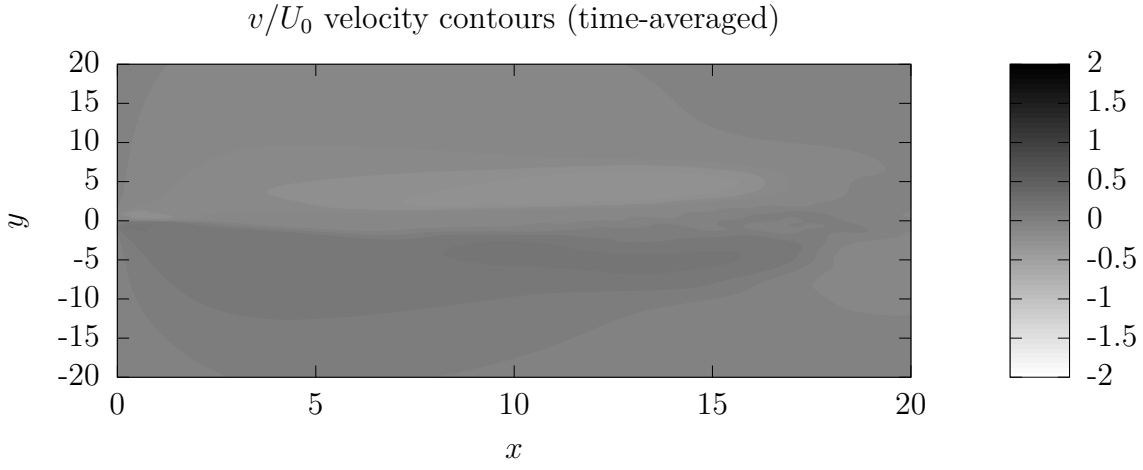

Figure 6.256: v-velocity contours for the short domain, no sponge-layer case.

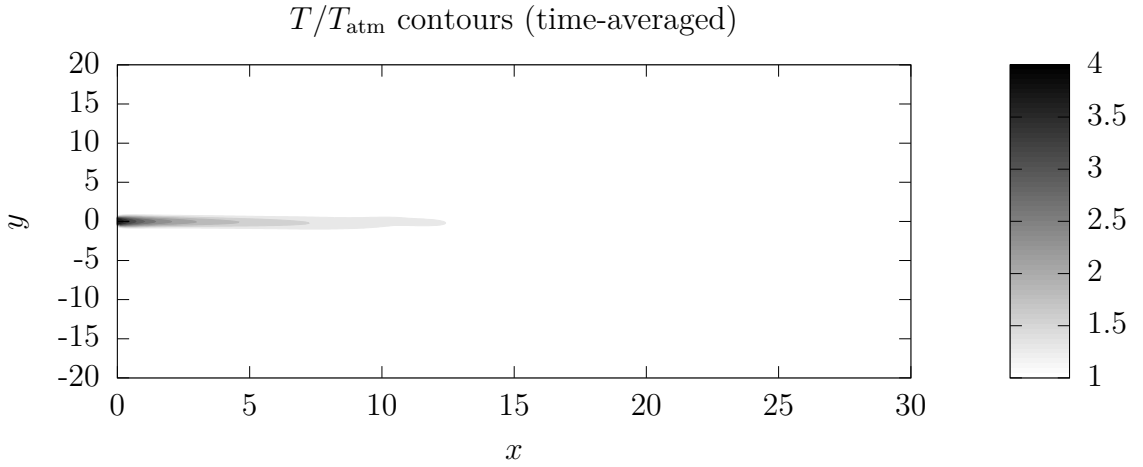

Figure 6.257: Temperature contours for the short domain, 10 unit sponge-layer with 5-times viscosity increase case.

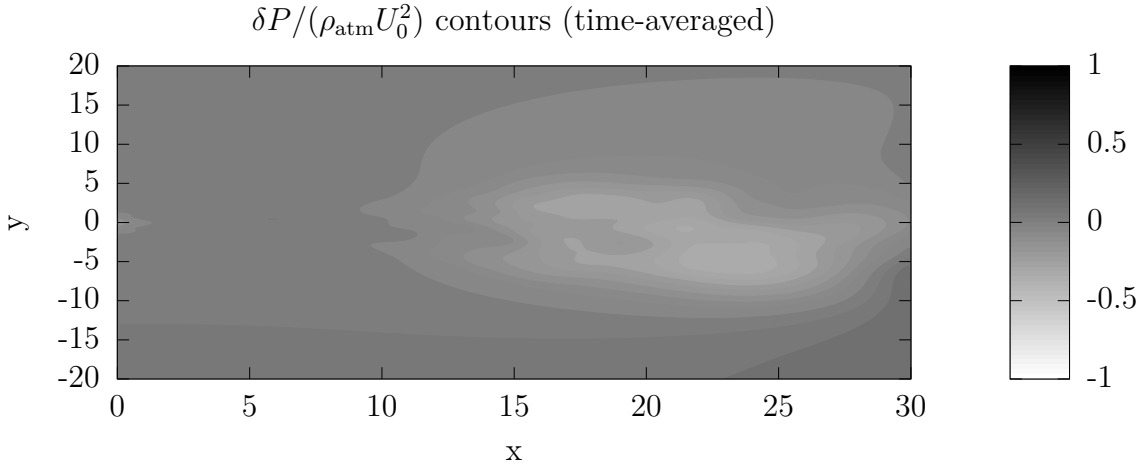

Figure 6.258: Pressure contours for the short domain, 10 unit sponge-layer with 5-times viscosity increase case.

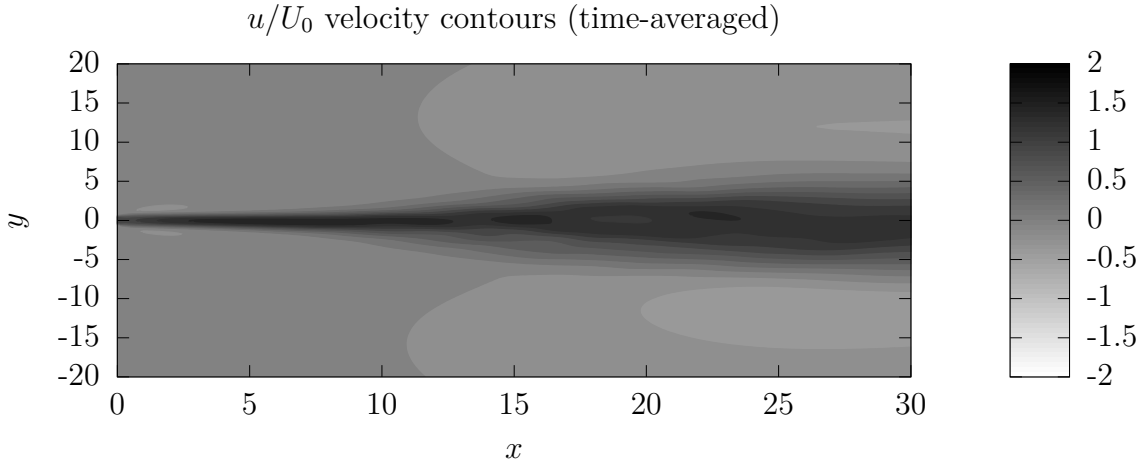

Figure 6.259: u-velocity contours for the short domain, 10 unit sponge-layer with 5-times viscosity increase case.

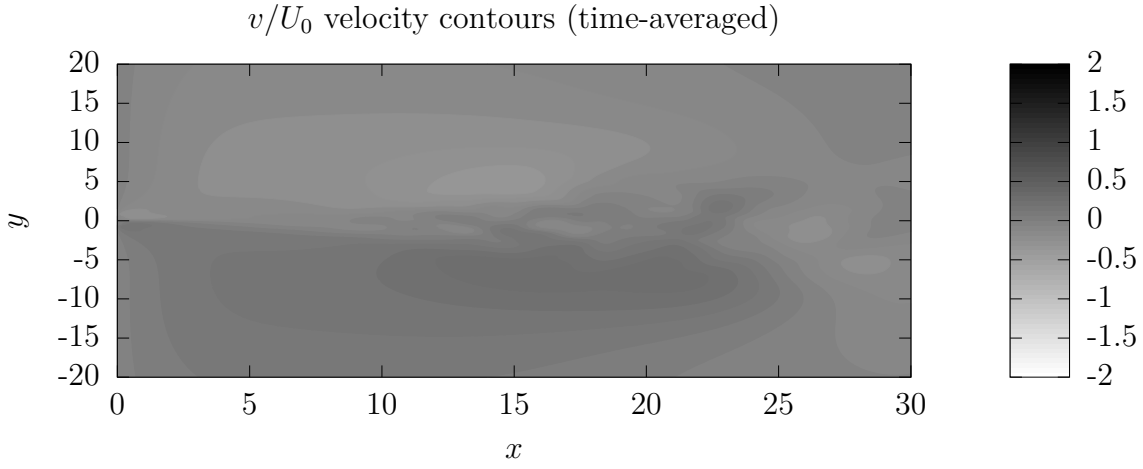

Figure 6.260: v-velocity contours for the short domain, 10 unit sponge-layer with 5-times viscosity increase case.

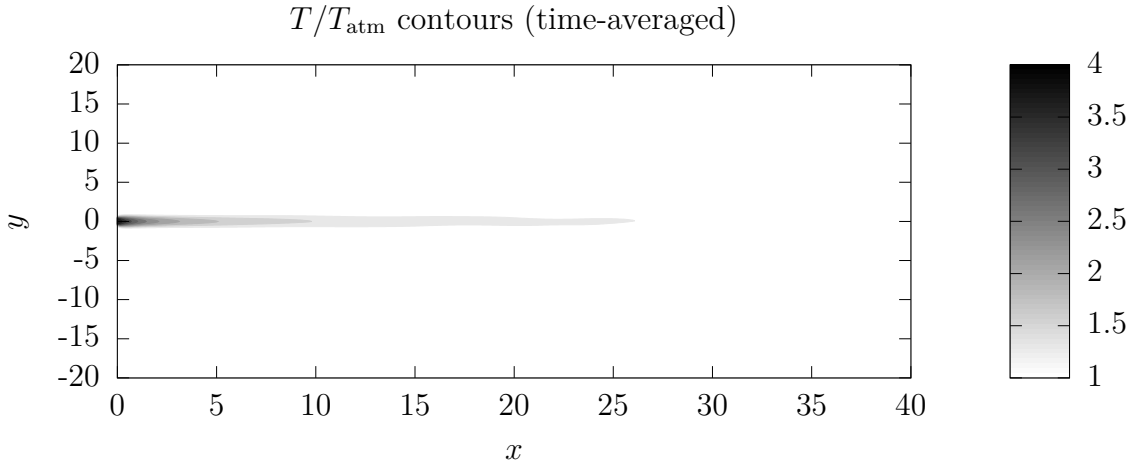

Figure 6.261: Temperature contours for the short domain, 20 unit sponge-layer with 5-times viscosity increase case.

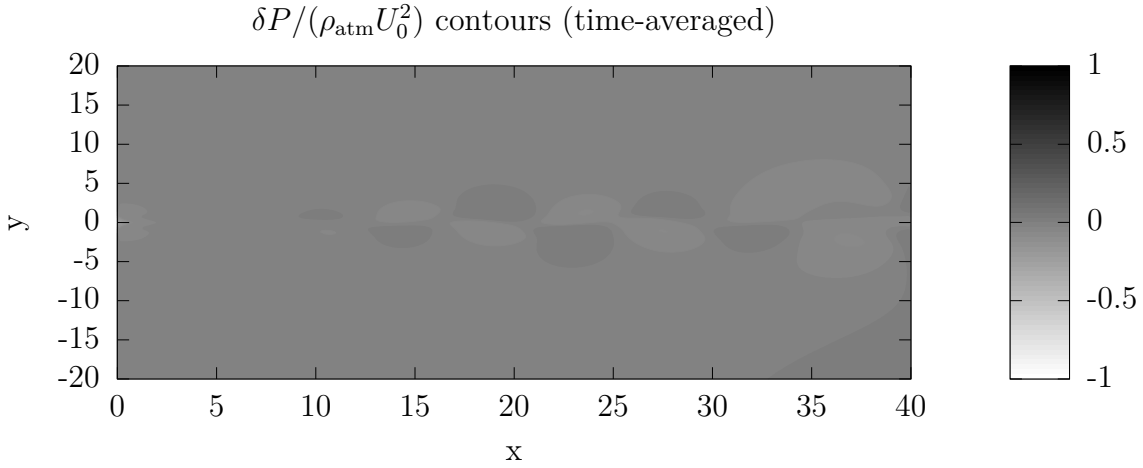

Figure 6.262: Pressure contours for the short domain, 20 unit sponge-layer with 5-times viscosity increase case.

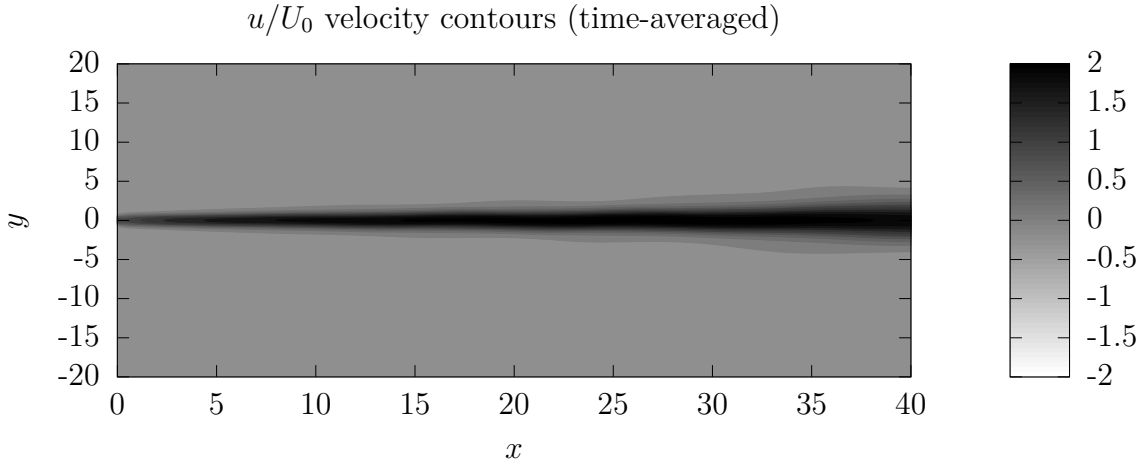

Figure 6.263: u-velocity contours for the short domain, 20 unit sponge-layer with 5-times viscosity increase case.

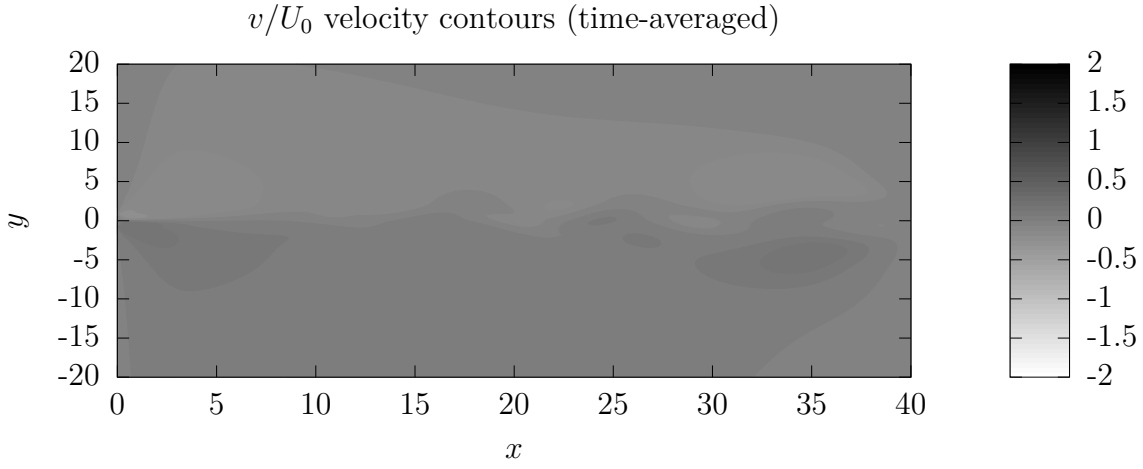

Figure 6.264: v-velocity contours for the short domain, 20 unit sponge-layer with 5-times viscosity increase case.

6.21 Instantaneous centerlines

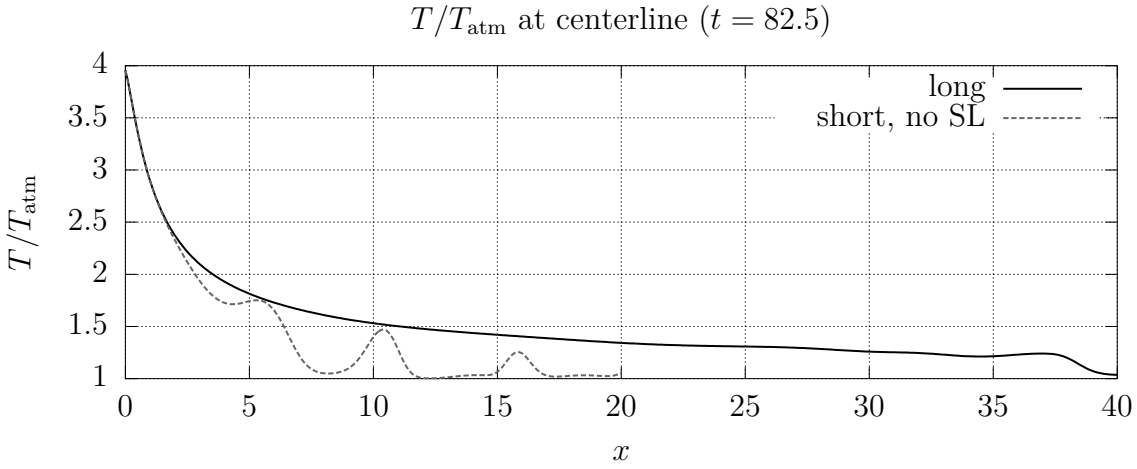

Figure 6.265: Comparison of long-domain temperatures with short domain, no sponge-layer temperatures at the centerline.

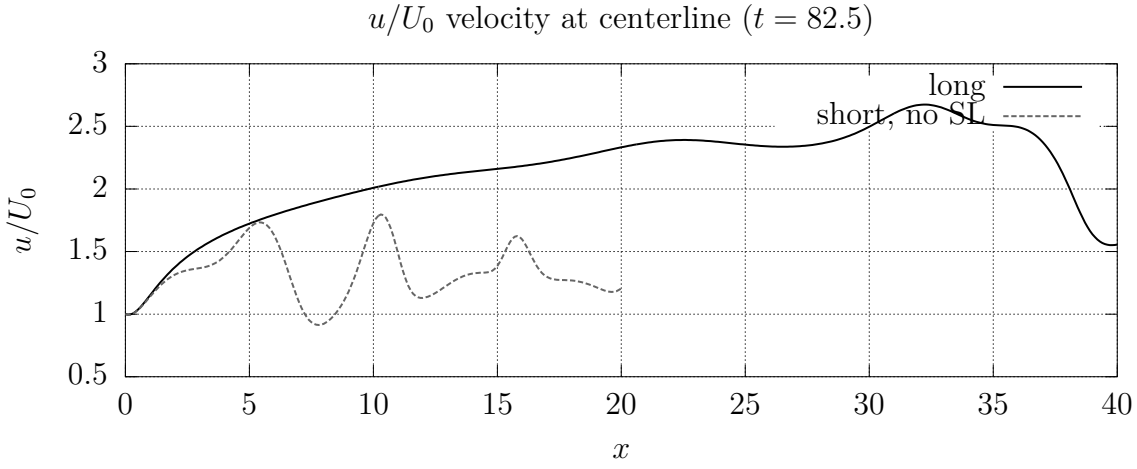

Figure 6.266: Comparison of long-domain u-velocity with short domain, no sponge-layer u-velocity at the centerline.

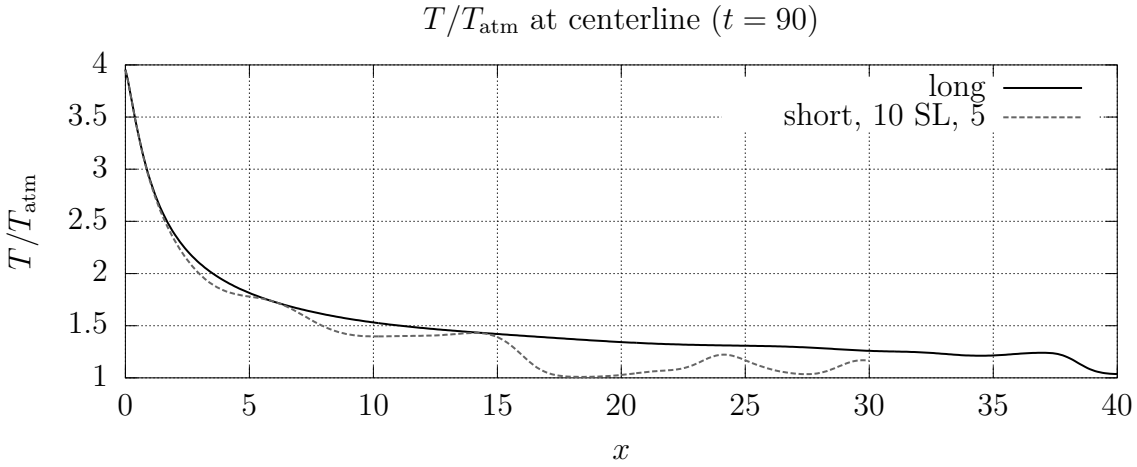

Figure 6.267: Comparison of long-domain temperatures with short domain, 10 unit sponge-layer with 5-times viscosity increase temperatures at the centerline.

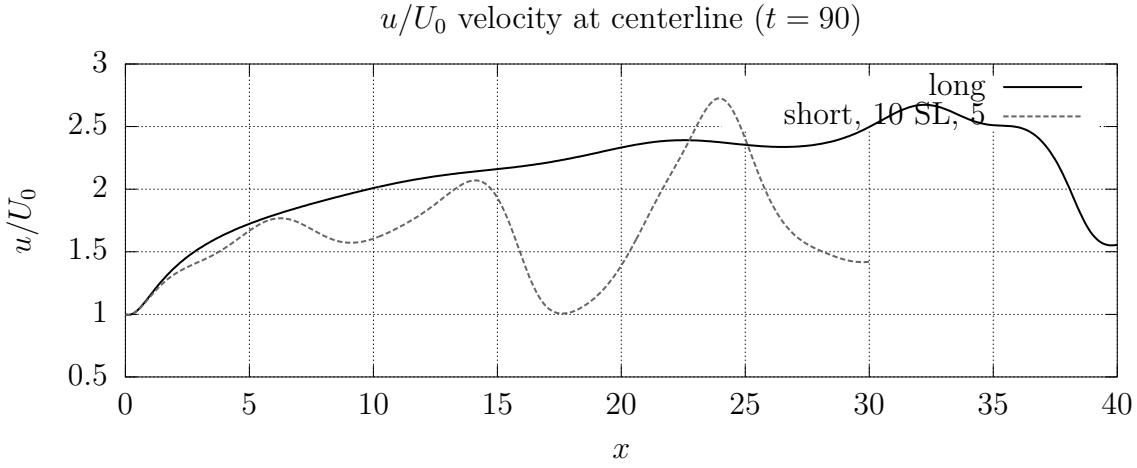

Figure 6.268: Comparison of long-domain u-velocity with short domain, 10 unit sponge-layer with 5-times viscosity increase u-velocity at the centerline.

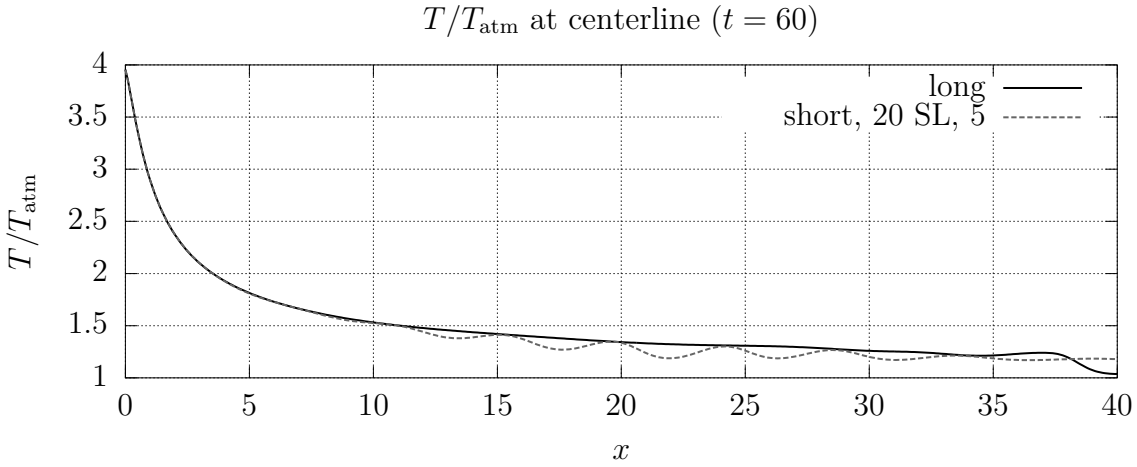

Figure 6.269: Comparison of long-domain temperatures with short domain, 20 unit sponge-layer with 5-times viscosity increase temperatures at the centerline.

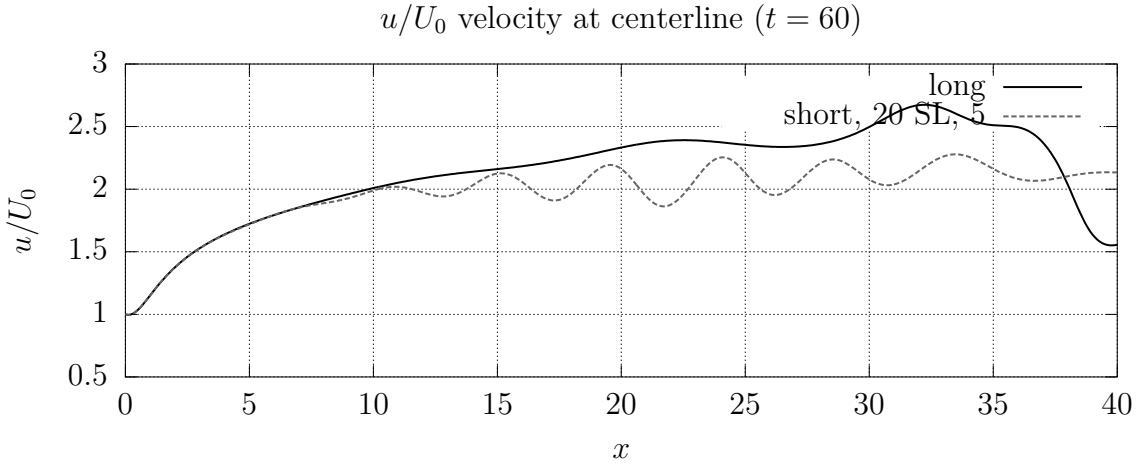

Figure 6.270: Comparison of long-domain u-velocity with short domain, 20 unit sponge-layer with 5-times viscosity increase u-velocity at the centerline.

6.22 Time-averaged centerlines

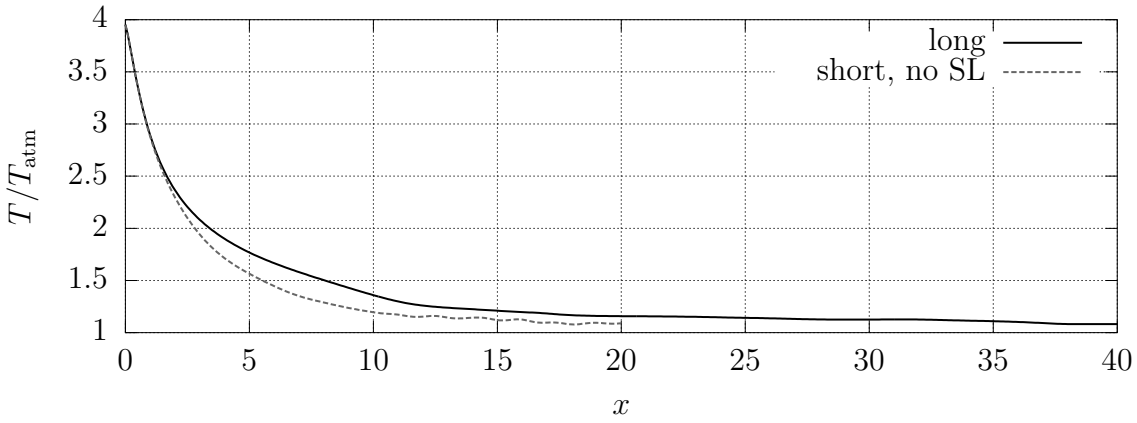

Figure 6.271: Comparison of long-domain time-averaged temperatures with short domain, no sponge-layer time-averaged temperatures at the centerline.

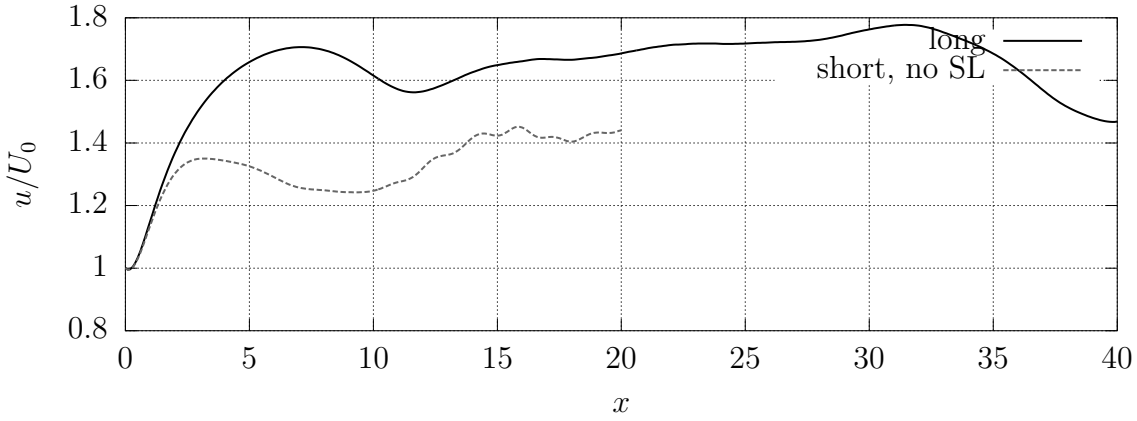

Figure 6.272: Comparison of long-domain time-averaged u-velocity with short domain, no sponge-layer time-averaged u-velocity at the centerline.

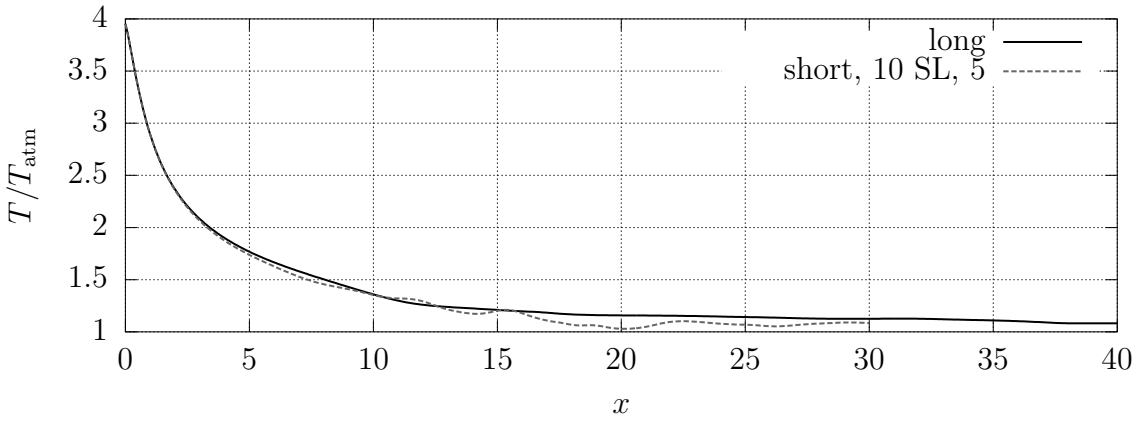

Figure 6.273: Comparison of long-domain time-averaged temperatures with short domain, 10 unit sponge-layer with 5-times viscosity increase time-averaged temperatures at the centerline.

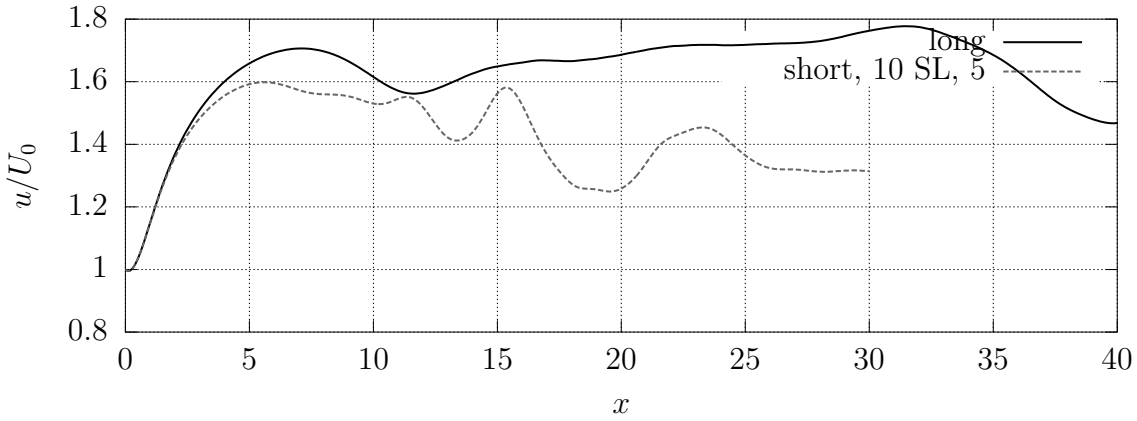

Figure 6.274: Comparison of long-domain time-averaged u-velocity with short domain, 10 unit sponge-layer with 5-times viscosity increase time-averaged u-velocity at the centerline.

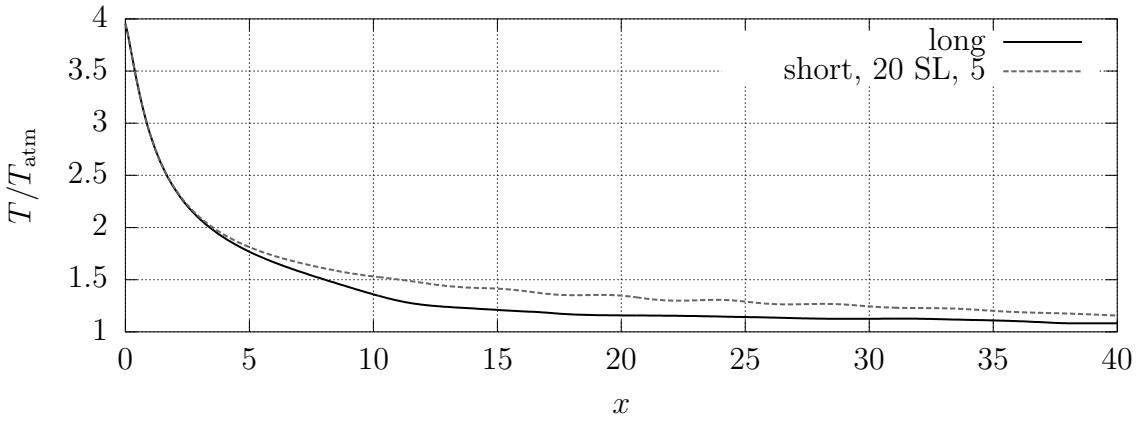

Figure 6.275: Comparison of long-domain time-averaged temperatures with short domain, 20 unit sponge-layer with 5-times viscosity increase time-averaged temperatures at the centerline.

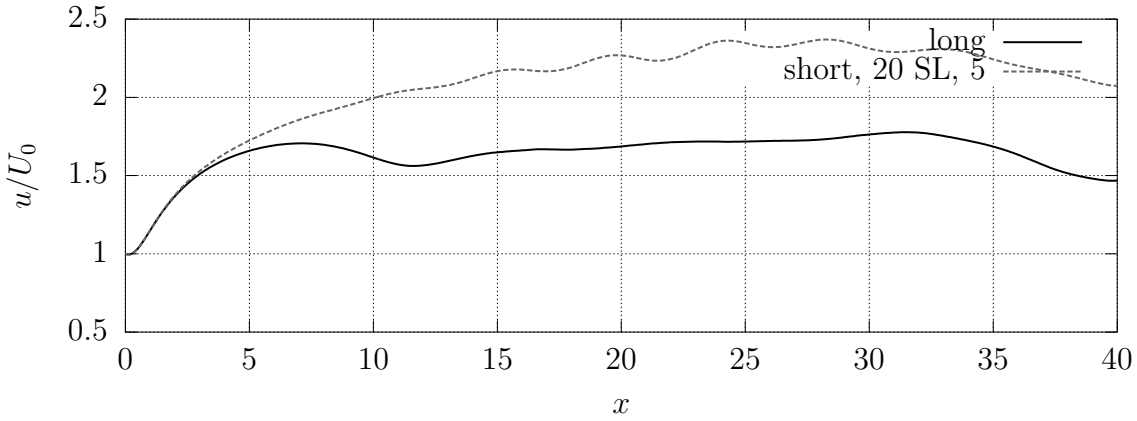

Figure 6.276: Comparison of long-domain time-averaged u-velocity with short domain, 20 unit sponge-layer with 5-times viscosity increase time-averaged u-velocity at the centerline.

6.23 Instantaneous outflow profiles

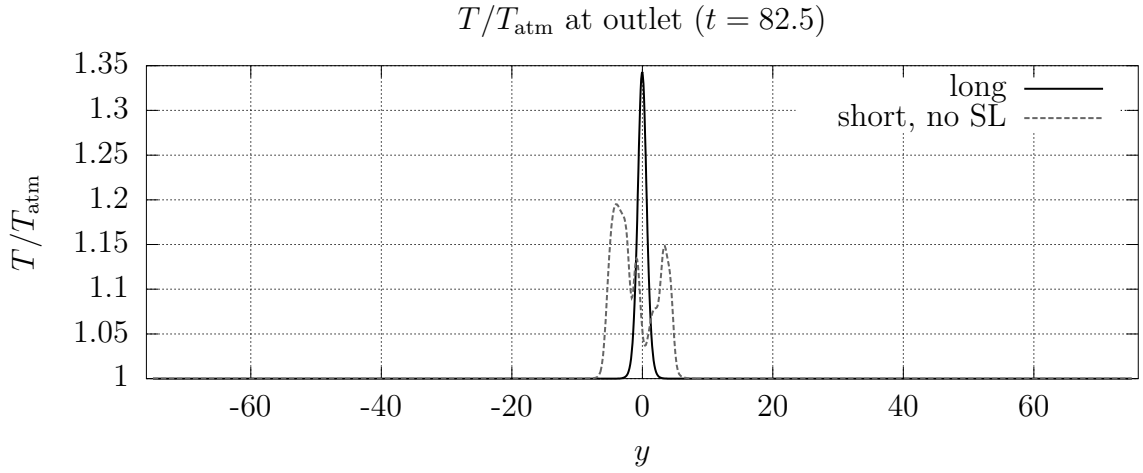

Figure 6.277: Temperature at the outlet for short domain, no sponge-layer case.

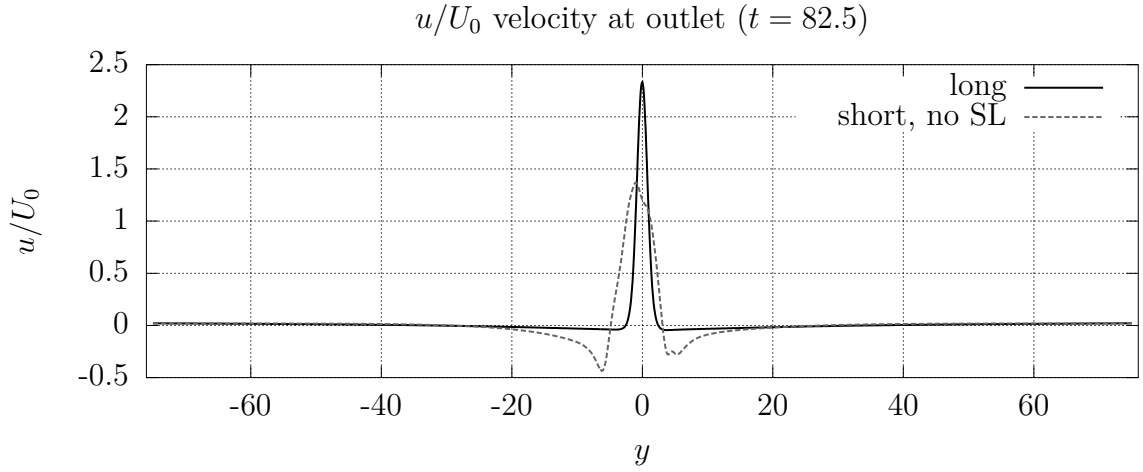

Figure 6.278: u-velocity at the outlet for short domain, no sponge-layer case.

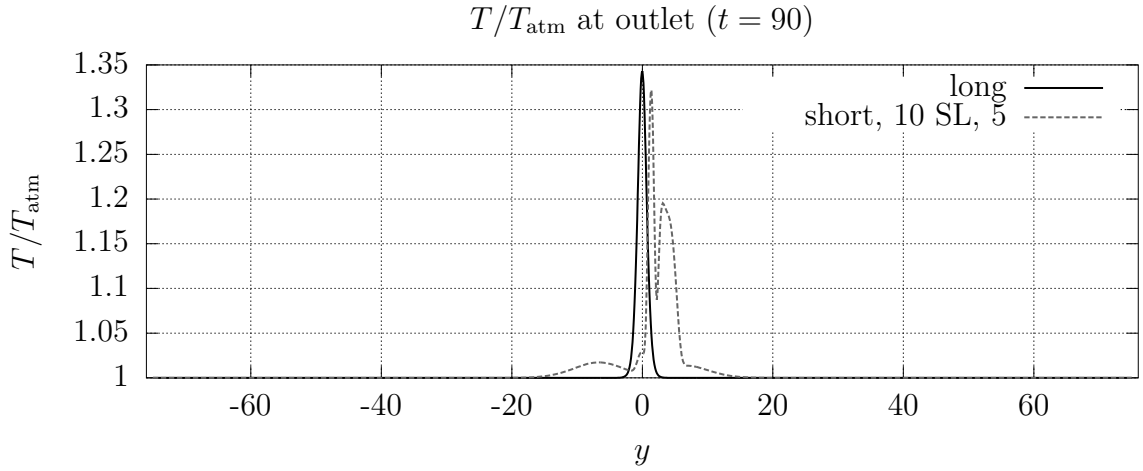

Figure 6.279: Temperature at the outlet for short domain, 10 unit sponge-layer with 5-times viscosity increase case.

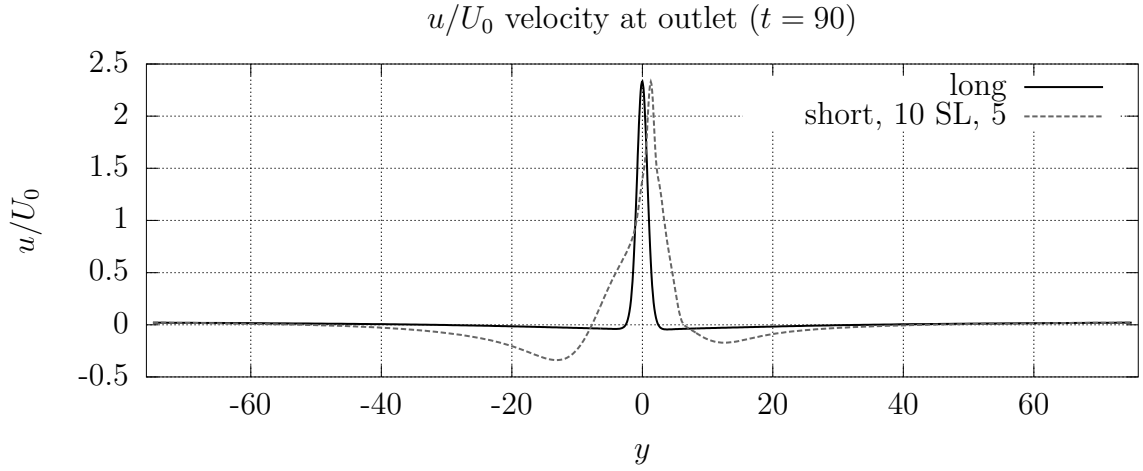

Figure 6.280: u-velocity at the outlet for short domain, 10 unit sponge-layer with 5-times viscosity increase case.

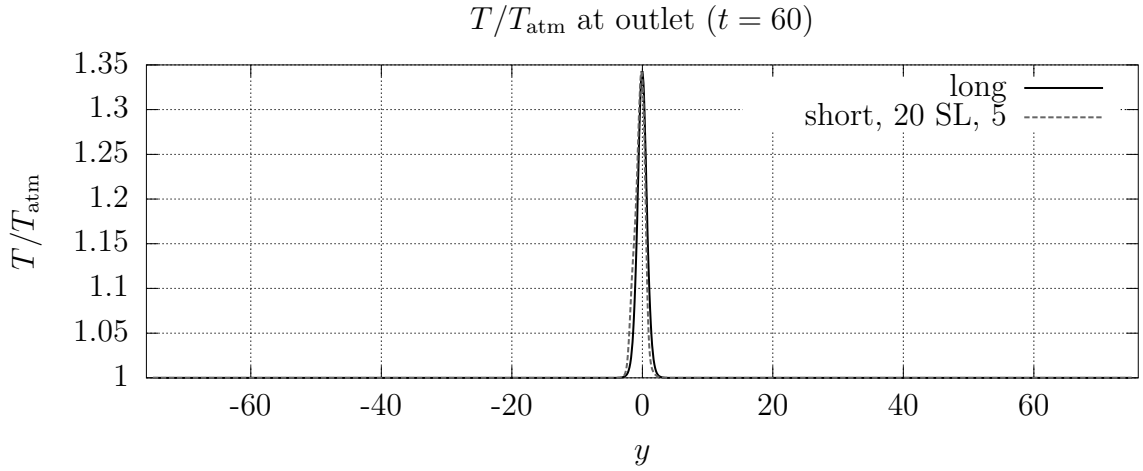

Figure 6.281: Temperature at the outlet for short domain, 20 unit sponge-layer with 5-times viscosity increase case.

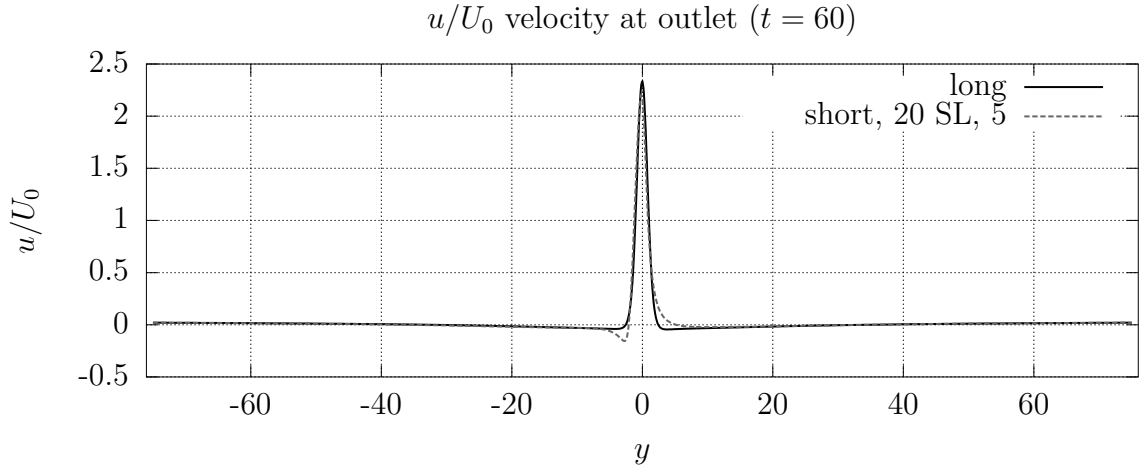

Figure 6.282: u-velocity at the outlet for short domain, 20 unit sponge-layer with 5-times viscosity increase case.

6.24 Time-averaged outflow profiles

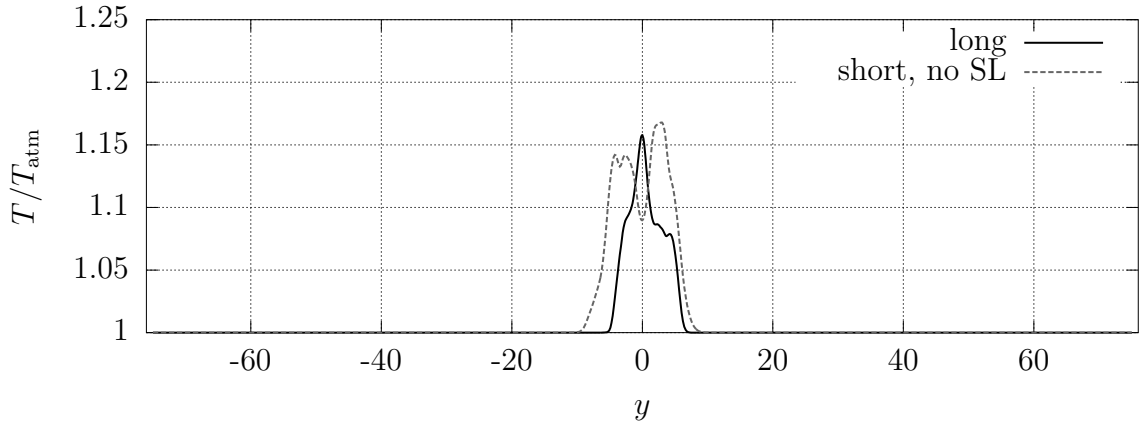

Figure 6.283: Time-averaged temperature at the outlet for short domain, no sponge-layer case.

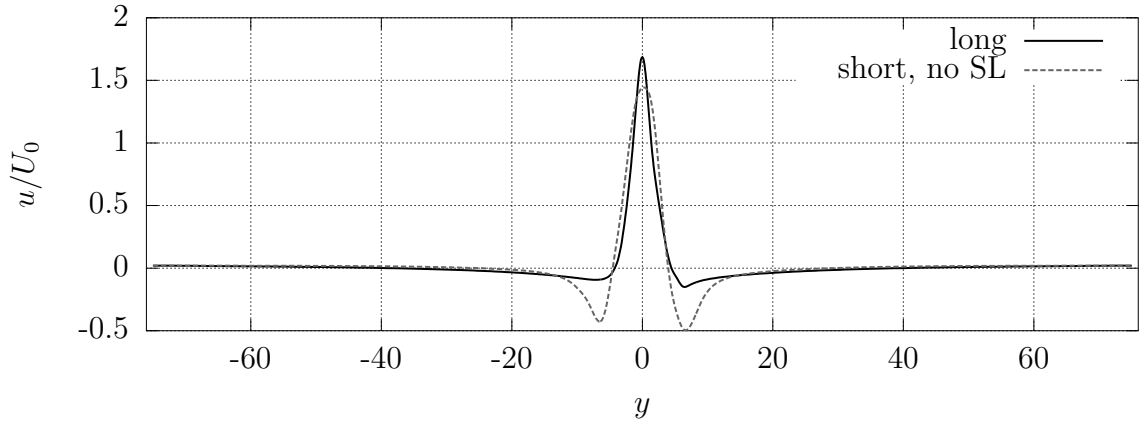

Figure 6.284: Time-averaged u-velocity at the outlet for short domain, no sponge-layer case.

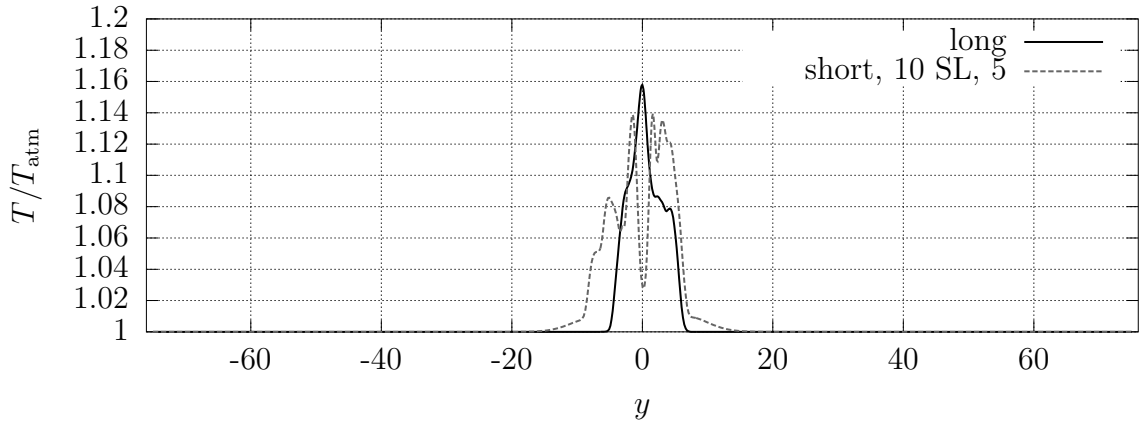

Figure 6.285: Time-averaged temperature at the outlet for short domain, 10 unit sponge-layer with 5-times viscosity increase case.

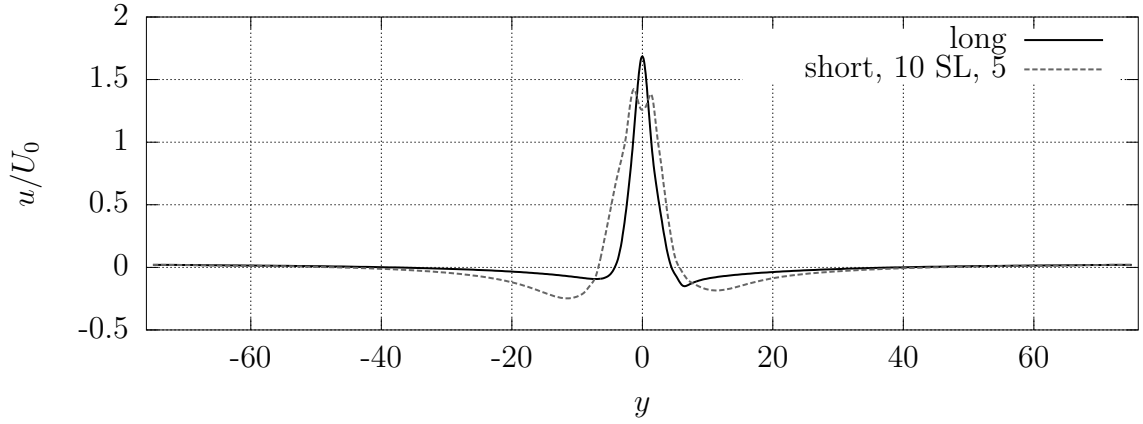

Figure 6.286: Time-averaged u-velocity at the outlet for short domain, 10 unit sponge-layer with 5-times viscosity increase case.

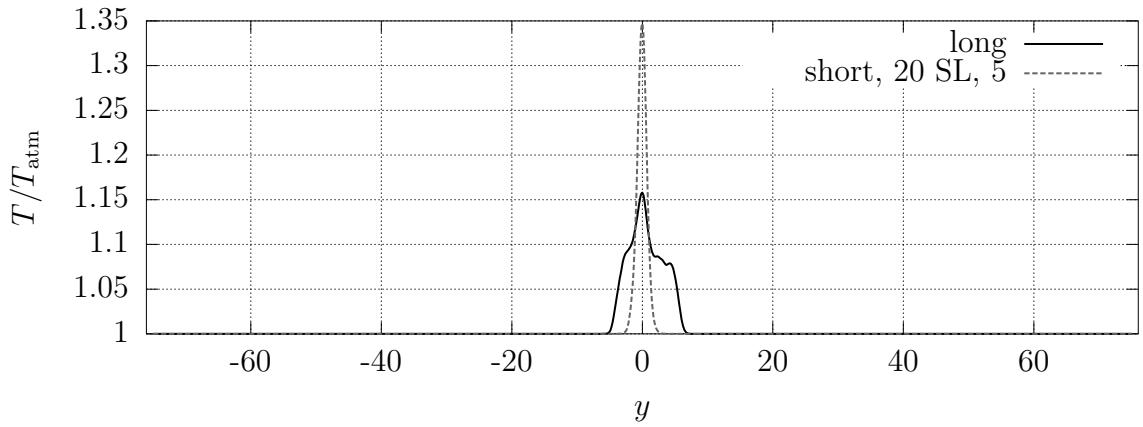

Figure 6.287: Time-averaged temperature at the outlet for short domain, 20 unit sponge-layer with 5-times viscosity increase case.

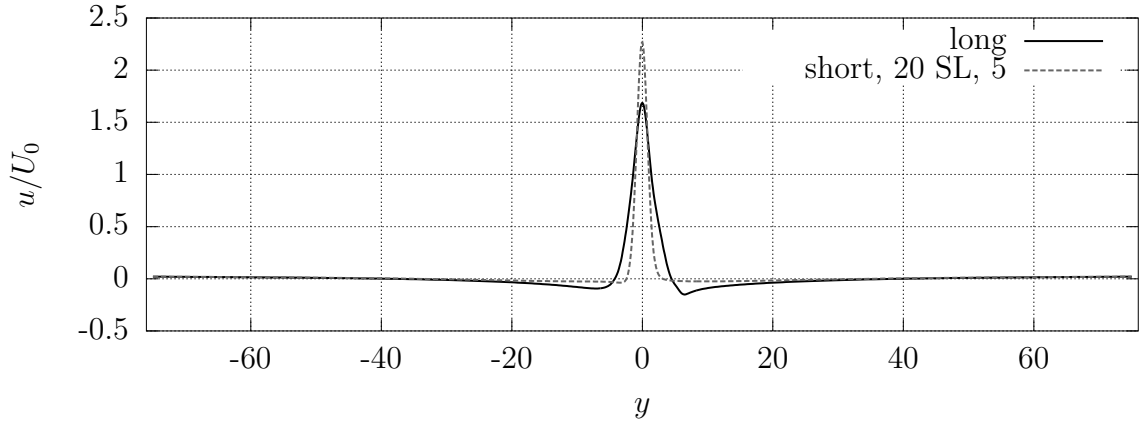

Figure 6.288: Time-averaged u-velocity at the outlet for short domain, 20 unit sponge-layer with 5-times viscosity increase case.

6.25 Probes

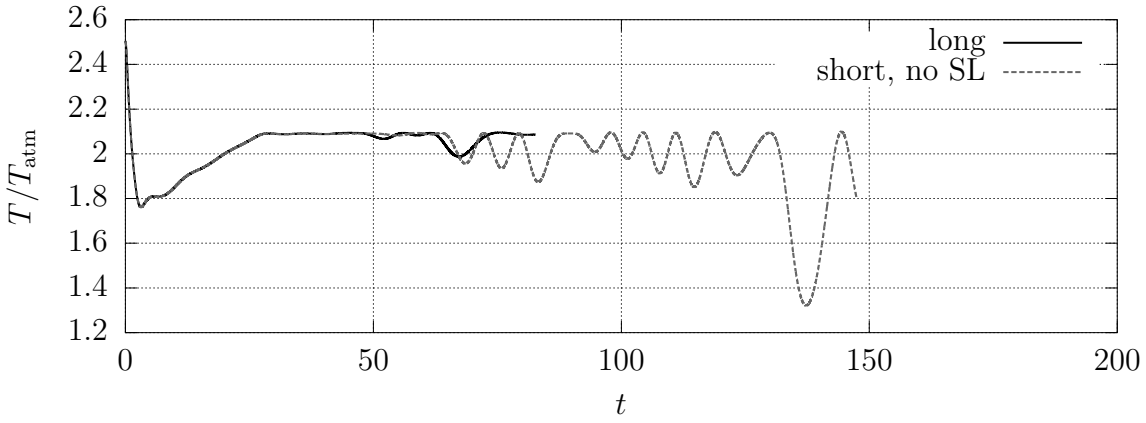

Figure 6.289: Centerline temperature probe one jet width from the inlet for short domain, no sponge-layer case.

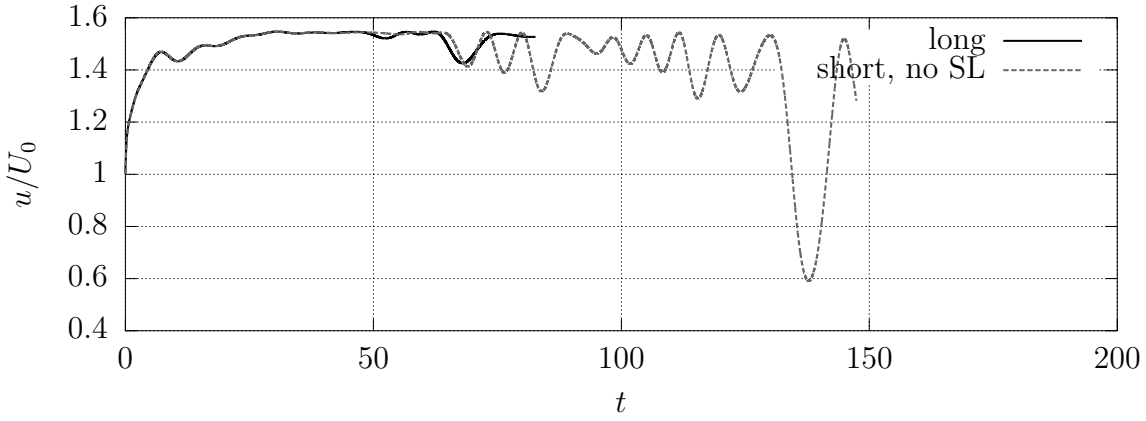

Figure 6.290: Centerline u-velocity probe one jet width from the inlet for short domain, no sponge-layer case.

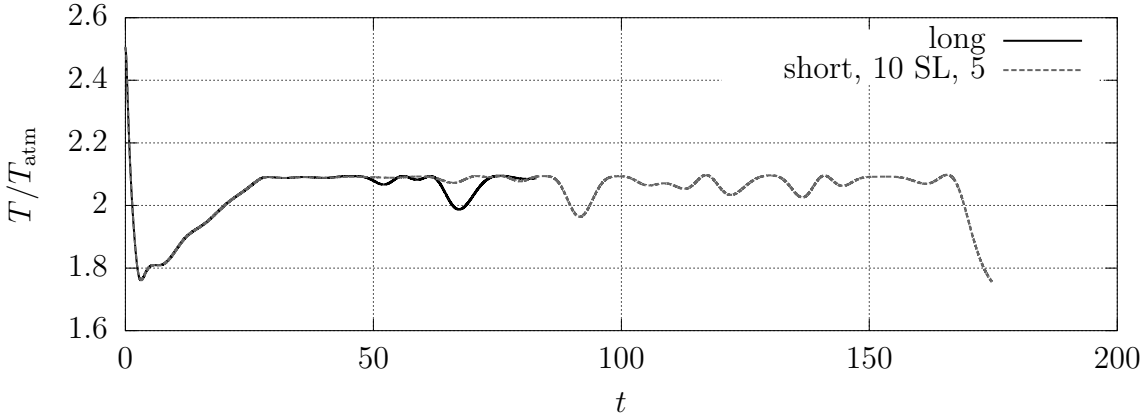

Figure 6.291: Centerline temperature probe one jet width from the inlet for short domain, 10 unit sponge-layer with 5-times viscosity increase case.

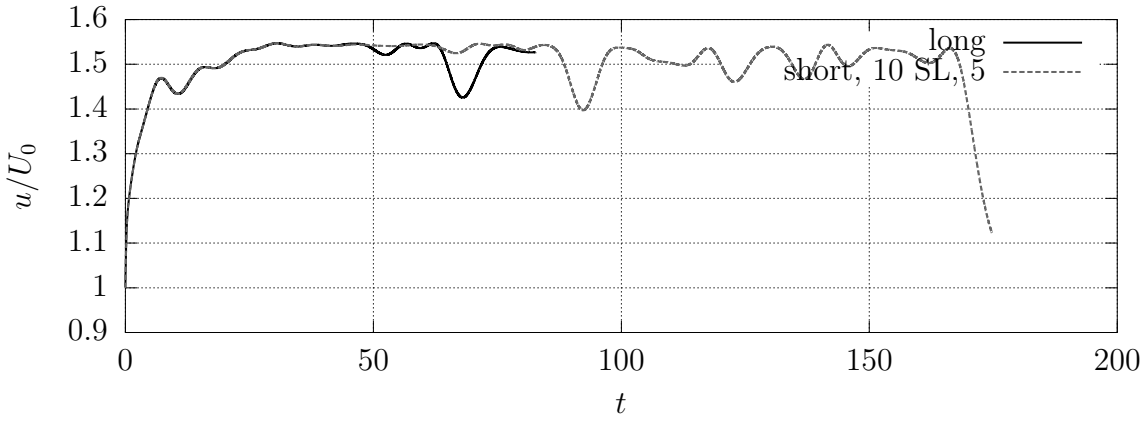

Figure 6.292: Centerline u-velocity probe one jet width from the inlet for short domain, 10 unit sponge-layer with 5-times viscosity increase case.

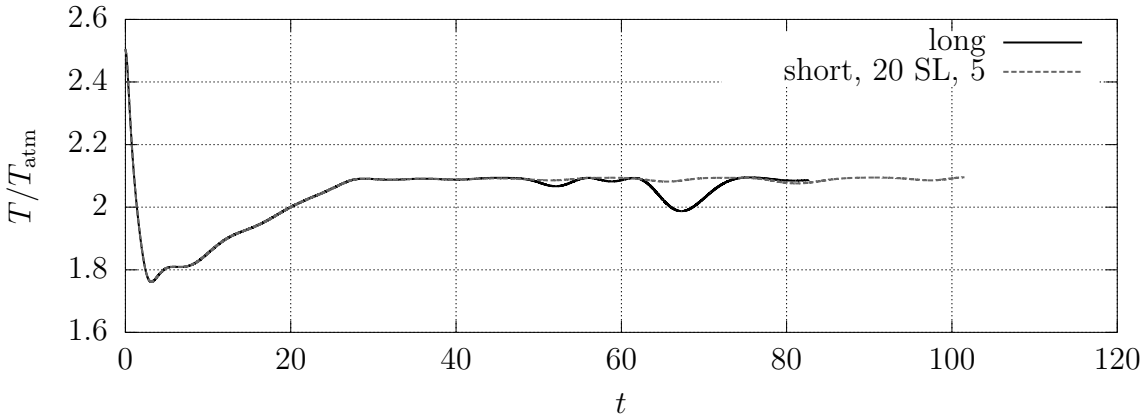

Figure 6.293: Centerline temperature probe one jet width from the inlet for short domain, 20 unit sponge-layer with 5-times viscosity increase case.

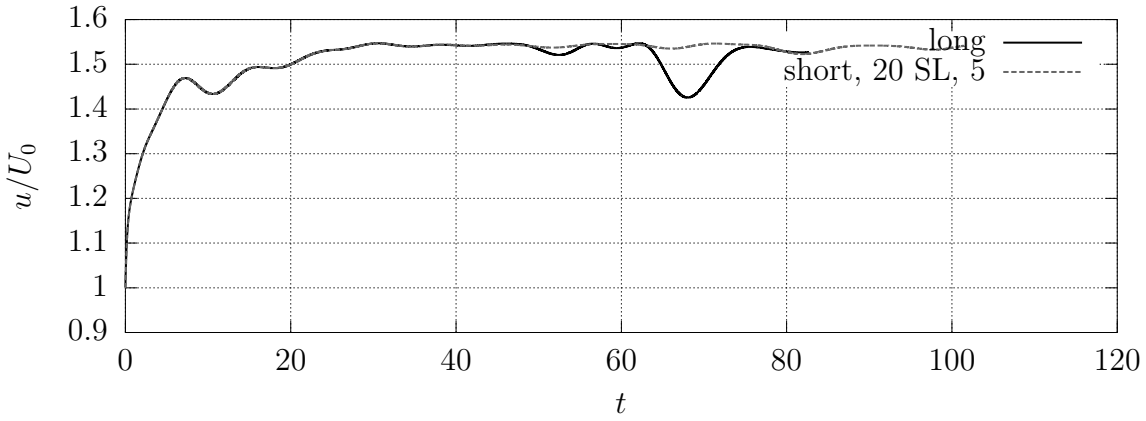

Figure 6.294: Centerline u-velocity probe one jet width from the inlet for short domain, 20 unit sponge-layer with 5-times viscosity increase case.

References

[AS03] S. Armfield and R. Street. "The pressure accuracy of fractional-step methods for the Navier-Stokes equations on staggered grids". In: *ANZIAM Journal* 44 (Jan. 2003), pp. C20–C39. ISSN: 1446-8735. URL: http://dev.journal.austms.org.au/ojs/index.php/ANZIAMJ/article/view/670 (cit. on p. 8).

[ATP84] D. E. Anderson, J. C. Tannehill, and R. H. Pletcher. *Computational Fluid Mechanics and Heat Transfer*. 1st. Hemisphere, Jan. 1984. ISBN: 0891164715 (cit. on p. 18).

[Bra13] L. Bravo. "Large Eddy Simulation of Boundary Layer Combustion". PhD thesis. University of Maryland, College Park, May 2013 (cit. on pp. 17, 24).

[CDS98] B. M. Cetegen, Y. Dong, and M. C. Soteriou. "Experiments on stability and oscillatory behavior of planar buoyant plumes". In: *Physics of Fluids* 10.7 (July 1998), pp. 1658–1665. ISSN: 10706631. URL: http://pof.aip.org/resource/1/phfle6/v10/i7/p1658_s1 (cit. on pp. 31–33, 42).

[Col04] T. Colonius. "Modeling Artificial Boundary Conditions for Compressible Flow". In: *Annual Review of Fluid Mechanics* 36.1 (2004), pp. 315–345. URL: http://www.annualreviews.org/doi/abs/10.1146/annurev.fluid.36.050802.121930 (cit. on pp. 1, 11–15).

[Dut88] P. Dutt. "Stable Boundary Conditions and Difference Schemes for Navier-Stokes Equations". In: *SIAM Journal on Numerical Analysis* 25.2 (Apr. 1988), pp. 245–267. ISSN: 0036-1429. URL: http://www.jstor.org/stable/2157314 (cit. on p. 10).

[FGP08] G. Fournier, F. Golanski, and A. Pollard. "A novel outflow boundary condition for incompressible laminar wall-bounded flows". In: *Journal of Computational Physics* 227.15 (July 2008), pp. 7077–7082. ISSN: 0021-9991. URL: http://www.sciencedirect.com/science/article/pii/S0021999108001794 (cit. on p. 4).

[GS87] P. M. Gresho and R. L. Sani. "On pressure boundary conditions for the incompressible Navier-Stokes equations". In: *International Journal for Numerical Methods in Fluids* 7.10 (1987), 1111–1145. ISSN: 1097-0363.

URL: http://onlinelibrary.wiley.com/doi/10.1002/fld.1650071008/abstract (cit. on pp. 5, 9).

[Hes02] G. Heskestad. "Fire Plumes, Flame Height, and Air Entrainment". In: *SFPE Handbook of Fire Protection Engineering*. 3rd ed. National Fire Protection Association, Mar. 2002, pp. 2.1–2.17. ISBN: 0877654514 (cit. on p. 44).

[Hir13] C. W. Hirt. *Boundary Conditions Outflow*. 2013. URL: http://www.flow3d.com/cfd-101/cfd-101-boundary-outflow.html (cit. on p. 3).

[KM85] J. Kim and P. Moin. "Application of a fractional-step method to incompressible Navier-Stokes equations". In: *Journal of Computational Physics* 59.2 (June 1985), pp. 308–323. ISSN: 0021-9991. URL: http://www.sciencedirect.com/science/article/pii/0021999185901482 (cit. on pp. 7, 9).

[McG+13] K. McGrattan et al. *Fire Dynamics Simulator (Version 6) Technical Reference Guide, Volume 1: Mathematical Model*. Special Publication 1018. Gaithersburg, MD: NIST, 2013. URL: https://code.google.com/p/fds-smv/ (cit. on pp. 3, 6).

[Ope11] OpenFOAM. *buoyantPressureFvPatchScalarField.C*. 2011. URL: http://foam.sourceforge.net/docs/cpp/a04319_source.html (cit. on p. 7).

[Orl76] I. Orlanski. "A simple boundary condition for unbounded hyperbolic flows". In: *Journal of Computational Physics* 21.3 (July 1976), pp. 251–269. ISSN: 0021-9991. URL: http://www.sciencedirect.com/science/article/pii/0021999176900231 (cit. on p. 4).

[Pet01] N. Petersson. "Stability of Pressure Boundary Conditions for Stokes and Navier–Stokes Equations". In: *Journal of Computational Physics* 172.1 (Sept. 2001), pp. 40–70. ISSN: 0021-9991. URL: http://www.sciencedirect.com/science/article/pii/S0021999101967543 (cit. on p. 10).

[Pie01] C. D. Pierce. "Progress-variable approach for large-eddy simulation of turbulent combustion". PhD thesis. Stanford, June 2001. URL: http://www.stanford.edu/group/ctr/pdf/charles_pierce_thesis.pdf (cit. on pp. 4, 17, 22).

[PV05] T. Poinsot and D. Veynante. *Theoretical and Numerical Combustion*. 2nd ed. R.T. Edwards, Inc., Jan. 2005. ISBN: 1930217102 (cit. on pp. 3, 10, 17–19, 21).

[SDC02] M. C. Soteriou, Y. Dong, and B. M. Cetegen. "Lagrangian simulation of the unsteady near field dynamics of planar buoyant plumes". In: *Physics*

of Fluids 14.9 (Aug. 2002), pp. 3118–3140. ISSN: 10706631. URL: http://pof.aip.org/resource/1/phfle6/v14/i9/p3118_s1 (cit. on p. 42).

[Tem91] R. Temam. "Remark on the pressure boundary condition for the projection method". In: *Theoretical and Computational Fluid Dynamics* 3.3 (Dec. 1991), pp. 181–184. ISSN: 0935-4964, 1432-2250. URL: http://link.springer.com/article/10.1007/BF00271801 (cit. on p. 8).

[Tre13] B. Trettel. *Issue 1924 - fds-smv - Transport of vorticity out of OPEN boundaries*. May 2013. URL: https://code.google.com/p/fds-smv/issues/detail?id=1924 (cit. on pp. 2, 6, 11, 12).

[Tro12] A. Trouvé. *Notes on the turbulent transition in plumes*. 2012 (cit. on p. 31).

[WSB10] C. Walchshofer, H. Steiner, and G. Brenn. "Robust Outflow Boundary Conditions for Strongly Buoyant Turbulent Jet Flames". In: *Flow, Turbulence and Combustion* 86.3-4 (Oct. 2010), pp. 713–734. ISSN: 1386-6184, 1573-1987. URL: http://www.springerlink.com/content/g62515106wu111r1/?MUD=MP (cit. on pp. 2–4, 12, 14).